

## CONTENS

### ADDRESS OF PUBLISHER & EDITOR'S OFFICE:

GDAŃSK UNIVERSITY  
OF TECHNOLOGY

Faculty of Ocean Engineering  
& Ship Technology  
G. Narutowicza 11/12  
80-233 Gdańsk, POLAND

tel.: +48 58 347 13 66  
fax: +48 58 341 13 66

### EDITORIAL STAFF:

Jacek Rudnicki  
| Editor in Chief  
Przemysław Wierzchowski  
| Scientific Editor  
Jan Michalski  
| Editor for review matters  
Aleksander Kniat  
| Editor for international  
relations  
Kazimierz Kempa  
| Technical Editor  
Piotr Bzura  
| Managing Editor

Price:  
single issue: 25 zł

Prices for abroad  
single issue:  
- in Europe EURO 15  
- overseas USD 20

### WEB:

[www.bg.pg.gda.pl/pmr/pmr.php](http://www.bg.pg.gda.pl/pmr/pmr.php)

ISSN 1233-2585

- 3 **Marcin Przywarty, Lucjan Gucma, Krzysztof Marcjan, Andrzej Bąk**  
*RISK ANALYSIS OF COLLISION BETWEEN PASSENGER FERRY AND CHEMICAL TANKER IN THE WESTERN ZONE OF THE BALTIC SEA*
- 9 **Cezary SPECHT, Mateusz MANIA, Marcin SKÓRA, Mariusz SPECHT**  
*ACCURACY OF THE GPS POSITIONING SYSTEM IN THE CONTEXT OF INCREASING THE NUMBER OF SATELLITES IN THE CONSTELLATION*
- 15 **Andrzej Pięta, Maciej Mikulski, Marek Melzacki, Kamil Czerwiński**  
*A PROPOSAL OF SIMULATION MODEL OF A WIND-STEERING SYSTEM FOR SAILING YACHTS, BASED ON SINGLE-STAGE SERVO-PENDULUM COUPLED WITH MAIN RUDDER*
- 23 **Hassan Ghassemi, Mojtaba Kamarlouei, Sajad Taj Golah Veysi**  
*A HYDRODYNAMIC METHODOLOGY AND CFD ANALYSIS FOR PERFORMANCE PREDICTION OF STEPPED PLANING HULLS*
- 32 **Zygmunt Paszota**  
*COMPARISON OF THE POWERS OF ENERGY LOSSES IN A VARIABLE CAPACITY DISPLACEMENT PUMP DETERMINED WITHOUT OR WITH TAKING INTO ACCOUNT THE POWER OF HYDRAULIC OIL COMPRESSION*
- 44 **Jerzy Girtler**  
*IDENTIFICATION OF DAMAGES OF TRIBOLOGICAL ASSOCIATIONS IN CRANKSHAFT AND PISTON SYSTEMS OF TWO-STROKE INTERNAL COMBUSTION ENGINES USED AS MAIN PROPULSION IN SEA-GOING VESSELS AND PROPOSAL OF PROBABILISTIC DESCRIPTION OF LOADS AS CAUSES OF THESE DAMAGES*
- 55 **Rafał Pawletko**  
*ANALYSING APPLICABILITY OF SELECTED METHODS TO SMOOTH INDICATOR DIAGRAMS OF MARINE MEDIUM-SPEED ENGINE*
- 62 **Jerzy Swirydczuk**  
*CLOCKING IN TURBINES: REMARKS ON PHYSICAL NATURE AND GEOMETRIC REQUIREMENTS*
- 71 **Dae Seung Cho, Nikola Vladimir, Tae Muk Choi**  
*SIMPLIFIED PROCEDURE FOR THE FREE VIBRATION ANALYSIS OF RECTANGULAR PLATE STRUCTURES WITH HOLES AND STIFFENERS*
- 79 **Janusz Kozak, Jakub Kowalski**  
*PROBLEMS OF DETERMINATION OF WELDING ANGULAR DISTORTIONS OF T - FILLET JOINTS IN SHIP HULL STRUCTURES*
- 86 **Adam Mroziński, Izabela Piasecka**  
*SELECTED ASPECTS OF BUILDING , OPERATION AND ENVIRONMENTAL IMPACT OF OFFSHORE WIND POWER ELECTRIC PLANTS*
- 93 **Marcin Zastempowski, Andrzej Bochat**  
*MATHEMATICAL MODELLING OF ELASTIC DEFLECTION OF A TUBULAR CROSS-SECTION*
- 101 **Wojciech Dzięgielewski, Bartosz Gawron, Andrzej Kulczycki**  
*LOW TEMPERATURE PROPERTIES OF FUEL MIXTURES OF KEROSENE AND FAME TYPE USED TO SUPPLY TURBINE ENGINES IN MARINE AND OTHER NON-AERONAUTICAL APPLICATIONS*

## Editorial

POLISH MARITIME RESEARCH is a scientific journal of worldwide circulation. The journal appears as a quarterly four times a year. The first issue of it was published in September 1994. Its main aim is to present original, innovative scientific ideas and Research & Development achievements in the field of :

### **Engineering, Computing & Technology, Mechanical Engineering,**

which could find applications in the broad domain of maritime economy. Hence there are published papers which concern methods of the designing, manufacturing and operating processes of such technical objects and devices as : ships, port equipment, ocean engineering units, underwater vehicles and equipment as well as harbour facilities, with accounting for marine environment protection.

The Editors of POLISH MARITIME RESEARCH make also efforts to present problems dealing with education of engineers and scientific and teaching personnel. As a rule, the basic papers are supplemented by information on conferences , important scientific events as well as cooperation in carrying out international scientific research projects.

### Scientific Board

**Chairman : Prof. JERZY GIRTLER - Gdańsk University of Technology, Poland**

**Vice-chairman : Prof. ANTONI JANKOWSKI - Institute of Aeronautics, Poland**

**Vice-chairman : Prof. MIROŚLAW L. WYSZYŃSKI - University of Birmingham, United Kingdom**

<b>Dr POUL ANDERSEN</b> Technical University of Denmark Denmark	<b>Prof. WOLFGANG FRICKE</b> Technical University Hamburg- Harburg Germany	<b>Prof. YASUHIKO OHTA</b> Nagoya Institute of Technology Japan
<b>Dr MEHMET ATLAR</b> University of Newcastle United Kingdom	<b>Prof. STANISŁAW GUCMA</b> Maritime University of Szczecin Poland	<b>Dr YOSHIO SATO</b> National Traffic Safety and Environment Laboratory Japan
<b>Prof. GÖRAN BARK</b> Chalmers University of Technology Sweden	<b>Prof. ANTONI ISKRA</b> Poznań University of Technology Poland	<b>Prof. KLAUS SCHIER</b> University of Applied Sciences Germany
<b>Prof. SERGEY BARSUKOV</b> Army Institute of Odessa Ukraine	<b>Prof. JAN KICIŃSKI</b> Institute of Fluid-Flow Machinery of PASci Poland	<b>Prof. FREDERICK STERN</b> University of Iowa, IA, USA
<b>Prof. MUSTAFA BAYHAN</b> Süleyman Demirel University Turkey	<b>Prof. ZYGMUNT KITOWSKI</b> Naval University Poland	<b>Prof. JÓZEF SZALA</b> Bydgoszcz University of Technology and Agriculture Poland
<b>Prof. VINCENZO CRUPI</b> University of Messina, Italy	<b>Prof. JAN KULCZYK</b> Wrocław University of Technology Poland	<b>Prof. TADEUSZ SZELANGIEWICZ</b> Technical University of Szczecin Poland
<b>Prof. MAREK DZIDA</b> Gdańsk University of Technology Poland	<b>Prof. NICOS LADOMMATOS</b> University College London United Kingdom	<b>Prof. WITALIJ SZCZAGIN</b> State Technical University of Kaliningrad Russia
<b>Prof. ODD M. FALTINSEN</b> Norwegian University of Science and Technology Norway	<b>Prof. JÓZEF LISOWSKI</b> Gdynia Maritime University Poland	<b>Prof. BORIS TIKHOMIROV</b> State Marine University of St. Petersburg Russia
<b>Prof. PATRICK V. FARRELL</b> University of Wisconsin Madison, WI USA	<b>Prof. JERZY MATUSIAK</b> Helsinki University of Technology Finland	<b>Prof. DRACOS VASSALOS</b> University of Glasgow and Strathclyde United Kingdom
	<b>Prof. EUGEN NEGRUS</b> University of Bucharest Romania	

# RISK ANALYSIS OF COLLISION BETWEEN PASSENGER FERRY AND CHEMICAL TANKER IN THE WESTERN ZONE OF THE BALTIC SEA

Marcin Przywarty, Ph. D.  
Lucjan Gucma, Assoc Prof.  
Krzysztof Marcjan, Ph. D.  
Andrzej Bąk, Assoc. Prof.  
Maritime University of Szczecin, Poland

## ABSTRACT

*This paper presents assumptions and process of the forming of a risk assessment model for collision between a passenger ferry departing from or approaching port of Świnoujście and a chemical tanker carrying a dangerous cargo. In order to assess navigational safety on the basis of data obtained from AIS system, were prepared probabilistic domains of ships, which made it possible to estimate number of navigational incidents as well as their spatial distribution, that consequently allowed to determine potentially dangerous areas. The next phase was formulation of a simulative model intended for the calculating of probability of collision between the ferry and chemical tanker as well as the determining of characteristic scenarios for such collision. This paper presents also an analysis of consequences of the collision with taking into consideration a damage of cargo tanks.*

**Keywords:** safety of navigation, navigational risk, ships domain, ships collisions, simulation methods

## Introduction

In view of a large number of narrow passages and shallow waters the Baltic Sea has been always a difficult area for navigation. In spite of investment projects undertaken to improve navigational safety in the Baltic Sea any significant drop in number of navigational incidents has been observed so far. In order to obtain a comprehensive image of navigational safety over the Baltic Sea it is necessary to have basic information on ship traffic flow. According to HELCOM data, total number of ships moving along certain routes per year exceeds 60 thousand.

To improve navigational safety traffic separation systems are introduced. They organize ship traffic by lowering traffic flow breadth, that is associated with lowering the distance between passing-by ships. In certain areas the distances between passing-by ships drop below a value at which navigational incidents may occur. To estimate size and shape of ship domains for different kinds of encounters as well as to determine a number and spatial distribution of navigational incidents, in this work were examined 4 crossings of main navigational routes in the water area in question and routes of passenger ferries sailing between Świnoujście and Ystad (Fig.1).

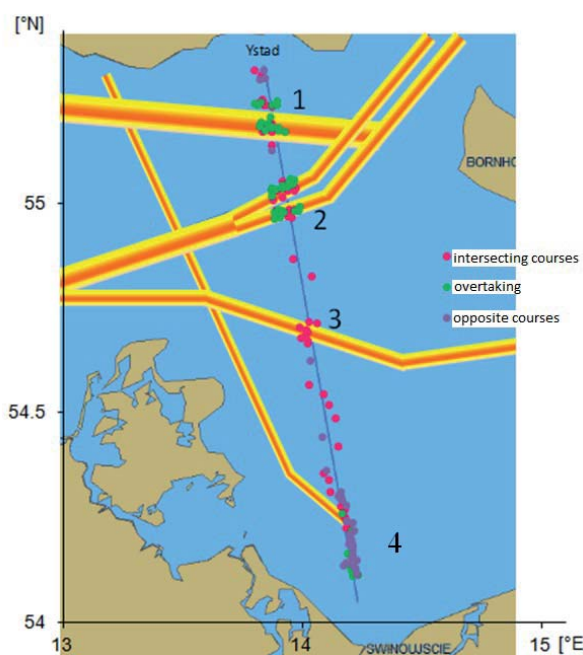


Fig. 1. The investigated water area with depicted points where navigational incidents occurred

Data concerning ship types and shipped cargoes, achieved from AIS system, are limited to the code in which the first digit stands for a type of ship (e.g. 6 – passenger ship, 8 – tanker), and the other digit – a type of shipped cargo:

- 1 – X category
- 2 – Y category
- 3 – Z category
- 4 – OS category

In this work occurrence probability was determined of the most dangerous incident, i.e. collision between a passenger ferry and chemical tanker carrying a dangerous cargo of X category, i.e. noxious liquids which, in case of their discharge to sea, could endanger sea resources or human health [2], and, consequences of such incident were also assessed.

### Preliminary assessment of navigational safety

The first phase of this work has consisted in estimation of a number of navigational incidents on the basis of analysis of actual data achieved from AIS system. To this end, for the selected water area probabilistic domains of ships were determined. Ship's domain should be meant as a certain area around the ship whose navigator would like to keep free from other objects either permanent or moving ones. To calculate parameters of the domains the methodology presented in the publication [3] was used. It makes it possible to determine limit distances in which majority of navigators (their number is determined by 1<sup>st</sup> local maximum of distribution of CPA distances) pass by other ships at different course angles in a given encounter situation. In Fig. 2 detail data dealing with shapes and sizes of the determined domains (marked blue), are presented. Additionally, the same domains, but diminished (marked green) and expanded (marked red) by 25%, are also depicted.

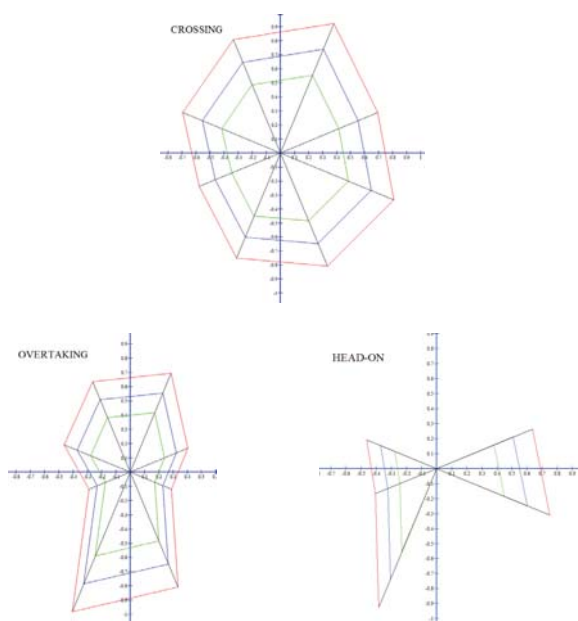


Fig.2. Domains determined for particular types of encounters

The domain determined for encounter on crossing courses is of a shape most close to circle. It shows that both the ships passing before bow of another ship (most often those having priority) and the ships passing behind stern of another ship (most often those giving way) have maintained a comparable passing distance. The largest number for encounters on crossing courses occurred in the sector of  $270^\circ \div 315^\circ$  (270 encounters, 20 incidents).

The domain for overtaking is of an elongated shape both in fore and aft part. It results from the fact that for such manoeuvre the points of the closest approach (CPA) occur usually when the overtaking ship is almost on the beam. Most encounters (about 80%) identified as the overtaking, reached CPA before reaching the beam position ( $270^\circ \div 90^\circ$ ).

For encounters on opposite (head-on) courses majority of the closest approach points happened around a on- the-beam position, 80% out of which – when passing port side. However it is rather surprising that as much as 20% of ships passed each other starboard as the Regulation 14 of the International Regulations for Preventing Collisions at Sea [COLREG] states that: if two ships go head to each other in such a way that it causes risk of collision then each of them is to so change its course as to be able to pass port side of the other.

On the basis of the determined domain parameters, number of navigational incidents which happened within one month in the examined water area, was determined for each type of the encounters. The incident (statistical one) was defined as a situation in which ships pass each other at a distance smaller than that determined for a given type of encounter and a given course angle. Detail data on the incidents are presented in Tab. 1

Tab. 1 Incidents between ships in the examined water area

Encounter type	Number of encounters	Number of incidents	Frequency of incidents [1/h]	Occurrence probability of an incident at encounter
Crossing courses	544	59	0.079	0.11
Overtaking	686	55	0.074	0.08
Opposite courses	364	33	0.044	0.09

In Fig. 1 positions of incidents are shown and, additionally, a type of encounter at which a given incident has happened, is distinguished by a colour. Incidents on crossing courses occurred especially in the places where the route of ferries crosses navigational routes of a high traffic. Incidents during the overtaking occurred close to ports and in the places where routes cross each other. Incidents on opposite courses took place close to ports, that is associated with lowering the traffic flow breadth and, in consequence, lowering the distance between passing ships. The areas most dangerous for navigation, where the highest concentration of incidents was observed, are determined by the following coordinates:

- 55° 10.170'N - 55° 14.598'N and 13° 48.138'E - 13° 53.712'E
- 54° 57.732'N - 55° 03.306'N and 13° 52.926'E - 13° 58.086'E
- 54° 06.678'N - 54° 21.342'N and 14° 05.394'E - 14° 14.160'E

### Stochastic model of navigational safety

To calculate occurrence probability of collision between passenger ferry and chemical tanker, a stochastic model of navigational safety assessment, developed by Institute of Sea Traffic Engineering, Maritime University of Szczecin, was implemented. Structure of the model is presented in Fig. 3. The model operates in the deliberately accelerated time flow in order to obtain a statistically sufficient number of scenarios.

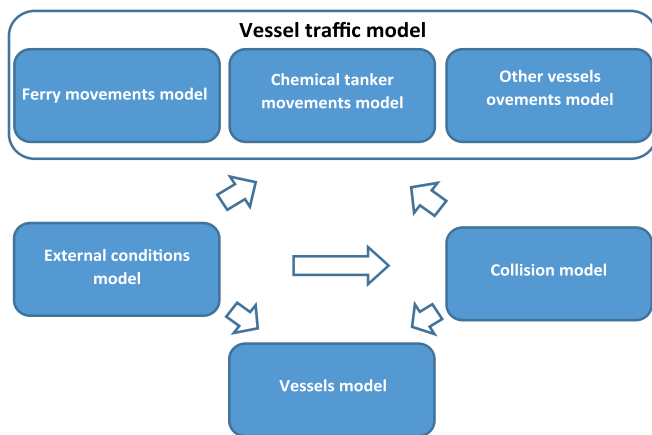


Fig. 3. Schematic diagram of structure of the model for navigational safety assessment

### Chemical tankers' traffic model

Traffic of chemical tankers is modelled by means of Poisson's non-homogeneous distribution whose parameters have been determined on the basis of actual data achieved from AIS system. Analysis of the data allowed to determine parameters of navigational routes as well as parameters of distributions describing traffic flow along the routes (a.o. length, draught and speed). The so determined navigational routes are presented in Fig. 4.

### Ferries' traffic model

Traffic of ferries is modelled on the basis of an actual sailing schedule of ferries travelling on routes for and from Świnoujście. Ferries' traffic parameters (a.o. speeds, turn points) as well as parameters of the ferries (a.o. values of their length, breadth and draught) are simulated on the basis of actual data taken from their technical documentation and also from AIS system. Differences in time of actual departures of ferries from a port in relation to scheduled ones are taken into account by using a probabilistic model. The model has been developed on the basis of actual observations carried

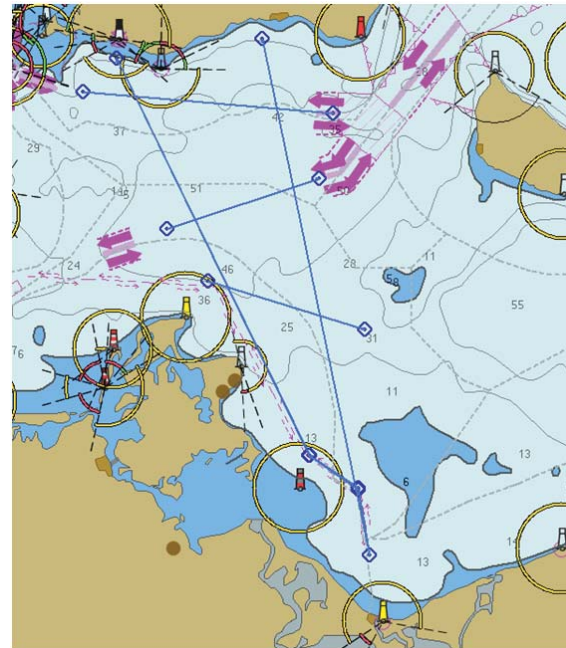


Fig. 4. The modelled navigational routes

out at Ferry Terminal, Świnoujście [6]. The investigations consisted in determination of parameters of a theoretical distribution which allows to simulate delays of ferries or their earlier departures out of port.

The following results were obtained from statistical analysis of the gathered data:

- The mean difference between actual and scheduled departure time of a ferry: 4min
- Maximum difference between actual and scheduled departure time of a ferry: 34 min
- Minimum difference between actual and scheduled departure time of a ferry: -9min (the ferry got away from the pier prior to scheduled time)
- Modal value: 3min
- Standard deviation: 8,2 min

The detail data subjected to statistical analysis are shown on the histogram (Fig. 5.)

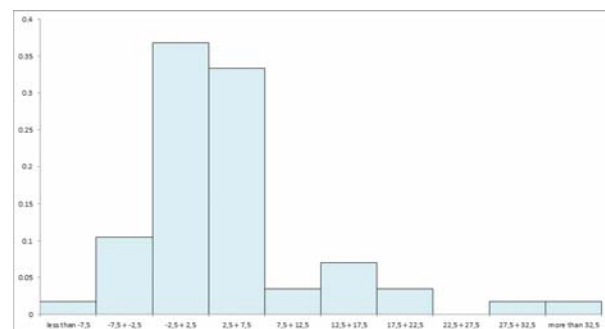


Fig. 5. Histogram of differences between actual and scheduled departure time of ferries from Świnoujście

On the basis of characteristics of the random variable and calculated parameters as well as the developed histogram of the variable, for further analysis theoretical distributions capable of describing the given random variable, have been selected. Analysis of matching of particular distributions has been conducted by means of Kolmogorov-Smirnov test as well as Anderson-Darling test. For both the tests the generalized distribution of extreme values has been found to be best describing differences between actual and scheduled departure time of ferries from Świnoujście.

### Model of external conditions

The model makes it possible to simulate many factors which can impact navigational safety, such as: water area depth, wind force and direction, wave height and direction, haze occurrence, day time, hours of sunrise and sunset. Data necessary for calculating parameters of distributions which describe external factors, have been achieved from Polish meteorological stations, navigational charts and own maritime experience of these authors.

### Model of collision between ferry and chemical tanker

Simulation of collision of ships has been conducted by means of a statistical model. It neglects several relationships, nevertheless, as it is based on statistical data, the obtained results are close to reality.

Number of ship encounters over the examined water area is the crucial (and simultaneously most difficult to determine) parameter which must be found in order to assess navigational safety. In research on ship traffic systems the use of simulative methods is the most effective approach for determining value of the parameter in question.

Therefore to determine number of ship encounters over the examined water area, has been conducted a simulation experiment where the earlier prepared ship traffic models were implemented. Encounter was defined to be a situation when ships pass by each other at the distance equal to or smaller than the assumed limit value. The limit values were assumed separately for different types of encounters on the basis of analysis of ship's domains (Fig. 2).

The next parameter to be determined in order to estimate navigational safety is a number of actual collisions of ships. The parameter was determined on the basis of analysis of actual data taken from HELCOM database. Only the collisions which happened in open waters of the south zone of the Baltic Sea were taken into consideration. The detail data used in the model are shown in Fig. 6.

The number of ship encounters obtained from the simulation experiment as well as the number of collisions of ships were used for the calculating of conditional probability of collision of ships at their encounter. The calculated values of the probability are presented in Fig. 7.

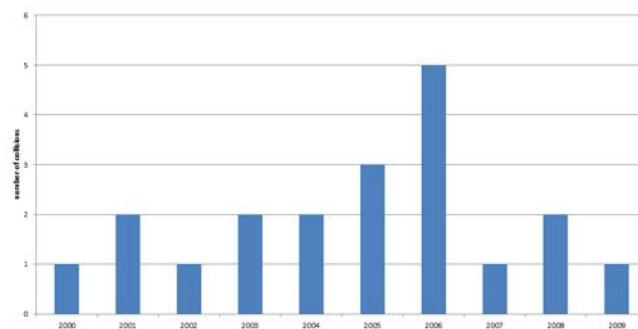


Fig.6 Number of collisions of ships in open waters of the south zone of the Baltic Sea

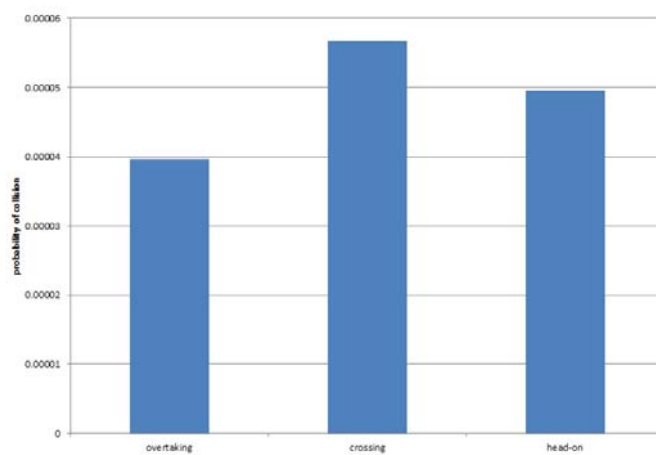


Fig. 7 Calculated values of the ship collision probability for various types of encounters

On determination of the ship collision probability, another simulation experiment was performed. It was aimed at determination of position and parameters describing the probability of collision between the passenger ferry sailing for or from Świnoujście and the chemical tanker carrying dangerous cargo. In order to determine sensitivity of the used model against changes in input parameters, the experiment was conducted for the mean domain based on the data taken from AIS system as well as the expanded domain and diminished one by 25%, respectively (Fig.2). Additionally, influence of simulation step was examined.

## Results

On collection and implementation of all necessary statistical data, was performed a simulation experiment aimed at determination of a number and spatial distribution of simulated incidents and accidents. Additionally, influence of settings on operation of the model was investigated. In the presented experiment 100 iterations were performed for each initial setting. One iteration covered duration of one year. As the statistical frequency of collisions appeared extremely low it was necessary to conduct an additional experiment covering a much greater number of iterations. 1000 iterations were

done to determine frequency and distribution of collisions. The detail results obtained from the experiment are presented in Fig. 8 and Tab. 2. The model operated in the deliberately accelerated time to make it possible to achieve statistically stable results.

Tab. 2. Results of the simulation experiment

Step of simulation [min]	Size of domain [%]	Number of iterations	Number of incidents	Change	Number of collisions	Mean time between collisions
1	100	100	111243	The reference quantity	0	-
3	100	100	67799	-39%	0	-
5	100	100	56201	-49%	0	-
1	75	100	84890	-24%	0	-
1	125	100	136904	+23%	0	-
1	100	1000	-	-	7	142.8 years

### Assessment of consequences of collision between passenger ferry and chemical tanker carrying dangerous cargo

In ship traffic engineering navigational risk is expressed in the form of product of occurrence probability of an accident and its consequences. Depending on a way in which the consequences are formulated, the following can be distinguished:

- the navigational risk for which accident consequences are expressed by physical indices calculated on the basis of mathematical description of accident dynamics ,
- the economic risk for which accident consequences are expressed by cost borne as a result of the accident.

In this work the consequences have been expressed by a volume of damaged structural material determined on the basis of energy absorbed during collision of ships.

One of the first, but still commonly used, statistical relationship which makes it possible to assess consequences of ship collisions is that proposed by Minorsky V. [4].

On the basis of an analysis of 26 ship collisions a relationship between volume of damaged structural material and energy of ship collisions, was established (Fig.8). The relationship is expressed as follows:

$$E = 47,09 R_T + 32,37 \text{ [MJ]} \quad (1)$$

where:

E – energy absorbed during collision [MJ]

$R_T$  – total volume of damaged structural material of both colliding ships [m<sup>3</sup>]

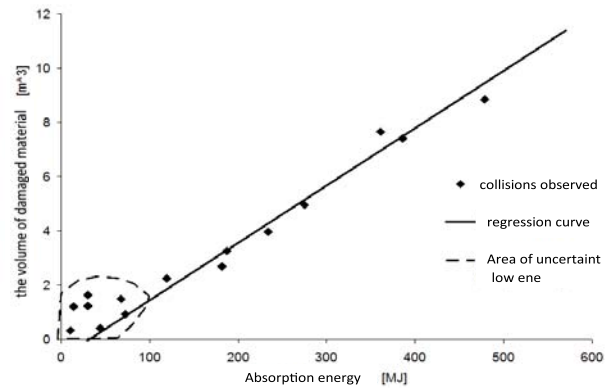


Fig. 8. Relationship between absorbed energy and volume of damaged structural material

In the presented work only one collision scenario was analyzed. In its subsequent phases should be developed a method allowing to investigate influence of changes in ship parameters and other significant factors on consequences resulting from collisions between a passenger ferry and chemical tanker.

For the presented analysis the following parameters were assumed:

- The collision happens under 90° angle between a passenger ferry of a size close to that of m/f Polonia and a chemical tanker carrying ammonia, on approach to port of Świnoujście.
- The chemical tanker's parameters: LOA = 129 m, B = 17.8 m, T = 8.6 m, V = 16.5 kn, total capacity - 8600m<sup>3</sup>, 3 tanks of about 3000 m<sup>3</sup> each (Fig. 9).
- The passenger ferry's parameters (based on those of m/f Polonia): LOA = 170 m, B = 28.0 m, T = 6.0 m, V = 20 kn, number of passengers - 918 (of crew members - 82).
- Encounter parameters: of the chemical tanker: COG = 270°, V = 12 kn, of the ferry: COG = 000°, V = 8 kn (speed reduced after a failed anti-collision manoeuvre).
- Description of the accident: as a result of navigational errors done by both officers of the watch, the ferry run into the middle part of the chemical tanker causing damage of a cargo tank amidships.

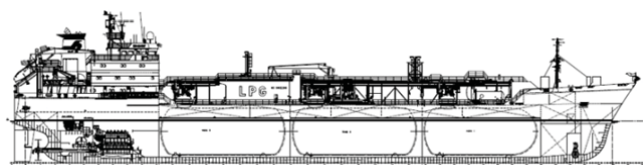


Fig. 9. The analyzed chemical tanker of 8600m<sup>3</sup> capacity

Collision energy was calculated by using the PIANC method [5]. The following results were obtained for further analysis:

The ships' collision energy  $E = 137,1$  MJ

The volume of damaged structural material  $R_T = 2.3$  m<sup>3</sup>

The radius of damaged area of ship's hull, (assumed spherical)  $r = 1.7$  m

The diameter of damaged area of cargo tank  $d = 0.2$  m

To determine tank damage consequences, was applied the software ALOHA<sup>®</sup> which has been made cost-free accessible by two US agencies: EPA (Environmental Protection Agency) and NOAA (National Oceanic and Atmospheric Administration) [1]. The software makes it possible to determine contamination zones as a result of a leakage of dangerous substances of various types. The following assumptions were done:

- The coordinates of place of the collision:  $\varphi = 53^\circ 57.0' N$ ,  $\lambda = 14^\circ 16.6' E$  (approach to Świnoujście)
- The chemical substance parameters; name: ammonia, molecular mass: 17.03 g/mol, AEGL-1 (60 min) = 30 ppm, AEGL-2 (60 min) = 160 ppm, AEGL-3 (60 min) = 1100 ppm.
- The weather conditions: easterly wind of the speed = 15 kn (abt. 7,7 m/s)
- The leakage parameters; tank capacity: 3000 m<sup>3</sup>, tank filling: 98%, circular damages of 0,2 m diameter, at 8,77 m level above the tank bottom, leakage in the form of two-phase mixture of gas and aerosol.

Fig. 10 shows spatial distribution of contamination of various intensity. Exposure levels (AEGL - Acute Exposure Guideline Levels) are defined to be a quantity of a chemical substance (in ppm) and exposure time which cause:

- AEGL-1 – feeling of discomfort
- AEGL-2 – serious and long-lasting negative consequences to health or leading to the worsening of capability to escape
- AEGL-3 – hazard for life or death

As clearly results from Fig. 10, in case of an unfavourable wind direction, not only ferry passengers and crews of the ships but also inhabitants of coastal dwellings can be exposed to serious consequences, including death. Staying within the zones (marked in the figure) for 60 min or longer may be hazardous to life or even lead to death (AEGL – 3 level – marked red, AEGL – 2 level – marked orange). At an unfavourable wind direction such hazard may concern a major part of Heringsdorf (Ahlbeck district) in which about 3500 inhabitants live.



Fig. 10. AEGL level zones after a theoretical leakage of ammonia from the examined chemical tanker on approach to port of Świnoujście

## Conclusions

This paper presents an analysis of consequences of a collision between passenger ferry and chemical tanker carrying dangerous substance. Despite the calculated probability of such collision is very low (one collision for about 150 years), its probable serious consequences may impair not only persons on board the ships which suffered the collision but also inhabitants of coastal dwelling places. For this reason hazard to such accidents should be investigated in detail, that would allow to undertake appropriate preventive actions.

## Bibliography

1. ALOHA<sup>®</sup> User's Manual NOAA and EPA, February 2007
2. IMO: Annex 6, Resolution MEPC.118(52), (Revised Annex II of MARPOL 73/78), Adopted on 15 October 2004
3. Gućma L., Marcjan K.: Probabilistic model of minimal passing distances of vessels navigating in Polish coastal waters. PSAM11&ESREL, 2012.
4. Minorsky V.: An Analysis of Ship Collision with Reference to Protection of Nuclear Power Ship. Journal of Ship Research, Vol. 3., 1959
5. PIANC: Report of the International Commission for Improving the Design of Fenders Systems. Supplement to PIANC Bulletin N 45. Brussels 1984
6. Przywarty M., Gućma L.: Model of Time Differences Between Schedule and Actual Time of Departure of Sea Ferries in the Świnoujście Harbour. Miscellaneous problems in Maritime Navigation, edited by Adam Weintrit, Tomasz Neuman, Gdynia 2011.

## CONTACT WITH THE AUTHOR

Marcin Przywarty  
Lucjan Gućma  
Krzysztof Marcjan  
Andrzej Bąk

Maritime University of Szczecin  
1-2 Waly Chrobrego St.  
70-500 Szczecin  
POLAND

# ACCURACY OF THE GPS POSITIONING SYSTEM IN THE CONTEXT OF INCREASING THE NUMBER OF SATELLITES IN THE CONSTELLATION

**Cezary SPECHT**, Prof.  
Gdynia Maritime University  
**Mateusz MANIA**, M. Sc.  
Gdynia Maritime University  
**Marcin SKÓRA**, M. Sc.  
Polish Naval Academy  
**Mariusz SPECHT**, B. Sc.  
Gdynia Maritime University

## ABSTRACT

*A possibility of utilising the GPS system for navigation and transport are fundamentally dependent on the accuracy in positioning. Two fundamental factors decisive for its value are the values of the User Range Error (URE) and Dilution of Precision (DOP), strictly related to the number of satellites forming the constellation. The nominal constellation of GPS satellites consists of 24 units which gives a possibility of identification of coordinates all over the globe. In the last few years, however, the nominal number of satellites in the constellation was much higher, and the URE value has been constantly increasing.*

*The authors of the paper try to estimate the impact of the changing number of GPS satellites on accuracy of position coordinates with a variable URE value. Mathematical model for estimating geometrical indicators' value, utilising data derived from the almanac files has been presented. Following a drawn-up algorithm and calculations made with Mathcad software, the authors carried out a comparative analysis of mean daily values of DOP indicators for a variable number of satellites included in the GPS constellation in the years 2001-2013. Then, the authors have established representative values of Two Distance Root Mean Square Error (2drms) 2D and 3D, and calculated a percentage increase of accuracy in the period under discussion.*

**Keywords:** GPS, User Range Error, Dilution of Precision, GPS Almanac, Accuracy of Positioning.

## Introduction

The GPS system plays a fundamental role in the process of object's navigation and geodetic measurements, utilising active geodetic satellite networks [1, 2], in which planning a campaign on the basis of the almanac data of the constellation is a key factor for carrying out accurate engineering measurements for inventorying and diagnostic purposes [3, 4]. In maritime navigation where safety is a core of the process [5], information on conditions of geometric satellite measurements, resulting in specific GPS positioning error, should be taken into consideration during the navigation at the stage of planning the construction of navigation infrastructure [6, 7] and monitoring vessel traffic [8, 9]. It is also an important element which utilises electronic navigation support tools, such as imaging – ECDIS [10, 11]. A similar situation can be found in the case of aviation

positioning, where GNSS technologies are at the initial stage of implementation within the systems of precision approach and landing of the aircraft [12], or dynamically today developing solutions integrating the GIS and GNSS systems in aviation [13].

One cannot fail to mention individual navigation, i.e. the use of GPS in non-professional applications, where GNSS receivers are widely used in tourism or sports, and accuracy characteristics strictly related to the constellation of satellites available to the user at the moment of measurement, are a decisive factor for their accuracy [14, 15], and availability.

Measuring errors which can be divided into three fundamental categories, influence the accuracy of determining position coordinates in the GPS system. The first category is errors caused by signal propagation, including errors resulting from ionospheric and tropospheric delays, and errors caused by received signal's multi-path routing. These issues will

not be discussed in further part of the paper. The second category includes errors resulting from spatial and ground segments' operations, i.e. satellite ephemeris errors, satellite clock errors, and errors caused by the constellation's geometry, represented by DOP indicators. The third group includes receivers' instrumental errors, which currently are not highly decisive for positioning accuracy [16]. Errors included in the second group may be assessed and included in the navigation message in a form of the User Range Accuracy (URA) [17]. According to the 2011 standard [18], the value of URA is a standard deviation of the standard User Range Error (URE). URE consist of satellite clock errors and their ephemeris errors [19]. The control segment traces a position of each individual satellite, defining a vector of errors of its position and clock, against the time standard UTC, maintained by the US Naval Observatory [20]. The US Federal Aviation Administration publishes quarterly data concerning current value of URA for the GPS system [21]. Detailed analyses connected with the value can be found in the book listed as [22]. The value of standard deviation (rms) of URE can be calculated through the function of errors in satellite location measured along-track, cross-track and radially, and satellite clock error as [23]:

$$URE = \sqrt{(0,98R - T)^2 + 0,141^2 (A^2 + C^2)}, \quad (1)$$

where:

- URE – User Range Error [m],
- R – satellite Radial Error [m],
- A – satellite Along-track Error [m],
- C – satellite Cross-track Error [m],
- T – satellite Clock Error [m].

Tab. 1 presents typical component error value for individual satellite blocks. The data have been analysed for 2010, when the segment consisted of the total of 31 satellites, 30 in operation. Space segment was created by satellites of three blocks, IIA, IIR and IIR-M, in a quantity of 11, 12 and 8 respectively [24].

Tab. 1. Typical component values of URE value in the function of GPS satellite block [23].

Error component	block IIA	block IIR	block IIR-M
R – radial [m]	0,243	0,130	0,145
A – along-track [m]	1,258	0,921	1,000
C – cross-track [m]	0,675	0,575	0,594
T – clock (time) [m]	1,074	0,384	0,498
URE [m]	<b>1,076</b>	<b>0,418</b>	<b>0,527</b>

Accuracy of determining position for the GPS system depends on the value of a selected geometrical indicator (DOP) and the User Equivalent Range Error (USERE), composed of both URE and User Equipment Error (UEE). The value of UEE for equipment manufactured in 1980s was on average 5,5 m (p = 0,95), whereas at present it is

1,6 m (p = 0,95) [25]. Therefore the above-presented formula for accuracy of position determination may be presented in the following form [26]:

$$drms = UERE \cdot DOP = \sqrt{URE^2 + UEE^2} \cdot DOP, \quad (2)$$

where:

- drms – Distance Root Mean Square Error (horizontal, vertical, spatial, clock), depending on the selected DOP indicator [m],
- UERE – User Equivalent Range Error [m],
- URE – User Range Error [m],
- UEE – User Equipment Error [m],
- DOP – suitable Dilution of Precision: GDOP, PDOP, HDOP, VDOP, and TDOP [-].

The equation for accuracy of position determination for the above presented GPS system, has a simplified form, thanks to which it is satisfactory and universal for numerous applications. It is correct, because all the calculations of pseudo-ranges are subject to normal distribution (Gaussian distribution). The following diagram (Fig. 1) presents a change in the value of the Two Distance Root Mean Square Error (2drms) 2D of the GPS system (p = 0,95) in the function of the variable URE value [22], with the assumption of UEE of 0,8m (rms) and HDOP indicator equal to 1,5.

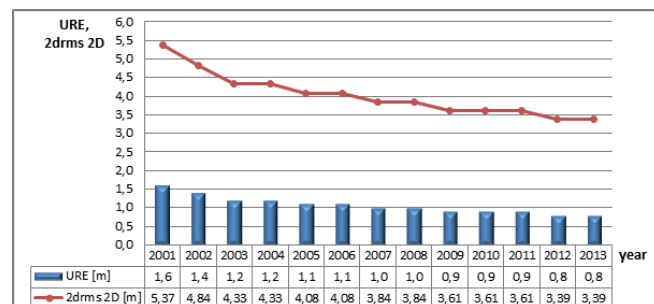


Fig. 1. Value of the Two Distance Root Mean Square Error (2drms) 2D for the GPS system, dependent on URE from 2001-2013. The URE value was estimated upon [22].

The US Department of Defence permanently monitors technical condition of equipment carrying out its tasks, and makes current data available to the users, facilitating forecasting the satellites' constellation. Current and archive data of the almanac, in various formats, are available at the website of the US Coast Guard Navigation Centre which is responsible for supplying current information on GPS to individual users. In order to stipulate a real number of satellites in the system in the years 2001-2013, all the almanac files for the period in question have been analysed (a total of 4188 files from the USCG website), and on their basis a diagram illustrating the number of satellites (both active and inactive) for the GPS constellation in the function of individual years was made (Fig. 2). Next, it will be the basis to calculate mean daily value of DOP indicators, dependent on the changing number of GPS satellites. The simplification used so far (adoption of a constant HDOP value), irrespective

of the number of satellites in the constellation, must be regarded as approximation the authors of the paper would like to avoid. Even more so that the number of satellites is constantly changing, thus decreasing (in the statistical sense of the word) the DOP value.

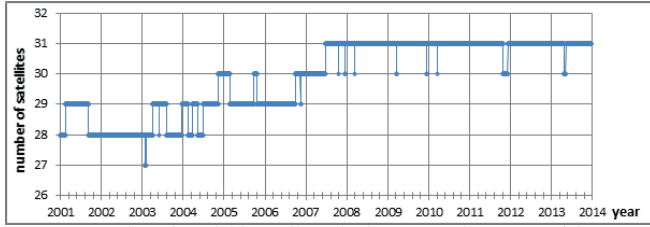


Fig. 2. Number of available satellites (both active and inactive) of the GPS system, derived from the almanac files (USCG) in the years 2001-2013.

In further part of the paper the authors carry out an analysis of the Two Distance Root Mean Square Error (2drms) 2D and 3D in the function of variable number of satellites, influencing the DOP values, and shrinking in years URE value.

### Determining the geometrical DOP coefficients' values

DOP coefficients are a measure of geometric conditions for determining positions. This is a scalar value which informs about spatial distribution of elements in relation to the observer. For a detailed description of DOP coefficients see [27]. The process of calculating the value of geometric coefficients for a given moment of observation should be started with determining coordinates of GPS satellites and the receiver in a system Earth-Centred Earth-Fixed (ECEF) at the right moment (assuming that the Kepler's laws define the satellite movement). Therefore the following data should be acquired for each individual satellite from the almanac files [28]:

- $t_{oa}$  – GPS Time of Applicability [s],
- $e_s$  – Eccentricity [-],
- $\delta i$  – Inclination Offset [semicircles], [rad], [°],
- $\dot{\Omega}$  – Rate of Right Ascension [semicircles/s], [rad/s], [°/s],
- $\sqrt{A}$  – Square Root of Semi-Major Axis [ ],
- $\Omega_0$  – Longitude of Orbital Plane [semicircles], [rad], [°],
- $\omega$  – Argument of Perigee [semicircles], [rad], [°],
- $M_0$  – Mean Anomaly [semicircles], [rad], [°].

The next step is the transformation of satellites' coordinates from the ECEF system into the ENU (East, North, Up), calculation of their elevation (topocentric altitude), and disregarding satellites with the altitude's negative value, or lower than that assumed, and for the other satellites – calculation of azimuths measured from the position of the receiver. Below can be seen a matrix of transformation between ECEF-ENU systems, taking a form of [29]:

$$F = \begin{bmatrix} -\sin(L) & -\sin(B) \cdot \cos(L) & \cos(B) \cdot \cos(L) \\ \cos(L) & -\sin(B) \cdot \sin(L) & \cos(B) \cdot \sin(L) \\ 0 & \cos(B) & \sin(B) \end{bmatrix}, \quad (3)$$

where: B, L – receiver's geodetic coordinates [rad],

which facilitates calculation of satellites coordinates in the ENU system:

$$\begin{bmatrix} X_{ENU} \\ Y_{ENU} \\ Z_{ENU} \end{bmatrix} = F^T \cdot \begin{bmatrix} X_s - X_u \\ Y_s - Y_u \\ Z_s - Z_u \end{bmatrix}, \quad (4)$$

where:

$X_{ENU}, Y_{ENU}, Z_{ENU}$  – satellite coordinates in the ENU system [m],  
 $X_s, Y_s, Z_s$  – satellite coordinates in the ECEF system [m],  
 $X_u, Y_u, Z_u$  – receiver coordinates in the ECEF system [m],  
 thus allowing to calculate on their basis the elevation (topocentric altitude) of the satellite:

$$el = \arctg \left( \frac{Z_{ENU}}{\sqrt{X_{ENU}^2 + Y_{ENU}^2}} \right) \quad (5)$$

and its azimuth:

$$Az = \begin{cases} 0 & \text{for } x_{ENU} = 0 \wedge y_{ENU} > 0; & \arctg \left( \frac{x_{ENU}}{y_{ENU}} \right) & \text{for } x_{ENU} > 0 \wedge y_{ENU} > 0 \\ 0,5\pi & \text{for } x_{ENU} > 0 \wedge y_{ENU} = 0; & 0,5\pi + \arctg \left( \frac{y_{ENU}}{x_{ENU}} \right) & \text{for } x_{ENU} > 0 \wedge y_{ENU} < 0 \\ \pi & \text{for } x_{ENU} = 0 \wedge y_{ENU} < 0; & \pi + \arctg \left( \frac{x_{ENU}}{y_{ENU}} \right) & \text{for } x_{ENU} < 0 \wedge y_{ENU} < 0 \\ 1,5\pi & \text{for } x_{ENU} < 0 \wedge y_{ENU} = 0; & 1,5\pi + \arctg \left( \frac{y_{ENU}}{x_{ENU}} \right) & \text{for } x_{ENU} < 0 \wedge y_{ENU} > 0 \end{cases} \quad (6)$$

And then, with the application of the line-of-sight matrix G:

$$G = \begin{bmatrix} \cos(el_1) \cdot \sin(Az_1) & \cos(el_1) \cdot \cos(Az_1) & \sin(el_1) & 1 \\ \cos(el_2) \cdot \sin(Az_2) & \cos(el_2) \cdot \cos(Az_2) & \sin(el_2) & 1 \\ \vdots & \vdots & \vdots & 1 \\ \cos(el_n) \cdot \sin(Az_n) & \cos(el_n) \cdot \cos(Az_n) & \sin(el_n) & 1 \end{bmatrix}, \quad (7)$$

where indexes 1-n denominate values for further individual satellites, and a covariance matrix:

$$C = (G^T \cdot G)^{-1}, \quad (8)$$

geometric coefficients may be calculated:

$$GDOP = \sqrt{C_{0,0} + C_{1,1} + C_{2,2} + C_{3,3}}, \quad (9)$$

$$PDOP = \sqrt{C_{0,0} + C_{1,1} + C_{2,2}}, \quad (10)$$

$$HDOP = \sqrt{C_{0,0} + C_{1,1}}, \quad (11)$$

$$VDOP = \sqrt{C_{2,2}}, \quad (12)$$

$$TDOP = \sqrt{C_{3,3}}. \quad (13)$$

## Simulation tests

In order to assess the impact of alteration in the number of satellites on the accuracy of positioning, an algorithm allowing for determination of geometric coefficients for any location or time, was worked out with the Mathcad software. Analyses were used to determine the mean daily value of the DOP coefficients in individual years. Out of each successive year, excluding the turning off of the GPS Selective Availability (SA) by US President Bill Clinton on 2nd May 2000 [30], the almanac file was selected; it was the file representing most frequent number of GPS satellites in a given year (Tab. 2), for which, afterwards, changes in the DOP value during a full stellar day (equivalent to double orbiting the globe by the GPS constellation) were obtained.

Tab. 2. Representative number of satellites in the years 2001-2013

Year	2001	2002	2003	2004	2005	2006	2007	2008	2009	2010	2011	2012	2013
Number of satellites	29	28	28	29	29	29	30	31	31	31	31	31	31

Calculations were carried out for Gdynia location (54° 32' N, 18° 32' E), a minimum elevation (topocentric altitude) of satellites equal to 0°, and a period of 23h 56' 4", i.e. a period after which a geometry of GPS constellation over a given point will be identical to that at the start of the observation. In order to receive equal brackets of analyses carried out, the value of 4 seconds was adopted as a step of making DOP calculations. These short brackets of analyses permitted for taking into account changes in geometric coefficients' values, which are usually disregarded by general access software applied in geodesy and navigation for analysis of constellation's geometry, with a typical calculation bracket of 10 minutes. Then mean values of geometric coefficients HDOP and PDOP were calculated for a given period of time (a stellar day) and Two Distance Root Mean Square Errors (2drms) 2D and 3D in the function of a variable value of URE, with the assumption of UEE equal to 0,8m (Fig. 3 and Fig. 4).

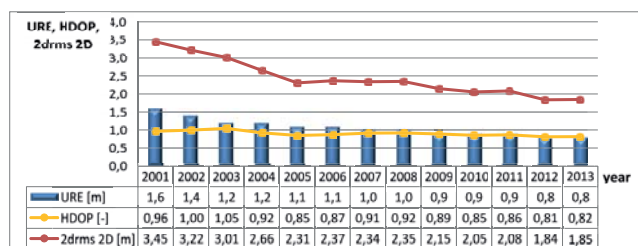


Fig. 3. Value of the Two Distance Root Mean Square Error (2drms) 2D for the GPS system, dependent on URE from 2001-2013

In order to estimate the impact of variable number of GPS satellites on accuracy of determination of position in reference to current URE value, it was suggested to adopt a relative (to the year 2001) percentage change in accuracy of determining 2D and 3D positions in the years 2001-2013, as presented in Fig. 1, with the application of equation:

$$\Delta 2drms = \frac{2drms_n - 2drms_{2001}}{2drms_{2001}} \cdot 100\%, \quad (14)$$

where n = 2001, 2002, ..., 2013.



Fig. 4. Value of the Two Distance Root Mean Square Error (2drms) 3D for the GPS system, dependent on URE from 2001-2013

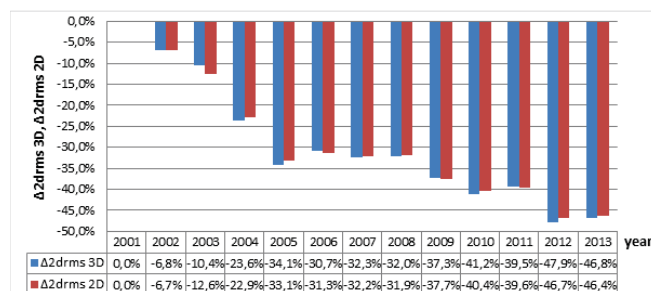


Fig. 5. Relative percentage change in accuracy of determining 2D and 3D positions in the years 2001-2013

## Discussion

The research shows that from the moment the Selective Availability was switched off, the system keeps improving its accuracy of positioning, which can be observed from the periodically (2001, 2008) published statistical data concerning the accuracy in a form of a standard. In the 2001 SPS standard, accuracy of positioning in a horizontal plane should not be higher than 13 m (p = 0,95), and in vertical one, 22 m (p = 0,95); in 2008 version, however, an average global positioning accuracy (p = 0,95) should not have exceeded 9 m and 15 m respectively. This means that the Δ2drms relative value alteration, calculated according to the 2001 standard, was -30,7 %. Similar result was obtained on the basis of the analyses discussed above, and it was -32,0 %.

It should be noticed, however, that the acquired absolute results of simulation tests do not include measurement errors related to the signal's propagation (ionospheric and tropospheric delays), discussed in the introduction, therefore they differ from the above-mentioned values, derived from the standards. The volume of errors depend to a large extent on the type of receiver used for determination of position, therefore they were on purpose omitted in the analyses.

Contemporary equipment receiving C/A signals at single L1 frequencies use diversified models of compensating these errors, and taking them into consideration would not be representative in the context of this research.

The target of the paper was to estimate the accrual of accuracy, therefore the authors carried out the research on the impact of variable number of the GPS satellites on the accuracy of determination of position coordinates with the variable value of URE. Simultaneously, a constant value of the User Equipment Error (UEE) equal to 0,8 m (rms) was assumed.

## Conclusions

1. The values of the User Range Error (URE) and geometric coefficients (DOP) are factors decisive for accuracy of positioning in the GPS system.
2. Although in some years the number of satellites was the same, geometric coefficients varied slightly, which was caused by the variable geometry of the GPS satellites' constellation.
3. An increase in the number of satellites from 28 to 31 resulted in a decrease in the value of the HDOP coefficient by 0,2, and PDOP - by 0,4.
4. In 2001-2013, decrease in the User Range Error had higher impact on the accuracy of positioning than the increase in the number of satellites.
5. On the average, the Two Distance Root Mean Square Error (2drms) 3D is 1,7 times higher than 2D.
6. In the period under analysis, the Two Distance Root Mean Square Errors (2drms) 2D and 3D decreased by almost 50%.

## Bibliography

1. Koc W., Specht C.: Application of the Polish Active GNSS Geodetic Network for Surveying and Design of the Railroad. Proceedings of the First International Conference on Road and Rail Infrastructure – CETRA 2010, 2010, pp. 757-762.
2. Skóra M., Specht C.: Comparative Analysis of Selected Active Geodetic Networks (in Polish).. Zeszyty Naukowe AMW, No. 3 (178), 2009, pp. 39-54.
3. Koc W., Specht C.: Results of Satellite Measurements of the Railway Tracks (in Polish), TTS -Technika Transportu Szybowego, No. 7-8, 2009, pp. 58-64.
4. Koc W., Specht C., Nowak A., Szulwic J., Szmagliński J., Skóra M., Specht M., Czarnik M.: Availability of Phase Solutions of GPS / GLONASS During the Geodesic Inventory of Railways – on the Example of Tramway Lines in Gdańsk (in Polish). TTS - Technika Transportu Szybowego, No. 9, 2012, pp. 3441-3451.
5. Czaplowski K.: The Fundamentals of Maritime and Inland Navigation (in Polish), Wydawnictwo Bernardinum, 2014.
6. Śniegocki H.: Safety of LNG Tankers During the Harbour Approach with Particular Emphasis on Changes of Existing Navigational Aids - with the External Port and the LNG Terminal in Swinoujście as an example (in Polish), 15th PPEEm Symposium, 2012.
7. Śniegocki H.: International Organizations Requirements Regarding the Breadth of the Port Approach for Biggest LNG Tankers (in Polish), Logistyka, No. 6, 2011.
8. Gackowska A., Śniegocki H.: AIS System in the Area of Pomeranian Bay (in Polish), 14th PPEEm Symposium, 2011, pp. 3751-3758.
9. Jaskólski K.: Availability of AIS Binary Data Transmission Based on Dynamic Measurements Performed on the Southern Baltic and the Danish Straits, Annual of Navigation, No. 20, 2013, pp. 25-36.
10. Weintrit, A.: Telematic Approach to e-Navigation Architecture, Communications in Computer and Information Science, Vol. 104, 2010, pp. 1-11.
11. Weintrit A.: Electronic Navigational Chart: Introduction to the Electronic Chart Display & Information System (ECDIS) (in Polish), Wydawnictwo Uczelniane WSM , Gdynia, 1997.
12. Oszczak B.: New Algorithm for GNSS Positioning Using System of Linear Equations, Proceedings of the ION GNSS'2013, 2013.
13. Oszczak B., Tanajewski D.: The Use of Geographical Information System at Local Airport Management, Proceedings of the International Conference on Environmental Engineering, 2014.
14. Specht C., Szot T., Specht M.:The Research on Accuracy of the Personal GPS Receivers in Dynamic Measurements (in Polish), TTS - Technika Transportu Szybowego, No. 10, 2013, pp. 2547-2555.
15. Specht M., Szot T.: Accuracy Analysis of GPS Sport Receivers in Dynamic Measurements, Annual of Navigation, No. 19(1), 2012, pp. 165-176.
16. Januszewski J.: GPS, Galileo and Other Satellite Navigation Systems (in Polish), PWN, Warsaw, 2006.
17. Banachowicz A., Bober R., Szewczuk T., Wolski A.: Study on Effect of System Geometry on Position Fixing Accuracy with GPS Receiver (in Polish), Zeszyty Naukowe AMW, No. 4 (175), 2008, pp. 15-24.
18. Interface Specification – Navstar GPS Space Segment / Navigation User Interfaces (IS-GPS-200), Revision F, 2011.

19. Wang Y., Li R.: The analysis of character of User Range Accuracy, China Satellite Navigation Conference (CSNC) 2013, Proceedings Lecture Notes in Electrical Engineering, Vol. 244, 2013, pp. 267-277.
20. Marquis W.: Increased Navigation Performance from GPS Block IIR, NAVIGATION: Journal of The Institute of Navigation, Vol. 50, No. 4, Winter 2003-2004, pp. 219-233.
21. William J. Hughes Technical Center : NSTB/WAAS T&E Team, Global Positioning System (GPS) Standard Positioning Service (SPS), Performance Analysis Report, FAA GPS Product Team, 2000-2010.
22. Bailey B.K.: GPS Modernization Update & Program Plans, Proceedings of the 13th Meeting of National Space-Based Positioning, Navigation, and Timing Advisory Board, 2014.
23. Heng L., Gao G.X., Walter T., Enge P.: Statistical Characterization of GPS Signal-In-Space Errors, Proceedings of the 2011 International Technical Meeting of The Institute of Navigation, 2011, pp. 312-319.
24. Januszewski J.: GPS system Today and in the Future (in Polish), Prace Wydziału Nawigacyjnego Akademii Morskiej w Gdyni, No. 24, 2010, pp. 17-29,
25. Global Positioning System Standard Positioning Service Performance Standard, 4th Edition, United States of America Department of Defense, 2008.
26. Grall P., Specht C.: Comparative Evaluation of GPS SPS Standards for Accuracy in Fixing Position (in Polish), Zeszyty Naukowe AMW, No. 3 (186), 2011, pp. 43-56.
27. Specht C.: The GPS System (in Polish), Wydawnictwo Bernardinum, 2007.
28. Interface Control Document – Navstar GPS Space Segment / Navigation User Interfaces (ICD-GPS-200), Revision C, 2000.
29. Grewal M. S., Weill L. R. and Andrews A. P.: Appendix C: Coordinate Transformations, in Global Positioning Systems, Inertial Navigation, and Integration, John Wiley & Sons, ?, 2002.
30. Office of the Press Secretary: Statement by the President Regarding the United States Decision on the Global Positioning System Accuracy, White House Press Release, 2000.

## CONTACT WITH AUTHOR

Cezary SPECHT  
Mateusz MANIA  
Mariusz SPECHT

Gdynia Maritime University,  
18 Sędzickiego St.  
81-374 Gdynia  
POLAND

Marcin SKÓRA

Polish Naval Academy  
Institute of Navigation and Maritime Hydrography  
69 Śmidowicza St.  
81-103 Gdynia  
POLAND

# A PROPOSAL OF SIMULATION MODEL OF A WIND-STEERING SYSTEM FOR SAILING YACHTS, BASED ON SINGLE-STAGE SERVO-PENDULUM COUPLED WITH MAIN RUDDER

**Andrzej Piętak**, Assoc. Prof.

**Maciej Mikulski**, Ph.D.

**Marek Melzacki**, M. Sc.

**Kamil Czerwiński**, B. Sc.

University of Warmia and Mazuria in Olsztyn, Poland

## ABSTRACT

*The aim of this study was to investigate possible application of fast design prototyping methods for wind-steering systems used in offshore sailing yachts. The development of such methods would help to speed up the construction work and reduce the scope of necessary experimental research, prior to implementation of the system. In the present work, based on an analysis of existing designs of windvane systems, a preliminary selection of the system configuration has been undertaken, in terms of a compromise between efficiency, performance, and design complexity. Construction design of a single-stage, servo – pendulum system, has been developed by using the Autodesk Inventor design package. Next, based on the design data, a simulation model of the system, has been produced by using Matlab - Simulink software and SimMechanics library. The model was further verified in terms of kinematics mapping with the use of Matlab visualization tools.*

**Keywords:** sailing yachts, wind-steering system, automation

## Introduction

Issue of automation of steering has reached greater and greater importance both for road, water and air craft. In the simplest application the problem consists in keeping a constant course respective to a given coordinate system (usually with respect to geographical north ). For deep-sea sailing ships (tall sail ships, sailing yachts) it is of a high importance to keep a constant course against direction of wind which, at a given position of sails, ensures propelling force to the ship. Wind - steering system is a device (in contrast to an electric giro-pilot) whose aim is to keep a constant course against wind. Windvane is set at a requested angle against an apparent wind direction. Motion of the windvane, when it departs from wind direction line, is transferred, through couplings, cords and hinges, to the main or auxiliary rudder or a balance tab which consequently corrects course of the yacht.

The concept of self-steering appeared as early as in the end of 15th century. However one of the first practical and well-documented applications of a self steering gear was the system installed by Martin-Marine on the yacht „Arielle” in 1936 [5]. This very simple system was not free of many drawbacks. In order to obtain a sufficiently large force on windvane for

putting the rudder into motion it was necessary to apply a large surface area of the windvane itself. The application of a vane with large surface area, in view of its large inertia, generated a large phase error in performance of the yacht steering gear. The features of the system limited its range of application.

The need of achieving a better precision of steering in a possibly broad range of weather conditions was forcing a natural evolution of self-steering systems. There are today a few specialty firms devoted to manufacturing and developing such devices [12, 13, 14]. The development of the systems comes mainly from experience gained by their producers. Results of reliable research work, both experimental and theoretical, on effectiveness of such systems are still lacking. A few attempts to a systematic description of self-steering gear – yacht systems were undertaken by Dąbrowski and Skórski [2, 3, 4]. The authors proposed a mathematical model of the self-steering gear – yacht system, solved in Matlab-Simulink environment. The model was verified by using data obtained from real-object tests. The concept proposed by Skórski was developed in an interesting way into research on possible application of active regulation of windvane jamming angle in order to improve properties of the system [6].

Progress in the field of the modelling of multi-mass systems has brought novel simulation tools. However there is still a need of conducting further research on self-steering systems for sailing yachts by implementing a modern approach to forming mathematical models. In this work SimMechanics software has been applied to create a simulation model of complex kinematic joints of a self-steering system based on a single-stage servo-pendulum coupled with main rudder of the yacht.

### Analysis of design solutions of wind-steering systems

The concept of wind-steering system has underwent a gradual evolution. A comprehensive description of implemented solutions can be found in the publication of Forthaman [5]. The systems both with auxiliary rudder (Fig.1.b; Fig.1.c) or direct coupling of the vane and main rudder (Fig.1.a) were considered. In case of the direct coupling, forces exerted on the vane were to overcome bearing friction forces, hydrodynamic force, drag resulting from motion transferring and those generated on rudder blade surface. The crucial issue of this design was too low force generated on windvane at light breeze. At a greater wind force yacht develops a greater speed, that results in a significant rise of hydrodynamic forces, hence an optional solution for such device would be to increase area of vane surface. However this becomes impractical and generates a large phase error [8].

For proper work of a wind-steering system, value of the force generated on its vane, which is a function of apparent wind speed and vane surface area, should be increased. Such effect can be reached by making use of water flow around moving hull as well as of interaction between intermediate mechanisms and an executive element. A helpful device may be e.g. a trimmer or servo-pendulum. In a hybrid design (with a servo-pendulum and additional trimmer, Fig.1.b) a crucial innovation was the introduction of an intermediate hydrodynamic device to support the work of the windvane interacting with the rudder. Trimmers had to change geometry of a body immersed in water flow around it, and as a result to change the generated hydrodynamic force and consequently to swing the servo-pendulum. In this case it was decisive to maintain an appropriate proportion between surface area of trimmer and that of pendulum blade. The solution has significantly increased sensitivity of the device but greatly complicated its construction itself.

Application of the windvane of horizontal rotational axis (Fig.1.c) made it possible to obtain a high amplitude of excitation even at slight departing from a given course by the yacht. It positively affected sensitivity and rate of reaction of the control system. The problem of achieving a sufficiently large force for rudder blade rotation was solved by separating the steering signal, i.e. windvane inclination, from the signal which excites steering moment.

The performed review of available design solutions has lead to selection, for further analysis, of a system with vertical windvane interacting with a single servo-pendulum

responsible for hydrodynamic amplification of wind steering signal. In the opinion of these authors the solution is an optimum compromise between effectiveness, operational accuracy and design complexity of the system.

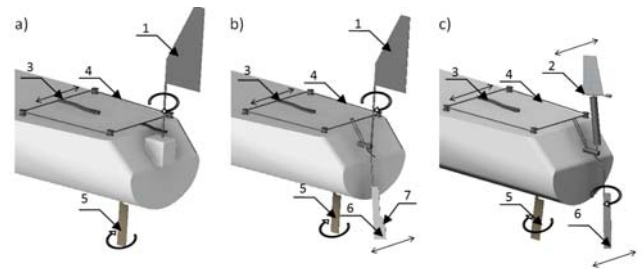


Fig. 1. Design solutions of wind-steering systems:  
a) a device of a direct impact of windvane onto main rudder;  
b) a device with servo-pendulum and auxiliary trimmer;  
c) a servo-pendulum device with horizontal rotation axis of windvane; 1 – windvane with vertical rotation axis; 2 – windvane with horizontal rotation axis; 3 – steering gear (tiller); 4 – system of pulley blocks and cables; 5 – main rudder blade; 6 – servo-pendulum blade; 7 – trimmer installed on pendulum blade;

### Design of wind-steering system with single-stage servo-pendulum

During initial work a conceptual design of wind-steering system was prepared by using Autodesk Inventor software [7]. Fig. 2 shows images of principal elements of the system in question. A schematic kinematic diagram of the whole wind-steering system and main rudder gear of a yacht is presented in Fig. 3

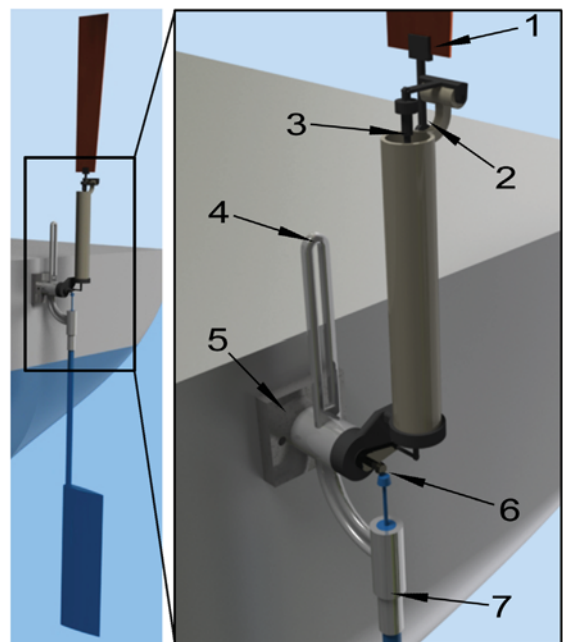


Fig. 2. Elements of construction of a wind-steering system, visualized by means of Autodesk Inventor software. 1- windvane; 2 – counterweight; 3 – push rod; 4 – pendulum arm, 5 – footing of winds-steering system (fixed upon yacht's transom); 6 – bevel gear; 7 – pendulum post

During sailing at a given course, the windvane is set according to apparent wind direction line. The counterweight keeps the windvane vertically. Similarly, the pendulum blade is so set as to make hydrodynamic force as low as possible. The system maintains equilibrium as long as the yacht does not start departing from a given course (under assumption that wind direction is unchanged). In such situation the windvane, under action of wind force applied to its surface, departs from its equilibrium position, that makes the system operating. Inclination of the windvane is transferred through the push rod to the toothed wheel of the bevel gear placed on the main post of the wind-steering system, stimulating this way rotation of the pendulum blade and changing its angle of attack.

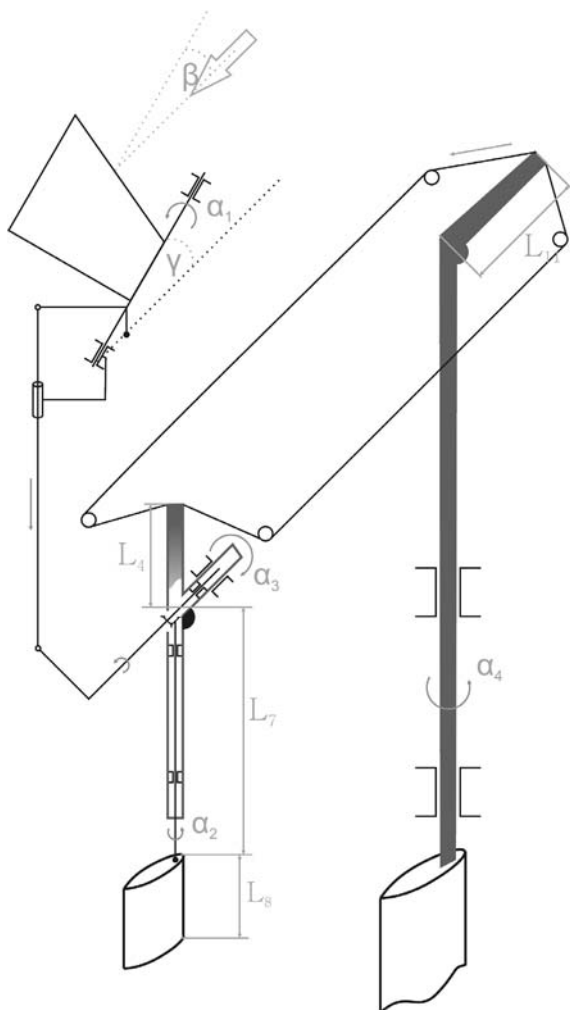


Fig. 3. Schematic diagram of kinematics of the wind - steering device - main rudder system.

$\beta$  - angle of departure from course,  $\gamma$  - windvane jamming angle;  
 $\alpha_1, \alpha_2, \alpha_3, \alpha_4$  - inclination angle of: windvane, pendulum blade, pendulum, main rudder, respectively;  $L_4, L_7, L_8$  - length of arm, post and pendulum blade, respectively;  $L_{11}$  - length of tiller

The hydrodynamic force generated on blade surface makes the pendulum rotating around a straight line which determines direction of yacht motion. Features of the bevel gear make it possible to incline the pendulum along with the

simultaneous decreasing of blade angle of attack, without any interference into position of the windvane, until the next equilibrium state is reached. This way the system aims at self-stabilization, that simultaneously limits maximum inclination of the pendulum and prevents it against sticking off the water. To this end, the pendulum arm (Fig. 2., item 4.) transfers steering moment to the tiller or steering wheel through the system of pulley blocks and cables. Rotation of the main rudder triggers return of the yacht to set course. Consequently, angle of inclination of wind direction from windvane axis decreases, hence aerodynamic force acting on it also decreases. The counterweight of the windvane gives rise to its return to equilibrium position, that generates pendulum blade rotation in the other direction. Shape of water flow round the blade leads to return of the pendulum arm to its initial position.

### Mathematical model of the wind-steering system with single-stage servo-pendulum

Operational effectiveness of the yacht - wind -steering device system considered as an automatic control system is affected by a very large number of factors such as: size and shape of windvane, construction and inertia moment of yacht, apparent wind speed, shape of auxiliary rudder blade, applied gear ratio, as well as friction forces, inclination angle of yacht from set course etc.

In order to analyse effectiveness of such system it is necessary to develop an adequate simulation model which would allow to select optimum parameters of the system in the aspect of possible steering in given sailing conditions. In the so defined problem the yacht- wind-steering device system is consisted of a few dozen of stiff solids (bodies) connected by means of passive mechanical elements. Geometrical and kinematic constraints are assigned to the stiff bodies and the forming of mathematical model in question consists in solving a Lagrange matrix equation for multi-mass system.

Analytical determination of appropriate matrix quantities is very difficult in case of a few dozen of elements. Taking into consideration geometrical complexity of such construction, these authors resigned from direct formulation of system's dynamic equations in favour of using a dedicated, object-orientated simulation environment. Matlab - Simulink software of Mathworks firm together with SimMechanics library [10] was applied. For modelling purposes the yacht - wind-steering device system was divided into 92 component elements. Fig. 4 presents the schematic block diagram of wind-steering system model. In the diagram, macro-elements are considered to be separate sub-models. The exemplary schematic diagram of the sub-model of the frame of wind-steering system is shown in Fig. 5.

In order to precisely reproduce dynamics of the system the Simulink makes use of parametrization procedure for particular mechanical elements by indicating location of their constraints, centre of gravity, mass and inertia moment tensor at initial instant. Only basic geometrical and material data for all component elements were assumed to be input parameters of the model.

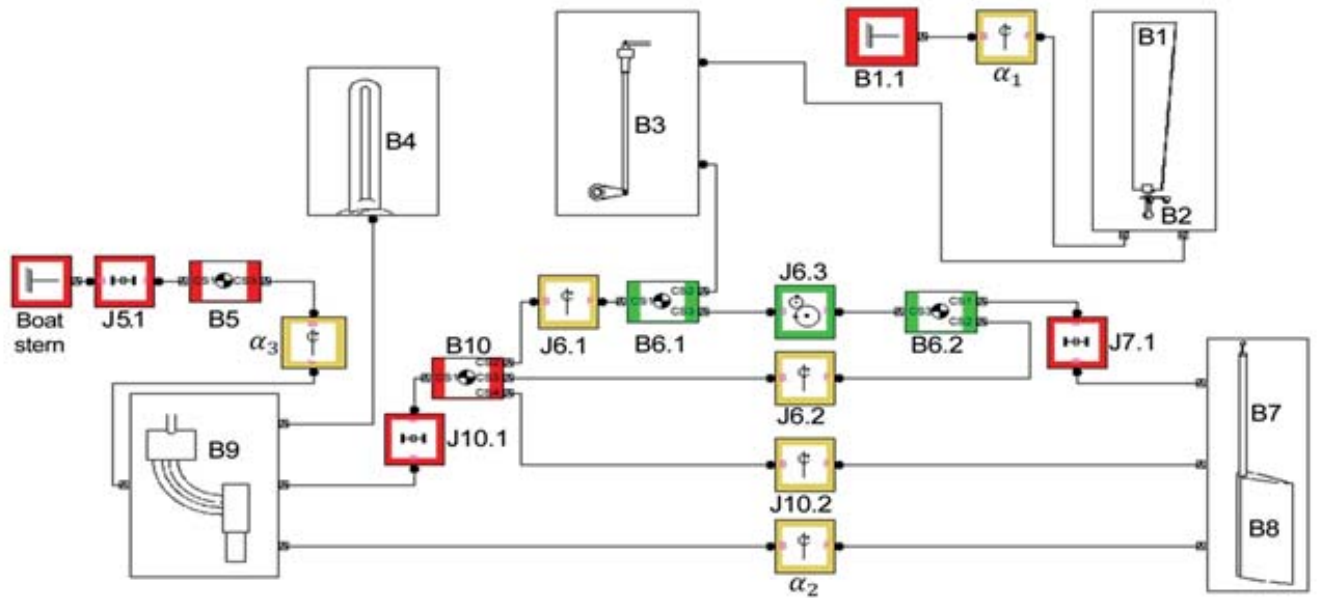


Fig.4. Schematic block diagram of wind-steering system model, prepared in Simulink (SimMechanics) environment. Symbol B represents particular mechanical elements, J – joints (welded, screwed or rotary ones). Numerical indices stand subsequently for a macro-element number (the same notion as in Fig.2) and number of a component element of the macro-element.

Tab. 1. Elements of sub-model of wind-steering system frame (Fig. 5.)

B 9		Wind-steering system frame			
		Bodies		Joints	
Symb.	Type	Description	Symb.	Description	
B 9.1	Pipe	Main axle of frame	J 9.1	Welded joint	
B 9.2	Cylinder	Vertical connection	J 9.2	Welded joint	
B 9.3	Cylinder	Horizontal connection	J 9.3	Welded joint	
B 9.4	Pipe	Windvane blade rotation axle			

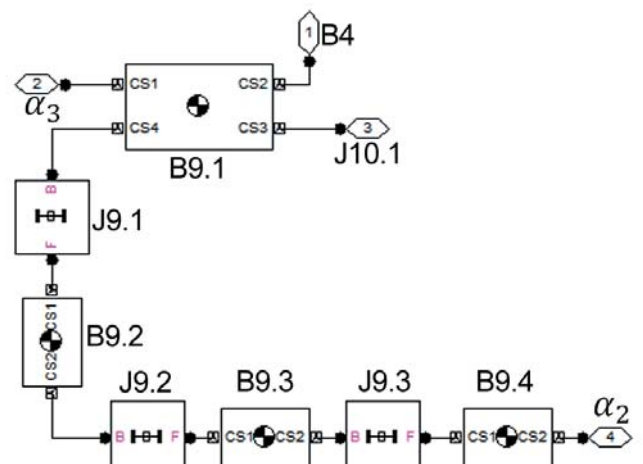


Fig. 5. Schematic block diagram of sub-model of wind-steering system frame, prepared in Simulink (SimMechanics) environment. Description of particular elements is given in Tab. 1.

The input data are sent to the mathematical model. They are taken from technical documentation of the device, generated by Autodesk Inventor software where the design project is under preparation. For modelling purposes was prepared an external sub-model intended for the calculating of element masses and inertia moments along axes of the coordinate system. The coordinate system was assumed yacht-fixed and so orientated as to get z-axis complying with yacht hull symmetry axis and y-axis pointing direction of hydrostatic buoyancy force. Under such assumptions all tensors form diagonal matrices. As in initial position all the elements of the wind-steering system are placed along one of three axes of the coordinate system, it can be possible to write the following for  $i^{th}$  elements:

The input data are sent to the mathematical model. They are taken from technical documentation of the device, generated by Autodesk Inventor software where the design project is under preparation. For modelling purposes was prepared an external sub-model intended for the calculating of element masses and inertia moments along axes of the coordinate system. The coordinate system was assumed yacht-fixed and so orientated as to get z-axis complying with yacht hull symmetry axis and y-axis pointing direction of hydrostatic buoyancy force. Under such assumptions all tensors form diagonal matrices. As in initial position all the elements of the wind-steering system are placed along one of three axes of the coordinate system, it can be possible to write the following for  $i^{th}$  elements:

$$M_i = \begin{bmatrix} I_{x,i} & 0 & 0 \\ 0 & I_{y,i} & 0 \\ 0 & 0 & I_{z,i} \end{bmatrix}$$

For instance, for the element 3.1, i.e. push rod (rod made of a material of  $\rho$  density, radius -  $r$ , length -  $L$ ):

$$\begin{cases} m_3 = \pi \rho_3 L_3 r_3^2 \\ I_{y,3} = \frac{1}{2} m_3 r_3^2 \\ I_{x,3} = I_{z,3} = \frac{1}{12} (3r_3^2 + L_3^2) \end{cases}$$

The remaining elements were parametrized in the same way.

According to the design project, the coupling of the wind-steering system with the main rudder was arranged by applying the system of pulley blocks and cables. Position of reverse blocks is determined by position of the end of main rudder tiller at its maximum inclination (90°). In the model in question the coupling was modelled as a massless gear of the ratio determined by the length of main rudder tiller and the length of wind-steering system arm. The simplification is deemed justified in view of a slight mass of the cables in comparison to the remaining mechanical elements. Analysing geometry of the coupling one can show that at a given inclination ( $\alpha_3$ ) of the arm of wind-steering system the main rudder will be rotated by the following angle :

$$\alpha_4 = 2 \arccos \left[ 1 - \frac{L_4}{L_{11}} \left( 1 - \cos \left( \frac{\alpha_3}{2} \right) \right) \right]$$

where:  $L_{11}$  and  $L_4$  are length of main rudder tiller and length of wind-steering system arm, respectively. Symbols used in the formulae (4)-(6) are highlighted in Fig. 3.

On the system should be additionally applied geometrical constraints connected with the slope angle of windvane axis,  $\gamma$ , (the so called vane jamming angle). In the case of strictly horizontal position of the axis ( $\gamma=90^\circ$ ) the windvane acts as a binary sensor. Even a slight departure of yacht from its course ( $\beta$ ) results in the maximum permissible inclination of the windvane. This makes reactions of the control system independent on magnitude of disturbance and may therefore generate switchover events and a lack of stability. On the other hand, in case of  $\gamma=0^\circ$ , a system of vertical windvane rotation axis with its main drawback (consisted in too low amplitude of steering signal), is obtained. The windvane jamming angle controls amplification of steering signal. Basing on an analysis of the system's geometry (Fig. 3) it is easy to show that, at a given value of the angle  $\gamma$  and departure of yacht from its course by the angle  $\beta$ , the windvane rotation angle can be expressed by the following relation:

$$\alpha_1 = \text{atan} \left( \frac{\tan \beta}{\sin \gamma} \right)$$

Analogous geometrical constraints can be also imposed onto the pendulum blade. By making its inclination possible an additional optimizing parameter capable of controlling hydrodynamic amplification of system's reaction, is obtained.

In case of the pendulum blade, to introduce an additional constraint for counteracting against its emersion off the water, is necessary. Construction of the wind-steering system is secured against this phenomenon in a natural way as a result of tending the blade angle of attack to zero during inclination of the pendulum out of its vertical position. Consequently, regardless of applied gear ratio, maximum value of the pendulum inclination amounts exactly as much as value of the inclination angle of the windvane in given conditions. However during selecting the system's geometrical parameters the yacht heel angle ( $\varphi$ ) should be taken into consideration. Analysis of the system's geometry leads to the relation for length of immersed part of the blade in function of heel angle, windvane inclination angle and pendulum length, as follows:

$$\Delta L = (L_7 + L_8) \cos(\alpha_3 + \varphi) - L_1 \cos(\varphi)$$

The elements of the system, numbered 1, 8, 11 (standing for the windvane, pendulum blade, main rudder blade - Fig. 2.) may be loaded with external excitations in the form of aero- and hydrodynamic forces. Analogously, in joints of kinematic pairs both dry and viscous friction takes place. Moreover, in case of the pendulum blade to take into account hydrostatic buoyancy forces is necessary. This paper is focused on verification of mathematical kinematic model only. A detail analysis of dynamics of the system will be presented in the next part of the work.

### Analysis of operational correctness of kinematic model

To make it possible to use the model for investigation of dynamic performance of the yacht - wind - steering - device system it is necessary to preliminarily analyse correctness of its operation. The verification contained two stages. In the first stage parametrization correctness of particular mechanical elements in simulation structure, was examined. To this end, Matlab V-R Toolbox, a visualization tool, was applied. By correct introduction of connections of geometrical constraints and values of tensors into considered project, an appropriate mapping of the system's geometry during visualization is reached. In Fig. 6 is presented a fragment of visualization of the mathematical model in which inertia moments of structural elements are taken into account.

Evaluation of conformity of the mathematical model consisted in comparison of elementary motions of wind-steering system, which result only from angular excitations in joints. The test on correctness of operation was parallelly conducted for the design project prepared with the use of Autodesk Inventor software and the mathematical model implemented within Simulink environment. Exemplary results of the simulation are presented below.

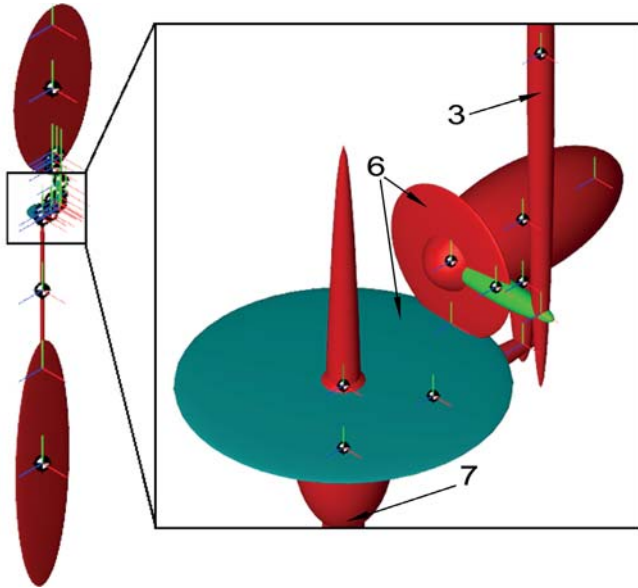


Fig. 6. Elements of wind-steering system kinematics visualized in Matlab software with the use of SimMechanics library; for notation – see Fig.2.

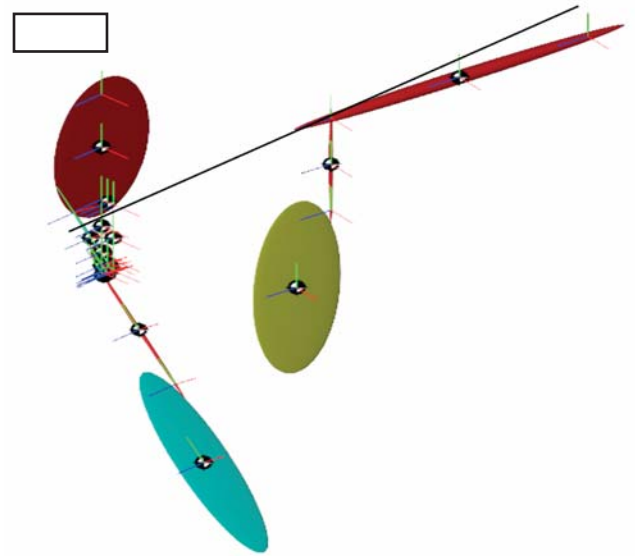


Fig. 9. Visualization of the mathematical model at inclination of the pendulum which generates inclination of the main rudder

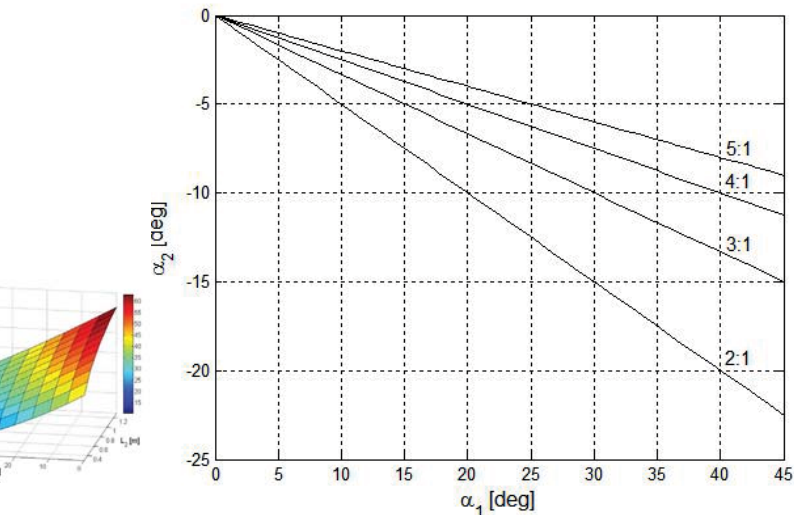


Fig. 7. Diagram of changes in the pendulum blade rotation angle ( $\alpha_2$ ) in function of the windvane inclination angle ( $\alpha_1$ ), for various values of the bevel gear ratio

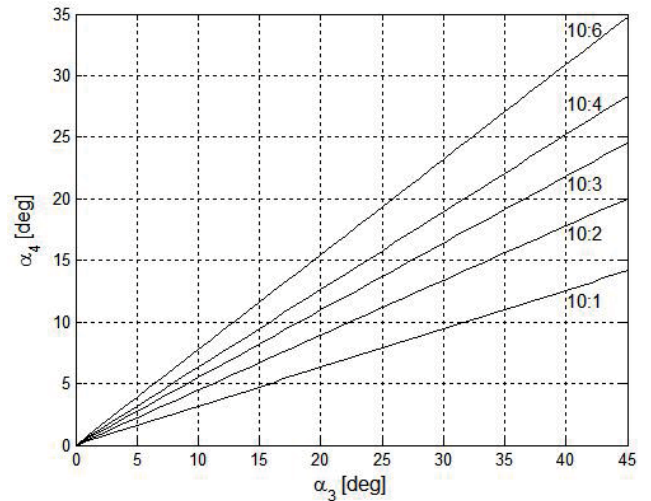


Fig. 10. Diagram of changes in the main rudder rotation angle ( $\alpha_4$ ) in function of the pendulum inclination angle ( $\alpha_3$ ) for various values of the ratio of the tiller length ( $L_{11}$ ) and wind-steering system arm ( $L_4$ )

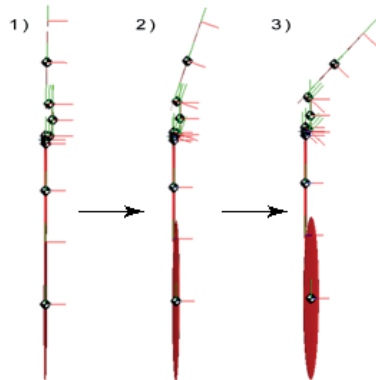


Fig. 8. Visualization of the mathematical model at set changes in position of the windvane. 1 - equilibrium position, 2 - intermediate position, 3- maximum inclination limited by constructional conditions

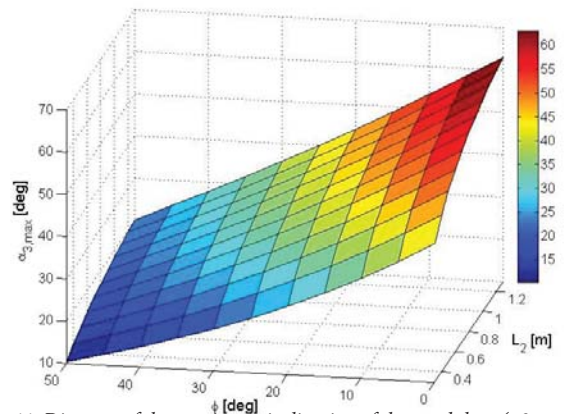


Fig. 11. Diagram of the maximum inclination of the pendulum ( $\alpha_{3max}$ ) in function of yacht's heel angle and the blade length ( $L_8$ ); under assumption on the constant length of the pendulum post  $L_7 = 0,6$  m and the length of wetted part of the pendulum blade, equal to 20%  $L_8$

## Conclusions

In designing the wind-steering systems for various types of yachts intended for the operating in extremely different weather conditions the crucial issue is to properly select geometrical parameters of such device. Choice of control characteristics may be preliminarily made on the basis of model calculations by using only basic data available from the builder or owner of the considered yacht. It diminishes time and cost of performing such adaptation.

It has been proved that the proposed mathematical model of the wind-steering system with single-stage servo-pendulum correctly reproduces performance of the actual system as far as its kinematics is concerned. After taking into account external excitations and friction in kinematic pairs the extended model may be used for fast prototyping the devices of the kind.

Moreover, in this work the main geometrical parameters of the system were preliminarily determined on the basis of analysis of construction of wind-steering systems and geometrical constraints imposed on them. It was shown that optimum values of control settings are contained within the following ranges:

- for the windvane jamming angle: about  $20^\circ$ ; alternatively, in order to reach a greater amplification, the angle may be regulated within the range of  $5^\circ \div 15^\circ$  accompanied with application of a constructional stopper to limit maximum inclination angle to  $40^\circ$ ;
- for the bevel gear ratio:  $3/1 \div 4/1$ ;
- for the ratio between the length of main rudder tiller and the length of wind-steering system arm:  $10/3 \div 10/2$  that ensures to transfer a properly large moment at maintaining a demanded range of rotation for main rudder.

## Bibliography

1. Anderson B. D.: The Physics of Sailing Explained. Adlard Coles Nautical, London, 2003
2. Dąbrowski Z., Skórski W. W.: Assesment of operational correctness of wind-steering system ( in Polish). *Przegląd Mechaniczny*, No. 5÷6/1996, pp. 3÷4
3. Dąbrowski Z., Skórski W. W.: Wind-steering system with double servo-mechanism ( in Polish). *Przegląd Mechaniczny*, No.5/2001, pp. 3÷4
4. Dąbrowski Z., Skórski W. W.: Introduction to theory of wind-steering systems ( in Polish). Wydawnictwo ITE-PIB ( Publishers), Warszawa-Radom, 2005
5. Forthman P. Ch.: Self-steering under sail. Autopilots and Wind-steering Systems. Mcgraw-Hill, London, 1998
6. Górecki P, Stankiwicz B., Szajkowski P.: Design of a wind-steering system with the active setting of windvane jamming angle ( in Polish). *Przegląd Mechaniczny*, No. 9/2004, pp. 23÷26

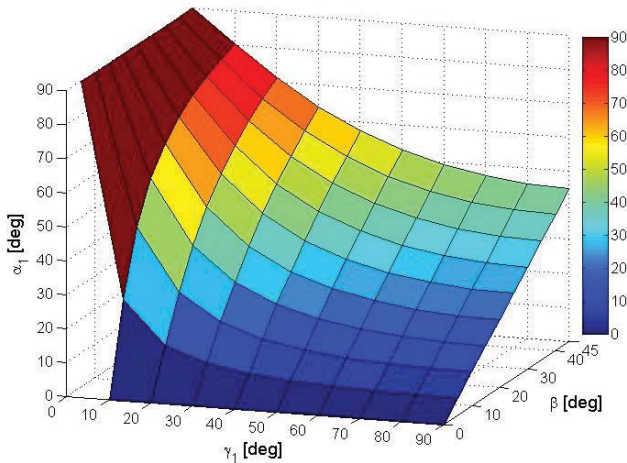


Fig. 12. The windvane inclination angle ( $\alpha_1$ ) in function of the windvane jamming angle ( $\gamma_1$ ) and the angle of yacht's departure from course, ( $\beta$ )

Analysing the diagram of Fig. 11 one can state that, under assumption on the permissible value of sailing yacht's heel angle not exceeding  $30^\circ$ , the pendulum inclination amplitude should be contained in the range of  $30^\circ \div 40^\circ$  (depending on a value of applied blade length) in order to ensure possible operation of the considered system in given conditions. The limitation of the maximum inclination angle can be obtained most easily by constraining windvane inclination. It may be reached with the use of a constructional limiter (stopper) or by adjustment of the windvane jamming angle ( $\gamma$ ).

Under assumption that the maximum permissible yacht's departure from its course amounts to  $\beta = 30^\circ$ , the windvane jamming angle equal to about  $20^\circ$  would be able to prevent the system against sudden loss of stability due to drop of the steering moment (owing to pendulum emerging off the water) in heavy sailing conditions (Fig. 11). On the other hand, greater values of the angle  $\gamma$  are deemed unfavourable because they would generate too low values of the angle  $\alpha_1$  at typical yacht departures from course, ranging  $\pm 10^\circ$ .

Maximum windvane inclination angle implies a range of applicable values of bevel gear ratio. Maximum value of lateral hydrodynamic force is reached, depending on an applied blade profile and Reynolds number determining kind of flow, for values of angle of attack equal to about  $10^\circ$  [9]. The above discussed conditions show that in the case in question it is possible to apply  $R_{6,1}/R_{6,2}$  ratio  $< 4/1$  (Fig. 7). It makes it possible to obtain an appropriately large value of the moment capable of rotating the pendulum blade. As results from elementary sailing theory, at increasing heel of yacht its arduency (i.e. its tendency to automatic departure from course toward wind's eye) grows [1]. In the conditions of  $30^\circ$  heel angle it is necessary, at least for some yachts, to make main rudder inclination greater than  $20^\circ$  in order to keep the yacht on its course [1]. Therefore the wind-steering system should cope with such inclinations. It is implied by the condition:  $L_{11}/L_4 < 10/3$  for the ratio between the length of main rudder tiller and length of arm of wind-steering system.

7. Jaskulski A.: Autodesk Inventor Professional 2014PL /2014+. Fusion/Fusion 360. Design methodology (in Polish). Wydawnictwo Naukowe PWN ( Publishers), Warszawa, 2013
8. Marchaj C.: Sail Performance Theory and Practice. Adlard Coles Nautical, London, 1996
9. Marchaj C.: Seaworthiness; the forgotten factor (in Polish). Almapress, Warsaw, 2002
10. Osowski S.: Modelling of dynamic systems by using Simulink language ( in Polish). Oficyna Wyd. Pol. Warsz. ( Publishing House of Warsaw Univ. of Techn.), Warsaw, 1999
11. Tarnowski W., Bartkiewicz S.: Mathematical modelling and computer simulation of continuous dynamic processes ( in Polish). Wydawnictwo Feniks ( Publishers), Koszalin, 1998
12. www.ariesvane.com. Aries Standard - Peter Matthiesen. Mollegade 54, Holm DK 6430 Nordborg, Denmark
13. www.selfsteer.com. Auto Helm. Scanmar International. 432 South 1st Street, Richmond CA, 94804-2107 USA
14. www.windpilot.com. Windpilot USA. Madeira Beach Fl ,33738-8565 USA

## CONTACT WITH AUTHOR

Andrzej Piętak  
 Maciej Mikulski  
 Marek Melzacki  
 Kamil Czerwiński

University of Warmia and Mazuria in Olsztyn  
 Faculty of Technical Sciences  
 Chair of Mechatronics  
 46 A, Słoneczna St.  
 10-710 Olsztyn,  
 POLAND

Tel.: +48 89 524 51 00

e-mail: [maciej.mikulski@uwm.edu.pl](mailto:maciej.mikulski@uwm.edu.pl)

# A HYDRODYNAMIC METHODOLOGY AND CFD ANALYSIS FOR PERFORMANCE PREDICTION OF STEPPED PLANING HULLS

Hassan Ghassemi, Assoc. Prof.  
Mojtaba Kamarlouei, M. Sc.  
Sajad Taj Golah Veysi, M. Sc.  
Amirkabir University of Technology, Tehran, Iran

## ABSTRACT

*Nowadays all efforts in planing hull research are focused on resistance reduction for achieving the highest speed in fast planing crafts. Furthermore, many fruitful research projects have been carried out on marine coatings, planing equipment, and optimization of propeller and hull form, which revolutionized industry of high - speed crafts and made them an efficient survival vehicle in coastal areas and rivers. In this paper the hydrodynamic performance of planing hulls are investigated by means of a modified Savitsky model for both non-stepped and stepped bodies. Meanwhile, in order to meet this goal reasonably, effective geometrical parameters of planing hull are investigated and then operational hydrodynamic characteristics of the craft are predicted by using a computational program. Finally, the calculation results are verified by means of a CFD- analysis model.*

**Keywords:** Planing hull, Hydrodynamic performance, CFD analyzed

## Introduction

Generally, there are three types of hulls in marine transport industry. Displacing hulls, semi-planing hulls and planing hulls. All of them can be however considered displacing ones when cruising at a low speed. Planing hulls, unlike the other two kinds, are obviously lifted by hydrodynamic pressure, instead of hydrostatic pressure. This goal is achieved by hull design considerations which help the vehicle to rise partially out of the water, then the wetted area reduces considerably that results in frictional drag reduction and subsequent rise of speed of the vehicle.

Nowadays planing vessels are applied as patrol boats, sport fishing vessels, service crafts, ambulances and rescue crafts, recreational and sport crafts. The geometry of stepped planing hull can be considered as two distinct planing bodies merged together close to the waterline. The theory of stepped planing hulls is the same as for simple planing vessels. However this theory cannot be used for afterbody of stepped ones because this part is faced with a disturbed free surface generated by forebody wake. The most significant characteristic feature of stepped planing hulls is the separation of the flow off the step at high speed, leading to partial ventilation of the afterbody, reducing the wetted surface and, consequently, hull resistance

without significant affecting the hydrodynamic lift. Therefore, the ventilated length is shortest along the keel. It increases with speed and is connected with the height of the keel in the flow attachment area above the keel, before the step[1].

It is generally known that step would be an advantageous item in planing hull design. For example, when the owner needs a specific weight distribution, or when a special type of propulsion system and power generation package are going to be applied in planing vessel, the best concept which meets these parameters is a stepped planing hull. On the other hand, the peak of total resistance in such vessels are lower than non-stepped ones. Fig. 1 (A) illustrates a stepped planing hull which is equipped with a free-surface-piercing propeller and ventilating rudder.

Despite, there is no adequate method for performance prediction of stepped planing hulls yet; nowadays most of the planing hulls are designed with step. Meanwhile, two methods may be used for hydrodynamic analysis of stepped planing hulls. The first method is to use computation fluid dynamics (CFD) and the second is to apply an experimental method which needs a model basin and other test facilities.

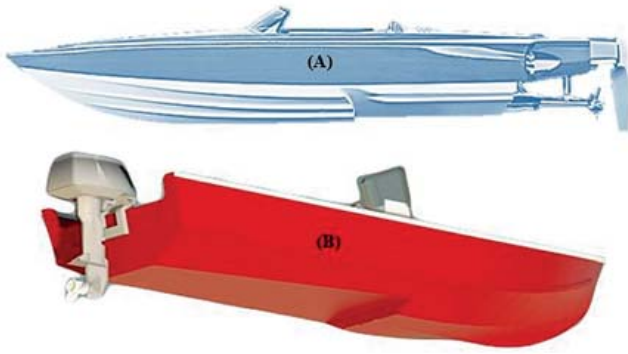


Fig. 1. Stepped planing hull

## Literature review

In one of the most famous research investigations on planing hulls, carried out by professor Savitsky in 1964, were introduced some mathematical approaches for frictional and pressure resistance, trim angle and some other hydrodynamic parameters based on a group of experiments done for the first time [2]. Before Savitsky's research, in 1963, Clement and Blount planned some experiments for investigation of the resistance and trim in five 62-series bodies [3]. In 2003 Savander and Rhee applied a numerical method for hydrodynamic parameters of planing hulls and verified their calculation outputs with experimental results [4]. Ghassemi and Ghiasi, in 2007, introduced a complex numerical method which includes both finite element and boundary element approaches to predict the hydrodynamic characteristics of planing hulls [5]. Simultaneously, Brizzolara and Serra studied numerically a fixed-position planing hull and compared the results with available experimental data. An average error of 10% in total drag prediction and 5% error in total lift prediction, showed the capability of numerical methods to obtain accurate results for planing hulls [6]. After that, in 2010, Ghassemi and Kohansal applied a numerical method based on boundary element method to investigate hydrodynamic parameters of different hull shapes [7]. Savitsky and Morabito, in 2010, investigated the wake produced by a step in afterbody of a stepped planing hull [8]. Svahn, in 2009, investigated lift distribution in mono-hulls, basing on Savitsky model, but introducing a great novelty consisted in consideration of a deadrise angle and local trim for afterbody of his model [9]. Garland and Maki, in 2012, did a numerical study on Two-Dimensional Stepped Planing Surface. Their results show that the lift-to-frictional-drag ratio varies very little with respect to the step location [10]. The determining of the hydrodynamic forces on the multi-hull tunnel vessel in steady motion has been investigated by Ghassabzadeh and Ghassemi. Their results included pressure distribution, trim angle, rise of centre of gravity and resistance at various speeds [11]. Recently, Radojcic et al. [12] presented a mathematical model of calm-water resistance for contemporary planing hull forms based on the USCG and TUNS series. They derived two speed-dependent mathematical models, simple and complex, to evaluate the calm-water resistance.

In this paper the main goal is to investigate the hydrodynamic characteristics of planing hulls including stepped and non-stepped models against the change of geometrical parameters of the planing body, with the use of a modified Savitsky model. In this paper,  $L_p$ , i.e. the distance measured from transom along keel to the place where normal force acts, and LCG, i.e. position of the centre of gravity, are not considered to be located in the same point as in case of analysis of a hull without step. Additionally,  $\Phi$ , i.e. the part of weight carried by the forebody of stepped planing hull is not considered a constant value and differs. Finally the applied model results have been verified with CFD calculations for a specific model at different Froude numbers.

## Non-stepped planing hull

In this paper, to meet an acceptable result for non-stepped planing hulls a computational program based on a modified Savitsky method, has been developed. Indeed, Savitsky method is based on a kinematic model test of planing hulls and is strongly supported by experimental data [2]. Also the most significant index of this computational algorithm would be the lift coefficient acting on deadrise of the vehicle,  $C_{L\beta}$ , which is not a constant value and changes in each iteration in order to find the best value. Fig. 2 shows the forces acting on the planing hull and its parameters, where  $a$ ,  $c$  and  $f$  are the arms of moments of drag, thrust and lift force, respectively;  $\tau$  and  $\varepsilon$  are the angle of trim and thrust line inclination relative to keel line, respectively.

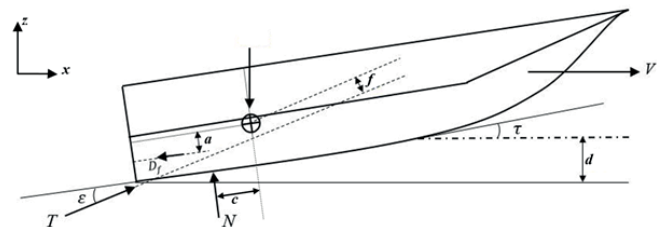


Fig. 2. Diagram of forces acting on non-stepped planing hull in vertical plane

## Calculation method and flow-chart

Stability equations for non-stepped planing hulls in longitudinal and vertical directions and in the centre of gravity can be defined as follows, according to Fig. 2:

$$\text{Longitudinal forces: } T \cos(\tau + \varepsilon) - N \sin \tau - D_f \cos \tau = 0 \quad (1)$$

$$\text{Vertical forces: } N \cos \tau + T \sin(\tau + \varepsilon) - mg - D_f \sin \tau = 0 \quad (2)$$

$$\text{Vertical moments with respect to centre of gravity: } N \cdot c + D_f \cdot a - T \cdot f = 0 \quad (3)$$

Undoubtedly, in each numerical computation method convergence condition plays a markedly role for achieving both reasonable outputs and CPU time. In this paper two constraint conditions are considered.

The first condition, Eq. (4), defines a satisfactory convergence of vertical moment computation.

$$F_{L\beta} L_p - mg LCG \leq \zeta_1 \quad (4)$$

where:

$$F_{L\beta} = \frac{1}{2} \rho U^2 B^2 C_{L\beta} \quad (5)$$

and  $L_p$  is calculated as follows:

$$L_p = 0.75 - \frac{\lambda B}{\frac{5.21 C_v^2}{\lambda^2} + 2.39} \quad (6)$$

While  $\rho$  is water density,  $U$  – vehicle speed,  $B$  - vehicle breadth and  $\lambda$  - mean wetted length-to-beam ratio.

The second condition is a satisfactory convergence of trim calculation, expressed by Eq. (7).

$$M_{tot} = mg \left[ \frac{c}{\cos \tau} (1 - \sin \tau (\sin(\tau + \varepsilon)) - f \sin \tau) \right] + D_f (a - f) \leq \zeta_2 \quad (7)$$

where  $\zeta_1$  and  $\zeta_2$  are constants assumed to be as little as  $1e-2$ .

The flow chart of the modified Savitsky method is shown in Fig. 3. As it can be seen, two constraints should be satisfied in order to finish the calculation cycle.

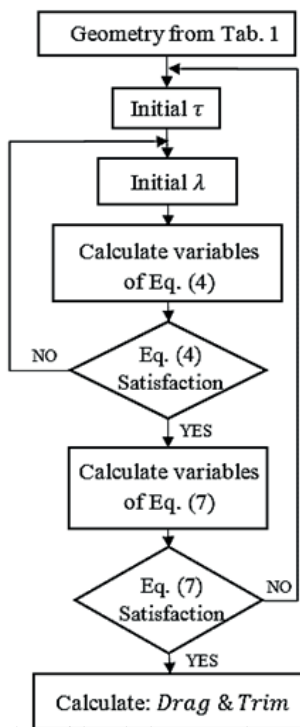


Fig.3. Flow chart of the calculation acc. the assumed method

## Calculation results

The output for an examined model is presented to show the effects of deadrise angle, longitudinal position of centre of gravity (LCG), and  $\frac{L}{B}$  ratio on trim and  $\frac{Drag}{L\beta}$  ratio in a given range of Froude number values. The model parameters are specified in Tab. 1.

Tab.1. Geometrical parameters of examined vehicle

Parameter	Value
Displacement ( $\Delta$ )	18.7 (t)
Deadrise angle ( $\beta$ )	13 (deg)
Breadth (B)	3.807 (m)
Longitudinal Centre of Gravity (LCG from aft)	6.695 (m)
Vertical Centre of Gravity (VCG)	0.8 (m)
Length -to - Breadth ratio ( $\frac{L}{B}$ )	4.09
Distance between T and centre of gravity (measured normal to T)	0.0380 (m)
Thrust- line inclination angle relative to keel -line	10 (deg)

Tab. 2 shows results of the verification. The trim calculated by using the prepared program and the reference trim achieved from a given program [13] are compared to each other and the respective error values at different speeds are presented in 4<sup>th</sup> row of Tab. 2.

Tab. 2. Comparison between program output and reference results[13].

Speed (Knots)	15	20	25	30	35	40	45
Calculated trim (degree)	2.4	2.96	3.3	3.26	3	2.67	2.36
Reference trim (degree)	2.53	3.03	3.36	3.33	3.07	2.74	2.41
Error (%)	5.13	2.31	1.78	2.1	2.28	2.55	2

Moreover, Fig. 4 shows the change of hydrodynamic parameters against the change of geometrical characteristics in a given range of Froude number values. Also, the effect of deadrise angle, longitudinal centre of gravity and  $\frac{L}{B}$  ratio on trim angle and  $\frac{Drag}{L\beta}$  ratio at different Froude number values is indicated in this figure, respectively. Obviously, in case of non-stepped planing hulls the increase of deadrise angle and LCG result in trim angle reduction and drag enhancement. On the contrary, the increase of  $\frac{L}{B}$  ratio rises the trim angle and decreases the  $\frac{Drag}{L\beta}$  ratio.

## Stepped planing hull

As it can be seen in Fig. 7, the body of stepped planing hulls is divided into two parts, fore and aft, and hydrodynamic forces and moments affect each part distinctly. The first reason for using stepped planing hull is to divide the wetted surface into smaller parts. For instance, in case of a single-step

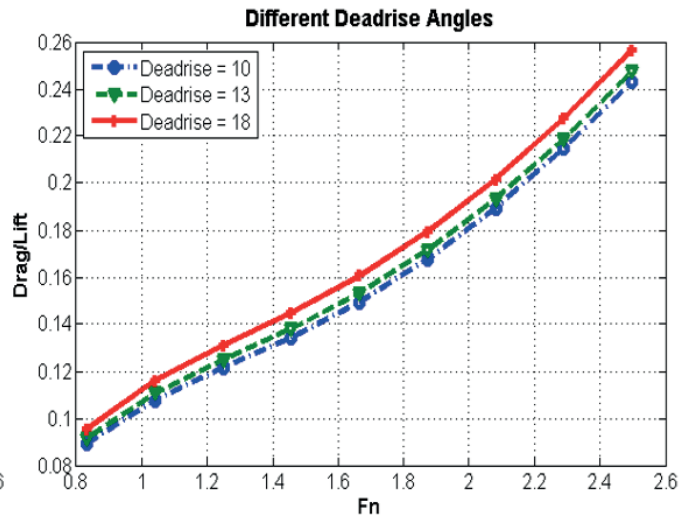
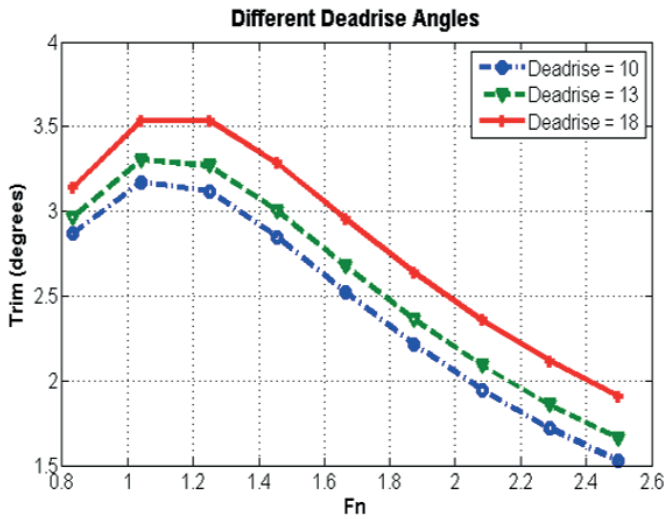


Fig.4. The change of trim and  $\frac{Drag}{Lift}$  ratio in function of Froude number  $F_n$  for three deadrise angle values

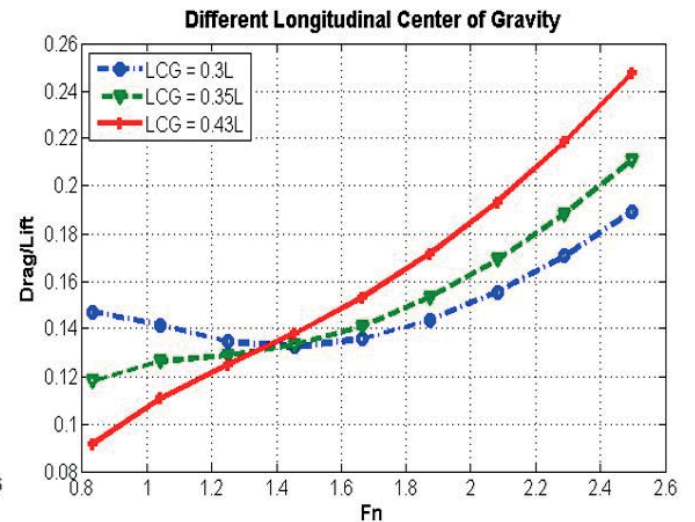
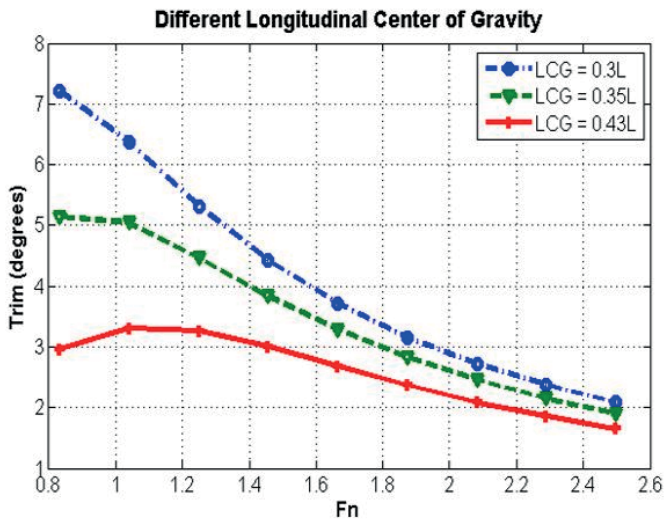


Fig.5. The trends of trim and  $\frac{Drag}{Lift}$  ratio in function of Froude number  $F_n$  for three LCG values

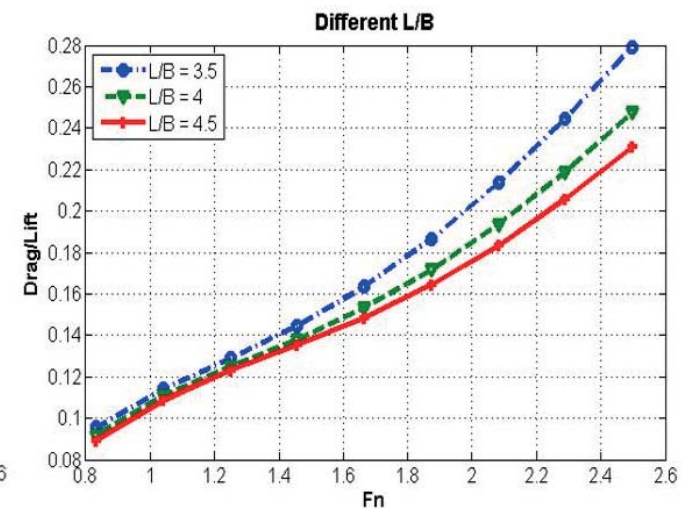
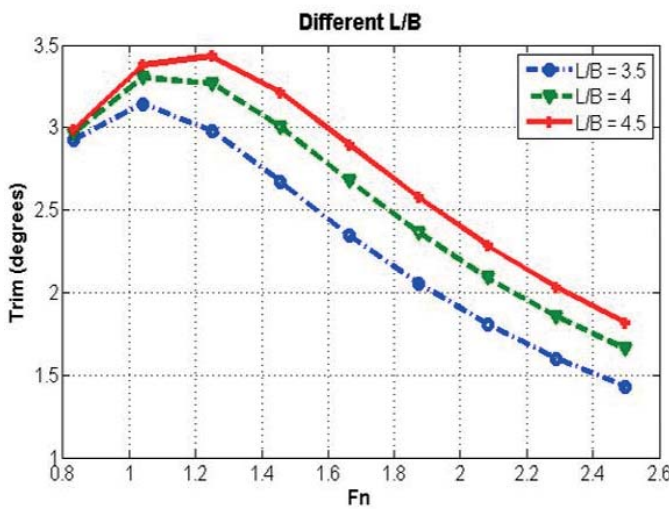


Fig. 6. The variation of trim and  $\frac{Drag}{Lift}$  ratio in function of Froude number  $F_n$  for three  $\frac{L}{B}$  values

planing hull its wetted surface is divided into two smaller areas. Therefore, as a result, amount of the lift generated in stepped planing hulls is markedly greater than lift force generated in case of a long continuous wetted surface in non-stepped ones. So this growth in lift force causes an efficient reduction of wet surface resulting in reduction of the frictional resistance. And,  $\Phi$  is the weight proportion assigned to forebody, and two indexes, 1 and 2, stand for forebody and afterbody properties, respectively.

### Hydrodynamics of afterbody

To estimate the wetted area of aft hull, it is obvious that wake field of forebody and its boundaries should be investigated. Wetted area of afterbody which is affected by forebody wake field can be seen in Fig. 7.

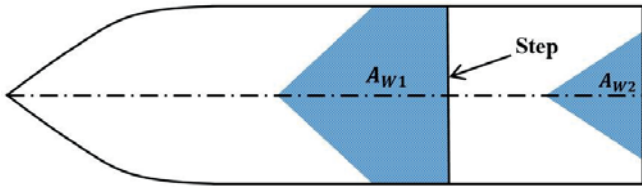


Fig. 7. Wetted area of forebody and afterbody of stepped planing hull

Savitsky and Morabito investigated the afterbody wake generated by step in a stepped planing hull and achieved some semi-experimental relations for the wake behind the step, using model tests. Basically, two important parameters resulting from their experiment, are  $X_{CL}$  and  $X_{\frac{1}{4}}$ . The first represents the distance between step and afterbody wetted surface, measured along keel line, and the other is that measured in one fourth of beam from the keel line. Local level waterline is also an effective parameter which is formed by a straight line connecting the first point of wetted surface in keel line and the first one in the  $\frac{1}{4}$  of beam. Fig. 8 shows the three quantities.

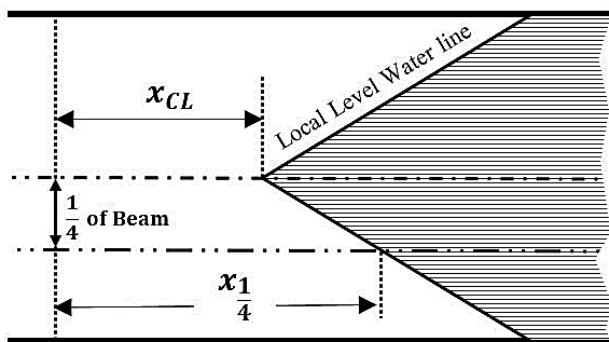


Fig. 8. Local waterline as a result of wake generated by step

Moreover, besides this difference in shape, it is assumed that the water behaves the same way meeting the aft hull as it does when hitting the fore hull. Then, to meet reasonable

results the effects of wake on afterbody are considered by using definition of some local parameters with L index such as  $\beta_{2L}$  which is local deadrise angle in aft hull. Actually, this angle is the difference between  $\beta$  and the inclined waterline in the afterbody due to wake field.

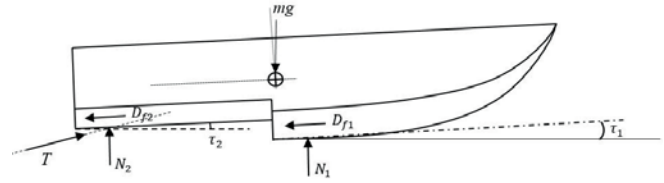


Fig. 9. Diagram of forces acting on stepped planing hull

Generally, pressure and frictional resistances are two greater parts of total resistance which includes spray, wave generation and other particular terms of resistance. Eq. (8) and (9) are used to estimate pressure and frictional resistance in forebody of stepped planing hull, respectively.

$$R_{p1} = \Phi mg \tan \tau_1 \quad (8)$$

$$D_{f1} = 0.5 \frac{\rho V_{m1}^2 \lambda_1 b_1^2}{\cos \beta} (C_f + \Delta C_f) \quad (9)$$

$$D_1 = \Phi mg \tan \tau_1 + \frac{D_{f1}}{\cos \tau_1} \quad (10)$$

The same for afterbody:

$$R_{p2} = (1 - \Phi) mg \tan \tau_2 \quad (11)$$

$$D_{f2} = 0.5 \frac{\rho V_{m2}^2 \lambda_2 b_2^2}{\cos \beta} (C_{f2} + \Delta C_f) \quad (12)$$

$$D_2 = (1 - \Phi) mg \tan \tau_2 + \frac{D_{f2}}{\cos \tau_2} \quad (13)$$

And,  $N_1$  and  $N_2$  are lift forces on forebody and afterbody which can be calculated by using well-known equations.

### Methodology and calculation flow chart

Stability equations for stepped planing hulls in longitudinal and vertical directions and in the centre of gravity can be defined according to Fig. 9 as follows:

$$\text{Longitudinal forces: } T \cos(\tau_2 + e) - N_1 \sin \tau_1 - N_2 \sin \tau_2 - D_{f1} \cos \tau_1 - D_{f2} \cos \tau_2 = 0 \quad (14)$$

$$\text{Vertical forces: } N_1 \cos \tau_1 + N_2 \cos \tau_2 + T \sin(\tau_2 + e) - mg - D_{f1} \sin \tau_1 - D_{f2} \sin \tau_2 = 0 \quad (15)$$

$$\text{Vertical moments with respect to centre of gravity: } N_1 c_1 + N_2 c_2 + D_{f1} a_1 + D_{f2} a_2 - Tf = 0 \quad (16)$$

And, the convergence conditions in this program are the same as in the case of non-stepped hulls. The main equations of force and moment differ in this section.

The first constraint equation for vertical forces is as follows:

$$F_{L1} + F_{L2} - mg \leq \zeta_2 \quad (17)$$

And the second constraint is the condition for a satisfactory convergence of moment calculations, which means that should be a definite positive value.

$$M_{total} = N_1c_1 + N_2c_2 + D_{f1}a_1 + D_{f2}a_2 - T \quad f \geq 0 \quad (18)$$

where a, c and f are the coefficients formerly defined. The calculation flow chart is shown in the Fig. 10. As shown in the chart, two constraints should be satisfied before the calculation processes are finished.

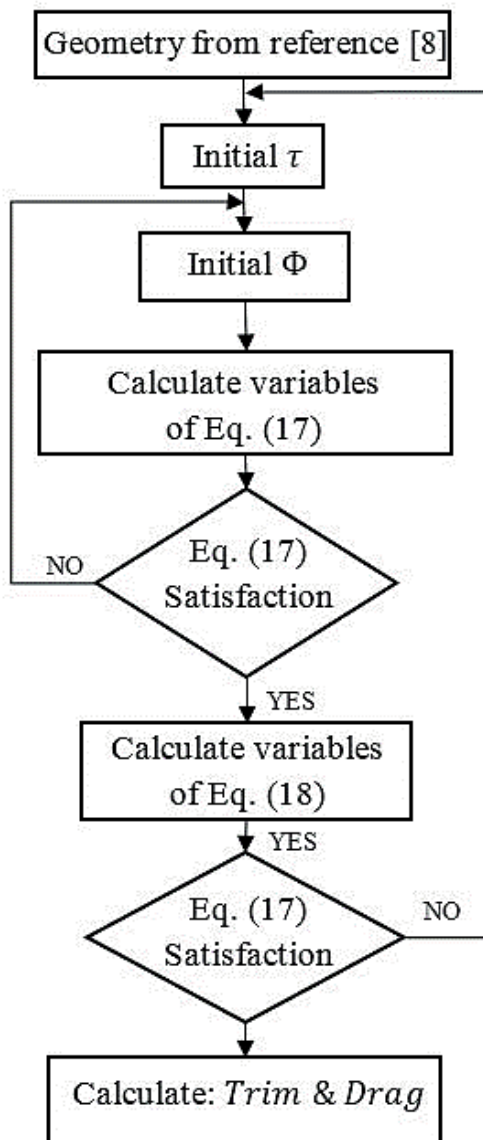


Fig. 10. Flow chart of the calculation program for stepped planing hulls

## Calculation results

Results obtained from the algorithm based on the modified Savitsky method for stepped planing hulls, concern a single-step planing hull. Then, the results are verified by using output from the precise model [9].

First, some basic characteristics of the selected planing hull are determined as follows:

HS = 0.05 (m)	e = 0.15 (m)	b <sub>1</sub> = 2 (m)
m = 4000 (kg)	LS = 2.5 (m)	b <sub>2</sub> = 2 (m)
β <sub>1</sub> = 11 (degrees)	LCG = 2.6 (m)	V = 35 (knot)
β <sub>2</sub> = 10 (degrees)	VCG = 0.5(m)	

Then a comparison between calculation results based on the prepared program and reference output, is done. Tab.3 shows trim angle, total resistance, and required power values obtained from both the program and reference model.

Tab. 3. Comparison between calculation program results and reference output [9].

Parameter	Reference calculations	Acc. prepared program	Error (%)
Trim (degrees)	4.4	4.36	1
Total Resistance (N)	5229	5154.1	1.4
Required power (HP)	128	124.5	2.7

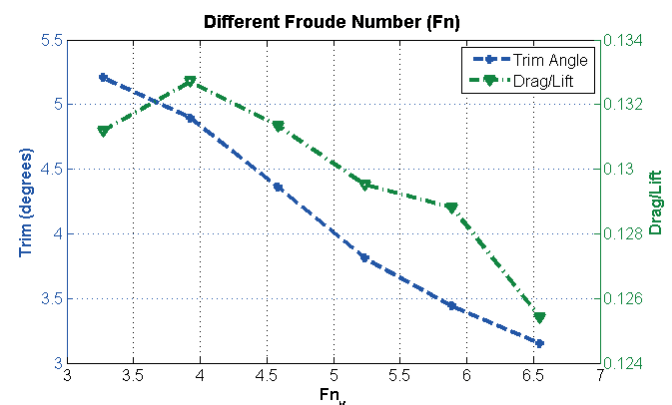


Fig. 11. The effect of volumetric Froude number on trim and  $\frac{Drag}{Lift}$  ratio

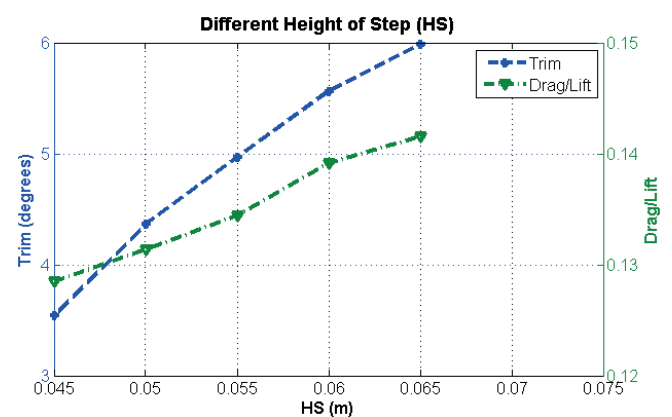


Fig. 12. The effect of the step height HS on trim and  $\frac{Drag}{Lift}$  ratio

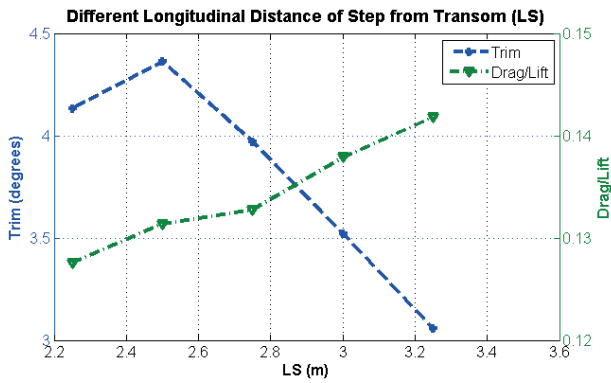


Fig. 13. The effect of the longitudinal distance of step LS on trim and  $\frac{Drag}{Lift}$  ratio

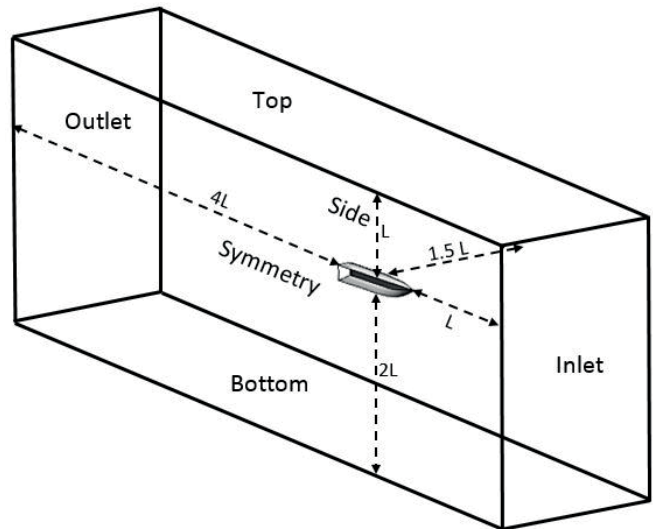


Fig. 15. Boundary condition definition

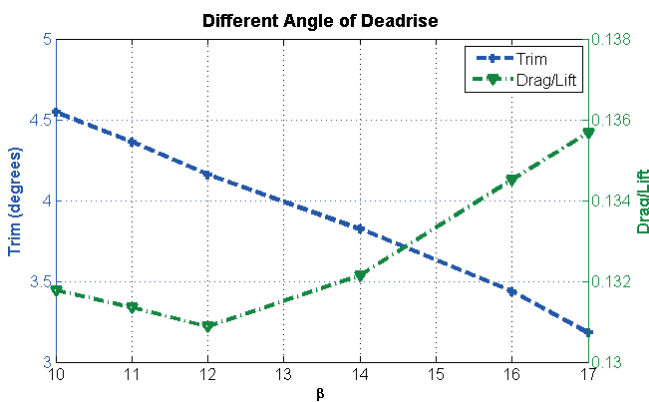


Fig. 14. The effect of deadrise angle on trim and  $\frac{Drag}{Lift}$  ratio

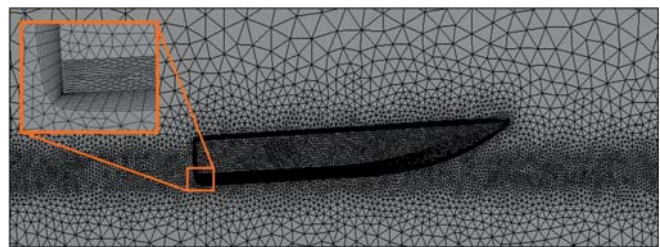


Fig. 16. FE mesh generated around the hull and within boundary layer

Generally, as can be seen in Fig. 11, in stepped planing hulls the amount of trim and  $\frac{Drag}{Lift}$  ratio decreases with the increase of volumetric Froude number value. Also the effect of the step height (HS), longitudinal distance of step from transom (LS), and deadrise angle on these two markedly important parameters, is shown in Fig. 12, 13, and 14, respectively.

### CFD analysis

The steady-state simulation has been carried out with the use of ANSYS CFX v.14 software. The boundary condition is divided into the parts, as shown in Fig. 15. As it can be seen in the figure the dimensions are so assumed as to achieve more adequate results.

To model the turbulent flow, the standard  $K - \epsilon$  is applied and a homogeneous water/air multiphase finite volume approach is used for modelling the free surface. Also a half body is only analysed in order to reduce the CPU time. Furthermore, an unstructured mesh with 5.1M elements is generated, and to obtain a reasonable  $Y^+$ , under 50, a specific boundary layer mesh is applied to near-wall regions. Obviously, for precise free surface modelling, number of mesh elements in free surface and water separation regions is assumed greater.

Before discussing CFD results and verification process, the following contours indicating the computed wave pattern at different Froude number values, are shown. As it can be seen in Fig. 17 the increasing Froude number values results in wave length growth, that leads to wave angle reduction.

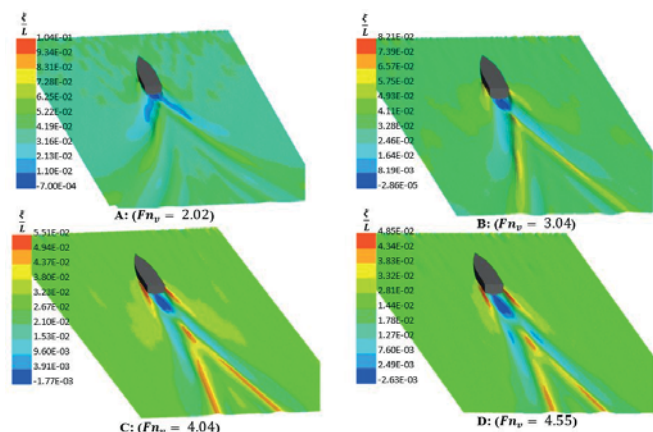


Fig. 17. Wave patterns at different volumetric Froude number values

Additionally, Fig. 18 shows pressure distribution on the stepped hull bottom surface. As shown in the Fig. 18 and 19, the points (A), (B), and (C) represent the peak pressure position in the afterbody, step and forebody, respectively.

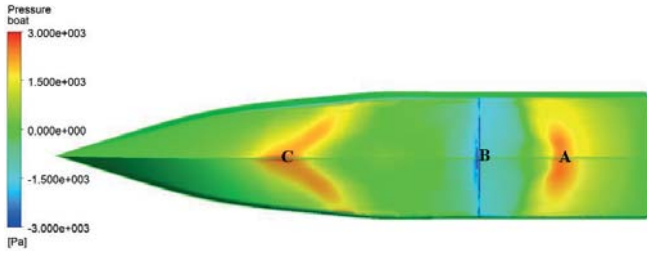


Fig.18. Pressure distribution contours on the bottom surface of stepped planing hull at  $Fn_v = 5.89$

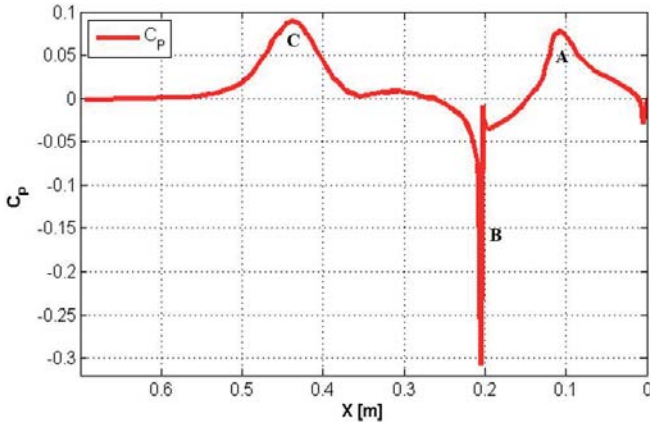


Fig. 19. Pressure coefficient distribution along the keel line of stepped planing hull at  $Fn_v = 5.89$

### Comparison between CFD and program results

To verify the program results thoroughly, CFD results are compared with program output. As can be seen in the following figures, CFD results are presented for various volumetric Froude number values for both non-stepped and stepped hull. And, in Tab. 4 the error values are shown. The minimum error values occur at  $Fn_v = 2.02$  and  $Fn_v = 5.89$ , and the maximum ones - at  $Fn_v = 4.55$  and  $Fn_v = 5.23$  for non-stepped and stepped hull, respectively.

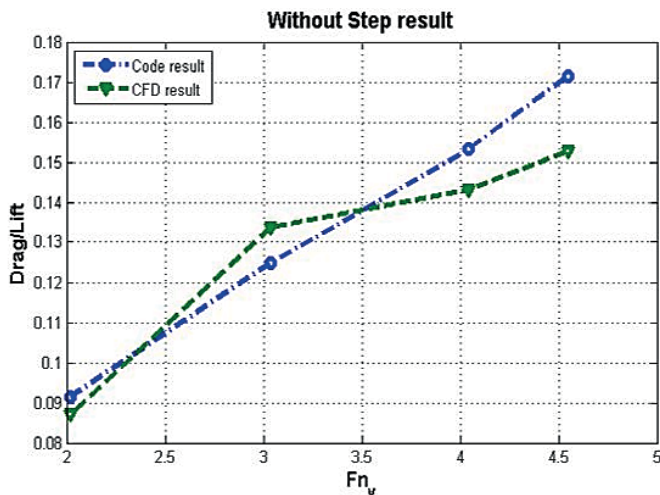


Table 4: Error values in function of volumetric Froude number

	Volumetric Froude Number	Drag/Lift ( code)	Drag/Lift ( progr.)	Errors (%)
Non-stepped hull	2.02	0.092	0.087	4.3
	3.04	0.125	0.134	7.2
	4.04	0.153	0.143	6.6
	4.55	0.171	0.152	10.1
Stepped hull	3.27	0.131	0.121	7.8
	3.92	0.133	0.141	6.3
	5.23	0.129	0.144	12.2
	5.89	0.128	0.122	4.2

### Conclusions

To conclude, in this work all efforts have been focused on achieving the best algorithm based on practical equations for both non- stepped and stepped planing hulls. Furthermore the effect of geometrical parameters on the performance of planing hulls, has been investigated. The obtained results show that in non- stepped planing hulls the increase of deadrise angle and LCG result in a drag rise and trim decline. On the contrary, ratio increase rises trim angle and decreases drag. On the other hand, for stepped planing hulls the rising of step height causes a significant rise in both drag and trim. Also the increase of deadrise angle and step-to-transom distance leads to drag increase and trim decrease. Finally the results obtained from the prepared program are reasonably proved by the performed CFD analysis.

### Acknowledgement

This research was supported by the Marine Research Center of Amirkabir University of Technology whose efforts are greatly acknowledged.

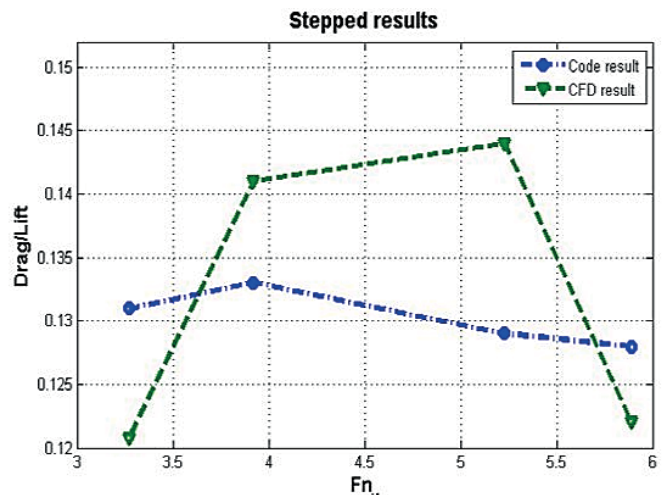


Fig. 20. Comparison between program (code) and CFD results in function of volumetric Froude number.

## Bibliography

1. O. M. Faltinsen: Hydrodynamics of High-Speed Marine Vehicles, Cambridge University Press, 2005.
2. D. Savitsky: Hydrodynamic Design of Planning Hull, Marine Technology, vol. 1, no. 1, pp. 71-95, 1964
3. C. E. P and B. D. L: Resistance Tests of a Systematic Series of Planning Hull Forms, Society of Naval Architects and Marine Engineers (SNAME), Hampton, 1963
4. B. R. Savander and S. H. Rhee: Steady Planning Hydrodynamics: Comparison of Numerical and Experimental Results, Fluent Users' Group, Manchester, NH, 2003
5. H. Ghassemi and M. Ghiasi: A Combined Method for the Hydrodynamic Characteristics of Planning Crafts, Ocean Engineering, vol. 35, no. 3-4, pp. 310-322, 2007
6. S. Brizzolara and F. Serra: Accuracy of CFD Codes in the Prediction of Planing Surfaces Hydrodynamic Characteristics, in : 2nd International Conference on Marine Research and Transportation, Naples, 2007
7. A. R. Kohansal and H. Ghassemi: A Numerical Modelling of Hydrodynamic Characteristics of Various Planning Hull Forms, Ocean Engineering, vol. 37, no. 5-6, pp. 498-510, 2010
8. D. Savitsky and M. Morabito: Surface Wave Contours Associated with the Forebody Wake of Stepped Planning Hulls, Marine Technology, vol. 47, no. 1, pp. 1-16, 2010
9. D. Svahn: Performance Prediction of Hulls with Transverse, Marina System Center for Naval Architecture, Stockholm, 2009
10. W. R. Garland and K. J. Maki: A Numerical Study of a Two-Dimensional Stepped Planing Surface, Journal of Ship Production and Design, vol. 28, no. 2, pp. 60-72, 2012
11. M. Ghassabzadeh and H. Ghassemi: Determining of the Hydrodynamic Forces on the Multi-hull Tunnel Vessel in Steady Motion, The Brazilian Society of Mechanical Sciences and Engineering, in press, 2013
12. D. Radojic, A. Zgradic, M. Kalajdzic and A. Simic: Resistance Prediction for Hard Chine Hulls in the Pre-Planing Regime, Polish Maritime Research, vol. 21, no. 2(82), pp. 9-26, 2014
13. H. Holm: Hydrodynamic Design of Planing Hulls- Online Program, Marine Hydrodynamics' Site NTNU University, Trondheim, 2002

## CONTACT WITH AUTHORS

Hassan Ghassemi  
Sajad Taj Golah Veysi  
Mojtaba Kamarlouei

Amirkabir University of Technology  
Department of Ocean Engineering  
Hafez Ave.  
Tehran  
IRAN

# COMPARISON OF THE POWERS OF ENERGY LOSSES IN A VARIABLE CAPACITY DISPLACEMENT PUMP DETERMINED WITHOUT OR WITH TAKING INTO ACCOUNT THE POWER OF HYDRAULIC OIL COMPRESSION

Zygmunt Paszota, Prof.  
Gdańsk University of Technology, Poland

## ABSTRACT

*Powers of energy losses in a variable capacity displacement pump are compared with or without taking into account the power of hydraulic oil compression. Evaluation of power of liquid compression in the pump was made possible by the use of method, proposed by the Author, of determining the degree of liquid aeration in the pump. In the method of determining the liquid aeration in the pump and of powers of volumetric losses of liquid compression a simplified formula  $(q_{pvc} \times \Delta p_{pi})/2$  was used describing the field of indicated work of volumetric losses  $q_{pvc}$  of liquid compression during one shaft revolution at indicated increase  $\Delta p_{pi}$  of pressure in the chambers. Three methods were used for comparing the sum of powers of volumetric losses  $\Delta P_{pvl}$  due to leakage and  $\Delta P_{pvc}$  of compression and also  $\Delta P_{Pm|\Delta p_{pi}}$  of mechanical losses resulting from increase  $\Delta p_{pi}$  of indicated pressure in the working chambers.*

**Keywords:** hydrostatic drive, variable capacity displacement pump, volumetric losses of hydraulic oil compression

## INTRODUCTION

In references [1–4], the Author attempted to evaluate the influence of working liquid compressibility on the picture of volumetric and mechanical losses in a high-pressure variable capacity displacement pump. The considerations were based on the assumptions made by the Author in the developed theoretical and mathematical models of torque of mechanical losses in the pump used in the hydrostatic drive [5–7]. **The models assume, that increase  $\Delta M_{Pm|\Delta p_{pi}, q_{pgv}}$  of torque of mechanical losses in the pump „working chambers - shaft” assembly, compared with torque of losses in that assembly in a no-load pump (when indicated increase  $\Delta p_{pi}$  of pressure in the working chambers equals to zero ( $p_{pi} = 0$ ) is proportional to torque  $M_{pi}$  indicated in the pump working chambers.**

In references [1–4], the Author introduced also **the working liquid compressibility coefficient  $k_{lc|p_n}$** . It determines the

degree of decrease of the active volume of working liquid displaced by the pump during one shaft revolution as an effect of increase  $\Delta p_{pi} = p_n$  of pressure in pump working chambers equal to the pump nominal pressure  $p_n$  (pressure  $p_n$  of the hydrostatic drive system where the pump operates). The pump active working volume  $Q_{pt|p_n}$  or  $Q_{pgv|p_n}$  is smaller compared with the active volume equal to theoretical working volume  $q_{pt}$  or geometrical working volume  $q_{pgv}$  (determined at the increase  $\Delta p_{pi}$  of pressure equal to zero –  $\Delta p_{pi} = 0$ ). Decreases then the indicated torque  $M_{pi}$  and indicated power  $P_{pi}$  in the pump working chambers which can be generated (and calculated) with the increase  $\Delta p_{pi}$  of pressure in the chambers, for example with  $\Delta p_{pi} = p_n$ . In effect, decreases also torque  $M_p$  on the pump drive shaft and power  $P_{pc}$  consumed by the pump on shaft that the pump driving motor can be loaded with.

In references [1 – 4] the Author searched for value of the

liquid compressibility coefficient  $k_{lc|p_n}$ , which, with increase  $\Delta p_{pi}$  of pressure in the working chambers equal to nominal pressure  $p_n$ , will give the increase  $\Delta M_{Pm|p_n, q_{Pgv}}$  of torque of mechanical losses proportional to  $q_{Pgv}$ , i.e. to indicated torque  $M_{P_i|p_n, q_{Pgv}}$ . The Author determined, in the tested pump HYDROMATIK A7V.58.1.R.P.F.00 [8], an approximate value of oil compressibility coefficient during the pump test as  $k_{lc|32MPa} = 0,030$ . Such value of the compressibility coefficient resulted also from aeration ( $\epsilon > 0$ ) of oil in conduits of the test stand.

In references [10, 11] the Author presents **the method of determining the value of liquid aeration coefficient  $\epsilon$  during pump operation in a hydrostatic drive system or on a test stand**, consisting in finding such value of  $\epsilon$ , with which calculated increase  $\Delta M_{Pm|p_n, q_{Pgv}}$  of torque of mechanical losses is proportional to indicated torque  $M_{P_i|p_n, q_{Pgv}}$  determined (calculated) at constant increase ( $p_{pi} = cte$ ) of pressure in the pump working chambers. The constant value of  $\Delta p_{pi}$ , assumed in searching for liquid aeration coefficient  $\epsilon$ , equals to pump nominal pressure  $p_n$  ( $\Delta p_{pi} = cte = p_n$ ).

Increase  $\Delta M_{Pm|p_n, q_{Pgv}}$  of torque of mechanical losses in the pump „working chambers - shaft” assembly, at a constant value of  $\Delta p_{pi}$  ( $\Delta p_{pi} = cte$ ), is (in Author’s opinion) proportional to the pump geometrical working capacity  $q_{Pgv}$ , therefore:

**only with taking into account the actual value of aeration coefficient  $\epsilon$  of liquid displaced by the pump, the (calculated) relation**

$$\Delta M_{Pm|p_n, q_{Pgv}} \sim q_{Pgv} \quad (1)$$

**can be obtained.**

At the same time, only with accounting for actual value of liquid aeration coefficient  $\epsilon$  the calculated increase  $\Delta M_{Pm|p_n, q_{Pgv}; \epsilon}$  of torque of mechanical losses tends to zero at the geometrical working capacity  $q_{Pgv}$  per one shaft revolution tending to zero:

$$\Delta M_{Pm|p_n, q_{Pgv} \rightarrow 0; \epsilon} \rightarrow 0 \text{ when } q_{Pgv} \rightarrow 0. \quad (2)$$

The calculated aeration coefficient  $\epsilon$  of oil used during tests of HYDROMATIK A7V.58.1.R.P.F.00 pump, corresponding to the situation described by the expressions (1) and (2) had the value  $\epsilon = 0,0135$  [8, 10, 11].

The method, proposed by the Author, of determining (calculating) the working liquid aeration coefficient  $\epsilon$  was for

the first time used in the research work carried out by Jan Koralewski into the influence of viscosity and compressibility of aerated hydraulic oil on volumetric and mechanical losses of a HYDROMATIK A7V.58.1.R.P.F.00 pump [8, 9, 12, 13].

**The method of determining (calculating) the aeration coefficient  $\epsilon$  of working liquid displaced by variable capacity per one shaft revolution displacement pump allows to subdivide the volumetric losses per one shaft revolution in pump working chambers into volumetric losses  $q_{Pvc}$  due to compressibility of aerated (or non-aerated) liquid and volumetric losses  $q_{Pvl}$  due to leakage in the pump.**

**The method allows also to evaluate the increase  $\Delta M_{Pm|\Delta p_{Pi}, q_{Pgv}}$  of torque of mechanical losses in the pump „working chambers - shaft” assembly being a function of torque  $M_{P_i|\Delta p_{Pi}, q_{Pgv}}$  indicated in the pump working chambers (by making possible more precise calculation of indicated torque  $M_{P_i}$ ).**

In Author’s opinion, the above mentioned possibilities have not existed so far. They are important for evaluation of volumetric losses due to leakage of liquid in the working chambers and for evaluation of mechanical losses in the pump „working chambers - shaft” assembly, i.e. are important for evaluation of a design solution of a displacement pump generating those losses, particularly operating in the conditions of high increase  $\Delta p_{pi}$  of pressure in the working chambers.

Aim of the work [14,15] was to develop a capability of evaluating the volumetric losses resulting from hydraulic oil compression in the pump working chambers as a function of the same parameters, which volumetric losses due to leakage, resulting from the quality of design solution of the pump, are evaluated as dependent on and also as a function of the oil aeration coefficient  $\epsilon$ . Therefore, it was necessary to develop a mathematical model describing the hydraulic oil compressibility coefficient  $k_{lc|\Delta p_{Pi}; b_p; \epsilon; \nu}$  as a relation to the ratio  $\Delta p_{pi}/p_n$  of indicated increase  $\Delta p_{pi}$  of pressure in the working chambers to the nominal pressure  $p_n$ , to the pump capacity coefficient  $b_p$ , to the oil aeration coefficient  $\epsilon$  and to the ratio  $\nu/\nu_n$  of oil viscosity  $\nu$  to reference viscosity  $\nu_n$ . Also presented was a mathematical model of volumetric losses  $q_{Pvc|\Delta p_{Pi}; b_p; \epsilon; \nu}$  of hydraulic oil compression in the pump working chambers in the form allowing to use it in the model of power of compression in the pump and also in the model of losses and pump energy efficiency.

It has to be noted, that, in order to simplify calculations of indicated torque  $M_{P_i}$  in the pump working chambers, the calculations taking into account the liquid compression in the chambers, the liquid compression curve was replaced by linear approximation as the change of volume is small. This simplification gives a slight error at small values of liquid aeration coefficient  $\epsilon$ , but the error increases at greater values of  $\epsilon$ . The evaluation of error due to the simplification can be made by comparing the sum of power of volumetric and mechanical losses in pump resulting from indicated increase

$\Delta p_{pi}$  of pressure in the working chambers determined without or with taking into account the power of liquid compression. However, **the balance of powers of losses determined without or with taking into account the power of liquid compression in the working chambers is mainly a tool of demonstrating the errors in evaluation of energy losses in pump resulting from not taking into account of the influence of liquid compression power.**

### DIAGRAM OF POWER INCREASE IN A DISPLACEMENT PUMP OPPOSITE TO DIRECTION OF POWER FLOW ACCOUNTING FOR POWER OF VOLUMETRIC LOSSES OF LIQUID COMPRESSION

The proposed method of determining the value of aeration coefficient  $\epsilon$  of working liquid displaced by a variable capacity displacement pump per one shaft revolution allows to estimate the subdivision of volumetric losses in the pump working chambers into volumetric losses  $q_{pvc}$  of compression and volumetric losses  $q_{pvl}$  due to leakage in the chambers. The method allows also to evaluate the increase  $\Delta M_{Pm}|\Delta p_{pi}$  of

torque of mechanical losses in the pump „working chambers - shaft” assembly.

Volumetric losses  $q_{pvc}$  of liquid compression,  $q_{pvl}$  of leakage and increase  $\Delta M_{Pm}|\Delta p_{pi}$  of torque of mechanical losses are losses of different character and at the same time different functions of increase  $\Delta p_{pi}$  of pressure in the working chambers.

Figure 1 presents and describes the diagram of increase of power in a displacement pump opposite to the direction of power flow eliminating the Sankey diagram of decrease of power in the direction of power flow which causes erroneous evaluation of losses in pump energy investigations. The proposed diagram accounts for the subdivision of power of volumetric losses in the pump working chambers into power of losses of liquid compression and power of losses due to leakage.

The diagram presents relation of power  $P_{pc}$  consumed by pump (power required by the pump from its driving (electric, internal combustion) motor) as a sum of pump useful power  $P_{pu}$  required of the pump by working liquid displaced by it (required of the pump by the hydrostatic system driven by it), power  $\Delta P_{pp}$  of pressure losses in the channels, power  $\Delta P_{pvl}$  of volumetric leakage in the working chambers, power  $\Delta P_{pvc}$  of liquid compression in the working chambers and power

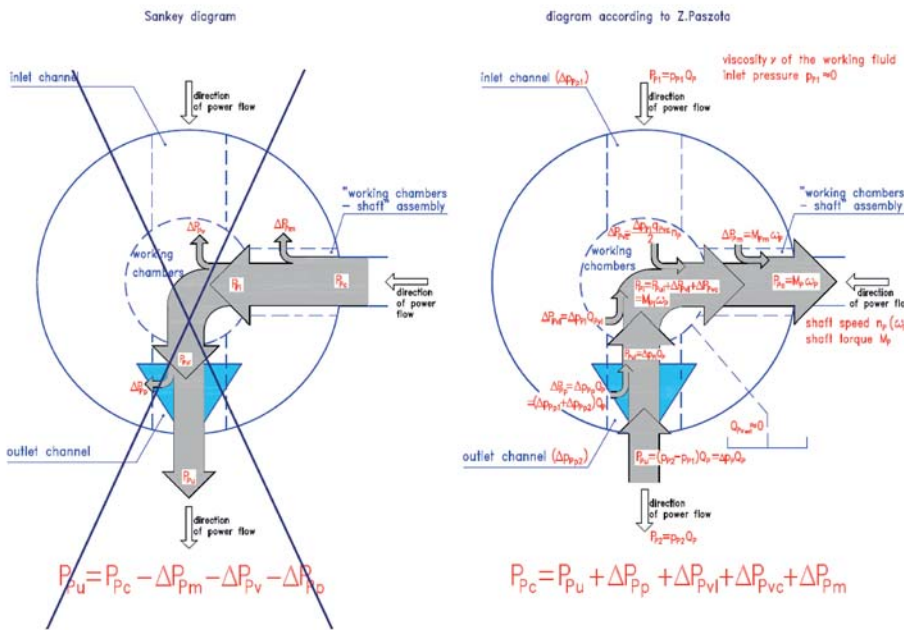


Fig.1 Diagram of power increase in a displacement pump opposite to the direction of power flow, eliminating the Sankey diagram of power decrease in the direction of power flow

Power increases from pump useful power  $P_{pu}$  required of pump by the pressed working liquid (required of pump by the driven hydrostatic system), to consumed power  $P_{pc}$  required by pump on its shaft from its driving (electric, internal combustion) motor.

Increase of power in the pump is an effect of powers of energy losses in it, resulting from quality of the displacement pump design solution generating those losses, and power of volumetric losses due to compression of the working liquid. Powers of losses in the pump resulting from quality of its structural solution are the following: power  $\Delta P_{pp}$  of pressure losses in the channels, power  $\Delta P_{pvl}$  of volumetric losses due to leakage in working chambers and power  $\Delta P_{pvc}$  of mechanical losses in the „working chambers - shaft” assembly.

Powers  $\Delta P_{pp}$ ,  $\Delta P_{pvl}$  and  $\Delta P_{pvc}$  of losses in the pump are functions of output parameters of the pump assembly, where the losses occur and diversified functions of liquid viscosity  $v$ :

- power  $\Delta P_{pp}$  of pressure losses in the channels is a function of pump capacity  $Q_p$  and of liquid viscosity  $v$ ,
- power  $\Delta P_{pvl}$  of volumetric losses due to leakage in the working chambers is a function of increase  $\Delta p_{pi}$  of pressure indicated in the chambers and of liquid viscosity  $v$ ,
- power  $\Delta P_{pvc}$  of mechanical losses in the „working chambers - shaft” assembly is a sum  $\Delta P_{pvc} = \Delta P_{pvc}|\Delta p_{pi}=0 + \Delta P_{pvc}|\Delta p_{pi}$  of power  $\Delta P_{pvc}|\Delta p_{pi}=0$  of losses resulting from torque  $M_{pm}|\Delta p_{pi}=0$  of losses in a no-load pump (at  $\Delta p_{pi} = 0$ ) and power  $\Delta P_{pvc}|\Delta p_{pi}$  of losses resulting from increase  $\Delta M_{pm}|\Delta p_{pi}$  of torque of losses proportional to torque  $M_{pm}$  indicated in the working chambers. Torque  $M_{pm}|\Delta p_{pi}=0$  of losses in a no-load pump depends on the liquid viscosity  $v$ , increase  $\Delta M_{pm}|\Delta p_{pi}$  of torque of losses is practically independent of the liquid viscosity  $v$ .

The greater is the liquid compressibility coefficient  $k_{lc|p_n}$  and the greater is the increase  $\Delta p_{pi}$  of pressure indicated in the working chambers, the greater is power  $\Delta P_{pvc}$  of volumetric losses of liquid compression.

Useful power  $P_{pu}$  in the working chambers:  $P_{pu} = P_{pu} + \Delta P_{pp}$

Power  $P_{pi}$  indicated in the working chambers:  $P_{pi} = P_{pu} + \Delta P_{pvl} + \Delta P_{pvc} = P_{pu} + \Delta P_{pp} + \Delta P_{pvl} + \Delta P_{pvc}$

Power  $P_{pc}$  consumed by pump on the shaft:  $P_{pc} = P_{pi} + \Delta P_{pvc} = P_{pu} + \Delta P_{pp} + \Delta P_{pvl} + \Delta P_{pvc} + \Delta P_{pvc}$

The proposed diagram eliminates the Sankey diagram of distribution of power in the pump causing erroneous evaluation of losses in the pump energy investigations.

$\Delta P_{pm}$  of mechanical losses in the pump „working chambers - shaft” assembly. Power  $\Delta P_{pm}$  of mechanical losses is a sum  $\Delta P_{pm} = \Delta P_{pm}|_{\Delta p_{pi}=0} + \Delta P_{pm}|_{\Delta p_{pi}}$  of power  $\Delta P_{pm}|_{\Delta p_{pi}=0}$  of losses resulting from torque  $M_{pm}|_{\Delta p_{pi}=0}$  of losses in no-load pump (at  $\Delta p_{pi} = 0$ ) and power  $\Delta P_{pm}|_{\Delta p_{pi}}$  of losses resulting from increase  $\Delta M_{pm}|_{\Delta p_{pi}}$  of torque of losses proportional to torque  $M_{pi}$  indicated in the working chambers.

Diagram of the increase of power in the pump may be described by the equation:

$$P_{pc} = P_{pu} + \Delta P_{pp} + \Delta P_{pvl} + \Delta P_{pvc} + \Delta P_{pm}|_{\Delta p_{pi}=0} + \Delta P_{pm}|_{\Delta p_{pi}} \quad (3)$$

Power  $\Delta P_{pp}$  of pressure losses in the pump channels and power  $\Delta P_{pm}|_{\Delta p_{pi}=0}$  of mechanical losses in the pump „working chambers - shaft” assembly (resulting from torque  $M_{pm}|_{\Delta p_{pi}=0}$  of losses in no-load pump (at  $\Delta p_{pi} = 0$ )) are independent of the increase  $\Delta p_{pi}$  of pressure in the working chambers.

Power  $\Delta P_{pvl}$  of volumetric losses due to leakage and power  $\Delta P_{pvc}$  of volumetric losses of liquid compression in the pump working chambers and also power  $\Delta P_{pm}|_{\Delta p_{pi}}$  of mechanical losses in the pump „working chambers - shaft” assembly (resulting from increase  $\Delta M_{pm}|_{\Delta p_{pi}}$  of torque of losses proportional to torque  $M_{pi}$  indicated in the working chambers) are dependent on increase  $\Delta p_{pi}$  of pressure in the chambers.

In the investigations of energy losses in pump we can easily determine the pump useful power  $P_{pu} = Q_p \Delta P_{pp}$ , power  $\Delta P_{pp} = Q_p \Delta p_{pp}$  of pressure losses in the channels, power  $\Delta P_{pm}|_{\Delta p_{pi}=0} = \omega_p \Delta M_{pm}|_{\Delta p_{pi}=0}$  of mechanical losses in the no-load pump ( $\Delta p_{pi} = 0$ ) „working chambers - shaft” assembly and power  $P_{pc} = \omega_p M_p$  consumed by the pump on the shaft.

The sum of power of volumetric losses  $\Delta P_{pvl}$  due to leakage and  $\Delta P_{pvc}$  of liquid compression and also power  $\Delta P_{pm}|_{\Delta p_{pi}}$  of mechanical losses (resulting from increase  $\Delta M_{pm}|_{\Delta p_{pi}}$  of torque of mechanical losses) results from the equation:

$$\Delta P_{pvl} + \Delta P_{pvc} + \Delta P_{pm}|_{\Delta p_{pi}} = P_{pc} - P_{pu} - \Delta P_{pp} - \Delta P_{pm}|_{\Delta p_{pi}=0} \quad (4)$$

The method of determining the aeration coefficient  $\varepsilon$  of liquid pressed by a variable capacity displacement pump makes it possible to subdivide the volumetric losses into losses  $q_{pvc}$  of liquid compression and losses  $q_{pvl}$  due to leakage and also to evaluate more precisely the increase  $\Delta M_{pm}|_{\Delta p_{pi}}$  of torque of mechanical losses. In effect, it makes it possible to evaluate powers  $\Delta P_{pvl}$ ,  $\Delta P_{pvc}$  and  $\Delta P_{pm}|_{\Delta p_{pi}}$  of three losses dependent on increase  $\Delta p_{pi}$  of pressure in the pump working chambers.

## INFLUENCE OF VOLUMETRIC LOSSES QPVC PER ONE SHAFT REVOLUTION DUE TO HYDRAULIC OIL COMPRESSION IN THE PUMP WORKING CHAMBERS ON EVALUATION OF VOLUMETRIC LOSSES QPVL DUE TO LEAKAGE OF OIL IN THE CHAMBERS AND ON EVALUATION OF TORQUE MPM OF MECHANICAL LOSSES IN THE PUMP „WORKING CHAMBERS - SHAFT” ASSEMBLY

Volumetric losses  $q_{pvc}$ , determined per one shaft revolution, of compression of liquid pressed in the pump working chambers are not attributable to the pump design solution. They result from the liquid compressibility itself and from aeration of the liquid. Main reason of working liquid aeration is air dissolved in the liquid (not having in such form any influence on its compressibility) and getting out of the liquid (in the form of bubbles) in the conditions of local (in the system conduits or in pump working chambers during their connection with pump inlet channel) drop of pressure below the atmospheric pressure. One of the reasons may be admitting by the hydrostatic system designer or user too low pressure in the pump inlet conduit, which may cause cavitation in the pump working chambers during their connection with the inlet channel.

Mathematical model of volumetric losses  $Q_{pvc}|_{\Delta p_{pi}; b_p; \varepsilon; v}$  per one shaft revolution resulting from compression of non-aerated ( $\varepsilon = 0$ ) or aerated ( $\varepsilon > 0$ ) hydraulic oil, determined at indicated increase  $\Delta p_{pi}$  of pressure in the pump working chambers, at pump capacity coefficient  $b_p$  (in the  $0 < b_p \leq 1$  range) and at the ratio  $v/v_n$  of oil viscosity  $v$  to reference viscosity  $v_n$  is described (with  $\Delta p_{pi} > 3,2\text{MPa}$ ) by the formula:

$$\begin{aligned} Q_{pvc}|_{\Delta p_{pi}; b_p; \varepsilon; v} &= k_{lc}|_{\Delta p_{pi}; b_p; \varepsilon; v} Q_{pgv} = \\ &= k_{lc}|_{\Delta p_{pi}; b_p; \varepsilon; v} b_p Q_{pt} = \\ &= \frac{1+b_p}{2b_p} \left[ k_{lc}|_{p_n; \varepsilon=0} (\Delta p_{pi} / p_n)^{a_{pc}} + \varepsilon \right] (v / v_n)^{a_{vc}} b_p Q_{pt} = \\ &= \frac{1+b_p}{2} \left[ k_{lc}|_{p_n; \varepsilon=0} (\Delta p_{pi} / p_n)^{a_{pc}} + \varepsilon \right] (v / v_n)^{a_{vc}} Q_{pt} . \end{aligned} \quad (5)$$

with exponent  $a_{pc} = 0,89$   
and with exponent  $a_{vc} = -0,12$ .

Coefficient  $k_{lc}|_{p_n; \varepsilon=0}$  of hydraulic oil compressibility is a coefficient of non-aerated oil compressibility. At nominal pressure  $p_n = 32\text{MP}$ , this coefficient is of an order  $k_{lc}|_{32\text{MPa}; \varepsilon=0} = 0,020$ .

**With a given value  $Q_p|_{p_n}$  of pump capacity per one shaft revolution, required of pump at nominal pressure ( $\Delta p_{pi} = p_n$ ) by the hydrostatic system fed by it, and simultaneously with the increasing value  $q_{pvc}$  of capacity losses per one shaft revolution due to liquid compressibility in the sum  $q_{pv} = q_{pvl} + q_{pvc}$  of volumetric losses per one shaft revolution,**

decreases the value  $M_{pi}$  of indicated torque in the working chambers and value  $M_p$  of torque on the pump shaft. Not taking into account of losses  $q_{pvc}$  in calculations of torque  $M_{pi}$  and treating  $q_{pv}$ , in the sum  $q_{pv} = q_{pvl} + q_{pvc}$  as  $q_{pvl}$ , results in increasing the calculated torque  $M_{pi}$  and decreasing the calculated torque  $M_{pm} = M_p - M_{pi}$  of losses in the pump „working chambers - shaft” assembly. This is an effect of the fact, that volumetric losses  $q_{pvl}$  per one shaft revolution (due to leakage) have approximately twice as big effect on the value of calculated torque  $M_{pi}$  indicated in the working chambers as the effect of the same value of volumetric losses  $q_{pvc}$  per one shaft revolution (due to liquid compression).

Figure 2 presents and describes the subdivision of intensity  $q_{pv} = q_{pvl} + q_{pvc}$  of volumetric losses per one shaft revolution in the pump working chambers, the losses dependent on indicated increase  $\Delta p_{pi}$  of pressure in the chambers, into intensity  $q_{pvl}|\Delta p_{pi}$  of volumetric losses per one shaft revolution due to working liquid (hydraulic oil) leakage and into intensity  $q_{pvc}|\Delta p_{pi}$  of volumetric losses per one shaft revolution due to liquid compression, the subdivision made at pump capacity coefficient  $b_p = 1$ .

The figure presents also the values  $Q_{Pt}|p_n$  of working liquid active volume displaced by the pump during one shaft revolution at  $\Delta p_{pi} = p_n$ , the volume determined with the assumption of non-compressible liquid (liquid compressibility coefficient  $k_{lc}|p_n = 0$ ) or with the assumption of compressible liquid with liquid aeration coefficient  $\varepsilon = 0$  or  $\varepsilon > 0$ , and also the values  $q_{pt}$  of theoretical working volume displaced at  $\Delta p_{pi} = 0$ , determined with assumption of  $k_{lc}|p_n = 0$  or with assumption of  $\varepsilon = 0$  or  $\varepsilon > 0$ , the values  $q_{pt}$  being the liquid active volume displaced by the pump at  $\Delta p_{pi} = 0$ .

Values  $Q_{Pt}|p_n; \varepsilon=0$  or  $Q_{Pt}|p_n; \varepsilon>0$  result from a sum of the value  $Q_P|p_n$  of pump capacity per one shaft revolution, required of the pump by the driven hydrostatic system at  $\Delta p_{pi} = p_n$ , and, with the assumption of compressible liquid, from intensity  $q_{pvl}|p_n$  of volumetric losses per one shaft revolution due to leakage in the working chambers at  $\Delta p_{pi} = p_n$  (leakage independent of liquid aeration, i.e. the same at  $\varepsilon = 0$  and  $\varepsilon > 0$ ). With the assumption of non-compressible liquid (liquid compressibility coefficient  $k_{lc}|p_n = 0$ ), the value  $Q_{Pt}|p_n; k_{lc}|p_n=0$  (equal to the value  $Q_{Pt}|k_{lc}|p_n=0$ ) results from a sum of value  $Q_P|p_n$  of pump capacity per one shaft revolution (required of the pump by the hydrostatic system), intensity  $q_{pvl}|p_n$  of losses due to leakage and intensity  $q_{pvc}|p_n; \varepsilon=0$  of losses due to compression of non-aerated liquid ( $\varepsilon = 0$ ).

The sum  $Q_P|p_n + q_{pvl}|p_n + q_{pvc}|p_n$  of the pump capacity  $Q_P|p_n$  per one shaft revolution (required of the pump by the driven hydrostatic system at  $\Delta p_{pi} = p_n$ ), the intensity  $q_{pvl}|p_n$

of volumetric losses per one shaft revolution due to leakage in working chambers at  $\Delta p_{pi} = p_n$  and the intensity  $q_{pvc}|p_n$  of volumetric losses per one shaft revolution due to compressibility of non-aerated ( $\varepsilon = 0$ ) or aerated ( $\varepsilon > 0$ ) liquid in the working chambers at  $\Delta p_{pi} = p_n$  decides of theoretical working volume  $q_{pt}$  per one shaft revolution, i.e. of the active volume displaced by the pump at  $\Delta p_{pi} = 0$ :

$$q_{pt} = Q_P|p_n + q_{pvl}|p_n + q_{pvc}|p_n. \quad (6)$$

The value  $Q_{Pt}|k_{lc}|p_n=0$  of theoretical working volume per one shaft revolution, determined with the assumption of non-compressible liquid (liquid compressibility coefficient  $k_{lc}|p_n = 0$ ) and the value  $Q_{Pt}|\varepsilon=0$  of theoretical working volume per one shaft revolution, determined with the assumption of non-aerated liquid ( $\varepsilon = 0$ ), result from a sum  $Q_{Pt}|p_n; \varepsilon=0$  (equal to  $Q_{Pt}|p_n; \varepsilon>0$ ) and intensity  $q_{pvc}|p_n; \varepsilon=0$  of losses due to compression of non-aerated liquid.

The value  $Q_{Pt}|\varepsilon>0$  of theoretical working volume per one shaft revolution, determined with the assumption of aerated liquid ( $\varepsilon > 0$ ), results from a sum of  $Q_{Pt}|p_n; \varepsilon>0$  (equal to  $Q_{Pt}|p_n; \varepsilon=0$ ) and intensity  $q_{pvc}|p_n; \varepsilon>0$  of losses due to compression of aerated liquid.

Figure 3 presents and describes the field of indicated work in the displacement pump working chambers during one shaft revolution. The work performed in working chambers decides of the value of torque  $M_{pi}$  indicated in the chambers.

Torque  $M_{pi}$  indicated in the chambers is a result of three works:

- work described as a product of capacity  $Q_P|p_n$  per one shaft revolution and indicated increase  $\Delta p_{pi} = p_n$  of pressure –  $Q_P|p_n \times p_n$ ,
- work described as a product of volumetric losses  $q_{pvl}$  due to leakage and indicated increase  $\Delta p_{pi} = p_n$  of pressure –  $q_{pvl}|p_n \times p_n$ ,
- work described, in approximation, as half of the product of volumetric losses  $q_{pvc}|p_n$  of liquid compression and indicated increase  $\Delta p_{pi} = p_n$  of pressure –  $(q_{pvc}|p_n \times p_n)/2$ .

Simplified formula describing indicated torque  $M_{pi}$  has the form:

$$M_{Pi}|\Delta p_{pi}=p_n; b_p=1 = \left( Q_P|p_n + q_{pvl}|p_n + \frac{q_{pvc}|p_n}{2} \right) \frac{p_n}{2\Pi}. \quad (7)$$

Not taking the liquid compressibility into account, i.e.

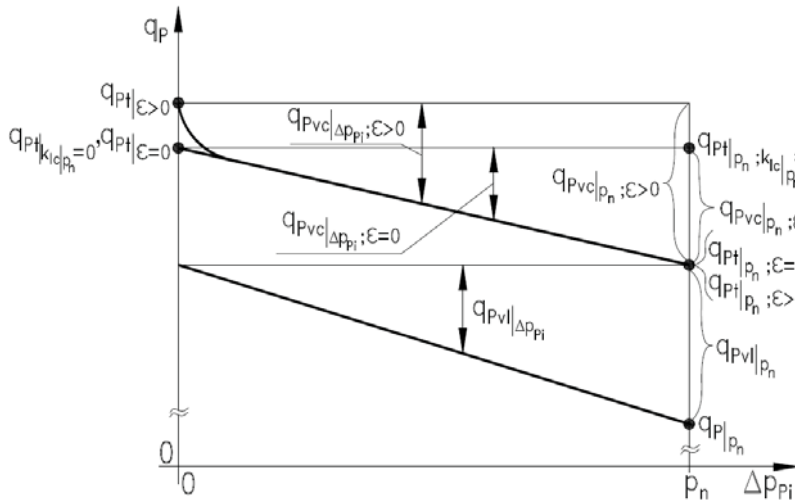


Fig.2 Subdivision of intensity of volumetric losses  $q_{P_i} = q_{P_{vl}} + q_{P_{vc}}$  per one shaft revolution in the pump working chambers, the losses dependent on indicated increase  $\Delta p_{P_i}$  of pressure in the chambers, into intensity  $q_{P_{vl}}|\Delta p_{P_i}$  of volumetric losses due to leakage (independent of liquid aeration coefficient  $\epsilon$ ) and intensity  $q_{P_{vc}}|\Delta p_{P_i}$  of volumetric losses due to liquid compressibility, the subdivision made at pump capacity coefficient  $b_p = 1$ :

$q_{P}|_{p_n}$  – pump capacity per one shaft revolution required of the pump by the hydrostatic system driven by it at  $\Delta p_{P_i} = p_n$ ,

$q_{Pt}|_{p_n}$  – required values of active working volume of working liquid displaced by the pump at  $\Delta p_{P_i} = p_n$  determined with the assumption of  $k_{lc}|_{p_n} = 0$  or with the assumption of  $\epsilon = 0$  or  $\epsilon > 0$ ,

$q_{P_i}$  – required values of theoretical working capacity per one shaft revolution, i.e. active volume of liquid displaced by the pump at  $\Delta p_{P_i} = 0$ , determined with the assumption of  $k_{lc}|_{p_n} = 0$  or with assumption of  $\epsilon = 0$  or  $\epsilon > 0$ .

Active working volume  $q_{Pt}|_{p_n}$  per one shaft revolution is a sum  $q_{Pt}|_{p_n} = q_{P}|_{p_n} + q_{P_{vl}}|_{p_n}$  of pump capacity  $q_{P}|_{p_n}$  per one shaft revolution (required of the pump by the driven hydrostatic system at  $\Delta p_{P_i} = p_n$ ) and intensity  $q_{P_{vl}}|_{p_n}$  of volumetric losses per one shaft revolution in the working chambers due to leakage at  $\Delta p_{P_i} = p_n$ ; with the assumption of non-compressible liquid, i.e.  $k_{lc}|_{p_n} = 0$ , the active volume  $q_{Pt}|_{p_n}; k_{lc}|_{p_n} = 0$  (equal to volume  $q_{Pt}|_{k_{lc}|_{p_n} = 0}$ ) is also increased by intensity  $q_{P_{vc}}|_{p_n}; \epsilon = 0$  of volumetric losses per one shaft revolution due to compression of non-aerated ( $\epsilon = 0$ ) liquid.

Theoretical working capacity  $q_{P_i}$  per one shaft revolution, i.e. active volume of liquid displaced by the pump at  $\Delta p_{P_i} = 0$ , is a sum  $q_{P_i} = q_{Pt} = q_{Pt}|_{p_n} + q_{P_{vc}}|_{p_n}$  of active working volume  $q_{Pt}|_{p_n}$  per one shaft revolution at  $\Delta p_{P_i} = p_n$  and of volumetric losses  $q_{P_{vc}}|_{p_n}$  per one shaft revolution due to compression of non-aerated ( $\epsilon = 0$ ) or aerated ( $\epsilon > 0$ ) liquid in the working chambers at  $\Delta p_{P_i} = p_n$ . Volume  $q_{P_i}$  is therefore a sum  $q_{P_i} = q_{P}|_{p_n} + q_{P_{vl}}|_{p_n} + q_{P_{vc}}|_{p_n}$  of pump capacity  $q_{P}|_{p_n}$  per one shaft revolution (required of the pump by the driven hydrostatic system at  $\Delta p_{P_i} = p_n$ ), intensity  $q_{P_{vl}}|_{p_n}$  of volumetric losses per one shaft revolution due to leakage in the working chambers at  $\Delta p_{P_i} = p_n$  and volumetric losses  $q_{P_{vc}}|_{p_n}$  per one shaft revolution due to compression of non-aerated ( $\epsilon = 0$ ) or aerated ( $\epsilon > 0$ ) liquid in the working chambers at  $\Delta p_{P_i} = p_n$ .

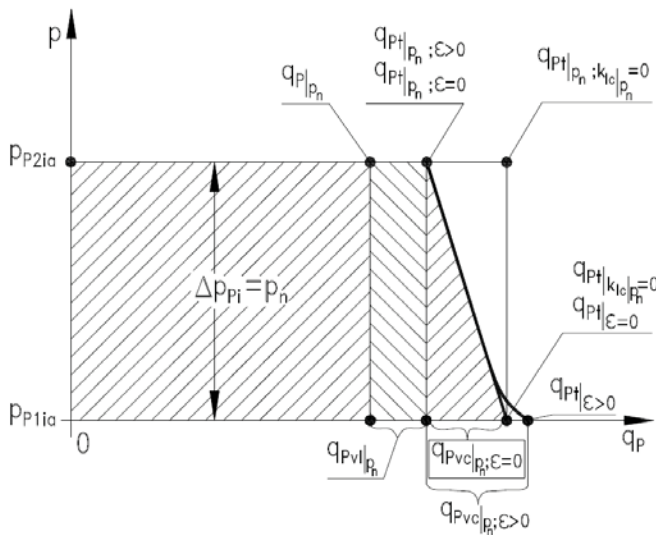


Fig.3 Area of indicated work field in the working chambers of displacement pump during one pump shaft revolution, deciding of the value  $M_{P_i}$  of torque indicated in the chambers at indicated increase  $\Delta p_{P_i}$  of pressure in the chambers equal to pump nominal pressure  $p_n - \Delta p_{P_i} = p_n$ , determined at the pump capacity coefficient  $b_p = 1$ :

$q_{P}|_{p_n}$  – pump capacity per one shaft revolution (required of the pump by the pump fed hydrostatic system) at  $\Delta p_{P_i} = p_n$ ,

$q_{Pt}|_{p_n}$  – required values of active volume of liquid displaced by the pump per one shaft revolution at  $\Delta p_{P_i} = p_n$ , determined with the assumption of  $k_{lc}|_{p_n} = 0$  or the assumption of  $\epsilon = 0$  or  $\epsilon > 0$ ,

$q_{P_i}$  – required values of theoretical working volume per one shaft revolution, i.e. active volume of liquid displaced by the pump at  $\Delta p_{P_i} = 0$ , determined with the assumption of  $k_{lc}|_{p_n} = 0$  or the assumption of  $\epsilon = 0$  or  $\epsilon > 0$ ,

$q_{P_{vl}}|_{p_n}$  – intensity of volumetric losses per one shaft revolution due to leakage in the working chambers at  $\Delta p_{P_i} = p_n$

$q_{P_{vc}}|_{p_n}$  – volumetric losses per one shaft revolution, calculated at  $\Delta p_{P_i} = p_n$ , due to liquid compressibility with the assumption of  $\epsilon = 0$  or  $\epsilon > 0$ ,

$q_{P}|_{p_n} p_n$  – a fragment of field of indicated work in the working chambers, a product of capacity  $q_{P}|_{p_n}$  per one shaft revolution (required of the pump by the fed hydrostatic system at  $p_{P_i} = p_n$ ) and increase  $\Delta p_{P_i} = p_n$  of pressure in the chambers,

$q_{P_{vl}}|_{p_n} p_n$  – a fragment of field of indicated work in the working chambers, a product of intensity  $q_{P_{vl}}|_{p_n}$  of volumetric losses due to leakage in the chambers (during displacement of the liquid by the pump at  $\Delta p_{P_i} = p_n$ ) and increase  $\Delta p_{P_i} = p_n$  in the chambers,

$(q_{P_{vc}}|_{p_n} p_n) / 2$  – a fragment of field of indicated work in the working chambers, approximately constituting half of the product of volumetric losses  $q_{P_{vc}}|_{p_n}$  due to compressibility of liquid in the chambers at  $\Delta p_{P_i} = p_n$  and increase  $\Delta p_{P_i} = p_n$  of pressure in the chambers.

Compared with the value  $q_{Pt}|_{p_n}$ , the theoretical working volume  $q_{P_i}$  is greater by a value  $q_{P_{vc}}|_{p_n}$  of volumetric losses due to compressibility of non-aerated ( $\epsilon = 0$ ) or aerated ( $\epsilon > 0$ ) liquid at  $\Delta p_{P_i} = p_n$ . Not taking into account the liquid compressibility, i.e. assuming that value  $q_{Pt}|_{p_n}; k_{lc}|_{p_n} = 0$  is equal to value  $q_{Pt}|_{k_{lc}|_{p_n} = 0}$ , results in the calculations with unjustified increase of the field of indicated work in the chambers per one shaft revolution and, in effect, with unjustified increase of the calculated torque  $M_{P_i}$  in the chambers

making the assumption that the quantity  $q_{Pt}|_{p_n; k_{lc}|_{p_n}=0}$  of displaced liquid is equal to theoretical working volume  $q_{Pt}|_{k_{lc}|_{p_n}=0}$  determined at  $\Delta p_{Pi} = 0$ , results in calculations with unjustified increase of the field of indicated work in the working chambers during one shaft revolution and, in effect, with unjustified increase of the calculated indicated torque  $M_{Pi}$  in the chambers.

### TORQUE MPM OF MECHANICAL LOSSES IN A DISPLACEMENT PUMP „WORKING CHAMBERS - SHAFT” ASSEMBLY AS A FUNCTION OF INCREASE $\Delta p_{Pi}$ OF PRESSURE IN THE WORKING CHAMBERS

In reference to papers [5 ÷ 7], figure 4 presents a picture of torque  $M_{Pm}|\Delta p_{Pi}; b_p; v$  of mechanical losses in a displacement pump as a function of increase  $\Delta p_{Pi}$  of pressure in the working chambers.

The proposed mathematical models describing the torque MPM of mechanical losses in the pump, related to theoretical models of the torque of mechanical losses, take the form:

- in a pump with theoretical (constant) capacity  $q_{Pt}$  per one shaft revolution ( $b_p = 1$ ):

$$M_{Pm}|\Delta p_{Pi}, v = k_{4.1} M_{Pt} \left( \frac{v}{v_n} \right)^{a_{vm}} + k_{4.2} M_{Pt} \frac{\Delta p_{Pi}}{p_n} =$$

$$\left[ k_{4.1} \left( \frac{v}{v_n} \right)^{a_{vm}} + k_{4.2} \frac{\Delta p_{Pi}}{p_n} \right] M_{Pt} = \quad (8)$$

$$= \left[ k_{4.1} \left( \frac{v}{v_n} \right)^{a_{vm}} + k_{4.2} \frac{\Delta p_{Pi}}{p_n} \right] \frac{q_{Pt} p_n}{2\Pi},$$

where:

$$k_{4.1} = \frac{M_{Pm}|\Delta p_{Pi}=0, b_p=1, v_n}{M_{Pt}} = \frac{M_{Pm}|\Delta p_{Pi}=0, b_p=1, v_n}{\frac{q_{Pt} p_n}{2\Pi}}, \quad (9)$$

$$k_{4.2} = \frac{\Delta M_{Pm}|\Delta p_{Pi}, b_p=1, v_n}{M_{Pi}} = \frac{\Delta M_{Pm}|\Delta p_{Pi}, b_p=1, v_n}{\frac{q_{Pt} \Delta p_{Pi}}{2\Pi}} =$$

$$= \frac{M_{Pm}|\Delta p_{Pi}, b_p=1, v_n - M_{Pm}|\Delta p_{Pi}=0, b_p=1, v_n}{\frac{q_{Pt} \Delta p_{Pi}}{2\Pi}} = \quad (10)$$

$$= \frac{M_{Pm}|\Delta p_{Pi}=p_n, b_p=1, v_n - M_{Pm}|\Delta p_{Pi}=0, b_p=1, v_n}{\frac{q_{Pt} p_n}{2\Pi}} =$$

$$= \frac{M_{Pm}|\Delta p_{Pi}=p_n, b_p=1, v_n - M_{Pm}|\Delta p_{Pi}=0, b_p=1, v_n}{M_{Pt}}.$$

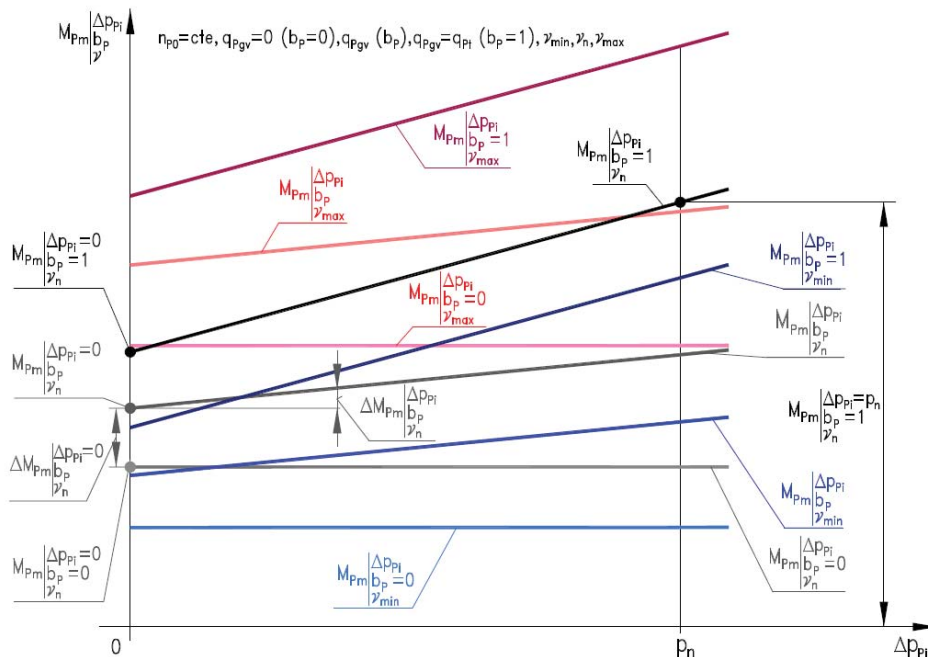


Fig.4 Torque  $M_{Pm}|\Delta p_{Pi}, b_p, v$  of mechanical losses in a piston (axial or radial) pump with crankcase filled with liquid and with variable capacity  $q_{pgv} = b_p q_{Pt}$  per one shaft revolution, as a function of the indicated increase  $\Delta p_{Pi}$  of pressure in the pump working chambers – graphical interpretation of theoretical model (9); capacity  $q_{pgv}$  per one shaft revolution (coefficient  $b_p$  of pump capacity):  $q_{pgv} = 0$  ( $b_p = 0$ ),  $q_{pgv} = q_{Pt}$  ( $b_p = 1$ ); liquid viscosity  $v_{min}, v_n$  and  $v_{max}$ . Torque  $M_{Pm}|\Delta p_{Pi}, b_p, v$  of mechanical losses in the pump without the crankcase filled with liquid is practically independent of the liquid viscosity  $v$  and is determined at the liquid reference viscosity  $v_n$ .

- in a pump with geometrical (variable) capacity  $q_{pgv}$  ( $q_{pgv} = b_p q_{pt}$ ) per one shaft revolution:

$$\begin{aligned}
 M_{Pm|\Delta p_{pi}, b_p, v} &= (k_{4.1.1} + k_{4.1.2} b_p) M_{Pt} \left( \frac{v}{v_n} \right)^{a_{vm}} + k_{4.2} M_{Pt} b_p \frac{\Delta p_{pi}}{p_n} = \\
 &= \left[ (k_{4.1.1} + k_{4.1.2} b_p) \left( \frac{v}{v_n} \right)^{a_{vm}} + k_{4.2} b_p \frac{\Delta p_{pi}}{p_n} \right] M_{Pt} = \\
 &= \left[ (k_{4.1.1} + k_{4.1.2} b_p) \left( \frac{v}{v_n} \right)^{a_{vm}} + k_{4.2} b_p \frac{\Delta p_{pi}}{p_n} \right] \frac{q_{pt} p_n}{2\Pi},
 \end{aligned} \quad (11)$$

where:

$$k_{4.1.1} = \frac{M_{Pm|\Delta p_{pi}=0, b_p=0, v_n}}{M_{Pt}} = \frac{M_{Pm|\Delta p_{pi}=0, b_p=0, v_n}}{\frac{q_{pt} p_n}{2\Pi}}, \quad (12)$$

$$\begin{aligned}
 k_{4.1.2} &= \frac{M_{Pm|\Delta p_{pi}=0, b_p=1, v_n} - M_{Pm|\Delta p_{pi}=0, b_p=0, v_n}}{M_{Pt}} = \\
 &= \frac{M_{Pm|\Delta p_{pi}=0, b_p=1, v_n} - M_{Pm|\Delta p_{pi}=0, b_p=0, v_n}}{\frac{q_{pt} p_n}{2\Pi}},
 \end{aligned} \quad (13)$$

$$\begin{aligned}
 k_{4.2} &= \frac{\Delta M_{Pm|\Delta p_{pi}, b_p, v_n}}{M_{Pi}} = \frac{\Delta M_{Pm|\Delta p_{pi}, b_p, v_n}}{b_p q_{pt} \Delta p_{pi}} = \frac{\Delta M_{Pm|\Delta p_{pi}, b_p=1, v_n}}{\frac{q_{pt} \Delta p_{pi}}{2\Pi}} = \\
 &= \frac{M_{Pm|\Delta p_{pi}=p_n, b_p=1, v_n} - M_{Pm|\Delta p_{pi}=0, b_p=1, v_n}}{\frac{q_{pt} p_n}{2\Pi}} = \\
 &= \frac{M_{Pm|\Delta p_{pi}=p_n, b_p=1, v_n} - M_{Pm|\Delta p_{pi}=0, b_p=1, v_n}}{M_{Pt}}.
 \end{aligned} \quad (14)$$

## COMPARISON OF THE POWERS OF THE ENERGY LOSSES IN A DISPLACEMENT PUMP DETERMINED WITHOUT OR WITH TAKING INTO ACCOUNT OF POWER OF HYDRAULIC OIL COMPRESSION – INVESTIGATIONS OF A HYDROMATIK A7V.58.1.R.P.F.00 PUMP [8 ÷ 15]

Let us determine a sum of power of volumetric and mechanical losses resulting from increase of pressure in the working chambers of a variable capacity per one shaft revolution displacement pump, at the indicated increase  $\Delta p_{pi}$  of pressure in the chambers equal to pump nominal pressure  $p_n$  ( $\Delta p_{pi} = p_n$ ), at the pump capacity coefficient  $b_p = 1$  and at the ratio  $v/v_n = 1$  of hydraulic oil viscosity  $v$  to reference viscosity  $v_n$ .

We shall use formula (4) for the purpose:

$$\Delta P_{Pvl} + \Delta P_{Pvc} + \Delta P_{Pm|\Delta p_{pi}} = P_{Pc} - P_{Pui} - \Delta P_{Pp} - \Delta P_{Pm|\Delta p_{pi}=0},$$

where the sum of pump useful power  $P_{Pui}$  and power  $\Delta P_{Pp}$  of pressure losses in the channels will be replaced by useful power  $P_{Pui}$  in the working chambers ( $P_{Pui} = P_{Pu} + \Delta P_{Pp}$ ) (Fig.1):

$$\Delta P_{Pvl} + \Delta P_{Pvc} + \Delta P_{Pm|\Delta p_{pi}} = P_{Pc} - P_{Pui} - \Delta P_{Pm|\Delta p_{pi}=0}. \quad (15)$$

The result obtained from formula (15) will be compared with results of investigations of volumetric and mechanical losses resulting from increase  $\Delta p_{pi}$  of pressure in the chambers evaluated with the proposed method of determining the degree of liquid aeration in a variable capacity displacement pump [10, 11]:

- without taking into account volumetric losses  $Q_{Pvc}|p_n$  of oil compression, i.e. with treating  $Q_{Pvc}|p_n$  as an element of the sum  $Q_{Pvl}|p_n + Q_{Pvc}|p_n$  of volumetric losses attributed to oil leakage in the chambers,
- with taking into account the volumetric losses  $Q_{Pvc}|p_n$  of oil compression in the chambers.

The comparison will be based on results of a HYDROMATIK A7V.58.1.R.P.F.00 pump investigation [8 ÷ 15].

Fig.5 presents an example of relation  $q_p = f(\Delta p_{pi})$  of capacity  $q_p$  per one shaft revolution to indicated increase  $\Delta p_{pi}$  of pressure in working chambers at pump capacity coefficient  $b_p = 1$  and at viscosity  $v_n = 35 \text{mm}^2\text{s}^{-1}$ . This is an example of searching for theoretical working capacity  $q_{pt}$  per one shaft revolution and of evaluation of subdivision of the intensity  $q_{pv}$  of volumetric losses into volumetric losses  $q_{pvl}$  due to leakage of oil in the chambers and volumetric losses  $q_{pvc}$  resulting from compression of non-aerated or aerated oil.

Fig.6 presents a picture of relations of increase  $\Delta M_{Pm|\Delta p_{pi}=p_n; b_p; \varepsilon; v_n}$  of mechanical losses in the pump „working chambers - shaft“ assembly to geometrical working capacity  $q_{pgv}$  (to pump capacity coefficient  $b_p$ ) at assumed values of oil elasticity modulus  $B$  and of oil aeration coefficient  $\varepsilon$ . The line corresponding to oil aeration coefficient  $\varepsilon = 0,0135$  corresponds to increase  $\Delta M_{Pm|\Delta p_{pi}=p_n; b_p; \varepsilon; v_n}$  of torque of mechanical losses proportional to torque  $M_{Pi}$  indicated in the working chambers.

The sum of powers of volumetric and mechanical losses resulting from increase  $p_{pi} = p_n$  of pressure in the working chambers determined by formula (15) and the sums determined in effect of direct definition of the individual powers of losses without and with taking into account the losses of oil compression in the chambers is presented below.

### 1. Sum $\Delta P_{Pvl}|p_n + \Delta P_{Pvc}|p_n + \Delta P_{Pm}|p_n$ of powers of losses determined by formula (15)

Data from pump investigations:

- capacity  $q_p|p_n = 55,009 \text{cm}^3 / \text{rev}$ ,
- indicated increase of pressure  $\Delta p_{pi} = p_n = 32,17 \text{MPa}$ ,
- rotational speed  $n_p|p_n = 24,73 \text{rev/s}$ ,
- torque on shaft at  $\Delta p_{pi} = p_n$   $M_p|p_n = 308,79 \text{Nm}$ ,
- torque on shaft at  $\Delta p_{pi} = 0$

$$M_p|\Delta p_{pi}=0 = M_{Pm|\Delta p_{pi}=0} = 6,376 \text{Nm}.$$

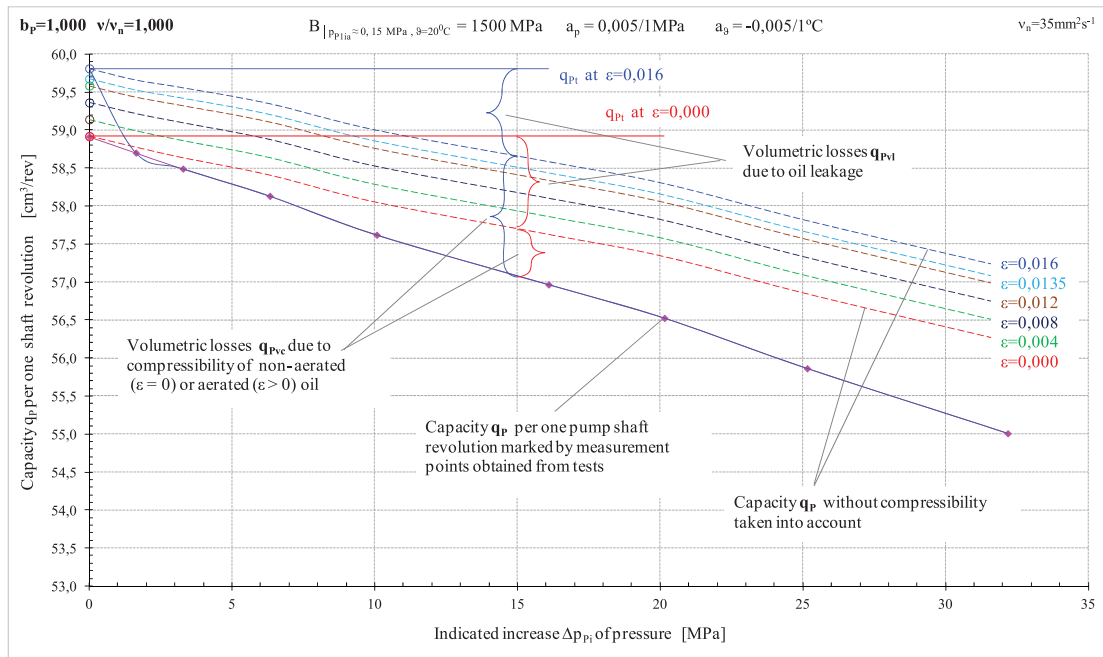


Fig. 5 Dependence of pump capacity  $q_p$  per one shaft revolution on the indicated increase  $\Delta p_{pi}$  of pressure in the working chambers, at the coefficient  $b_p = 1$  of pump capacity; the values  $q_{pgv}$  of geometrical working volume and  $q_{pt}$  of theoretical working volume per one shaft revolution (determined at  $\Delta p_{pi} = 0$ ) and subdivision of the intensity  $q_{pv} = q_{pvl} + q_{pvc}$  of volumetric losses per one shaft revolution into volumetric losses  $q_{pvl}$  due to oil leakage in the chambers and volumetric losses  $q_{pvc}$  due to compressibility of non-aerated (or aerated) oil dependent on the value of oil aeration coefficient  $\epsilon$  ( $\epsilon = 0$  to  $0,016$ ); viscosity coefficient  $\nu/\nu_n = 1$ , oil temperature  $\vartheta = 430C$  (pump of the HYDROMATIK A7V.DR.1.R.P.F.00 type) [8, 9].

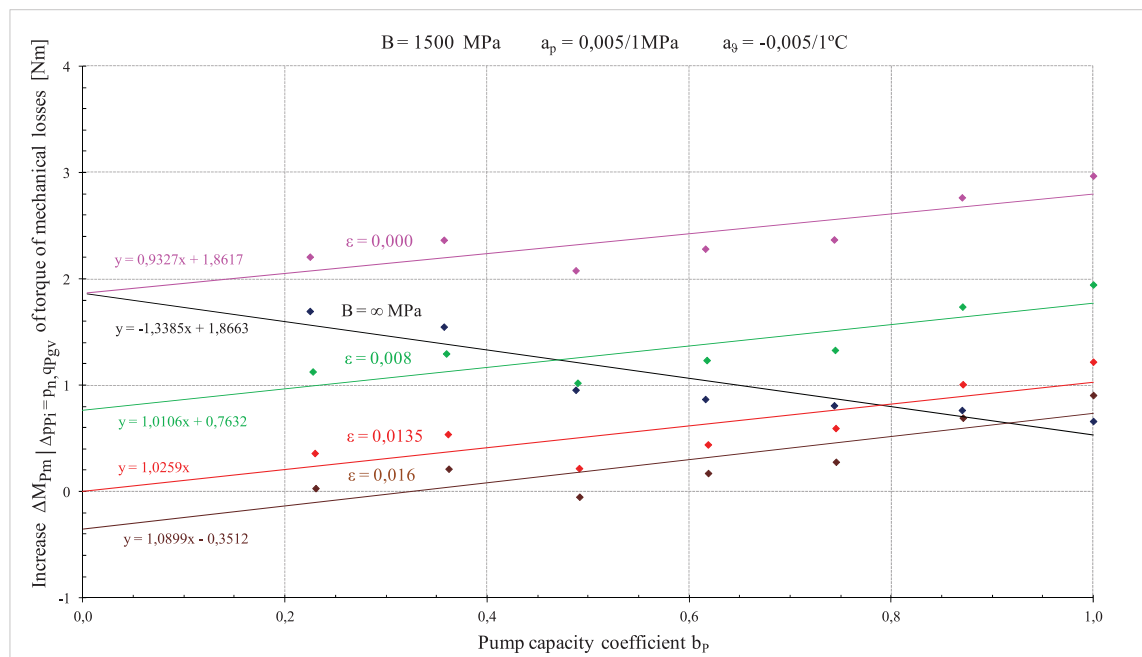


Fig. 6 Picture of the relations of increase  $\Delta M_{Pm} |_{\Delta p_{pi} = 32 MPa; q_{pgv}}$  of torque of mechanical losses in the pump „working chambers - shaft” assembly (pump HYDROMATIK A7V.58.DR.1.R.P.F.00 type) to the geometrical working capacity  $q_{pgv}$  ( $b_p$  coefficient) with assumed values of modulus  $B$  of hydraulic oil elasticity and oil aeration coefficient  $\epsilon$  [10, 11]

Useful power in pump working chambers:

$$P_{Pui|p_n} = q_P \times p_n \times n_P =$$

$$= 55,009 \text{cm}^3 / \text{rev} \times 32,17 \text{MPa} \times 24,73 \text{rev} / \text{s} = 43763 \text{W}$$

Power of mechanical losses in no-load pump:

$$\Delta P_{Pm|\Delta p_{p_i}=0} = M_{Pm|\Delta p_{p_i}=0} \times 2\Pi n_P =$$

$$= 6,376 \text{Nm} \times 2\Pi \times 24,73 \text{rev} / \text{s} = 991 \text{W}$$

Consumed power on pump shaft:

$$P_{Pc|p_n} = M_{P|p_n} \times 2\Pi n_{P|p_n} =$$

$$= 308,73 \text{Nm} \times 2\Pi \times 24,73 \text{rev} / \text{s} = 47972 \text{W}$$

Sum of power of losses:

$$\Delta P_{Pv|p_n} + \Delta P_{Pvc|p_n} + \Delta P_{Pm|p_n} = P_{Pc|p_n} - P_{Pui|p_n} - \Delta P_{Pm|\Delta p_{p_i}=0} =$$

$$= 47972 \text{W} - 43763 \text{W} - 981 \text{W} = 3218 \text{W}$$

## 2. Sum $\Delta P_{Pv|p_n} + \Delta P_{Pm|p_n}$ of powers of losses determined with not taking into account the volumetric losses of oil compression in the chambers

Data from pump investigations:

- capacity  $q_{P|p_n} = 55,009 \text{cm}^3 / \text{rev}$ ,
- theoretical capacity  $q_{Pt} = 58,914 \text{cm}^3 / \text{rev}$ ,
- volumetric losses due to leakage  
 $q_{Pv|p_n} = q_{Pt} - q_{P|p_n} = 3,905 \text{cm}^3 / \text{rev}$ ,
- indicated increase of pressure  $\Delta p_{p_i} = p_n = 32,17 \text{MPa}$ ,
- rotational speed  $n_{P|p_n} = 24,73 \text{rev} / \text{s}$ ,
- increase of torque of mechanical losses  
 $\Delta M_{Pm|p_n} = 0,533 \text{Nm}$

Power of volumetric losses due to leakage in the working chambers:

$$\Delta P_{Pv|p_n} = q_{Pv|p_n} \times p_n \times n_{P|p_n} =$$

$$= 3,905 \text{cm}^3 / \text{rev} \times 32,17 \text{MPa} \times 24,73 \text{rev} / \text{s} = 3107 \text{W}$$

Power of mechanical losses in the „working chambers - shaft” assembly resulting from increase  $\Delta M_{Pm|p_n}$  of torque of losses:

$$\Delta P_{Pm|p_n} = \Delta M_{Pm|p_n} \times 2\Pi n_{P|p_n} =$$

$$= 0,533 \text{Nm} \times 2\Pi \times 24,73 \text{rev} / \text{s} = 83 \text{W}$$

Sum of powers of losses:

$$\Delta P_{Pv|p_n} + \Delta P_{Pm|p_n} = 3107 \text{W} + 83 \text{W} = 3190 \text{W}$$

## 3. Sum $\Delta P_{Pv|p_n} + \Delta P_{Pvc|p_n} + \Delta P_{Pm|p_n}$ of powers of losses determined with taking into account the volumetric losses of oil compression in the chambers at oil aeration coefficient $\varepsilon = 0,0135$ (at compressibility coefficient $k_{lc|p_n}$ )

Data from pump investigations:

- capacity  $q_{P|p_n} = 55,009 \text{cm}^3 / \text{rev}$ ,
- theoretical capacity  $q_{Pt} = 59,668 \text{cm}^3 / \text{rev}$ ,
- volumetric losses due to compression  
 $q_{Pvc|p_n} = 2,026 \text{cm}^3 / \text{rev}$ ,
- volumetric losses due to leakage  
 $q_{Pv|p_n} = 2,633 \text{cm}^3 / \text{rev}$ ,
- indicated increase of pressure  $\Delta p_{p_i} = p_n = 32,17 \text{MPa}$ ,
- rotational speed  $n_{P|p_n} = 24,73 \text{rev} / \text{s}$ ,
- increase of torque of mechanical losses  
 $\Delta M_{Pm|p_n} = 1,026 \text{Nm}$

Power of volumetric losses of oil compression in the working chambers determined by a simplified formula:

$$\Delta P_{Pvc|p_n} = \frac{q_{Pvc|p_n} \times p_n}{2} \times n_{P|p_n} =$$

$$= \frac{2,026 \text{cm}^3 / \text{obr} \times 32,17 \text{MPa}}{2} \times 24,73 \text{obr} / \text{s} = 806 \text{W}$$

Power of volumetric losses due to leakage in the working chambers:

$$\Delta P_{Pv|p_n} = q_{Pv|p_n} \times p_n \times n_P =$$

$$= 2,633 \text{cm}^3 / \text{obr} \times 32,17 \text{MPa} \times 24,73 \text{obr} / \text{s} = 2095 \text{W}$$

Power of mechanical losses in the „working chambers - shaft” assembly resulting from increase  $\Delta M_{Pm|p_n}$  of torque of losses:

$$\Delta P_{Pm|p_n} = \Delta M_{Pm|p_n} \times 2\Pi n_P =$$

$$= 1,026 \text{Nm} \times 2\Pi \times 24,73 \text{obr} / \text{s} = 159 \text{W}$$

Sum of powers of losses:

$$\Delta P_{Pvc|p_n} + \Delta P_{Pv|p_n} + \Delta P_{Pm|p_n} =$$

$$= 806 \text{W} + 2095 \text{W} + 159 \text{W} = 3060 \text{W}$$

Sum 3218W of powers of losses – volumetric losses  $\Delta P_{Pv|p_n}$  and  $\Delta P_{Pvc|p_n}$  in the working chambers and

mechanical losses  $\Delta P_{Pm|p_n}$  in the „working chambers - shaft” assembly, the losses resulting from increase  $\Delta p_{p_i} = p_n$  of pressure in the working chambers, described by formula (15), is a result of balance of pump useful power  $P_{Pu|p_n}$ , power  $P_{Pc|p_n}$  consumed by the pump as well as power  $\Delta P_{Pp}$  of pressure losses in the channels and power  $\Delta P_{Pm|\Delta p_{p_i}=0}$  of mechanical losses in the „working chambers - shaft” assembly of no-load pump.

**This balance bears the least errors.**

**Sum 3190W of powers of losses** – volumetric losses  $\Delta P_{Pv|p_n}$  and mechanical losses  $\Delta P_{Pm|p_n}$ , determined without taking into account the volumetric losses of oil compression in the chambers, results from the accuracy of evaluation of capacity  $Q_p|p_n$  per one shaft revolution and theoretical capacity  $q_{pt}$ , i.e. volumetric losses  $Q_{Pv|p_n} = Q_{pt} - Q_p|p_n$  treated as leakage.

The sum 3190W of power of losses is a value of approximately 0,991 of the sum 3218W of losses, which confirms the great accuracy of measurements and careful processing of the results.

However, **not taking into account the oil aeration and oil compressibility** (and also not determining the corresponding theoretical capacity  $q_{pt}$  per one shaft revolution) **makes the evaluation of volumetric losses  $Q_{Pv|p_n}$  due to leakage in the chambers and increase  $\Delta M_{Pm|p_n}$  of torque of mechanical losses in the „working chambers - shaft” assembly deformed. It makes a proper evaluation of the pump design solution, as a source of volumetric and mechanical losses, impossible.**

**Sum 3060W of power of losses**  $\Delta P_{Pv|p_n} + \Delta P_{Pvc|p_n} + \Delta P_{Pm|p_n}$  determined with taking the volumetric losses of oil compression in the working chambers into account, at the oil aeration coefficient  $\epsilon = 0,0135$  (oil compressibility coefficient

$k_{lc|p_n} = 0,034$ ) by means of the proposed method [10, 11], with simplified formula  $\Delta P_{Pvc|p_n} = \frac{q_{Pvc|p_n} \times p_n}{2} \times n|p_n$

determining power of volumetric losses of oil compression in the working chambers is a value of approximately 0,991 of the sum 3218W of power of losses determined with formula (15).

The difference  $3218W - 3060W = 158W$  is a value of approximately 0,003 of power  $P_{pc} = 47972W$  consumed on the pump shaft.

**An important gain of this method is obtaining the possibility of evaluation of values and proportions of the volumetric losses  $Q_{Pvc|p_n}$  of oil compression and  $Q_{Pv|p_n}$  due to leakage of oil in the working chambers as well as correct evaluation of increase  $\Delta M_{Pm|p_n}$  of torque of mechanical losses in the pump „working chambers - shaft” assembly.**

## CONCLUSIONS

1. Objective of the work was comparison of powers of energy losses in a variable capacity displacement pump determined without or with taking into account the power of hydraulic oil compression. Evaluation of power of liquid compression in the pump was made possible by the use of method, proposed by the Author, of determining the degree of liquid aeration in the pump [10,11].
2. In the method of determining the liquid aeration in the pump and of power of volumetric losses of liquid compression a simplified formula  $(q_{pvc} \times \Delta p_{p_i})/2$  was used describing the field of indicated work of volumetric losses  $q_{pvc}$  of liquid compression during one shaft revolution at indicated increase  $\Delta p_{p_i}$  of pressure in the chambers.
3. Based on the results of investigations of a HYDROMATIK A7V.58.1.R.P.F.00 pump [8 ÷ 15] a sum of powers of volumetric losses  $\Delta P_{Pv|p_n}$  due to leakage and  $\Delta P_{Pvc|p_n}$  of compression as well as  $\Delta P_{Pm|p_n}$  of mechanical losses resulting from increase  $\Delta p_{p_i} = p_n$  of indicated pressure in the pump working chambers was compared:
  - as a difference between power  $P_{Pc|p_n}$  consumed on the shaft and the sum of useful power  $P_{Pu|p_n}$ , power  $\Delta P_{Pp}$  of pressure losses in the channels and power  $\Delta P_{Pm|\Delta p_{p_i}=0}$  of mechanical losses in no-load pump (at  $\Delta p_{p_i} = 0$ ),
  - as a sum of losses evaluated with the proposed method [10, 11] of determining the degree of liquid aeration in the pump:
    - without taking into account of volumetric losses  $q_{pvc}$  of oil compression in the chambers,
    - with taking into account the volumetric losses  $q_{pvc}$  of oil compression.

## BIBLIOGRAPHY

1. Paszota Z.: Effect of the working liquid compressibility on the picture of volumetric and mechanical losses in a high pressure displacement pump used in a hydrostatic drive. Part I Energy losses in a drive system, volumetric losses in a pump //International Scientific-Technical Conference Hydraulics and Pneumatics, Wrocław, 16 – 18 maja 2012 / Ośrodek Doskonalenia Kadr SIMP - Wrocław : ODK SIMP we Wrocławiu, 2012
2. Paszota Z.: Effect of the working liquid compressibility on the picture of volumetric and mechanical losses in a high pressure displacement pump used in a hydrostatic drive. Part II Mechanical losses in a pump //International Scientific-Technical Conference Hydraulics and

- Pneumatics, Wrocław, 16 – 18 maja 2012 / Ośrodek Doskonalenia Kadr SIMP - Wrocław: ODK SIMP we Wrocławiu, 2012
3. Paszota Z.: Effect of the working liquid compressibility on the picture of volumetric and mechanical losses in a high pressure displacement pump used in a hydrostatic drive. Part I Energy losses in a drive system, volumetric losses in a pump// Polish Maritime Research, 2/2012, Vol. 19
  4. [4] Paszota Z.: Effect of the working liquid compressibility on the picture of volumetric and mechanical losses in a high pressure displacement pump used in a hydrostatic drive. Part II Mechanical losses in a pump // Polish Maritime Research, 3/2012, Vol.19
  5. Paszota Z.: Theoretical and mathematical models of the torque of mechanical losses in the pump used in a hydrostatic drive (in Polish). Chapter in the monograph: „Research, design, production and operation of hydraulic systems” (in Polish) Adam Klich, Antoni Kozieł and Edward Palczak editors. „Cylinder” Library. „Komag” Mining Mechanisation Centre, Gliwice, 2011
  6. Paszota Z.: Theoretical and mathematical models of the torque of mechanical losses in the pump used in a hydrostatic drive (in Polish). „Napędy i sterowanie”, scientific monthly, 10/2011
  7. Paszota Z.: Theoretical models of the torque of mechanical losses in the pump used in a hydrostatic drive Polish Maritime Research, 4 / 2011, Vol. 18
  8. Koralewski J.: Effect of the liquid viscosity on the energy characteristics of variable capacity piston pump (in Polish). Doctor dissertation (continued). Gdańsk University of Technology, Faculty of Ocean Engineering and Ship Technology
  9. Koralewski J.: Effect of oil viscosity and compressibility on determination of volumetric losses in a variable capacity piston pump (in Polish). Paper submitted to the „Cylinder” 2013 Conference. Centrum Mechanizacji Górnictwa „Komag”, Gliwice, 2013
  10. Paszota Z.: Method of determining the degree of liquid aeration in a variable capacity displacement pump Polish Maritime Research, 3 / 2013, Vol. 20
  11. Paszota Z.: Method of determining the degree of liquid aeration in a variable capacity displacement pump (in Polish). „Napędy i sterowanie”, scientific monthly, 11/2013
  12. Koralewski J.: Influence of viscosity and compressibility of aerated oil on determination of volumetric losses in a variable capacity piston pump (in Polish). „Napędy i sterowanie”, scientific monthly, 11/2013
  13. Koralewski J.: Influence of viscosity and compressibility of aerated oil on determination of volumetric losses in a variable capacity piston pump Polish Maritime Research, 4 / 2013, Vol. 20
  14. Paszota Z.: Mathematical model defining volumetric losses of hydraulic oil compression in a variable capacity displacement pump (in Polish) „Napędy i sterowanie”, scientific monthly, 10/2014
  15. Paszota Z.: Mathematical model defining volumetric losses of hydraulic oil compression in a variable capacity displacement pump Paper submitted for publication in the “Polish Maritime Research” journal

#### **CONTACT WITH THE AUTHOR**

Zygmunt Paszota

Gdańsk University of Technology  
11/12 Narutowicza St.  
80 - 233 Gdańsk  
**POLAND**

# IDENTIFICATION OF DAMAGES OF TRIBOLOGICAL ASSOCIATIONS IN CRANKSHAFT AND PISTON SYSTEMS OF TWO-STROKE INTERNAL COMBUSTION ENGINES USED AS MAIN PROPULSION IN SEA-GOING VESSELS AND PROPOSAL OF PROBABILISTIC DESCRIPTION OF LOADS AS CAUSES OF THESE DAMAGES

Jerzy Girtler, Prof.  
Gdańsk University of Technology, Poland

## ABSTRACT

*The article discusses damages of essential tribological associations in crankshaft and piston systems of large power two-stroke engines used as main engines, which take place during transport tasks performed by those ships. Difficulties are named which make preventing those damages impossible, despite the fact that the technical state of engines of this type is identified with the aid of complex diagnostic systems making use of advanced computer technology. It is demonstrated that one of causes of the damages is the lack of research activities oriented on recognising random properties of the loads leading to those damages. A proposal is made for the loads acting at a given time  $t$  on tribological associations in crankshaft and piston systems of internal combustion engines used as main engines to be considered as random variables  $Q_t$ . At the same time the loads examined within a given time interval  $t_1 \leq t \leq t_2$  would be considered stochastic processes  $\{Q(t): t \geq 0\}$ . Essential properties of the loads of the abovementioned tribological associations are named and explained by formulating hypotheses which need empirical verification. Interval estimation is proposed for estimating the expected value  $E(Q_t)$  of the load  $Q_t$  acting at time  $t$ . A relation is indicated between the mechanical load and the thermal load acting on tribological associations in the ship main engine crankshaft and piston system. A suggestion is formulated that a stochastic form of the relation between these types of load is to be searched for, rather than statistic relation, and a proposal is made to measure the intensity (strength) of the stochastic relation using the Czuprow's convergence coefficient.*

**Keywords:** probability, friction associations, crankshaft and piston system, semi-Markov process, marine internal combustion engine, wear

## INTRODUCTION

In sea transport, ships are frequently driven using gearless propulsion systems with diesel engines as main engines (Fig. 1). Due to difficult conditions of their operation, especially in stormy weather, (Fig. 2) the cooperation of each main engine (1) and propeller (8) in a given propulsion system (Fig. 1) is executed at different points of the performance field (operating field) of this engine (Fig. 3). The main engines are frequently forced to operate in the overload field (Fig. 4), in which they are excessively loaded. As a result, their tribological associations are subject to fast wear and damages, which can sometimes be very widespread. Propulsion systems of numerous sea-going vessels such as container ships, bulk carriers, and tankers, make use of two-stroke, turbocharged, low-speed, crosshead, large-power, reversible, direct-power diesel engines (Fig. 5). Damages of tribological associations in this type of engines lead to

substantial financial losses of ship-owners, which are not only connected with necessary repair, frequently done in ship repair yards, but also with ship stoppages which make performing transport services impossible [21]. Moreover, damages of those engines taking place during navigation in stormy weather (Fig. 2) lead, as a rule, to ship's foundering. To prevent these damages, engine producers equip them with diagnosing systems (SDG), which make more and more frequent use of computer technology. A list of such computer-aided systems includes: CoCoS (Computer Controlled Surveillance System) worked out by MAN B&W Diesel Group, and CBM (Condition-Based Maintenance) worked out by Wartsila. These systems enable to identify technical states of ship main engines, being the diagnosed systems (SDN). Unfortunately, both

systems (SDN and SDG), altogether bearing the name of the diagnostic system (SD), are not adapted to generate a complete diagnosis which would include instantaneous diagnosis, genesis, and prognosis, as well as to make decisions based on the statistical decision-making theory. That is a reason why damages of ship main engines still take place during ship operation. These damages, especially those concerning tribological associations, are carefully documented in photos (Fig. 6, Fig. 12) and meticulously described by engine users and producers. Difficulties in preventing the abovementioned damages are connected with the use of deterministic, and not probabilistic description of wear of engine elements. This refers both to linear (surface) wear, mainly connected with sliding friction taking place in friction associations, and volumetric wear resulting from the appearance of microcracks and their further propagation inside the abovementioned elements. To change this situation, random nature of wear processes and the resultant damages is to be taken into account to make a basis for probabilistic description of both the course of wear of tribological associations of engine elements, and the loads being their sources.

Most heavily loaded main engine elements include tribological associations in the crankshaft and piston system and the cylinder liners (Fig. 5). That is why the analysis presented in this article mainly refers to probabilistic properties of thermal and mechanical loads of elements composing these associations.

### PROPERTIES OF LOADS AND SAMPLE DAMAGES OF TRIBOLOGICAL ASSOCIATIONS IN MAIN ENGINE CRANKSHAFT AND PISTON SYSTEMS

Properties of loads which lead to damages of tribological associations in crankshaft and piston systems are presented

here in the form of scientific hypotheses, complemented by relevant explanations. Each hypothesis is an empirically verifiable statement which includes syntactic implication. Part of this statement situated before the syntactic implication is a probable cause of the fact described in the part situated after the implication. The properties of the abovementioned loads are described using a probabilistic approach. This approach is necessary because the loads generated during the operation of friction associations are random variables and should be regarded as functions which attribute a numerical value to each random phenomenon having the form of load record. The random nature of these phenomena results from randomly changing atmospheric and sea conditions (WAM) in which ships perform their transport tasks [4, 5, 6, 26]. Depending on those conditions, (Fig. 1) the screw propeller (8) of each ship generates a randomly changing thrust force ( $T_N$ ) which leads to randomly changing load of the crankshaft and piston system (9) of the main engine (1).

Randomly changing atmospheric and sea conditions (WAM) can be affected by many factors, such as: temperatures, air pressure and humidity, height, natural precipitation, wave direction and speed, sea currents, wind direction and speed, hull trims and rolls, oscillatory hull motions (including heaving, pitching, swaying, rolling), etc. These conditions are a source of time dependent action of mechanical loads (pressures, forces, and moments) and thermal loads (heat fluxes, temperatures, temperature gradients) directed towards the main engine crankshaft system and, consequently, to its tribological associations. Similar loads are also generated due to: harbour manoeuvres, navigation in water regions (channels) of limited depth and width, hull fouling by algae and crustaceans, course change with respect to wave and wind directions, different hull load, etc. Moreover, large gas forces are randomly generated by the main engines, with the resultant inertia forces and torques of crankshaft and piston systems

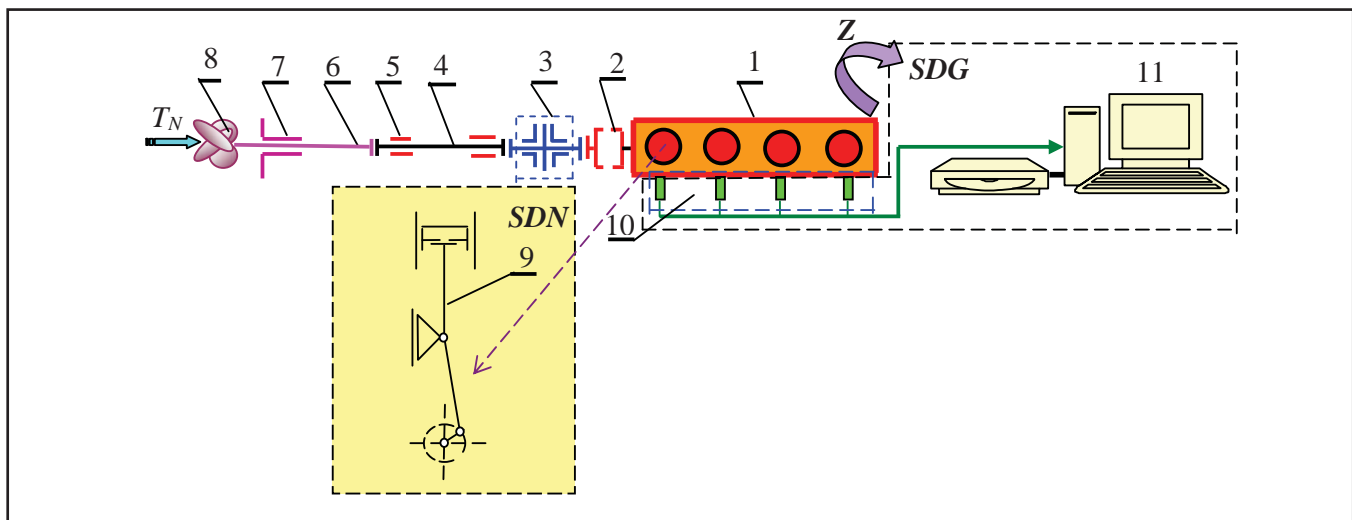


Fig. 1. Functional scheme of the propulsion system without gearbox (direct drive) and a diesel engine. Attention is focused on the crosshead crankshaft and piston system (9) as SDN (with SDG): SDN – diagnosed system (crankshaft and piston system), Z – disturbances, SDG – diagnosing system, 1 – main (diesel) engine, 2 – disengaging (elastic) coupling, 3 – thrust bearing with thrust shaft, 4 – intermediate shaft, 5 – shaft support bearings, 6 – propeller shaft, 7 – propeller shaft pipe, 8 – screw propeller, 9 – crosshead engine crankshaft and piston system, 10 – SDG measuring instruments, 11 – SDG computer unit

transmitted to ship screw propellers. The above loads can be large, especially in cases of cargo ships, such as container ships, tankers, and bulk carriers, which have high draught and screw propellers of over 9 m in diameter and mass exceeding 100 t [28, 29, 30]. These loads become remarkably larger when the main engines work during ship navigation in stormy weather (Fig. 2). In these conditions the randomly changing part of load of these engines increases significantly, which leads to similar increase of the loads of tribological associations in their crankshaft and piston systems, with their intensive wear and damages as a further consequence.

Stormy weather at sea is a reason why crankshaft and piston systems of main engines are frequently heavily loaded (overloaded) with maximal power generated in engine cylinders, and accompanied by extremely large inertia forces when the stern is lifted by the undulated sea and the propeller protrudes above the water surface.



Fig. 2. View of a ship performing transport task in stormy weather [33]

Another source of crankshaft and piston system load changes are unavoidable changes of the rate of fuel injected, depending on current needs, to the main engine combustion chambers to obtain the ship speed necessary to perform transport tasks in the conditions determined by propeller characteristic changes provoked by changing sea conditions. This situation makes the engine operate in different areas of its performance field. Figure 3 shows possible performance field areas (1) of the main engine (2) of a given type which drives directly the screw propeller (3).

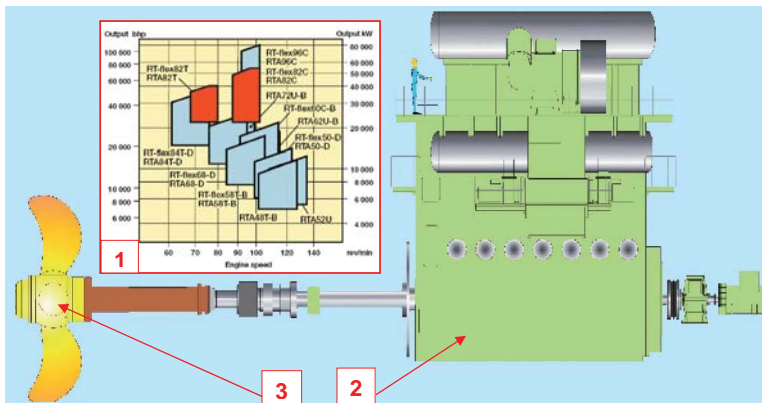


Fig. 3. Propulsion system often used on container ships, bulk carriers, and tankers [1]: 1 – performance fields of different engine families, delivered by their producer, 2 – two-stroke low-speed engine, 3 – screw propeller

If possible, the engine is loaded in such a way that it can operate in a contracted area, i.e. the area which allows the engine to reach its overall efficiency ( $\eta_o$ ) as high as possible, for instance  $\eta_o = 0,55$ . Randomly changing atmospheric and sea conditions (WAM) are a reason why randomly changing main engine loads and, consequently, crankshaft and piston system loads can be shifted to different areas of engine performance field, including the engine overload area (Fig. 4).

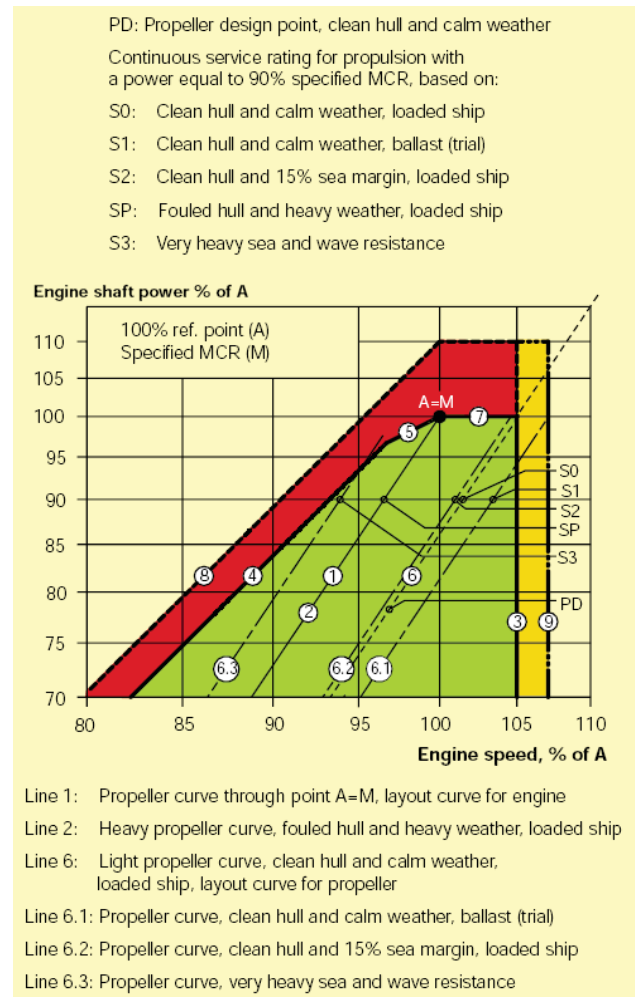


Fig. 4. Engine operation area with marked curves and points of different engine loads resulting from current WAM conditions [31]

The operation of the ship main engine crankshaft and piston system, defined as SDN, is controlled by SDG, which nowadays is more and more frequently equipped with a computer (Fig. 1). The use of these systems (SDG) aims at arriving at such control of engine operation that the engine load does not lead to excessive wear and resultant widespread damage of, most of all, cylinder liners, pistons and their rings, and journals and bushes of main, crankshaft, and crosshead bearings (Fig. 5) [33].

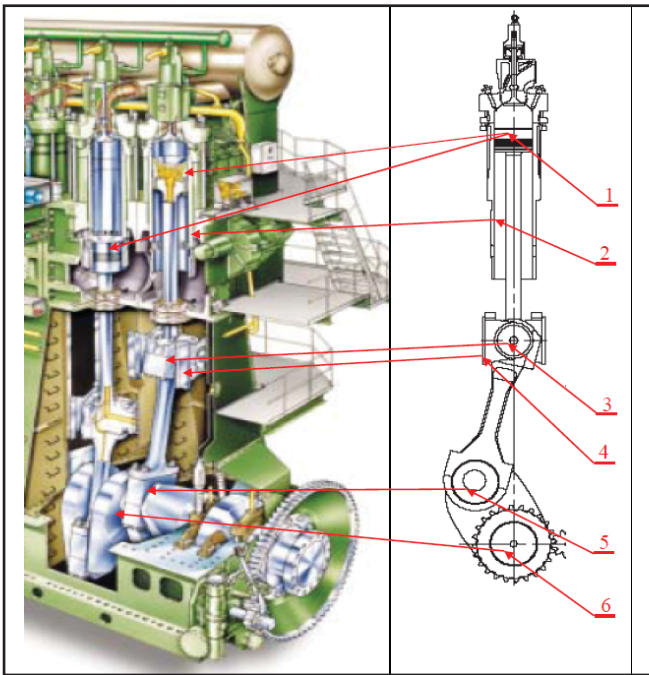


Fig. 5. Elements of main friction associations in SG: 1 – piston, 2 – cylinder liner, 3 – crosshead bearing (journal and bush), 4 – crosshead shoe sliding along the guideway, 5 – crankshaft bearing (journal and bush), 6 – main bearing (journal and bush)

Despite the use of a computerised SDG, the producer cannot predict the course of wear of engine elements and its scale at a given time of engine operation. Consequently, they cannot prevent damages of tribological associations illustrated in Figs. 6÷12. That is why damages, sometimes very widespread, of (Fig. 5): side surfaces of the piston 1 and its rings, inner (bearing) surfaces of the cylinder liner 2, crosshead bearings 3, crosshead shoes 4, crankshaft bearings 5, and main bearings 6 can be observed during main engine operation. Sample cases of excessive wear and resultant damages are shown in Figs. 6÷11 for: piston 1 and its rings (Fig. 6), cylinder bearing surface 2 (Fig. 7), journal of the crosshead bearing 3 (Fig. 8) and its lower bush 1 mounted in the connecting rod head (Fig. 10b), crosshead shoe 4 (Fig. 9), lower bush 2 of the crankshaft bearing 5 (Fig. 10c), and main bearing journal 6 (Fig. 11).

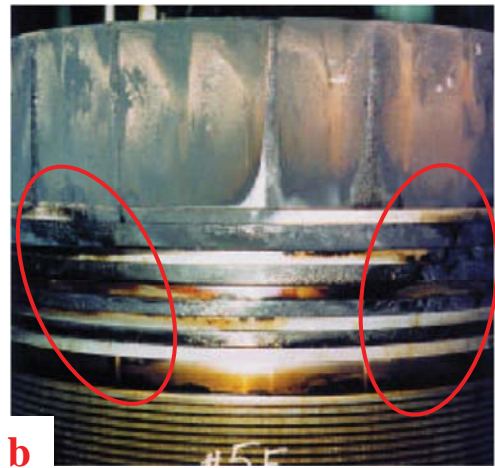


Fig. 6. View of: a) side surfaces of piston 1, excessively worn due to friction (Fig. 5), b) cracked piston rings with losses of material [15, 37]

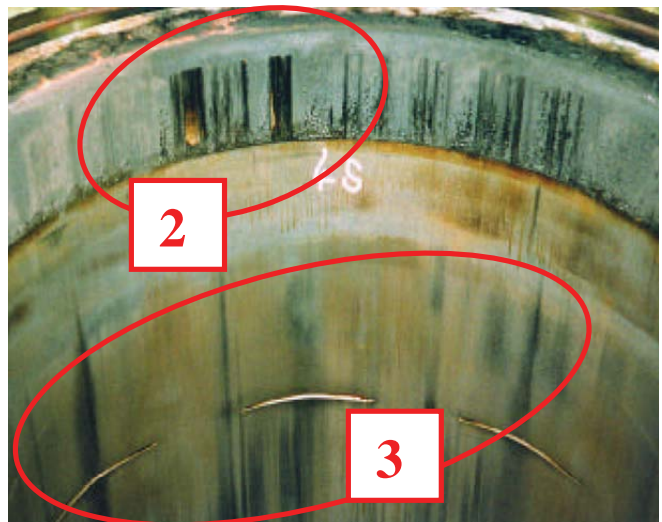


Fig. 7. Views of: indentation 1, corrosion wear 2, and traces of seizure 3 of the inner (bearing) surface of the cylinder liner 2 (Fig. 5) [15, 32]



a

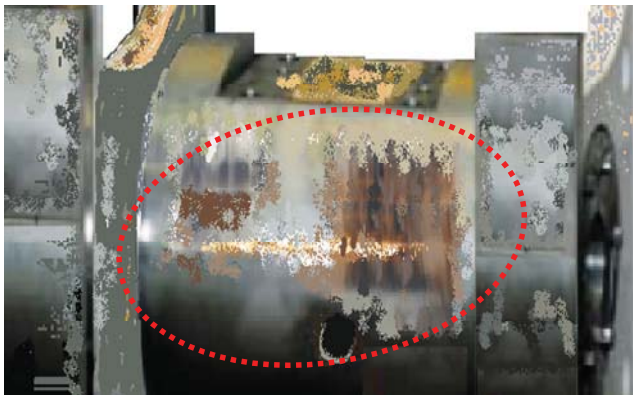


Fig. 8. View of traces of seizure and corrosion wear resulting from overheating of the crosshead bearing journal 3 (Fig. 5) [39]

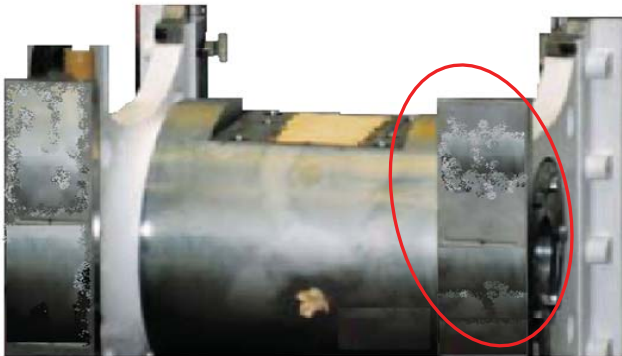


Fig. 9. View of excessive friction and corrosion wear, accompanied by local deep losses of material in the surface layer of the crosshead shoes 3 (Fig. 5) [36]

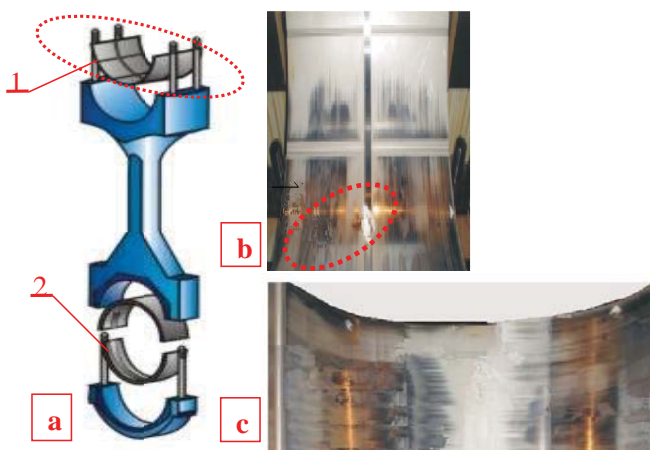


Fig. 10. Views of: a) connecting rod, b) excessive wear of the sliding surface of the lower bush 1 of the connecting rod head bearing; c) excessive wear of the sliding surface of the lower bush 2 of the crankshaft bearing 5 (Fig. 5) [35, 36]

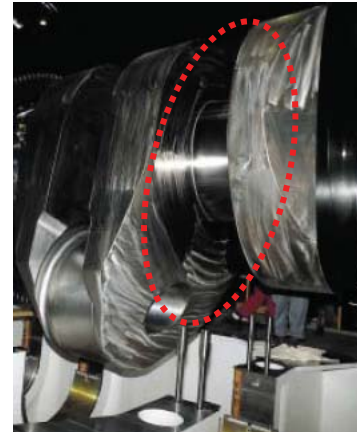


Fig. 11. View of excessive friction wear of the main bearing bush of the crankshaft 6 (Fig. 5) [15, 35]

The presented examples show that friction associations in ship main engines are exposed to widespread damages during engine operation, therefore reasons of difficulties in constructing SDGs which would be able to prevent such damages are to be recognised. The preformed research suggests that the main reason of the above difficulties are random properties of their loads, with large dispersion.

## PROPERTIES OF LOADS OF TRIBOLOGICAL ASSOCIATIONS IN MAIN ENGINE CRANKSHAFT AND PISTON SYSTEMS

Examining the time-history of load  $\{Q(t); t \geq 0\}$  of an arbitrary tribological association in any crankshaft and piston system enables to record real realisations  $q_i(t)$ ,  $i = 1, 2, \dots, n$ , of this process [3, 4, 13, 17]. Three sample realisations of the process  $\{Q(t); t \geq 0\}$  which have been recorded starting from time  $t_r$  are shown in Fig. 12.

This figure shows that at each time  $t$  the load  $Q_t$  as a random variable can take one of three possible values (with certain probability):  $q_1, q_2, q_3$ . The role of variables  $q(t)$  can be played, for instance, by: lubricating oil pressure, temperature and heat released by friction in the friction association, etc.

Consequently, the random variables  $Q_t$  analysed at an arbitrary time  $t_r \leq t \leq t_z$  (Fig. 12) of engine operation compose a family of random variables. Therefore the process of loading of friction associations in an arbitrary crankshaft and piston system is a stochastic process  $\{Q(t); t \geq 0\}$ , i.e. a function the values of which are random variables assigned to a given time  $t$  of their action. Here  $t$  as the process parameter is not a random variable [4, 6, 9, 13, 20].

In this situation the following hypothesis  $H_1$  can be

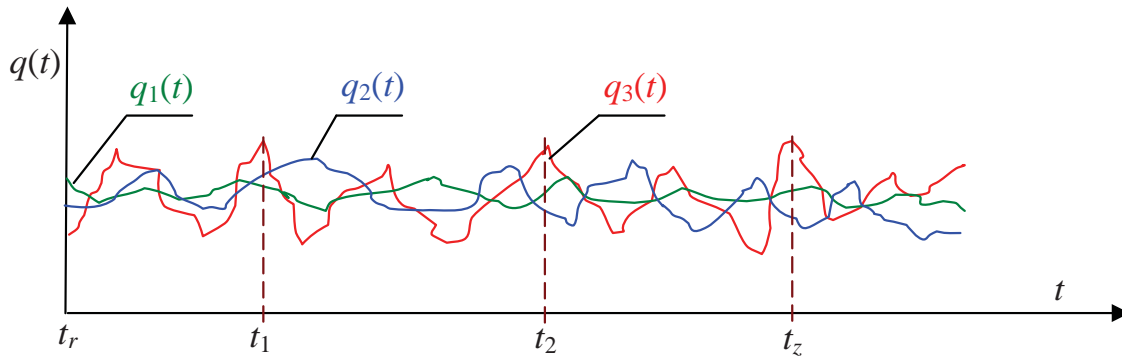


Fig. 12 Sample realisations of the process  $\{X(t): t \geq 0\}$  of load of an arbitrary internal combustion engine crankshaft and piston system;  $t$  – time of engine operation during which energy conversion takes place,  $t_r$  – examination start time,  $t_z$  – examination stop time

formulated: **the process of loading of an arbitrary friction association in each crankshaft and piston system of a arbitrary ship main engine is the stochastic process, because the association load values assigned to arbitrary times  $t$  are random variables.**

Hence the loads of tribological associations in the ship main engine crankshaft and piston systems analysed at an arbitrary time  $t$  of engine operation are to be considered as random variables  $Q(q, t)$ , where  $q$  is an event understood as the load value recorded at time  $t$  which should be considered the realisation of this random variable. In other words: at a given time  $t$  there exists  $Q(t) = q$ . That is why when examining the time dependent load of an arbitrary tribological association of each ship main engine crankshaft and piston system, this load should be considered a random (stochastic) process  $\{Q(t): t \geq 0\}$  [6, 5, 18, 19, 23].

Probabilistic description of each stochastic process requires working out limited-dimension distributions of this process. That means that working out the  $n$ -dimensional distribution of the load process  $\{Q(t): t \geq 0\}$  requires working out  $n$ -dimensional random vectors  $[Q(t_1), Q(t_2), Q(t_3), \dots, Q(t_n)]$  for all parameters  $t_1, t_2, t_3, \dots, t_n$ . This distribution, having the form of  $n$ -dimensional distribution function  $F$ , is given by the formula:

$$F(q_1, q_2, q_3, \dots, q_n, t_1, t_2, t_3, \dots, t_n) = P\{Q(t_1) < q_1, Q(t_2) < q_2, Q(t_3) < q_3, \dots, Q(t_n) < q_n\} \quad (1)$$

Continuous load changes can be only assessed and taken into account in the distribution (1) when the realisations of the process  $\{Q(t): t \geq 0\}$  are recorded continuously, otherwise the abovementioned real process of loading of friction associations of tribological systems should be considered the stochastic process which is discrete in states. In this situation the process should be described using an  $n$ -dimensional distribution having the following form:

$$P(q_1, q_2, q_3, \dots, q_n, t_1, t_2, t_3, \dots, t_n) = P\{Q(t_1) = q_1, Q(t_2) = q_2, Q(t_3) = q_3, \dots, Q(t_n) = q_n\} \quad (2)$$

When examining  $n$  realisations of the load  $Q_i$  as the random variable at an arbitrary time  $t$ , we arrive at the results in the form of  $q_{t(i)}$  ( $i = 1, 2, 3, \dots, n$ ), (Fig. 12). These results enable to calculate the value of the statistics  $\bar{Q}_t$ , which is the mean value  $\bar{q}_t$  calculated from [3, 9, 13, 17]:

$$\bar{q}_t = \frac{1}{n} \sum_{i=1}^n q_{t(i)} \quad (3)$$

where:

$q_{t(i)}$  – value of the load  $Q_i$  recorded during  $i$ -th examination

The statistics  $\bar{Q}_t$  has the asymptotically normal distribution  $N\left(E(Q_t); \frac{\sigma_t}{\sqrt{n}}\right)$  regardless of the functional form of the distribution of the random variable  $Q_t$ . Here:  $E(Q_t)$  and  $\sigma_t$  are, respectively, the expected value and the standard deviation of the random variable (load)  $Q_t$ . This statistics can be almost always used, as for  $n \geq 4$  the concurrence of distribution of the statistics  $\bar{Q}_t$  to normal distribution  $N\left(E(Q_t); \frac{\sigma_t}{\sqrt{n}}\right)$  is very fast. Adopting an assumption that the load  $Q_t$  examined at time  $t$  has normal distribution  $N(E(Q_t); \sigma)$  does not constitute a practical limitation, as the statistics  $\bar{Q}_t$  always has the asymptotically normal distribution [9, 13, 17]. The statistics  $\bar{Q}_t$  is consistent and unbiased, and hence it is the best estimator of the unknown expected value  $E(Q_t)$  of the load  $Q_t$  as the random variable. The results of examination of the load  $Q_t$  can be used for calculating, along with the mean value  $\bar{q}_t$ , also the standard deviation  $s_t$  from the formula [9, 13, 17]:

$$s_t = \sqrt{\frac{1}{n} \sum_{i=1}^n (q_{t(i)} - \bar{q}_t)^2} \quad (4)$$

The statistics  $s_t$  given by the formula (2) is consistent and asymptotically unbiased, and hence again, it is the best estimator of the standard deviation  $\sigma$  of the random variable  $Q_t$ . The values of  $\bar{q}_t$  and  $s_t$  obtained during the load examination

make it possible to assess the expected value  $E(Q_t)$  of the load in the interval form using the formula [9, 13, 17]:

$$P \left\{ \bar{q}_t - t_{\alpha, n-1} \frac{s_t}{\sqrt{n-1}} \leq E(Q_t) \leq \bar{q}_t + t_{\alpha, n-1} \frac{s_t}{\sqrt{n-1}} \right\} \quad (5)$$

where:

$t_{\alpha, n-1}$  – Student's  $t$ -distribution parameter.

The above approach to the examination of loads of tribological associations in ship main engine crankshaft and piston systems enables to determine the course of the stochastic process  $\{Q(t): t \geq 0\}$  along with its expected value  $E[Q(t)]$  and two margins, which are the upper margin  $E[Q(t) + \sigma[Q(t)]$  and the lower margin  $E[Q(t) - \sigma[Q(t)]$  (Fig. 13), i.e. the interval

$$E[Q(t) - \sigma[Q(t)]] \leq E[Q(t)] \leq E[Q(t) + \sigma[Q(t)]] \quad (6)$$

This results from the fact that at an arbitrary time of their action, the loads of tribological associations in ship main engine crankshaft and piston systems are random variables  $Q_t$  with the expected value  $E(Q_t)$  and the variance  $D^2(Q_t)$ . When examined within the time interval  $(t_r, t_z)$ , i.e. when  $t_r \leq t \leq t_z$  ( $t_r$  – examination start time,  $t_z$  – examination stop time), these loads compose a set of random variables  $Q_t$  which are the instantaneous states of the stochastic process  $Q(t)$  with the expected value  $E[Q(t)]$  and the variance  $D^2[Q(t)]$ . Indeed, the values of  $E[Q(t)]$  and  $D^2[Q(t)]$  of the stochastic process  $Q(t)$  depend on time  $t$ , as the values of  $E(Q_t)$  and  $D^2(Q_t)$  are different for different times  $t$ . Nevertheless, the values of  $E[Q(t)]$  and  $D^2[Q(t)]$  of the process  $Q(t)$  are not random functions, because the values of  $E(Q_t)$  and  $D^2(Q_t)$  are not random variables, but are constant for a given time  $t$  and the given set of random variables  $Q_t$  [4, 5, 16, 21, 27, 28]. A sample realisation of the stochastic process  $\{Q(t): t \geq 0\}$  which reveals the dependence of the expected value  $E[Q(t)]$  and the variance  $D^2[Q(t)]$  on time  $t$  is illustrated in Fig. 13.

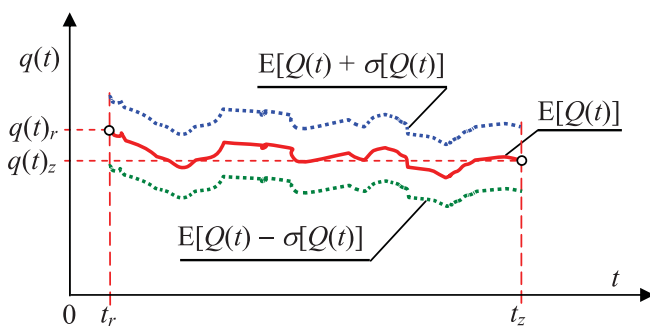


Fig. 13. Sample realisation of the stochastic process  $Q(t)$  illustrating changes of load  $Q$  at time  $t$ :  $Q(t)$  – load at time  $t$ ,  $q(t)$  – realisation of the process  $Q$  at time  $t$ ,  $q(t)_r$  – expected value of the process  $Q$  at time  $t_r$ ,  $q(t)_z$  – expected value of the process  $Q$  at time  $t_z$ ,  $t_r$  – examination start time,  $t_z$  – examination stop time,  $t$  – time as process parameter,  $E[Q(t)]$  – expected value of  $Q$ ,  $\sigma[Q(t)]$  – standard deviation of  $Q$

The load of friction associations in the ship main engine crankshaft and piston system can be considered a combination of mechanical load ( $Q_M$ ) and thermal load ( $Q_C$ ), expressed by the following formula:

$$Q(t) = f[Q_M(t), Q_C(t)] \quad (7)$$

where:

$Q$  – total load of the friction association in a given engine crankshaft and piston system,

$Q_M$  – mechanical load of the friction association,

$Q_C$  – thermal load of the friction association,

$t$  – time of engine action (operation).

Hence, at least two stochastic processes can be considered in empirical load examination, which are  $\{Q_M(t): t \geq 0\}$  and  $\{Q_C(t): t \geq 0\}$ . These processes are components of the vector process  $\{Q(t): t \geq 0\}$  [4, 7, 20, 28].

We can write for the loads  $Q_M$  and  $Q_C$  that at an arbitrary time  $t$  they are vectors with the following components:

$$Q_M : [p_{\max L}, P_L, P_N, P_{TL}, P_{TC}, P_B, N_{TL}, N_{TC}, \dots] \quad (8)$$

$$Q_C : [\dot{q}, \nabla T, t_L, t_C, t_{ol}, \dots] \quad (9)$$

where:

$p_{\max L}$  – maximal bearing pressure (in the oil wedge),

$P_L$  – force carried by the bearing,

$P_N$  – normal force of the piston pressure against the cylinder liner surface,

$P_{TL}$  – friction force in the (main, connecting rod, or crosshead) bearing,

$P_{TC}$  – friction force between the piston with rings and the cylinder liner,

$P_B$  – inertia force acting on the connecting rod bearing,

$N_{TL}$  – friction power loss caused by friction in the bearing,

$N_{TC}$  – friction power loss caused by friction between the piston and the cylinder liner surface,

$\dot{q}$  – density of the heat flux penetrating through the surface,

$\nabla T$  – temperature gradient,

$t_L$  – temperature of the (main, connecting rod, or crosshead) bearing,

$t_C$  – temperature of the cylinder liner,

$t_{ol}$  – temperature of the lubricating oil in the bearing, etc.

It results from relations (8) and (9) that the load imposed on friction associations in each ship main engine crankshaft and piston system depends on many quantities (parameters, indices), therefore it can be considered a stochastic process being a superposition of a number of individual processes (in the simplest case: processes  $Q_M$  and  $Q_C$ ). This interpretation of loads of friction associations in crankshaft and piston systems is convenient for general considerations, but can be of little applicability in practice.

In general, loading of friction associations in the internal combustion engine crankshaft and piston system can be understood as a process, the states of which can be interpreted

as random variables. As seen from relations (8) and (9), this process is a multidimensional process, therefore at each time  $t_k$  ( $k = 1, 2, \dots, n$ ) the following  $n$  random variables:  $Q_1, Q_2, \dots, Q_n$  are to be taken into account. These variables can represent  $n$  different quantities (parameters, indices) of the examined load (for instance,  $Q_1 = p_{\max L}$ ,  $Q_2 = P_L$ ,  $Q_3 = P_N$ ,  $Q_4 = Q_p$  etc.).

When analysing simultaneously a number of individual properties of the load of friction associations in the crankshaft and piston system, a set on  $n$  random variables composing an  $n$ -dimensional random variable  $Q$  is obtained.

In order to simplify further considerations we can limit our analysis by assuming that the random variable  $Q$  is a two-dimensional variable ( $Q_M, Q_C$ ). Since the measurements are repeated periodically we can assume that the variables  $Q_M$  and  $Q_C$  are stepwise (discrete) random variables. The realisations of these variables are the quantities  $q_{Mi}$  and  $q_{Ci}$  respectively, therefore the realisation of the random variable ( $Q_M, Q_C$ ) is the pair ( $q_{Mi}, q_{Ci}$ ). This variable takes values ( $q_{Mi}, q_{Ci}$ ) with certain probability  $p(q_{Mi}, q_{Ci})$ , which is the probability of simultaneous occurrence of events  $Q_M = q_{Mi}$  and  $Q_C = q_{Ci}$ .

The set of the abovementioned probabilities  $p(q_{Mi}, q_{Ci})$  composes a two-dimensional distribution of the random variable ( $Q_M, Q_C$ ). The distribution  $p(q_{Mi}, q_{Ci})$  meets the following condition [9, 13, 17]:

$$\sum_{i=1}^k \sum_{j=1}^k p(q_{Mi}, q_{Cj}) = 1. \quad (10)$$

The marginal distribution of the random variable  $Q_M$  is the following

$$p(q_{Mi}) = \sum_{j=1}^k p(q_{Cj}, q_{Mi}), \quad (11)$$

while the distribution of the random variable  $Q_C$  has the following form:

$$p(q_{Cj}) = \sum_{i=1}^k p(q_{Mi}, q_{Cj}) \quad (12)$$

It results from these considerations that physical quantities which characterise the load, for instance  $p_{\max L}, t_L$  [2, 19, 23], determine both mechanical and thermal load of each friction association in the internal combustion engine crankshaft and piston system. Therefore it is evident that there exists a relation between mechanical load and thermal load of this association. Since both loads are random processes, this relation is expected to be of stochastic nature. Consequently, the following hypothesis  $H_2$  can be formulated for this relation: **there is a stochastic relation between mechanical load  $Q_M(t)$  and thermal load  $Q_C(t)$  of an arbitrary tribological association in the internal combustion engine crankshaft and piston system, because certain variants of one of those variables are accompanied by different variants of the other variable.** Hence the conclusion

that the relation between the loads  $Q_M(t)$  and  $Q_C(t)$  cannot be described using ordinary algebraic equations. This conclusion is obvious, as the load depends on a large number of factors, including those which cannot be measured [18, 19, 23].

The level to which the load  $Q_C$  is determined by the load  $Q_M$ , or  $Q_{m_i}$  ( $i = 1, 2, \dots, n$ ), as independent variables, can differ much. A situation may occur in practice that one independent variable  $Q_M$  almost entirely determines the dependent variable  $Q_C$ . It may also happen that a number of independent variables  $Q_{M_i}$  only minimally affect the dependent variable  $Q_C$  and vice versa, the examined variable  $Q_C$ , as the independent variable affects slightly the dependent variables  $Q_{M_i}$ . For instance, the engine works at low rotational speed and low power output, and simultaneously the crack of the oil line decreases the amount of the lubricating oil delivered to the main and connecting rod bearings. In this situation, despite low load  $Q_M$ , technically dry friction which develops in friction associations leads to the appearance of very high thermal load  $Q_C$  and bearing seizure as a final effect. This example illustrates the need for taking into account the intensity (strength) of the stochastic relation between  $Q_M$  and  $Q_C$ .

The intensity (strength) of the stochastic relation between  $Q_M(t)$  and  $Q_C(t)$  can be assessed during empirical examination using the formula [13]:

$$T_{MC}^2 = T_{CM}^2 = \frac{\chi^2}{N\sqrt{(k_M - 1)(k_C - 1)}}, \quad (13)$$

where:

- $k_M$  – number of variants of the variable  $Q_M$ ;
- $k_C$  – number of variants of the variable  $Q_C$ ;
- $N$  – marginal number of variants of the variable  $Q_M$  or  $Q_C$ ;
- $\chi^2$  – value calculated from the chi-square formula;
- $T_{(\bullet)}^2$  – Czuprow's convergence coefficient.

It can be proved [13] that  $T_{MC}$  takes values from [0,1]. This coefficient is equal to zero ( $T_{MC} = 0$ ) when no relation exists between the values of processes  $Q_M$  and  $Q_C$ , while the value equal to one ( $T_{MC} = 1$ ) testifies to the existence of a functional relation. Generally, the existence of the dependence between random variables  $Q_M$  and  $Q_C$  can be checked by analysing probabilities given by formulas (10) ÷ (12).

Comparing loads of arbitrary tribological associations in crankshaft and piston systems which are recorded in successive working cycles, we can conclude that they are different. Consequently for a given time  $t$ , when examining the load of tribological associations of the engine crankshaft and piston system in particular engine operation cycles for instance at times  $t_1, t_2, \dots$  (Fig. 12), we get different values of this load. Hence, obtaining a certain (expected) value of the load is a random event, because in the same operating conditions existing during the empirical examination the expected value can be recorded or not. That means that the load increments become less and less dependent on each other when the time spread  $\Delta t = t_2 - t_1$  is increased [3, 19, 20, 23].

Based on the above considerations the following hypothesis

$H_3$  can be formulated: *the load of an arbitrary friction association in the internal combustion engine crankshaft and piston system is the process with asymptotically independent increments, because the increasing time spread between the times at which the load is examined (measured) makes its values less and less depended on each other.*

The next property which characterises changes of the load of tribological associations in the engine crankshaft and piston system is that the examined load does not reveal any oriented (monotonic) changes. Consequently we can assume that the peak values of the loads of the above associations appear accidentally. The lack of monotonicity of engine load changes allows us to formulate the following hypothesis  $H_4$ : *the load of friction associations in the engine crankshaft and pistons system is a stationary process, because for a long time interval no monotonicity is observed in the load changes* [4, 6, 12, 19, 23, 26].

Past examinations of diesel engines have revealed that the load of their crankshaft and piston systems is changing continuously in such a way that its values measured after very short time intervals are strongly correlated with each other. On the other hand, when the time spread between load measurements performed on each crankshaft and piston system increases, the correlation between these loads decreases. Hence the load values of an arbitrary crankshaft and piston system measured after time intervals (or times) which are very distant from each other can be considered independent. This property bears the name of asymptotic independence of load values [3, 20]. This asymptotic independence between the load values measured (or calculated) at times  $t_1$  and  $t_2$  (Fig. 12) reflects the fact that the increasing  $\Delta t = t_2 - t_1$  leads to the decrease of the dependence between these values.

The above opinions on properties of loads of friction associations in crankshaft and piston systems of an arbitrary ship main engine can lead to the appearance of new opportunities to define a relation between the wear of these associations and their load, once relevant empirical examinations are performed. This can positively stimulate research activities oriented on analysing loads and wear of tribological associations taking into account their random aspects. Studies in this area have not been undertaken so far, but publications can be found in the literature which suggest that there are grounds for studying this subject [3, 7, 16, 26]. The wear and loads of internal combustion engine crankshaft and piston systems are most often analysed based on a deterministic approach [2, 8, 10, 11, 19, 22, 23, 24, 25]. However, the loads of associations in these systems should be analysed at an arbitrary time  $t$  as random variables  $Q_t$  which compose the stochastic process  $\{Q(t): t \geq 0\}$ , hence there is a need to work out a research plan and methodology taking into account probabilistic aspect of these loads. This will enable to examine the wear of these associations as the effect of their load, taking into account the relation:

$$T_{MC}^2 = T_{CM}^2 = \frac{\chi^2}{N\sqrt{(k_M - 1)(k_C - 1)}}, \quad (14)$$

In formula (14) the wear  $Z_t$  is a random variable which at time  $t$  takes the value  $\bar{z}_t$ , provided that the load  $Q_t$  exists and has the value  $\bar{q}_t$ .

## REMARKS AND CONCLUSIONS

Sea-going vessels can perform transport tasks in conditions of heavy undulation of the seawater surface layer and strong wind counteracting their motion. All this creates unfavourable conditions for operation of tribological associations in ship main engine crankshaft and piston systems, which can lead to extremely high loads and resultant damages of these associations, with sea disasters as possible final consequences.

The load imposed to each tribological association in the abovementioned systems can be considered a random variable  $Q_t$ , with asymptotically normal distribution  $N\left(E(Q_t); \frac{\sigma_t}{\sqrt{n}}\right)$  regardless of the functional form of the load distribution.

When examined at an arbitrary time of its action (operation), the load of each tribological association in the crankshaft and piston system of an arbitrary main engine can be considered a multidimensional random variable. Consequently, the process of loading of each internal combustion engine crankshaft and piston system should be examined based on the assumption that the process is multidimensional and stochastic. Hypotheses are proposed to justify the assumptions that the process of loading of the crankshaft and piston system of an arbitrary diesel engine can be considered: stochastic with asymptotically independent increments, stationary, and ergodic, and that there exists a stochastic relation between its mechanical load and thermal load. The intensity of the stochastic relation between these loads can be assessed empirically using the Czuprow's convergence test.

## BIBLIOGRAPHY

1. Aeberli K.: New high-economy engines for panama containerships and large tankers, Wartsila Switzerland Ltd, Winterthur, September 2007
2. Brun R.: High-speed diesel engines (in Polish). WKiŁ, Warsaw 1973
3. Gercbach I.B., Kordonski Ch., B.: Reliability models of technical objects (in Polish). WNT, Warsaw 1968
4. Girtler J.: Controlling the process of operation of marine internal combustion engines based on the diagnostic decision-making model (in Polish). ZN AMW, nr 100A, Gdynia 1989
5. Girtler J., Kuzmider S., Plewiński L.: Selected issues of operation of sea-going vessels in the aspect of safety of navigation. Monograph (in Polish). WSM, Szczecin 2003
6. Girtler J.: Diagnostics as condition for controlling the operation of marine internal combustion engines (in Polish). Studia Nr 28, WSM, Szczecin 1997

7. Girtler J.: Issue of changes in technical states of a Diesel engine as the results of wear of its tribological systems. *Zeszyty Naukowe Akademii Morskiej w Szczecinie*, 31 (103), 2012
8. Girtler J., Korczewski Z., Mańczak J.: Conception of diagnosing self-ignition engines fed with biofuels in operation conditions. *Journal of Polish CIMAC*. Vol. 5, No 2, 2010
9. Greń J.: Models and tasks of mathematical statistics (in Polish). PWN, Warszawa 1968
10. Korczewski Z.: Analysing the potential for application of the phase shift method in endoscopic examination of marine engines. *Polish Maritime Research*. No 1(77), Vol. 20, 2013
11. Korczewski Z.: Endoscopic image processing and analysis of pistons' service failures of marine diesel engines. *Journal of Polish CIMAC*. Vol. 7, No 2, 2012
12. Kozłowiecki H.: Bearings of piston internal combustion engines (in Polish). WKiŁ, Warsaw 1982
13. Krzysztofiak M., Urbanek D.: Statistical methods (in Polish). PWN, Warszawa 1979
14. Krasowski P.: Pressure and velocity distribution in slide journal bearing lubricated micropolar oil. *Journal of Polish CIMAC*. Vol. 5, No 1, 2010
15. Łosiewicz Z.: Analysing operating conditions of large power two-stroke low-speed ship main engines, and causes and results of damages of their main tribological systems (in Polish). Proceedings of the VII International Scientific and Technical Conference „Explo-Diesel & Gas Turbine 2014”. Gdańsk – Gdynia – Karlskrona, 23 – 27 May, 2014 r., on CD
16. Niewczas A.: Fundamentals of the stochastic model of friction caused wear in application to durability issues of machine elements (in Polish). *Zeszyty Naukowe, Mechanika nr 19*, Politechnika Radomska 1989
17. Pawłowski Z.: Mathematical statistics (in Polish). PWN, Warsaw 1980
18. Piotrowski I., Witkowski K.: Marine internal combustion engines (in Polish). Ed. TRADEMAR, Gdynia 1996
19. Piotrkowski I., Witkowski K.: Operation of marine internal combustion engines (in Polish). AM, Gdynia 2002
20. Rozanov Ju.A.: Stacionarnye sluczajnye processy. *Fitmazgiz, Moskva* 1963
21. Rudnicki J.: The evaluation of the vibration measurement usability of electronic indicator LEMAG „PREMET C”. *Journal of Polish CIMAC*. Vol. 6, No 2, 2011
22. Serdecki W.: Determination of compression ring wall pressure distribution. *Journal of Polish CIMAC*. Vol. 5 No 1, 2010
23. Wajand J.A., Wajand J.T.: Medium- and high-speed piston internal combustion engines (in Polish). WNT, Warsaw 2005
24. Włodarski J. K.: Operation of marine engines – friction and wear (in Polish). WSM, Gdynia 1998
25. Włodarski J. K.: Damages of bearings in marine internal combustion engines (in Polish). *Wydawnictwo Akademii Morskiej w Gdyni, Gdynia* 2003
26. Girtler J.: Identifying conditions of operation of crankshaft and piston systems in ship main engines (in Polish). Report on completion of the own research project performed within the framework of the research project of the Ministry of Science and Information Technology (no. N N509 494638) entitled: “Decision making based control of the process of operation of crankshaft and piston systems in main propulsion engines of sea-going vessels with the aid of technical diagnostics and taking into account safety and environment protection”. Project manager: Prof. Jerzy Girtler, D.Sc. *Prace badawcze nr 1/10 /PB. WOiO PG, Gdańsk*, 2010
27. Girtler J.: Working out a set of technical and energy states of ship main engine crankshaft and piston systems which are essential for ship safety (in Polish). Report on completion of the own research project performed within the framework of the research project of the Ministry of Science and Information Technology (no. N N509 494638) entitled: “Decision making based control of the process of operation of crankshaft and piston systems in main propulsion engines of sea-going vessels with the aid of technical diagnostics and taking into account safety and environment protection”. Project manager: Prof. Jerzy Girtler, D.Sc. *Prace badawcze nr 2/10/PB. WOiO PG, Gdańsk*, 2010
28. Girtler J., Łosiewicz Z.: Mathematical models of the process of operation of power devices and systems, and verification of these models in the aspect of their applicability in the operating decision making process (in Polish). Report on completion of the own research project performed within the framework of the research project of the Ministry of Science and Information Technology (no. N N509 494638) entitled: “Decision making based control of the process of operation of crankshaft and piston systems in main propulsion engines of sea-going vessels with the aid of technical diagnostics and taking into account safety and environment protection”. Project manager: Prof. Jerzy Girtler, D.Sc. *Prace badawcze nr 3/10/PB. WOiO PG, Gdańsk*, 2010.

29. Joel Donnet News Worlds' Heaviest Ship propeller, built in the Netherlands. Joel Donnet News No 26, Sidebar 1996
30. Joel Donnet News, New World Record for a propeller at Lip's. Joel Donnet News No 58, Sidebar 1997
31. Propulsion Trends in Container Vessels. MAN B&W Diesel A/S, Copenhagen 2001
32. RTA Type Engines, Characteristics of Cylinder Liner and Piston Ring Wear. Service Information Bulletin No DUQ1-02E, Diesel United Sulzer, 1991
33. RTA-C. Technology review. Wartsila NSD Corporation Ltd, Helsinki 2004
34. Service Experience 2007, MAN B&W Engines The ME/ME-C and MC/MC-C Series. MAN B&W Diesel AS, Copenhagen 2007
35. Sulzer RT-flex 60C, Wartsila Corporation, Helsinki 2004
36. Transportation Safety Board of Canada. Marine Investigation Report M00L0034, Main Engine fires, 2001
37. Warsash Maritime Centre. The Learning Resource for Maine Engineers, Southampton Solent University, Southampton 2005

#### **CONTACT WITH THE AUTHOR**

Jerzy Girtler

Gdańsk University of Technology  
11/12 Narutowicza St.  
80 - 233 Gdańsk  
**POLAND**

## ANALYSING APPLICABILITY OF SELECTED METHODS TO SMOOTH INDICATOR DIAGRAMS OF MARINE MEDIUM-SPEED ENGINE

Rafał Pawletko, Ph. D.

Gdynia Maritime University, Poland

### ABSTRACT

*The article analyses the applicability of selected smoothing methods to smooth indicator diagram curves and to filter disturbances. An intermediate goal of the study was an attempt to extract disturbances recorded during pressure curve smoothing, which are believed to be a source of important diagnostic information.*

*Within the framework of the reported analysis, a comparison was made between the moving average method, the Savitzky-Golay filter, and the frequency filtration method. The research was performed on a marine medium-speed engine Sulzer 3A1 25/30, which has a relatively long indicator passage.*

**Keywords:** indicator diagrams, smoothing waveforms, filtering disturbances

### Introduction

Measuring the pressure inside the cylinders of marine piston engines is an important issue when analysing both the combustion course, and the technical state of the engine. A basic area in which the information concerning the cylinder pressure is used refers to the assessment of heat emission characteristics based on the first law of thermodynamics [4, 6, 7]. These characteristics can then make a basis for: verifying the prepared combustion process simulation models, developing new concepts of combustion systems, analysing the behaviour of alternative fuels and fuel injection systems, etc.

Reliable information on the combustion process can be used for on-line control of engine operation. Controlling the course of combustion may also result in limiting the emission of toxic fuel components. For instance, contemporary electronically controlled marine engines can operate in a so called Low NOX mode (economical mode with limited emission of toxic compounds).

A condition to obtain reliable heat emission characteristics is the smooth and disturbance-free pressure curve. Meeting this condition in practice is extremely difficult. A number of important factors concerning cylinder pressure measurements can be named which remarkably deform the recorded pressure time-histories:

- the pressure sensor is situated on the indicator valve and not directly inside the combustion chamber;
- the indicator valve is connected with the combustion chamber through the indicator passage, the length and volume of which can be relatively large, depending on the engine structure;
- pressure measurements making use of the indicator passage lead to phase and amplitude disturbances of the recorded signal, and introduce oscillating disturbances generated by vibrations of the gas column inside the passage;
- measurements performed in changing pressure and high temperature conditions place very high demands on the used sensors in terms of their accuracy and reliability;
- the used measuring systems are susceptible to electric disturbances generated both by engine subsystems, and other engine power plant units which emit the electromagnetic field.

A reliable and disturbance-free pressure curve makes a basis for further analysed of the combustion process. Despite remarkable development in production of pressure sensors and measuring systems, a problem which still needs solving concerns postprocessing of the already recorded time-histories. An obligatory procedure in this situation is averaging pressure curves recorded in a number of measuring cycles.

Depending on the adopted system, this averaging can include from ten to several tens of realisations. In most cases, however, averaging is not sufficient, especially in analyses of heat emission characteristics, and complementary numerical data filtering or smoothing turns out necessary.

The article analyses the applicability of selected smoothing methods to smooth the indicator diagram curves, with an intermediate attempt to extract the disturbances recorded during pressure curve smoothing. These disturbances are believed to be a source of important diagnostic information.

### **Types and sources of disturbances in indicator diagram measurements**

Disturbances affecting the waveform of the indicator diagram curve can be divided into two basic groups. The first group refers to the nature of pressure measurements in marine engine cylinders, in particular to the presence of the indicator passage. The second group includes disturbances of electrical origin, generated by engine systems and auxiliary devices, and recorded by the measuring lines. The latter type of disturbances gains in importance in the marine power plant environment [5].

Pressure sensors are mounted on the indicator valve, and not directly inside the engine cylinder. Depending on the engine structure, the length of the indicator passage linking the indicator valve with the combustion chamber can reach one meter. Such a passage, of a relatively large length and small diameter, is a possible source of both absolute pressure estimation errors, and phase errors resulting from the fact that the pressure wave covers the distance between the combustion chamber and the measuring sensor. According to [3], the geometry of the indicator passage and the rotational speed of the engine affect remarkably the waveform of the indicator curve. The maximal pressure estimation error increases with the increasing length of the indicator passage and with the increasing rotational speed of the engine, and decreases with the increasing diameter of the indicator passage. No effect of the engine load on the pressure estimation error has been detected [3].

The examination reported in [2] has revealed strong relation between the diameter of the indicator passage and that of the sensor. It was demonstrated that when these two diameters are close to each other, this may enable to eliminate resonance frequencies and record a curve which is free of oscillating disturbances.

The effect of the passage which connects the combustion chamber with the indicator sensor on the waveform of the measured curves has also been confirmed in [2]. There, a proposal was made to modify the structure of the indicator passage and to install an additional indicator sensor adapter to eliminate resonance vibrations.

The problem of disturbances introduced by indicator passages is of high importance, which has been confirmed by results of other analyses in this area. However, despite high theoretical potential for introducing structural modifications to the indicator passage in order to minimise the measuring errors, especially in the resonance frequency ranges, this

approach is unlikely to be widely used in practice. An alternative for structural modifications is an attempt to smooth the recorded curves and/or to filter the disturbances during data postprocessing [2].

### **Data smoothing methods used in indicator diagram postprocessing**

A basic method of indicator diagram smoothing, which is in a wide use nowadays, is averaging a number of curves recorded in stationary conditions. This averaging, which can include from ten to several tens of realisations, enables to eliminate, first of all, random disturbances recorded in single realisations.

The most popular method to smooth the measured data is the moving average method, which consists in replacing each value in the data set by the value averaged over the interval of a given width. This procedure is equivalent to a low-passing filter with the response given by the following equation:

$$y_s(i) = \frac{1}{2N+1} (y(i+N) + y(i+N-1) + \dots + y(i-N))$$

where:

$y_s(i)$  – smoothed value at  $i$ -th point,

$N$  – number of points taking part in averaging on each side of the central point  $y_s(i)$ ,

$2N+1$  – width of the moving interval of averaging.

A generalisation of the method making use of the moving average is the Savitzky-Golay filter [8]. Filter coefficients are calculated by approximating the real curve with a polynomial of a given order, using the least-squares method. Like for the moving average method, the approximation is conducted within the moving interval of a given width, and that is why the Savitzky-Golay filter bears the name of the moving polynomial approximation. The use of a polynomial of a sufficiently high order enables to obtain high smoothing efficiency without losing essential information carried by the original signal. The Savitzky-Golay filter is very efficient in terms of preservation of high-frequency signal components, but can be less efficient, as compared to the moving average method, in eliminating random noise.

While the moving approximation can be considered natural extension of the moving average concept, the use of multiple moving approximation to process the measured data should be considered an achievement of utmost importance. The moving approximation consist in calculating the approximated value at one point within the approximation interval. This interval moves along the measuring axis, or is on-line created when new measuring data are delivered to the analysing systems. The data set which is used as an approximation basis for a subsequent step (passing), contains the results of approximation from the previous approximation step. In each step, new sets of coefficients are calculated for the approximating formula.

Disturbances can also be filtered out from the indicator diagrams using directly numerical filters. Taking into account

the nature of these disturbances, of highest applicability in this situation will be the low-pass filters with limited impulse response due to the linear nature of the phase shift [1].

### Research rig

The experiment was performed on the research rig the main element of which was the marine four-stroke engine Sulzer 3A125/30. Basic technical specifications of the engine are the following:

- product designation – 3 A1 25/30
- number of cylinders – 3
- cylinder diameter [mm] – 250
- piston stroke [mm] – 300
- piston displacement [cm<sup>3</sup>] – 14726
- nominal power [kW] – 408
- rotational speed [rpm] – 750
- compression ratio – 13

A1 25/30 type engines are used as main propulsion on small ships and for driving electric current generators in ship power plants.

Indication was done using the electronic indicator Unitest 201, the angular resolution of which is 0,5° OWK. The measurements were performed using 6353A24 sensors made by Kistler. All measurements were done for the engine rotational speed of 750 rpm.

The gas passage connecting the indicator with the combustion chamber in this engine is relatively long and has a complicated shape (Fig. 1).

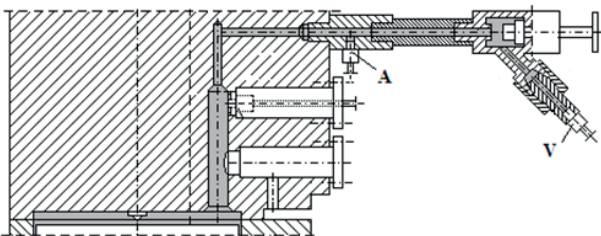


Fig. 1. Gas passage and indicator valve structure, with the distribution of combustion pressure sensors within the cylinder space of the examined engine A25: A – pressure sensor and measuring point with 7523A10 adapter made by Kistler, V – indicator valve

### Smoothing indicator diagrams of the laboratory engine A1 25/30

The indicator diagram of the engine A1 25/30 is a pressure curve with disturbances of various nature. A1 25/30 is a medium-speed engine with a relatively long and complicated indicator passage. A sample indicator curve for this engine is shown in Fig. 2. The curve was obtained as an average of 16 realisations.

#### Curve smoothing using the moving average method

The here reported research started with an attempt to smooth the indicator pressure curve using the moving

average method. First, single smoothing was applied with the moving interval consisting of  $k = 20$  points. The original and smoothed waveforms are shown in Fig. 3, while their derivatives are presented in Fig. 4.

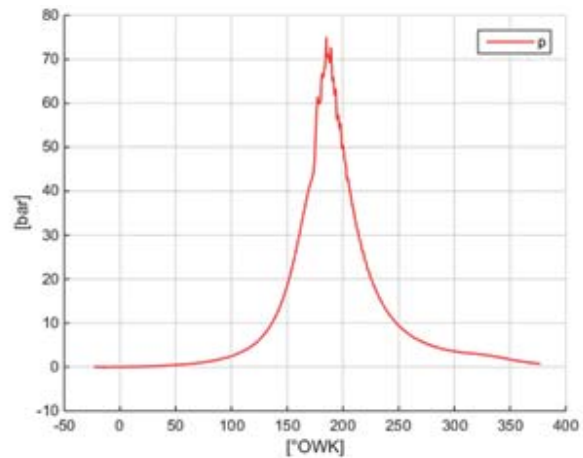


Fig. 2. Indicator diagram of the engine A1 25/30

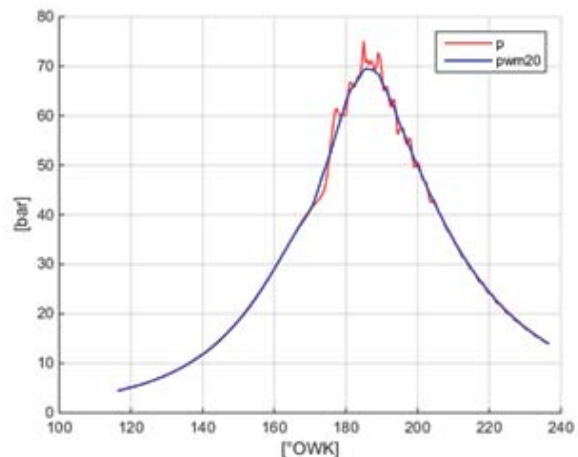


Fig. 3. Indicator curve smoothed using the moving average method with the moving interval consisting of  $k = 20$  points (pwm20), as compared to the original curve (p)

Despite the use of the moving interval consisting of 20 points, the obtained waveform of the derivative  $dpwm20$  is not sufficiently smooth. An additional limitation of the moving average method is that it introduces some phase error, which can be observed on the smoothed derivative, when compared to that of the unsmoothed pressure curve. The theoretical start of the combustion is at about 172° OWK, while the angle value determined from the smoothed derivative is situated at about 169° OWK. The phase error in this case is approximately equal to 4° OWK. Increasing the number of points composing the averaging interval (interval width) above 20 does not lead to the improvement of smoothing quality, and at the same time introduces further phase and amplitude errors.

Better results of smoothing can be obtained using so-called multiple smoothing, proposed in [5]. The method consists in

repeatable application of the smoothing procedure, with the same or similar parameters, to the already smoothed curve. This approach makes it possible to use a narrower smoothing interval. Figure 5 shows the results of smoothing after one (pwm1) and four successive repetitions of the smoothing procedure (pwm4). In each time the smoothing interval consisted of  $k=5$  points.

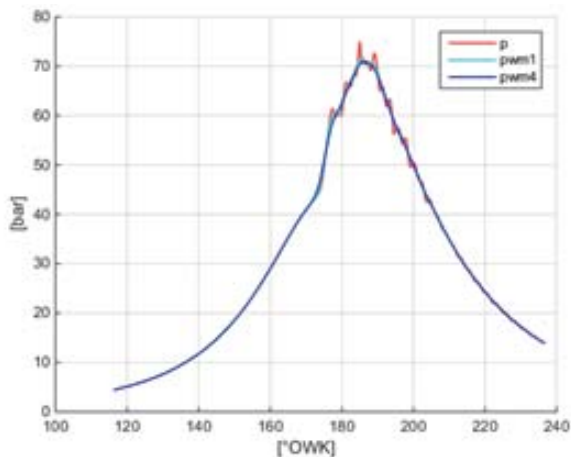


Fig. 5. Indicator curve smoothed using the moving average method with the moving interval consisting of 5 points, after single smoothing (pwm1) and four repetitions of smoothing (pwm4)

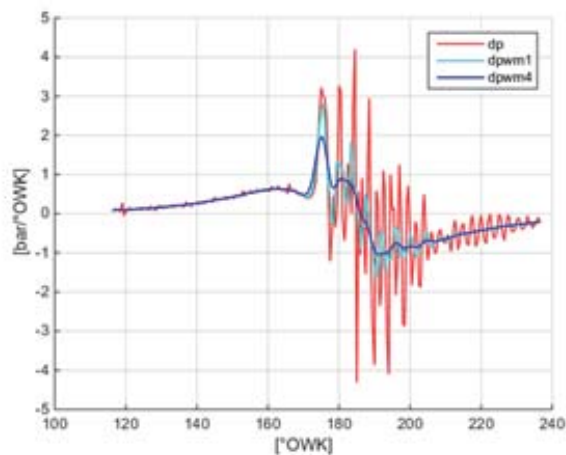


Fig. 6. Derivatives of the original curve (dp) and the smoothed curves (dpwm1) and (dpwm4)

Four repetitions of the smoothing procedure enabled to filter effectively the disturbances, see Fig. 6, without introducing visible deformations and phase errors. The smoothed waveform is close to the original one, especially in the vicinity of the beginning of the combustion when the pressure increases dramatically. Multiple smoothing enabled to obtain the derivative waveform which is acceptable in terms of disturbances and free of significant phase and amplitude errors.

### Curve smoothing using the Savitzky-Golay filter

The results of fourfold smoothing with the aid of the moving average method (pwm4) were compared with those obtained using the Savitzky-Golay filter (pwg4). In the latter case, use was made of the 3rd order polynomial, and the width of the interval was equal to 12 points. The smoothing was repeated four times. The waveforms obtained using these two methods are compared, along with the corresponding derivatives, in Figs. 7 and 8.

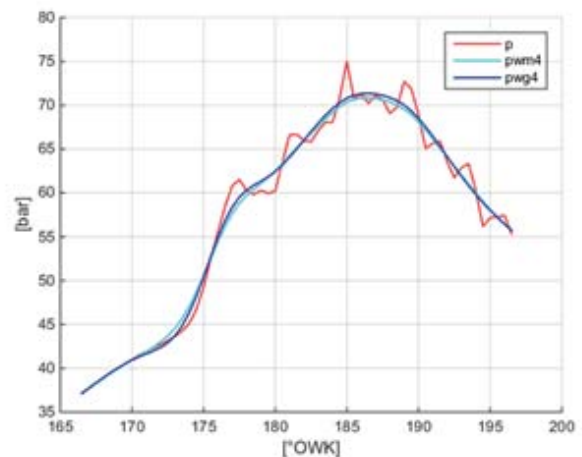


Fig. 7. Indicator curve smoothed using the moving average method with the interval consisting of  $k=5$  points (pwm4), and the Savitzky-Golay filter with the interval consisting of  $k=12$  points (pwg4). In both cases smoothing was repeated four times.

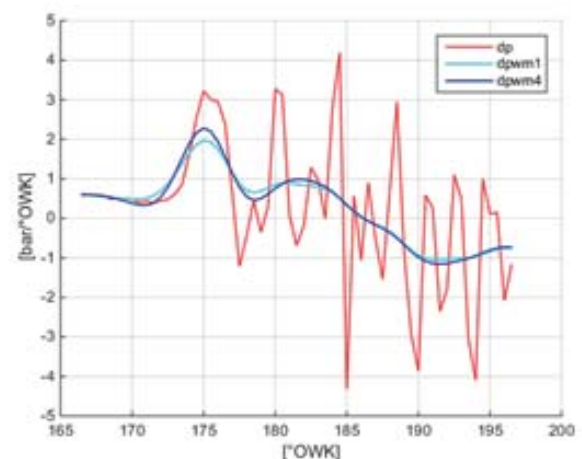


Fig. 8. Derivatives  $dpwm4$  and  $dpwg4$  of smoothed curves  $pwm4$  and  $pwg4$

Fourfold applications of the smoothing procedures based on the above two methods have returned similar results. Better robustness of the Savitzky-Golay filter can be observed in the areas of rapid curve changes, for instance at the beginning of the combustion. The curve smoothed using the filter is

closer to the original shape, and introduces smaller phase and amplitude errors. This effect is especially noticeable on the waveforms of the calculated derivatives.

### Curve smoothing using the dedicated low-pass filter

Analyses of indicator diagram postprocessing frequently indicate low efficiency of filtering based on the moving average methods [1], in particular in the frequency domain. As a consequence, an attempt was made to use a low-pass filter for smoothing purposes. Since the overwhelming majority of disturbances is situated in the upper part of the frequency range, the use of this filter is expected to effectively eliminate disturbances without losing important data within the frequency range of interest.

An essential issue in designing the low-pass filter is selecting the cut-off frequency. Its value depends on the nature of the observed disturbances and the engine rotational speed. The cut-off frequency should be selected individually for a given engine, which is a considerable limitation of the method.

In the here reported case, before selecting the cut-off frequency the power spectral density was prepared for the examined indicator curve to evaluate signal energy distribution in particular frequency bands. The power spectral density of this curve is shown in Fig. 9.

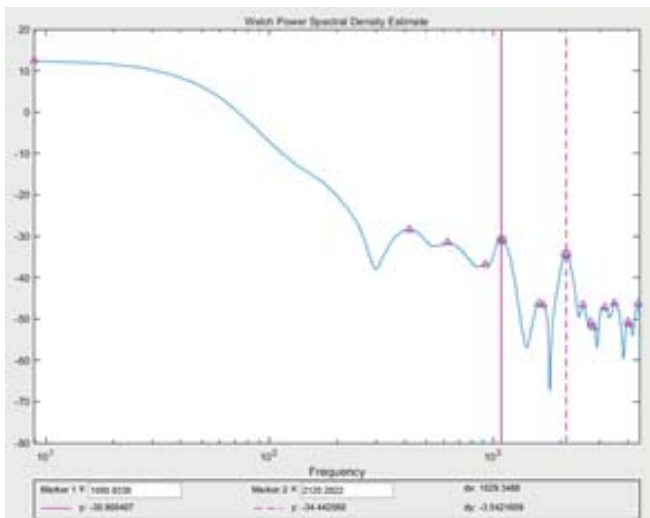


Fig. 9. Power spectral density of the pressure signal

The power spectral density curve reveals a decreasing trend for the increasing frequency, the local minimum of which is situated close to 1,8 kHz. Moreover, two local maxima can be observed at frequencies approximately equal to 1,1k Hz and 2,1 kHz. Their presence may be connected with the disturbances introduced by the indicator passage.

Based on the signal spectrum curve a decision was made to assume the cut-off frequency for the designed filter at the level of 1 kHz. The designed filter is the 20th order low-pass filter with limited impulse response and Kaiser window. The effects of the use of this filter are shown in Figs. 10 and 11.

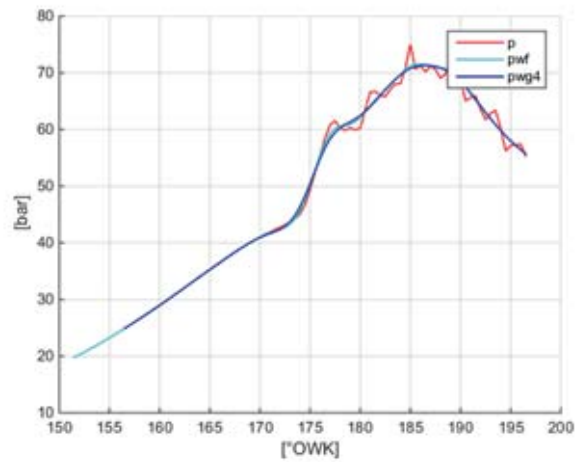


Fig. 10. Indicator curve smoothed using the low-pass filter with cut-off frequency of 1 kHz (pwf), as compared to the curve smoothed using the Savitzky-Golay filter (pwg4)

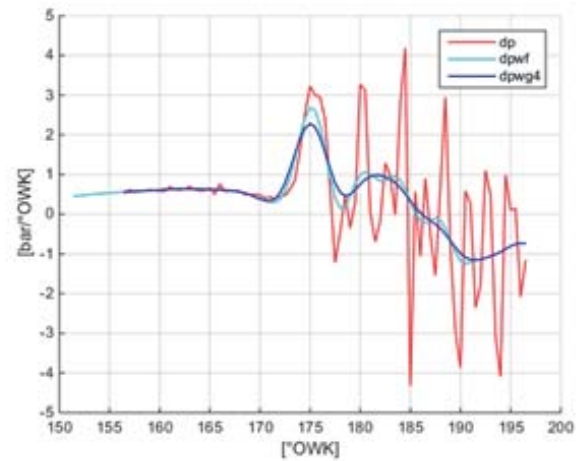


Fig. 11. Derivatives dpwf and dpwg4 of the smoothed curves pwf and pwg4

The use of the low-pass filter with the cut-off frequency of 1 kHz enabled to obtain a curve which is very similar to that smoothed by multiple application of the Savitzky-Golay filter. However, its derivative, dpwf in Fig. 11, reveals a number of small waves. Decreasing the cut-off frequency to 800 Hz has made it possible to eliminate these waves and to obtain the analogous curve to that representing the Savitzky-Golay filter, see Fig. 12.

### Analysing disturbances of laboratory engine A1 25/30 indicator diagrams

For each successive smoothing step, the smoothing deviation (disturbance) can be calculated as:

$$dif_{l-1;l} = dif_{l-1} - dif_l$$

where:

$dif_{l-1;l}$  – disturbance extracted for the given smoothing

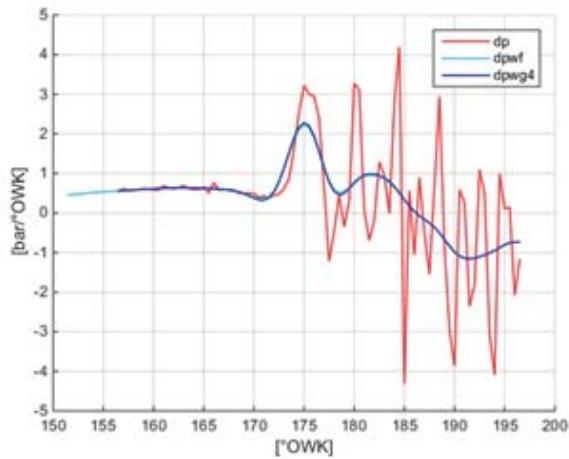


Fig. 12. Derivatives of curves smoothed using the low-pass filter with cut-off frequency of 800 Hz (*dpf*) and the Savitzky-Golay filter (*dpg4*)

Figure 13 shows a set of disturbances {dif1,dif2,dif3,dif4} extracted in four successive steps of *p* curve smoothing, performed with the aid of the Savitzky-Golay filter. The applied filter made use of the 3rd order polynomial and the interval consisting of *k*=12 points.

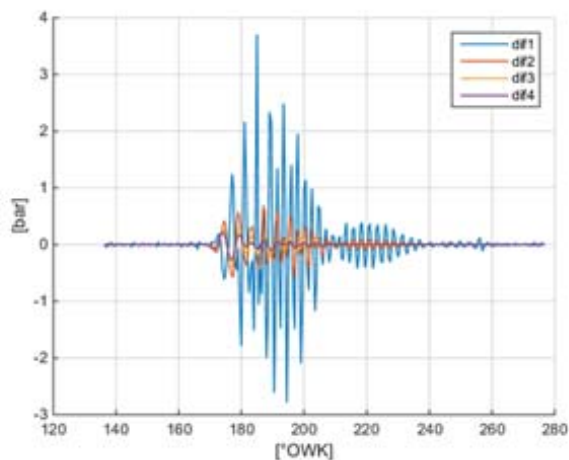


Fig. 13. Disturbances extracted in four successive steps of *p* curve approximation making use of the 3rd order polynomial with *K*=12 (Fig. 1). Angle interval from 180 to 240° OWK

Bearing in mind processes which generate the curve *p* being the object of smoothing, it can be easily noticed that the extracted disturbances (Fig. 13) are mainly caused by gas oscillations initiated in the short measuring passage behind the combustion chamber by rapid start of the combustion process.

Figure 14 shows similar disturbance curves extracted for the angle interval between 70 and 140° OWK, i.e. before the start of the combustion process.

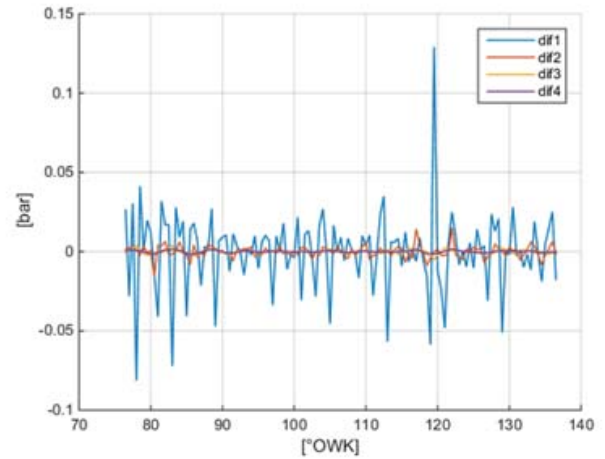


Fig. 14. Disturbances extracted in four successive steps of *p* curve approximation making use of the 3rd order polynomial with *z K*=16 (Fig.1). Angle interval from 80 to 140° OWK

The amplitude of the disturbances extracted before the start of the combustion process is lower by one order of magnitude, but their frequencies in both intervals are similar. Figures 15 and 16 show the disturbance signal frequency spectra for these two angle intervals.

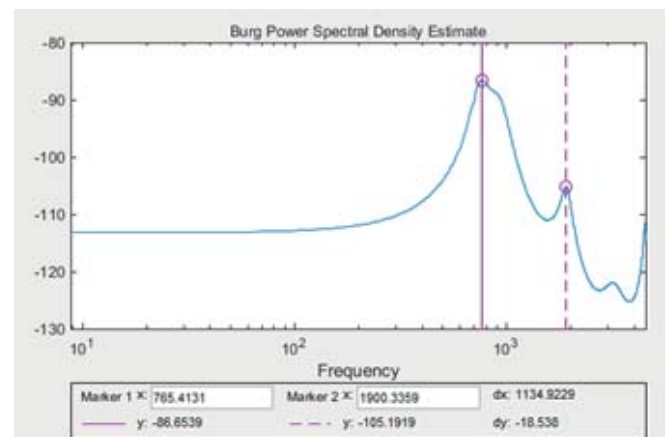


Fig. 15. Amplitude spectrum of disturbances extracted after step 1 of smoothing. Angle interval from 80 to 140° OWK.

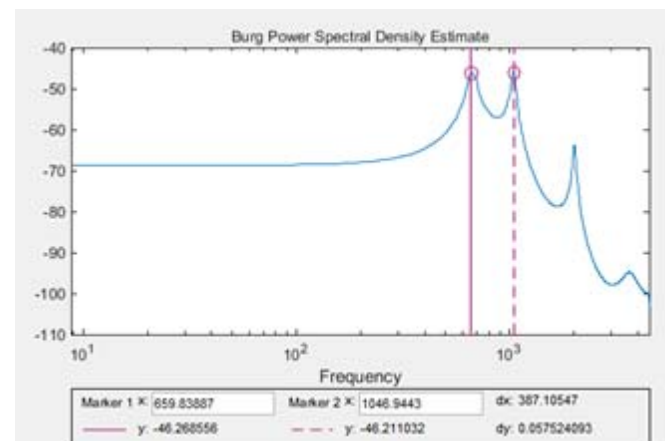


Fig. 16. Amplitude spectrum of disturbances extracted after step 1 of smoothing. Angle interval from 180 to 240° OWK

The dominating frequency in the disturbance spectrum recorded before the start of the combustion process, the interval between 80° and 140° OWK (Fig. 15), is 765 Hz. Another local maximum which can be observed in this curve is situated at 1900 Hz. In case of the spectrum recorded after the beginning of the combustion process, two clear maxima can be observed for the frequencies of 659 Hz and 1046 Hz, accompanied by a lower local maximum at 2014 Hz.

### Conclusions

The examined smoothing methods applied to indicator diagrams of the medium-speed marine engine have made it possible to effectively filter out disturbances. However, the moving average method and the Savitzky-Golay filter need multiple smoothing with a relatively narrow moving interval to get satisfactory results. Single smoothing making use of a wide interval removes part of essential information from the original pressure curve.

The Savitzky-Golay filter was recognised as a better tool than the moving average method for smoothing rapid changes of the pressure curve, for instance the curve section corresponding to the beginning of the combustion process. The moving average method also introduces larger phase and amplitude errors.

High efficiency of curve filtering in the frequency domain has also been confirmed. The use of the low-pass filter with properly selected parameters enabled to obtain identical results as for the Savitzky-Golay filter.

Analysing the disturbances extracted from the indicator diagrams indicates that they are mainly caused by gas oscillations initiated in the short measuring passage behind the combustion chamber by rapid start of the combustion process.

### Bibliography

1. Dey K., Characterization and rejection of noise from in-cylinder pressure traces in a diesel engine, Electronic Theses and Dissertations, Paper 121, 2012
2. Fujio N., Makato I., Errors of an Indicator due to a Connecting Passage, JSME 621.43.018.86
3. Hountalas D. T., Anestis A., Effect of Pressure Transducer Position on Measured Cylinder Pressure Diagram of High Speed Diesel Engines. Energy Convers, Mgmt Vol. 39, No. 7, pp 589-607, 1998
4. Pawletko, R., Polanowski, S, Influence of fuel injection system faults of marine diesel engine on the heat release characteristics, Combustion Engines, 154(3), 2013
5. Polanowski, S, Application of movable approximation and wavelet decomposition to smoothing-out procedure of ship engine indicator diagrams, Polish Maritime Research 2(52) Vol 14, pp. 12-17, 2007

6. Polanowski, S, Assessing diagnostic applicability of heat release characteristics determined based on ship engine indicator diagrams, Polish Maritime Research 3(61) Vol 16; pp. 32-35, 2009
7. Rychter, T., Teodorczyk, A., Mathematical modelling of piston engine operation cycle (in Polish), PWN, Warsaw 1990
8. Savitzky, A., Golay, M. J., Smoothing and differentiation of data by simplified least squares procedures, Analytical chemistry 36.8, 1964
9. Wlocardyk M.T., High accuracy glow-plug integrated cylinder pressure sensor for closed loop engine control, SAE Paper 2006-01-0184, 2006

### CONTACT WITH AUTHOR

Rafał Pawletko

Gdynia Maritime University,  
81-87 Morska St.  
81-225 Gdynia  
POLAND

# CLOCKING IN TURBINES: REMARKS ON PHYSICAL NATURE AND GEOMETRIC REQUIREMENTS

Jerzy Swirydczuk, Assoc. Prof.  
Institute of Fluid-Flow Machinery  
Polish Academy of Science, Poland

## ABSTRACT

*The article discusses two issues relating to the clocking phenomenon in turbines, which are the physical course of stator wake deformation in rotor passages and its further interaction with downstream stator blades, and turbine geometry parameters which are believed to be most favourable for clocking. In both cases, the results presented in the article have made it possible to verify and reformulate the previously accepted opinions.*

**Keywords:** turbines, clocking, wakes, vortices, blade counts

## Introduction

Clocking, also sometimes referred to as indexing, consists in changing the circumferential position of one stator (or rotor) row by rotating it with respect to the other stator (rotor) in a multistage fluid-flow machine. Provided that certain geometric conditions are met, it can be realised in all types of fluid-flow machines, including those used in marine industry. A basic motivation for investigating and applying clocking in turbines was an attempt to control the wake interaction in the clocked rows and this way to improve turbine performance. Flow effects generated by clocking were the object of examination of numerous researchers. Huber et al. investigated them experimentally on a two-stage turbine with blade counts in consecutive rows equal to 54:50:54:50 [1]. Their experiments revealed that about 0.8 % of efficiency gain can be obtained due to clocking. For the same turbine, a numerical analysis for the two-dimensional midspan geometry was performed by Griffin et al. [2], who correctly predicted the clocking position corresponding to the maximal efficiency, although the predicted efficiency gain was only equal to 0.5 %, i.e. remarkably less than that obtained in the experiment. Clocking effects in a 1-1/2 stage turbine have been numerically simulated by Eulitz et al. [3] and Dorney and Sharma [4] who concluded that larger unsteady pressure amplitudes on the blades correspond to higher-efficiency configurations. This conclusion was later confirmed by Cizmas and Dorney [5], although an opposite trend was also reported by Griffin [2] and Dorney et al. [6]. Reinmoller et al. [7]

studied experimentally and numerically clocking related phenomena in a 1.5 stage axial turbine. Relative efficiency changes in their experiment amounted to 1.0 %, against 0.7 % in the corresponding calculations.

The effect of airfoil clocking on a six-row turbine has been also investigated by Cizmas and Dorney [8]. A comprehensive analysis of the clocking phenomenon presented in that paper included rotor clocking, clocking of multiple rows, and the concept of full turbine clocking, including all rotor and stator rows. For the examined turbine the second-stage clocking produced larger efficiency gains than the third-stage clocking, which was true for both rotor and stator. The results presented in the article also revealed that rotor clocking can be a source of efficiency gains being twice as large as those produced by stator clocking.

Li Wei et al examined numerically clocking effects in a 1.5 stage axial low-pressure turbine in which the blade count ratio in the clocked stators was  $n_{s1} : n_{s2} = 84 : 126 = 2:3$ , obtaining only 0.1 % efficiency gain [9].

The present article discusses two opinions on clocking, which have been formulated based on the knowledge gained in experimental investigations and numerical studies of the phenomenon. The first of them refers to the physical nature of wake/blade interactions in the clocked rows and says that the greatest benefits of clocking are achieved when the wake of the upstream stator impinges on the downstream stator leading edge, while an efficiency drop is observed when the wake is convected through the middle of the downstream stator passage [2, 3, 4, 7]. The second opinion refers to

geometric requirements for the clocked rows and says that larger efficiency benefits can be obtained when the blade count ratio of the clocked rows is close to one, and when it is far from unity the clocking brings practically no effect. This opinion can be found in articles by Arnone et al. [10-12]. Also other authors apply a procedure which scales the geometry of the examined turbine stages with slightly differing blade counts to obtain the blade count ratio exactly equal to one [6,8].

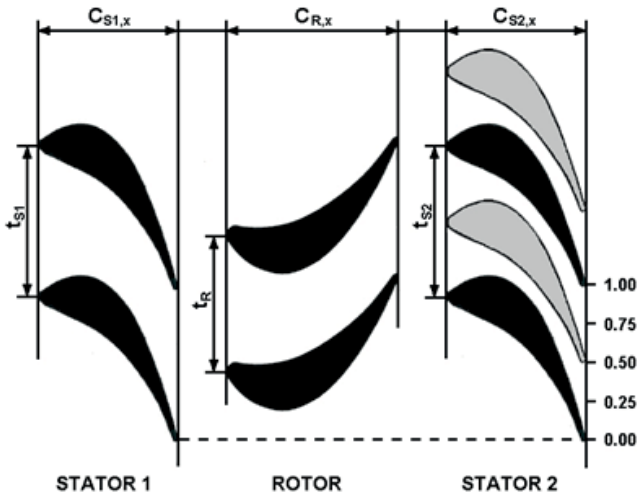


Fig. 1. Stator clocking

### Wake deformation and physical nature of clocking

As mentioned in the Introduction, clocking in a multistage fluid-flow machine consists in rotating one stator/rotor row with respect to the other. Fig. 1 explains technical realisation of stator clocking in a turbine by presenting two clocking positions of the second stator. Numbers on the right represent the values of a parameter assumed as the measure of clocking which expresses the ratio of the current rotation angle  $\alpha$  to its full clocking range  $\alpha_{clock}$ , which in classical clocked rows with the same blade counts:  $n_{S1} = n_{S2}$ , is equivalent to the rotation by the angle  $\alpha_i$  corresponding to one blade pitch. The basic configuration, labelled by the clocking parameter assumed as 0.0, is where the trailing (or leading) edges of the clocked stators  $S_1$  and  $S_2$  are situated along the same line parallel to the turbine axis, the dashed line in Fig. 1. The second position (gray profiles) is obtained by rotating circumferentially stator  $S_2$  by an angle  $0.5\alpha$  at corresponding to half of the stator pitch.

All clocking effects generated in stator  $S_2$  are believed to be the result of its interaction with the wakes shed from the trailing edges of blades composing the  $S_1$  cascade, therefore the starting point for the present analysis of the physical nature of clocking will be the analysis of deformation experienced by  $S_1$  wakes on their way through rotor R passages. Throughout the history, this process was modelled and interpreted in various ways depending on current knowledge on the inner structure and behaviour of stator wakes. In one of first wake models, proposed by Meyer [13], the wake was simply represented by a so-called "negative jet", being a regular area of velocity disturbances in

the otherwise uniform flow. The stator wakes, convected with the main flow, were chopped into smaller parts by downstream rotor blades, modelled as straight line segments. While flowing through the rotor, the wake segments preserved their initial shapes and behaved as negative jets generating secondary velocity field which transported the fluid from the pressure side to the suction side of the rotor passage.

Then, attempts were made to include the ability of the wake to deform on its way through the rotor passage. Smith [14] observed that the circulation around the rotor blade makes the opposite ends of the wake segment move with different velocities. As a consequence, the segment is stretched and sheared in the rotor passage, and when the wake leaves the rotor it forms a saw-like shape rather than preserves the initial continuous structure. The first attempt to capture wake deformation was made by Lienhart [15] who modelled the wake using the potential flow with a sequence of isolated vortices generated in the vicinity of blade trailing edges. Once generated, the vortices moved with the local flow velocity through the rotor, thus contributing to unsteady flow effects inside the rotor passages. Successive wake deformation stages were numerically simulated, and unsteady fluctuations of potential forces generated in each row were calculated. This model was modified by Krammer [16] who extended the vortex model of the wake by adding two contra-rotating rows of vortices along the wake axis to simulate the velocity defect. Thus this wake model, consisting of two types of vortices, was able to combine potential and viscous effects. He presented the course of wake deformation individually for viscous and potential parts, and calculated their impact on unsteady forces generated on the rotor. It is noteworthy that despite a discrete representation, the wakes in those papers were still treated in a classical manner, as continuous bands of fluid in otherwise inviscid and incompressible flow, with the velocity deficit changing uniformly along the wake axis.

Much more accurate modelling of the stator wake and its interaction with the rotor cascade was possible thanks to the development of specialised 3D codes to solve Reynolds Averaged Navier-Stokes (RANS) equations for turbulent, compressible, and viscous flows in fluid-flow machines. In those codes the stator wakes were obtained as part of the solution and their characteristics did not have to be assumed a priori. Experimental verification of the obtained results was, as a rule, good.

Early RANS calculations made use of relatively coarse grids and produced wakes which had the form of regular bands of higher entropy, without visible traces of inner structure. Estimating clocking gains from these calculations has led to a commonly accepted conclusion, mentioned in the Introduction, that the best clocking configuration is when the  $S_1$  wake impinges on the leading edges of  $S_2$  blades while passing of the wakes through the middle of the  $S_2$  passages results in efficiency drop. Fig. 2 illustrates these two most and least favourable cases by presenting instantaneous patterns of unsteady entropy distributions in the passages of the both clocked stators and the rotor moving between them. Different stator/rotor blade count ratio provides an opportunity to observe consecutive stages of the  $S_1$  wake motion through the  $S_2$  cascade.

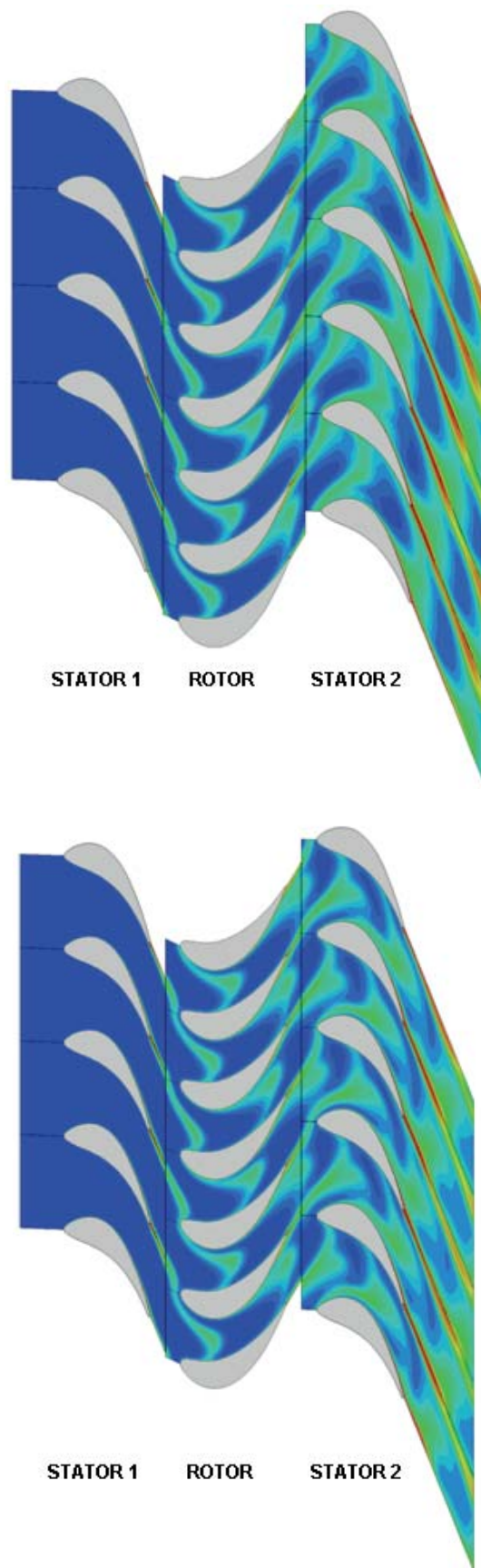


Fig. 2. Stator clocking configurations: advantageous (up) and disadvantageous (down)

More recent experiments oriented on taking more detailed insight into the inner structure of stator wakes revealed characteristic frequencies in the flow signals recorded in the wake, which testified to the presence of regular minor structures in the wake area [17, 18]. Also numerical computations performed for isolated stators at sufficiently fine grids and time steps allowed to produce wake patterns revealing two rows of well developed vortices having the structure similar to that of the von Karman vortex street, [19-22].

Some initial attempts to take into account vortex dynamics when analysing the stator wake motion through the rotor cascade have been published. A most detailed study was done by Kost et al. [23], Tiedemann and Kost [24] and Hummel [25], who examined experimentally and numerically unsteady flow fields generated by stator wakes in rotor passages of a full size aero-engine high-pressure turbine stage having 43 stator blades and 64 rotor blades. Visual studies of the flow inside the rotor passages performed by Kost et al. with the aid of coolant injected to the flow at the vicinity of stator blade trailing edges have revealed that on its way through the rotor passage the stator wake forms two separate areas of different-sign vorticity which move one after the other through the passage, thus creating the earlier mentioned negative jet between the blade walls, clearly observed on the numerically calculated distributions of velocity vectors.

In their experimental study, Tiedemann and Kost focused on final effects of the deformation of stator wakes in the rotor passage and their further interaction with the rotor wakes. They recorded velocity and pressure fluctuations at the rotor passage exit for different positions of stator clocking with respect to the positions of the measuring sensors. Based on the obtained results they concluded that the impingement of the S1 wake on the leading edge of a hypothetical stator S2 would decrease the fluctuations, which may affect the development of the stator's boundary layer and the resultant losses. They also observed considerable reduction in flow incidence angle variations caused by the passing stator wakes which, according to their opinion, would also contribute to the benefits of clocking.

The stator/rotor wake interaction in the same turbine has been examined numerically by Hummel. In his calculations the structure of the stator wake observed downstream of the rotor also revealed two well separated areas of positive and negative vorticity which behaved in the same way as that experimentally observed by Kost et al. One of conclusions from his study was that stator vortices, when interacting with the rotor wakes on its both side, increase the strength of rotor vortices when the velocity vectors generated by the stator vortex and the rotor vortex coincide with each other in the area between them, and decreases when these vectors are opposite to each other.

The process of stator wake deformation in rotor passages was also studied by Swirydczuk [26,27] who used for this purpose a model of potential flow with vortex singularities representing stator and rotor wakes. Figure 3 shows an instantaneous pattern of stator and rotor wake vortices. The form of the stator wake in front of the rotor, before

deformation, is shown on the left. The wake consists of a segment of the von Karman vortex street the main axis of which is parallel to the direction of the flow velocity  $c_1$  in the stator reference frame. The wake vortices with positive (counterclockwise) rotation are marked green, while those of negative (clockwise) rotation – red. Moreover, small black dots which can be observed close to the vortices indicate positions which they would occupy when solely convected with the main flow, without vortex interactions with each other and flow boundaries. Large black circles on the right represent the rotor vortices. The stator wake approaches the rotor cascade flowing from the direction defined by the flow velocity  $w_1$  in the rotor reference frame. When inside the rotor passage, it deforms in such a way that two groups of vortices of positive and negative rotation sign,  $+\Gamma_{S1}$  and  $-\Gamma_{S1}$  respectively, can be clearly seen.

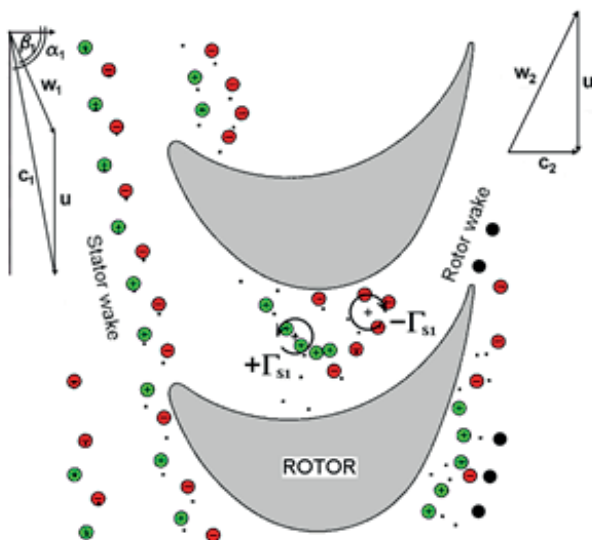


Fig. 3. Stator wake deformation inside rotor passage

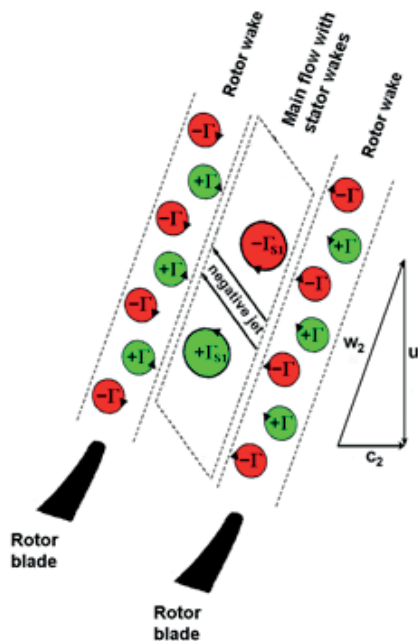


Fig. 5. Scheme of wake structure downstream of rotor R cascade

Further behaviour of the stator and rotor wakes can be observed in Fig. 4 being a compilation of the results presented in [23-27]. All wakes leave the rotor moving, generally, in the direction of the main flow velocity  $w_2$ . In this reference frame the stator vortices move one after another. However, in the reference frame connected with the  $S_2$  cascade their motion is controlled by the flow velocity component  $c_2$  which is, as a rule, almost parallel to the turbine axis. As a consequence, in this reference frame the  $S_1$  vortices move side by side like a vortex pair in the main  $c_2$  direction only slightly modified by their mutual interaction. In this context, the descriptions of the  $S_1$  wake motion which were mentioned at the beginning and which say that “the wake of the upstream stator impinges on the downstream stator leading edge”, or “is convected through the middle of the downstream stator passage” seem to be rather imprecise, as configurations can be imagined in which one  $S_1$  vortex impinges on the  $S_2$  blade while the other flows through the middle of the  $S_2$  passage, or both vortices flow inside one and the same the passage, or on opposite sides of one and the same blade. Figure 5 shows two extreme configurations in which the negative vortex flows through the passage and the positive vortex impinges on the blade leading edge (case a), or when the roles of the vortices are reversed (case b).

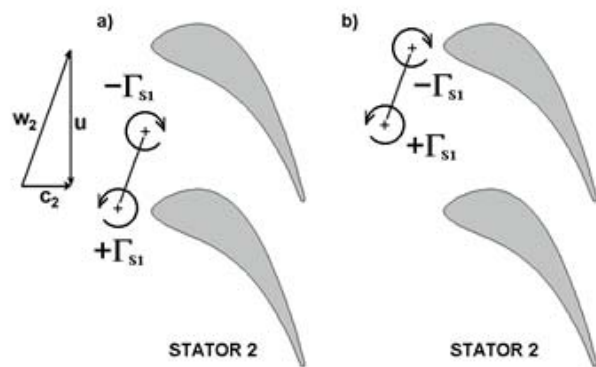


Fig. 5. Characteristic positions of  $S_1$  wake vortices with respect to stator  $S_2$  blades, where negative (a) or positive (b) vortex flows through  $S_{12}$  passage.

Looking at the  $S_1$  wake/ $S_2$  cascade interaction from the point of view of stator  $S_2$  performance, the best situation is when the moving vortex increases the velocity on the suction side and/or decreases the velocity on the pressure side of the  $S_2$  blade, thus increasing the pressure differences between blade sides and the resultant lifting force. In the  $S_2$  cascade geometry shown in Fig 5 this conditions is met by the vortex  $+\Gamma_{S1}$  while the other vortex  $-\Gamma_{S1}$  acts in the opposite way, i.e. unfavourably increases the velocity on the pressure side and decreases on the suction side of the stator  $S_2$  blade. All this leads to the conclusion that the situation which is favourable for turbine performance is case b) when the negative vortex  $-\Gamma_{S1}$  is destroyed in the head-on collision with the  $S_2$  blade leading edge while the positive vortex  $+\Gamma_{S1}$  moves relatively untouched through the centre of the  $S_2$  passage, thus increasing the lift of both blades composing the passage.

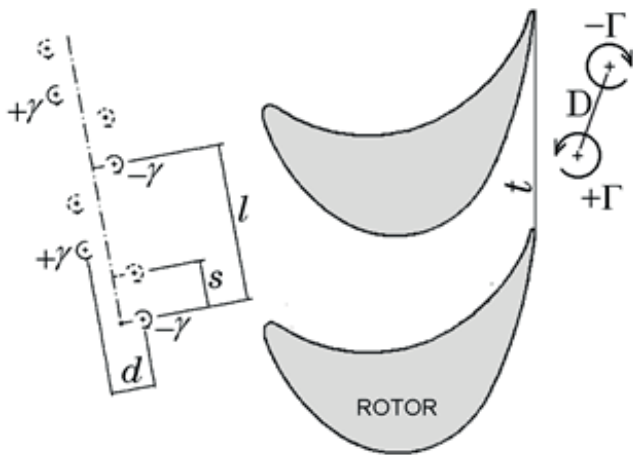


Fig. 6. Parameters of vortex structures upstream and downstream of rotor

The two vortex/blade configurations shown in Fig. 5 have been selected to illustrate basic features of vortex/blade interaction. As was already mentioned, a variety of other positions of the vortex pair  $(-\Gamma_{S1}, +\Gamma_{S1})$  with respect to the stator  $S_2$  blade are possible, depending on geometrical and flow parameters concerning the both stators and the rotor, see Fig. 6. The stator  $S_1$  geometry, especially the thickness and shape of the blade trailing edges and flow conditions in their vicinity, determine the strengths  $+\gamma$  and  $-\gamma$  of the  $S_1$  wake vortices and characteristic spatial distances of the von Karman street, which are:  $l$  – the distance between two vortices of the same rotation sign, and  $d$  – the distance between the opposite-sign rows. Of some importance for further interaction can also be the phase shift  $s$  of the entire von Karman structure with respect to the arbitrary basic position at the moment when the wake is cut off by the rotor blade [26]. The rotor geometry, in turn, decides upon the final strengths  $+\Gamma_{S1}$  and  $-\Gamma_{S1}$  of the  $S_1$  wake vortices leaving the rotor and the distance  $D$  between them. For the same parameters of the wake approaching the rotor, the final parameters of the two vortices:  $+\Gamma_{S1}$ ,  $-\Gamma_{S1}$ , and  $D$ , can be different depending on the pitch  $t$  between the rotor blades, which controls the length of the wake segments cut off by consecutive rotor blades and, consequently, the number of vortices composing each segment. Also of some importance is the flow turning angle which may affect the course of the  $S_1$  wake deformation inside the rotor  $R$  passage. Due to the abovementioned variety of parameters affecting the  $S_1$  wake/ $S_2$  cascade interaction, its exact course and effects in a given turbine can only be obtained from CFD calculations performed for the geometry and flow conditions in this turbine.

When discussing clocking in real turbines it is also noteworthy to mention that the here presented analysis of stator wake behaviour bases on a two dimensional model which omits all three-dimensional effects connected, among other factors, with the presence of other vortex structures, such as horse-shoe and passage vortices for instance. Consequently, the above description of the course and effects of clocking can only be valid in those turbine regions in which the assumption about flow two-dimensionality is justified.

In turbine stages, especially those with radial blades, this region usually extends over a large central part of the passage, only excluding tip and hub areas where the activity of the three-dimensional vortices is dominating. In the abovementioned central part, a condition for the clocking to generate most remarkable and regular effects is parallel alignment of relevant pairs of blade edges: the  $S_1$  trailing edge with the  $R$  leading edge, and the  $R$  trailing edge with the  $S_2$  leading edge, to provide opportunities for nearly two-dimensional wake/blade interaction. It, however, does not mean that any clocking effects cannot be recorded in other turbine stage geometries. As the review of the literature shows, clocking effects can be recorded even in a turbine with an untypical stator-to-rotor blade count ratio  $n_s : n_r = 16 : 96 = 1 : 6$  in which the stator trailing edge is inclined to the radial rotor leading edge by as much as about 22 [deg] and, as a consequence, certain fragments of the wake shed from one stator blade pass, at the same time, through six consecutive rotor passages [28]. This result is explained by the fact that, irrelevant of the scale of complexity and three-dimensionality of the flow, in a given clocking configuration the same fragments of flow structures leaving the rotor repeatedly impinge on and come into interaction with the same parts of the  $S_2$  blades. But, despite certain effects of clocking recorded, the information on this phenomenon gained from such untypical turbines is of little applicability in terms of extension to other geometries.

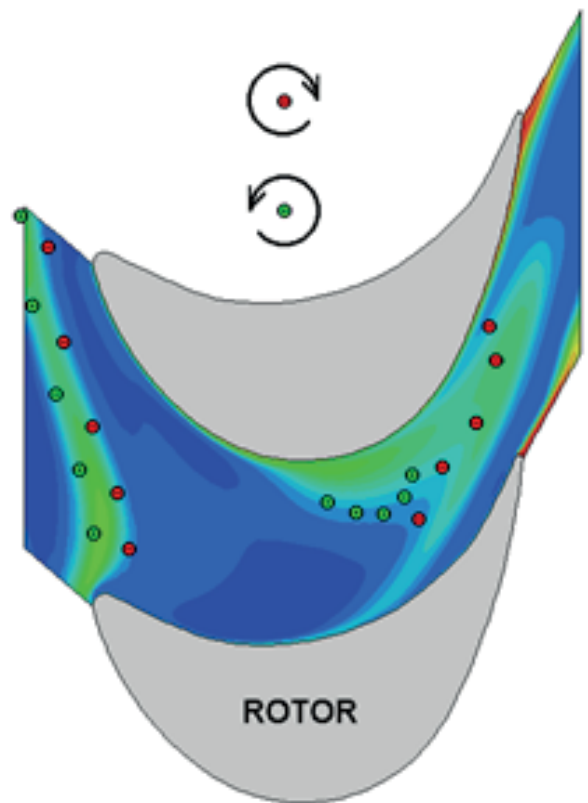


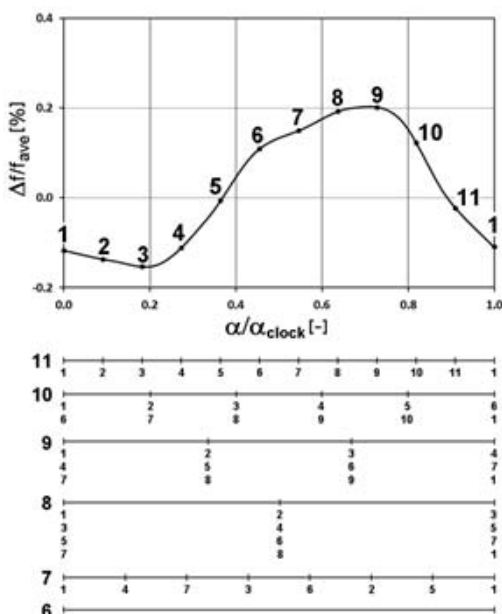
Fig. 7. Configuration of stator wake vortices inside rotor passage calculated using VDT against the entropy distribution obtained from CFD calculations.

Finally, let us discuss the question whether there is any discrepancy between the earlier and presently formulated opinions about favourable and unfavourable positions of the  $S_1$  wake with respect to  $S_2$  blades from the point of view of clocking. Figure 7 shows an instantaneous distribution of  $S_1$  wake vortices obtained from calculations based on Vortex Dynamics Theory on the background of the entropy distribution calculated by a CFD code solving Navier-Stokes equations complemented with a relevant turbulence model, here the  $k-\omega$  SST model. We can notice that the area occupied by the negative (red) vortices coincides with the most distinctive front part of the CFD wake, while the positive (green) vortices do not have a clear representation in the CFD wake. When the wake has the form of a band of smooth velocity defect (or entropy increase, as in Fig. 2) without traces of coherent vortices, which is a standard pattern in clocking analyses based on CFD calculations, its deformed front part is frequently considered a representation of the entire wake and its impingement on the stator blade leading edge is believed to cover the full course of its interaction with the stator. In this context, the opinion on its head-on collision with the stator blade leading edge being the most favourable case of clocking is exactly the same as that formulated based on the vortex theory, which is only extended by including the presence of the other wake vortex  $+\Gamma_{S1}$ .

### Geometry conditions

A commonly accepted general condition for clocking between two stators is the identity of their blade counts  $n_{s1} = n_{s2}$ . In this case all stator  $S_2$  blades experience simultaneously the same clocking effects and the total result for the entire stator can be calculated by multiplying the elementary effect experienced by a single blade by the number of blades. Let us analyse now what happens when the condition  $n_{s1} = n_{s2}$  is not strictly met.

a)  $n_{s2} < n_{s1}$



b)  $n_{s2} > n_{s1}$

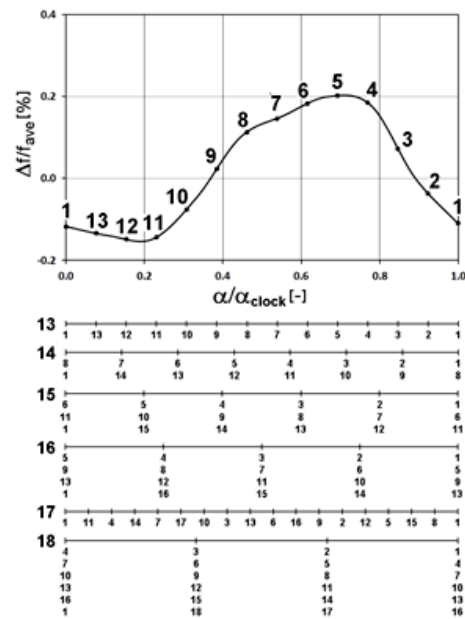


Fig 8. Clocking potential for  $n_{s1} \neq n_{s2}$

For these studies let us employ a curve shown in Fig 8 which presents a hypothetical distribution of changes of an arbitrary parameter  $f$  experienced at a given time by a single  $S_2$  blade after rotating it by the assumed clocking angle  $\alpha$ . The rotation range covers one interval  $\alpha_{clock}$  of clocking repeatability and all  $f$  values refer to one instantaneous time  $\tau$  of rotor rotation, i.e. one instantaneous configuration of stator  $S_1$  / rotor / stator  $S_2$  cascades (To avoid misinterpretation it is necessary to stress here that the curve in Fig. 8 is not similar to typical clocking characteristics which usually present time-histories of parameter changes recorded individually for each clocking angle. In this sense the presented curve represents sort of cross-section of a set of those characteristics for a given time, and will change for different times.). Let us assume that this curve was prepared for a turbine with stator blade counts  $n_{s1} = n_{s2} = 12$ , i.e. for a classical case of clocking geometry. As already mentioned, in this case each point of the curve, point 1 for instance, represents the clocking effect  $f$  experienced not only by a single blade of concern, but also by all remaining  $S_2$  blades. The resultant total clocking effect for the entire cascade  $S_2$  at time  $\tau$  can be calculated by multiplying the current value of  $f$  by the number of blades. The clocking repeatability interval  $\alpha_{clock}$  is in this case equal to the angle  $\alpha_t$  of  $S_2$  rotation by one pitch, here:  $\alpha_{clock} = \alpha_t = 2\pi/12$ .

Now, let us imagine that we remove one blade from stator  $S_2$ , thus creating the blade count ratio  $n_{s1} : n_{s2} = 12 : 11$ . In this case the blade pitch in  $S_2$  becomes larger than that in  $S_1$  and the clocking effect experienced by each  $S_2$  blade at time  $\tau$  is not the same anymore. For instance, when one of the blades, arbitrarily denoted as blade(1), is at the position  $\alpha/\alpha_{clock} = 0.0$ , the next blade (2) takes the position marked 2 on the curve in Fig. 8, the blade (3) takes the position 3 - and so on. As a consequence, the total clocking effect for the entire cascade  $S_2$  is the sum of 11 different values read at 11 equidistant points on the curve. The angle  $\alpha_p$ , describing the cascade part along

which different clocking effects are observed on the blades, extends to  $2\pi$ , i.e. the entire circumference. Consequently, all positive and negative effects of clocking observed at the same time cancel each other and their total effect on the entire stator  $S_2$  is close to zero.

Continuing the above procedure, let us remove another blade. In this case the blade count ratio is  $n_{S1} : n_{S2} = 12 : 10$ . A remarkable difference between this and the previous case is that now there are pairs of  $S_2$  blades which take the same position with respect to stator  $S_1$ , which are: blades 1 and 6, 2 and 7, 3 and 8, 4 and 9, and 5 and 10. Consequently, the number of blades which experience different effects of clocking at the same time is twice as small as in the previous case, and the angle  $\alpha_p$  of clocking effect extension is reduced to  $\pi$ . Further blade removals lead to 3 sections of 3 blades for a 9-bladed row, 4 sections of 2 blades for an 8-bladed row, 1 section of 7 blades, and finally 6 sections of 1 blade. These results are depicted schematically below the left-hand diagram in Fig. 8.

Now let us move in the opposite direction and increase the initial number of  $S_2$  blades by one. This way the blade pitch in  $S_2$  becomes smaller than that of  $S_1$ , and again, each blade will experience a different clocking effect at the same time  $\tau$ . This time, however, when we take the curve from Fig 8 as the reference pattern, the order of blades experiencing particular clocking effects is reversed, see the right-hand diagram. Further reasoning on adding extra blades to the stator  $S_2$  is similar to that when they were removed. The resultant numbers of blades experiencing the same clocking effect when  $n_{S2}$  is increased from 12 to 18 are shown in Fig 8 below the right-hand diagram.

In this context a question can be raised whether any changes of operating parameters of the turbine can be obtained by clocking when  $n_{S1} \neq n_{S2}$ . In fact they can, but their real range, measured as the interval  $\alpha_{clock}$  of effective  $S_2$  clocking, is very limited. When  $\text{abs}(n_{S1} - n_{S2}) = 1$  and there are no repetitions in relative  $S_1/S_2$  blade configurations, the clocking interval  $\alpha_{clock}$  simply corresponds to the difference between the blade pitches in the clocked rows, as the rotation by an angle larger than  $\alpha_{clock}$  will be a repetition of a blade configuration from within this range, only with another blade taking the “basic” position.

When the blade counts provide opportunities for a number of  $S_2$  blades to take the same position with respect to the  $S_1$  cascade, this decreases the number of blades experiencing different clocking effects and the resultant clocking interval is larger, as obtained by multiplying the basic value by the number of repetitions.

Without pure mathematical proof, the following general formula can be proposed for the clocking interval  $\alpha_{clock}$  of two arbitrary rows with blade counts  $n_{S1}$  and  $n_{S2}$ :

$$\alpha_{clock} = \frac{2\pi}{n_{S1}n_{S2}} \text{gcd}(n_{S1}, n_{S2})$$

In this formula the fraction  $2\pi/(n_{S1} * n_{S2})$  represents the basic value, which is true for cascades with arbitrary blade

counts without common divisors, and  $\text{gcd}(n_{S1}, n_{S2})$  is the greatest common divisor of blade counts  $n_{S1}$  and  $n_{S2}$  which takes into account repetitions of identical relative blade positions.

The values of characteristic clocking parameters for cases  $n_{S1} \neq n_{S2}$  and  $n_{S2}$  changing from 6 to 18 are given in Tab. 1. New symbols  $n_{S2R}$  and  $n_{S2S}$  in the table represent the number of  $S_2$  blades which occupy the same position with respect to stator  $S_1$  and the number of different-value  $S_2$  blades in one sequence. In particular,  $n_{S2R} = 1$  means that different clocking effects are recorded on all  $S_2$  blades, along the entire row circumference, while  $n_{S2S} = 1$  means that each  $S_2$  blade experiences the same clocking effect.

Tab. 1. Characteristic clocking parameters for cases:  $n_{S1} \neq n_{S2}$

$n_{S1}$	$n_{S2}$	$\alpha_p$	$n_{S2R}$	$n_{S2S}$	$\alpha_{clock}$
12	12	-	12	1	$\frac{2\pi}{12}$
12	11	$2\pi$	1	11	$\frac{1}{11} * \frac{2\pi}{12}$
12	10	$\pi$	2	5	$\frac{2}{10} * \frac{2\pi}{12}$
12	9	$2\pi/3$	3	3	$\frac{3}{9} * \frac{2\pi}{12}$
12	8	$\pi/2$	4	2	$\frac{4}{8} * \frac{2\pi}{12}$
12	7	$2\pi$	1	7	$\frac{1}{7} * \frac{2\pi}{12}$
12	6	$\pi/3$	6	1	$\frac{6}{6} * \frac{2\pi}{12}$
12	13	$2\pi$	1	13	$\frac{1}{13} * \frac{2\pi}{12}$
12	14	$\pi$	2	7	$\frac{2}{14} * \frac{2\pi}{12}$
12	15	$2\pi/3$	3	5	$\frac{3}{15} * \frac{2\pi}{12}$
12	16	$\pi/2$	4	4	$\frac{4}{16} * \frac{2\pi}{12}$
12	17	$2\pi$	1	17	$\frac{1}{17} * \frac{2\pi}{12}$
12	18	$\pi/3$	6	3	$\frac{6}{18} * \frac{2\pi}{12}$

We can see from formula 1 that the narrowest opportunities for clocking are offered by two cascades with blade counts without common divisors, and in this case  $\alpha_{clock}$  is the result of pure division of the full angle  $2\pi$  by the product of the two blade counts. The existence of common blade count divisors provides opportunities for increasing the clocking interval, and for the most extreme case, when  $n_{S1} = n_{S2}$ , it leads to the classical case of clocking in which  $\alpha_{clock}$  is equivalent to  $\alpha_t$ . In this sense, to justify the opinion quoted at the beginning of this chapter: the case when the blade counts of the clocked rows differ by one can be considered one of worst cases for

clocking, as in this case the blade counts usually do not have common divisors.

For arbitrary pairs of cascades  $S_1$  and  $S_2$ , especially those without common divisors, the interval  $\alpha_{\text{clock}}$  of effective clocking is a small fraction of the angle  $\alpha_t$ . In this context, taking into account that clocking experiments are usually performed within the angle interval equal to  $\alpha_t$  and not to  $\alpha_{\text{clock}}$ , a question should be raised whether rotating the  $S_2$  cascade by a larger angle than  $\alpha_{\text{clock}}$  will provide any clocking effects. The answer is positive, but certain difficulties can occur when interpreting the obtained results. To make this more clear let us illustrate the problem based on the initially analysed classical case of clocking, when  $n_{S1} = n_{S2} = 12$ . For this case  $\alpha_{\text{clock}} = \alpha_t$  and, what is obvious, rotating the  $S_2$  cascade by an arbitrary small angle  $\alpha_c$  within the range  $(0, \alpha_t)$ , will produce a curve similar to that shown in Fig. 8. But the same curve will be obtained when we rotate repeatedly the cascade by the angle  $\alpha_t + \alpha_c$ , or more generally:  $\alpha_t + n \cdot \alpha_c$  where  $n$  is an arbitrary positive integer, and the only difference is that we record the values in different cascade passages. What is more, when we rotate the cascade by  $\alpha_t - \alpha_c$ , we obtain the same curve in qualitative and quantitative terms, but with the sequence of points ordered in the opposite direction. A most complicated and most difficult for interpretation case would be when the cascade was repeatedly rotated by an angle  $\alpha_t + \alpha_c$  and the angle  $\alpha_c$  was close to  $0.5 \cdot \alpha_t$ . The sequence of points obtained for this case would be accidental and their real position on the curve could only be found by subtracting full multiples of  $\alpha_t$  for each point individually to reduce it to the basic interval  $(0, \alpha_t)$ .

The same effect will be observed when recording the effects of clocking for cascades with  $n_{S1} \neq n_{S2}$ . But unlikely the classical case in which the angle  $\alpha_{\text{clock}} = \alpha_t$  has a clear physical representation which can be easily used to assess the interval to which a given point belongs and to reduce it to the basic interval  $(0, \alpha_t)$ , for  $n_{S1} \neq n_{S2}$  the need for reducing the results to the basic interval  $(0, \alpha_{\text{clock}})$  is not so evident. But without doing this we can obtain a curve with an accidentally ordered sequence of points.

## Conclusions

The article discusses two aspects of clocking in turbines with the aim to check the accuracy of commonly accepted opinions concerning the physical nature of clocking and geometric parameters of turbine stages which are believed to be more or less favourable for this phenomenon. The first opinion says that most favourable case of stator clocking in the turbine is when the wake of the upstream stator impinges on the downstream stator leading edge, while in the least favourable case the wake flows through the middle of the stator passage. The vortex dynamics theory based analysis has proved that the above opinion may refer to the negative vortex  $-\Gamma_{S1}$ , one of two vortices created from the stator  $S_1$  wake during its interaction with the rotor cascade. The other vortex,  $+\Gamma_{S1}$ , when passing through the 2<sup>nd</sup> stator passage generates positive flow disturbances and its possible destabilisation after head-on collision with the stator blade leading edge would be unfavourable for turbine performance.

The second opinion says that highest performance improvement can be obtained in turbines in which blade count ratios of the clocked rows is close to one, and when it is far from unity the clocking effect can be negligible. The here presented analysis of instantaneous distributions of flow parameters affected by clocking in turbines in which  $n_{S1} \neq n_{S2}$  has shown that the highest angular range of clocking is obtained when  $n_{S1}$  is exactly the same as  $n_{S2}$ , while the case when they slightly differ, by one for instance, can be considered one of the worst cases from the point of view of turbine performance improvement. A heuristic formula to calculate the range of the effective clocking interval  $\alpha_{\text{clock}}$  for turbines with arbitrary blade count ratios of the clocked rows is proposed.

## References:

1. Huber, F. W., Johnson, P. D., Sharma, O. P., Staubach, J. B., Gaddis, S. W., 1996, "Performance Improvement Through Indexing of Turbine Airfoils. Part 1: Experimental Investigation", ASME J. Turbomach., Vol. 118, pp. 630–635.
2. Griffin L. W., Huber F. W., Sharma O. P., 1996, "Performance Improvement Through Indexing of Turbine Airfoils. Part 2: Numerical Simulation". ASME J. Turbomach., Vol. 118, pp. 636–642
3. Eulitz, F., Engel, K., Gebbing, H., 1996, "Numerical Investigation of the Clocking Effects in a Multistage Turbine," ASME Paper 96-GT-26, 1996
4. Dorney, D., Sharma, O. P., 1996, "A Study of Turbine Performance Increases Through Airfoil Clocking," AIAA Paper 96-2816, 1996
5. Cizmas P.G.A., Dorney D., 2000, "The Influence of Clocking on Unsteady Forces of Compressor and Turbine Blades", International Journal of Turbo and Jet Engines, Vol. 17, No. 2, pp. 133-142
6. Dorney, D. J., Croft, R. R., Sondak, D. L., Stang, U. E., Twardochleb, C. Z., 2001, "Computational study of clocking and embedded stage in a 4-stage industrial turbine", ASME Paper 2001-GT-509
7. Reinmoller U., Stephan B., Schmidt S., Niehuis R., 2002, "Clocking Effects in a 1.5 Stage Axial Turbine – Steady and Unsteady Experimental Investigations Supported by Numerical Simulations", ASME Journal of Turbomachinery, Vol. 124, No. 1, pp. 52-60
8. Cizmas P.G.A., Dorney D., 1999, "Parallel Computation of Turbine Blade Clocking", International Journal of Turbo and Jet Engines. Vol. 16, No. 1, pp. 49–60
9. Li Wei, Zhu Xiao-cheng, Ouyang Hua, Du Zhao-hui, 2012, "Numerical Simulation of Clocking Effect on Blade Unsteady Aerodynamic Force in Axial Turbine", Journal of Thermal Science, Vol. 21, No. 5, pp 474-482

10. Arnone A., Marconcini M., Pacciani R., 2000, "On the Use of Unsteady Methods in Predicting Stage Aerodynamics Performance", Proc International Symposium on Unsteady Aerodynamics, Aeroacoustics, and Aeroelasticity of Turbomachines ISUAAAT, Lyon, France, pp.24-36
11. Arnone A., Marconcini M., Pacciani R., Schipani C., Spano E., 2002, "Numerical Investigation of Airfoil Clocking in a Three-Stage Low-Pressure Turbine", Journal of Turbomachinery, Vol. 124, pp 61-68
12. Arnone, A., Marconcini, M., Greco, A., Spano, E., 2004, "Numerical Investigation of Three-Dimensional Clocking Effects in a Low Pressure Turbine", ASME Journal of Turbomachinery, Vol. 126, pp. 375-384
13. Meyer, R. X., 1958, "The Effect of Wakes on the Transient Pressure and Velocity Distributions in Turbomachines," ASME Journal of Basic Engineering, Vol. 80, pp. 1544-1552
14. Smith, L. H., 1966, "Wake Dispersion in Turbomachines," ASME Journal of Basic Engineering, Vol. 88, September, pp. 688-690
15. Lienhart, W., 1974, "Berechnung der instationären Strömung durch gegeneinander bewegte Schaufelgitter und der Schaufelkraftschwankungen", VDI-Forschungsheft, 562, VDI Verlag, Düsseldorf
16. Krammer, P., 1982, "Computation of Unsteady Blade Forces in Turbomachines by Means of Potential Flow Theory and by Simulating Viscous Wakes", ASME Paper 82-GT-198
17. Sieverding, C. H., Heinemann, H., 1990, "The Influence of Boundary Layer State on Vortex Shedding From Flat Plates and Turbine Cascades", ASME Journal of Turbomachinery, vol. 112, pp. 181-187
18. Cicatelli, G., Sieverding, C. H., 1997, "The Effect of Vortex Shedding on the Unsteady Pressure Distribution Around the Trailing Edge of a Turbine Blade," ASME Journal of Turbomachinery, Vol. 119, pp. 810-819
19. Mensink, C., 1996, "Numerical Prediction of Periodic Vortex Shedding in Subsonic and Transonic Turbine Cascade Flows", International Journal for Numerical Methods in Fluids, Vol. 22, pp. 881-897
20. Currie, T. C., Carscallen, W. E., 1998, "Simulation of Trailing Edge Vortex Shedding in a Transonic Turbine Cascade," ASME Journal of Turbomachinery, Vol. 120, pp. 10-19
21. Arnone, A., Marconcini, M., Pacciani, R., 1999, "On the Use of Dual Time Stepping in Unsteady Turbomachinery Flow Calculations," ERCOFTAC Bulletin No. 42, September, pp. 37-42
22. Magagnato, F., 1999, "Unsteady flow past a turbine blade using non-linear two-equation turbulence models," Proceedings III European Conference on Turbomachinery: Fluid Dynamics and Thermodynamics, London, March, pp. 221-230
23. Kost, F., Hummel, F., Tiedemann, M., 2000, "Investigation of the Unsteady Rotor Flow Field in a Single HP Turbine Stage," Proceedings ASME TURBO EXPO 2000, May 8-11, Munich, Germany, Paper 200-GT-432, pp. 1-11
24. Tiedemann M., Kost F., 2001, "Some aspects of Wake-Wake Interactions Regarding Turbine Stator Clocking", ASME J. Turbomachinery, Vol. 123, pp.526-533
25. Hummel, F., 2001, "Wake-Wake Interactions and Its Potential for Clocking in Transonic High Pressure Turbine," Proceedings ASME TURBO EXPO 2001, June 4-7, New Orleans, U.S.A, Paper 2001-GT-0302, pp. 1-9
26. Swirydczuk J., 2002, "Vortex Dynamics of the Stator Wake-Rotor Cascade Interaction", ASME J. Fluids Engineering, Vol. 124, pp. 400-412
27. Swirydczuk J., 2013, "Wake-blade interaction in steam turbine stages", Polish Maritime Research, Vol. 20, No. 2 (78), pp. 30-40
28. Kryszynski J.E., Blaszczyk J. R., Smolny A., 2005, "Stator Clocking Effects on 3D Flow in a Two-Stage Low-Pressure Turbine", Proc ASME TURBO EXPO 2005, Power for Land, Sea and Air, June 6-9, 2005, Reno-Tahoe, Nevada, USA, Paper GT2005-68811, pp. 1-12

## **CONTACT WITH AUTHOR**

Jerzy Swirydczuk

Institute of Fluid-Flow Machinery  
Polish Academy of Science  
14 J. Fiszer St  
80-231 Gdańsk  
Poland

jerzy.swirydczuk@imp.gda.pl

# SIMPLIFIED PROCEDURE FOR THE FREE VIBRATION ANALYSIS OF RECTANGULAR PLATE STRUCTURES WITH HOLES AND STIFFENERS

**Dae Seung Cho**, Ph.D.  
Pusan National University, Busan, Korea

**Nikola Vladimir**, Ph.D.  
University of Zagreb, Zagreb, Croatia

**Tae Muk Choi**, Ph.D.  
Createch Co. Ltd., Busan, Korea

## ABSTRACT

*Thin and thick plates, plates with holes, stiffened panels and stiffened panels with holes are primary structural members in almost all fields of engineering: civil, mechanical, aerospace, naval, ocean etc. In this paper, a simple and efficient procedure for the free vibration analysis of such elements is presented. It is based on the assumed mode method and can handle different plate thickness, various shapes and sizes of holes, different framing sizes and types as well as different combinations of boundary conditions. Natural frequencies and modes are determined by solving an eigenvalue problem of a multi-degree-of-freedom system matrix equation derived by using Lagrange's equations. Mindlin theory is applied for a plate and Timoshenko beam theory for stiffeners. The applicability of the method in the design procedure is illustrated with several numerical examples obtained by the in-house developed code VAPS. Very good agreement with standard commercial finite element software is achieved.*

**Keywords:** energy approach, plate with hole, stiffened panel, thick plate, VAPS software, free vibration analysis

## INTRODUCTION

Different kinds of rectangular plate systems, for instance thick plates, plates with holes, stiffened panels, stiffened panels with holes etc., can be found in all fields of engineering: civil, mechanical, aerospace, naval, ocean, etc. The free vibration analysis of such elements is an important issue in the design process. The finite element method (FEM) is nowadays an advanced and widespread numerical tool for that purpose and gives a complete solution to the vibration analysis of complex systems. However, the preparation of a model is a rather time-consuming task which makes it reasonable to apply it, usually, at the end of the detail design stage, after all the structural members, their dimensions and boundary conditions have been completely defined. In this sense, at the preliminary design stage when the principal dimensions are being selected, it is useful to have some simplified method at hand.

Although the thick plate theory represents an issue for very long time, i.e. since the first works published by Reissner and Mindlin [1 ÷ 2], its complexity caused by shear influence and rotary inertia makes it still a challenging problem, and it is not surprising that there are numerous references on this topic.

As can be seen in the literature survey presented by Liew et al. [3], many concepts, based both on analytical and numerical solution of equilibrium equations, have been worked out. There are various analytical methods whose main drawback is the applicability limited only to simply supported plates or plates with two opposite edges simply supported. They differ depending on which functions are kept as fundamental when reducing the system of differential equations of motion. Some methods operate with three, two, or even one function [4 ÷ 5]. For the vibration analysis of plates with arbitrary edge constraints, including also elastically restrained edges, different variants of the Rayleigh-Ritz (energy) method are on disposal. The accuracy of such methods is dependent on the chosen set of orthogonal functions for the assumed natural modes, where two dimensional polynomials or static Timoshenko beam deflection functions, [6] and [7 ÷ 9], respectively, can be used. In the context of FEM application in the vibration analysis of thick plate, a shear locking problem should be mentioned. Namely, in the Mindlin thick plate theory shear deformations are taken into account, and the application of ordinary low-order finite element is not capable to reproduce pure bending modes in the limiting case of a thin plate. This shear locking problem arises due to

inadequate dependence between the transverse deflection and two rotations. However, it has been successfully overcome by different types of procedures developed in recent years [10 ÷ 15].

An overview of methods for the vibration analysis of plates with holes is presented in [16], where the advantages and drawbacks of different methods, for instance the finite difference method [17], the Rayleigh-Ritz [18] and the optimized Rayleigh-Ritz method [19], FEM [20], etc., are discussed.

In the case of stiffened panels, to the authors' knowledge, there are a rather limited number of references to their dynamic analysis [21]. Generally, the most common methods applied to the vibration analysis of stiffened plates can be classified into closed-bound solutions, energy methods, and other numerical methods [21 ÷ 22].

In the case of the vibration analysis of stiffened panels with holes, only a few references, based on the application of the finite element method, are available. Sivasubramonian et al. [23] studied the effect of curvature and hole size on square panels with different boundary conditions applied to the shell element having seven degrees of freedom per node. Sivasubramonian et al. [24] also applied the same finite element to both stiffened and unstiffened plate with holes and presented comparative results. Recently, Srivastava [25] applied the finite element method to the vibration analysis of stiffened panels with a single hole and different boundary conditions, under partial edge loading.

This paper reviews the application of the assumed mode method to the vibration analysis of thick plates, plates with multiple holes, and stiffened panels. In addition, expressions for partial stiffeners and carlings are presented. It should be emphasized that only the flexural global modes of the above structures are considered.

Further, it is shown that the method can also be applied to stiffened panels with holes. The effect of stiffeners is taken into account by adding their potential and kinetic energy to the potential and kinetic energy of the plate, respectively. Similarly to this, the potential and kinetic energies of the holes are subtracted from the corresponding energies of the plate, respectively. In this sense different combinations of topologies can be taken into account by appropriate manipulation with potential and kinetic energies of particular components. The computational tool VAPS (Vibration Analysis of Plate Systems) based on the assumed mode method has been developed and different numerical examples are analysed. The developed procedure is shown to be very simple, fast and accurate. Its main advantage in comparison with FEM is very fast model preparation. It is therefore recommended for practical use in the preliminary design phase of plate-like systems, when effects of different topologies, materials, boundary conditions, etc. on dynamic response are being investigated.

## OUTLINE OF THE MATHEMATICAL FORMULATION

The mathematical model for the vibration analysis of different plate systems based on the assumed mode method is already applied in [8], [16] and [21], and here its outline with

some extensions is given. The Mindlin thick plate theory [2] which takes shear influence and rotary inertia into account is adopted in the model. The Mindlin theory operates with three general displacements, i.e. plate deflection  $w$ , and angles of cross-section rotation about the  $x$  and  $y$  axes,  $\psi_x$  and  $\psi_y$ , respectively.

In the derivation of the eigenvalue problem which is necessary to obtain the free response, the Lagrange's equation is applied. In this sense the expression for total system potential,  $V$ , and kinetic energy,  $T$ , respectively is required. In the case of a solid plate, the total system energy is equal to the plate energy:

$$V = V_p, \quad T = T_p \quad (1)$$

Potential and kinetic energies for the plate with holes yield:

$$V = V_p - V_h, \quad T = T_p - T_h, \quad (2)$$

and for the stiffened panel

$$V = V_p + V_s, \quad T = T_p + T_s \quad (3)$$

Analogously to this, one can write for the potential and kinetic energy of a stiffened panel with holes:

$$V = V_p + V_s - V_h, \quad T = T_p + T_s - T_h \quad (4)$$

In the above expressions  $V_p$  is the plate strain energy,  $V_s$  represents the strain energy of stiffeners and  $V_h$  is the strain energy of a hole. Similarly,  $T_p$  is the plate kinetic energy, while  $T_s$  and  $T_h$  are the kinetic energies of the stiffeners and hole, respectively.

### Energy of rectangular plate

By introducing the dimensionless parameters  $\zeta = x/a$ ,  $\eta = y/b$ ,  $\alpha = a/b$  and  $S = kGh/D$  for a rectangular plate of length  $a$  and width  $b$  with arbitrary boundary conditions, one can write for its potential and kinetic energies [8]:

$$\begin{aligned} V_p = & \frac{D}{2\alpha} \int_0^1 \int_0^1 \left[ \left( \frac{\partial \psi_\xi}{\partial \xi} \right)^2 + \alpha^2 \left( \frac{\partial \psi_\eta}{\partial \eta} \right)^2 \right. \\ & + 2\nu\alpha \frac{\partial \psi_\xi}{\partial \xi} \frac{\partial \psi_\eta}{\partial \eta} + \frac{1-\nu}{2} \left( \alpha \frac{\partial \psi_\xi}{\partial \eta} + \frac{\partial \psi_\eta}{\partial \xi} \right)^2 \\ & \left. + S \left[ \left( \frac{\partial w}{\partial \xi} - a\psi_\xi \right)^2 + \alpha^2 \left( \frac{\partial w}{\partial \eta} - b\psi_\eta \right)^2 \right] \right] d\xi d\eta \\ & + \int_0^1 [K_{R_{x1}} \psi_\xi^2(0, \eta) + SK_{T_{x1}} w^2(0, \eta)] d\eta \\ & + \alpha^2 \int_0^1 [K_{R_{y1}} \psi_\eta^2(\xi, 0) + SK_{T_{y1}} w^2(\xi, 0)] d\xi \\ & + \int_0^1 [K_{R_{x2}} \psi_\xi^2(1, \eta) + SK_{T_{x2}} w^2(1, \eta)] d\eta \\ & + \alpha^2 \int_0^1 [K_{R_{y2}} \psi_\eta^2(\xi, 1) + SK_{T_{y2}} w^2(\xi, 1)] d\xi, \end{aligned} \quad (5)$$

$$T_p = \frac{\rho ab}{2} \int_0^1 \int_0^1 \left[ h \left( \frac{\partial w}{\partial t} \right)^2 + \frac{h^3}{12} \left( \frac{\partial \psi_\xi}{\partial t} \right)^2 + \frac{h^3}{12} \left( \frac{\partial \psi_\eta}{\partial t} \right)^2 \right] d\xi d\eta \quad (6)$$

where  $K_{Tx1} = (k_{Tx1} a/kGh)$ ,  $K_{Tx2} = (k_{Tx2} a/kGh)$ ,  $K_{Ty1} = (k_{Ty1} a/kGh)$  and  $K_{Ty2} = (k_{Ty2} a/kGh)$  are dimensionless stiffness values at  $x = 0$ ,  $x = a$ ,  $y = 0$  and  $y = b$ , respectively, and correspond to the translational spring constants per unit length  $k_{Tx1}$ ,  $k_{Tx2}$ ,  $k_{Ty1}$  and  $k_{Ty2}$  [8],[16]. In the same manner,  $K_{Rx1} = (k_{Rx1} a/D)$ ,  $K_{Rx2} = (k_{Rx2} a/D)$ ,  $K_{Ry1} = (k_{Ry1} b/D)$  and  $K_{Ry2} = (k_{Ry2} b/D)$  are for the rotational spring constants per unit length  $k_{Rx1}$ ,  $k_{Rx2}$ ,  $k_{Ry1}$  and  $k_{Ry2}$  at boundaries, respectively. The following quantities are related to the x direction:  $a$ ,  $k_{Tx1}$ ,  $k_{Tx2}$ ,  $k_{Rx1}$  and  $k_{Rx2}$ . Other quantities ( $b$ ,  $k_{Ty1}$ ,  $k_{Ty2}$ ,  $k_{Ry1}$  and  $k_{Ry2}$ ) are relevant for the y direction [16]. Also  $\rho$  represents plate material density,  $h$  is the plate thickness,  $k$  is the shear correction factor, while  $\nu$  is the Poisson's ratio. Further,  $D$  represents plate flexural stiffness  $D = Eh^3/(12(1-\nu^2))$ , while  $E$  and  $G = E/(2(1+\nu))$  are Young's and shear moduli, respectively.

### Energy of holes

In a similar way as for the plate without holes, one can write for the potential and kinetic energy of the rectangular hole shown in Fig. 1a, respectively:

$$V_{rh} = \frac{D}{2\alpha} \int_{y_{ro}-b_{ro}}^{y_{ro}+b_{ro}} \int_{x_{ro}-a_{ro}}^{x_{ro}+a_{ro}} \left[ \left( \frac{\partial \psi_\xi}{\partial \xi} \right)^2 + \alpha^2 \left( \frac{\partial \psi_\eta}{\partial \eta} \right)^2 + 2\nu\alpha \frac{\partial \psi_\xi}{\partial \xi} \frac{\partial \psi_\eta}{\partial \eta} + \frac{1-\nu}{2} \left( \alpha \frac{\partial \psi_\xi}{\partial \eta} + \frac{\partial \psi_\eta}{\partial \xi} \right)^2 + S \left( \left( \frac{\partial w}{\partial \xi} - a\psi_\xi \right)^2 + \alpha^2 \left( \frac{\partial w}{\partial \eta} - b\psi_\eta \right)^2 \right) \right] d\xi d\eta \quad (7)$$

$$T_{rh} = \frac{\rho ab}{2} \int_{y_{ro}-b_{ro}}^{y_{ro}+b_{ro}} \int_{x_{ro}-a_{ro}}^{x_{ro}+a_{ro}} \left[ h \left( \frac{\partial w}{\partial t} \right)^2 + \frac{h^3}{12} \left( \frac{\partial \psi_\xi}{\partial t} \right)^2 + \frac{h^3}{12} \left( \frac{\partial \psi_\eta}{\partial t} \right)^2 \right] d\xi d\eta \quad (8)$$

In Fig. 1a,  $x_{rh}$  and  $y_{rh}$  denote the longitudinal and transverse coordinates of the rectangular hole centre of gravity, and  $a_{rh}$  and  $b_{rh}$  are equal to one half of its length and width. Analogously to the rectangular hole, the potential and kinetic energies of the elliptical hole shown in Fig. 1b yield:

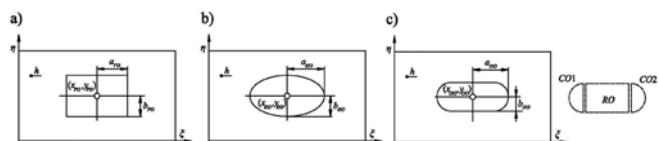


Fig. 1. Rectangular plates with different hole shapes; a) rectangular, b) elliptic, c) oval [16]

$$V_{eh} = \frac{D}{2\alpha} \int_{y_{eo}-b_{eo}}^{y_{eo}+b_{eo}} \int_{x_{eo}-a_{eo}}^{x_{eo}+a_{eo}} \sqrt{1 - \left( \frac{\eta - y_{eo}}{b_{eo}} \right)^2} \left[ \left( \frac{\partial \psi_\xi}{\partial \xi} \right)^2 + \alpha^2 \left( \frac{\partial \psi_\eta}{\partial \eta} \right)^2 + 2\nu\alpha \frac{\partial \psi_\xi}{\partial \xi} \frac{\partial \psi_\eta}{\partial \eta} + \frac{1-\nu}{2} \left( \alpha \frac{\partial \psi_\xi}{\partial \eta} + \frac{\partial \psi_\eta}{\partial \xi} \right)^2 + S \left( \left( \frac{\partial w}{\partial \xi} - a\psi_\xi \right)^2 + \alpha^2 \left( \frac{\partial w}{\partial \eta} - b\psi_\eta \right)^2 \right) \right] d\xi d\eta \quad (9)$$

$$T_{eh} = \frac{\rho ab}{2} \int_{y_{eo}-b_{eo}}^{y_{eo}+b_{eo}} \int_{x_{eo}-a_{eo}}^{x_{eo}+a_{eo}} \sqrt{1 - \left( \frac{\eta - y_{eo}}{b_{eo}} \right)^2} \left[ h \left( \frac{\partial w}{\partial t} \right)^2 + \frac{h^3}{12} \left( \frac{\partial \psi_\xi}{\partial t} \right)^2 + \frac{h^3}{12} \left( \frac{\partial \psi_\eta}{\partial t} \right)^2 \right] d\xi d\eta \quad (10)$$

If one introduces  $x_{eh} = y_{eh}$  in the equations (9) and (10), the potential and kinetic energies of the circular hole are obtained. As in previous case,  $x_{ch}$  and  $y_{ch}$  in Fig. 1b denote the longitudinal and transverse coordinates of the elliptic hole centre of gravity, while  $a_{ch}$  and  $b_{ch}$  are the major and minor semi-axes of the hole, respectively. An oval hole, which can often be found in ships and offshore structures, can be treated as a combination of rectangular and semi-circular holes, Fig. 1c, where  $x_{oh}$  and  $y_{oh}$  are the longitudinal and transverse coordinates of the oval hole centre of gravity, while  $a_{oh}$  and  $b_{oh}$  are equal to one half of its length and width, respectively.

In this way, its potential and kinetic energies can be written in the following form:

$$T_{oh} = T_{ch1} + T_{rh} + T_{ch2}, \quad V_{oh} = V_{ch1} + V_{rh} + V_{ch2} \quad (11)$$

and can be calculated with the above-listed formulae. In addition, the procedure can be applied to multiple holes, but then the hole potential and kinetic energies have to be calculated separately, and subtracted from the corresponding energies of the plate without holes.

### Energy of stiffeners

The potential and kinetic energy of stiffeners placed in the longitudinal and transverse directions yield:

$$V_s = \frac{a}{2} \sum_{r=1}^{n_x} \left[ \int_0^1 \left( \frac{EI_{x_r}}{a^2} \left( \frac{\partial \psi_\xi}{\partial \xi} \right)^2 + K_{x_r} A_{w_x} G \left( \frac{\partial w}{\partial \xi} - \psi_\xi \right)^2 + \frac{GJ_{x_r}}{a^2} \left( \frac{\partial \psi_\eta}{\partial \xi} \right)^2 \right) d\xi \right] + \frac{b}{2} \sum_{r=1}^{n_y} \left[ \int_0^1 \left( \frac{EI_{y_r}}{b^2} \left( \frac{\partial \psi_\eta}{\partial \eta} \right)^2 + K_{y_r} A_{w_y} G \left( \frac{\partial w}{\partial \eta} - \psi_\eta \right)^2 + \frac{GJ_{y_r}}{b^2} \left( \frac{\partial \psi_\xi}{\partial \eta} \right)^2 \right) d\eta \right]_{\xi=\xi_r} \quad (12)$$

$$T_s = \frac{a}{2} \sum_{r=1}^{n_x} \left[ \int_0^1 \left\{ \rho I_{Rx_r} \left( \frac{\partial \psi_\xi}{\partial t} \right)^2 + \rho A_{w_x} \left( \frac{\partial w}{\partial t} \right)^2 \right\}_{\eta=\eta_r} d\xi \right] + \frac{b}{2} \sum_{r=1}^{n_y} \left[ \int_0^1 \left\{ \rho I_{Ry_r} \left( \frac{\partial \psi_\eta}{\partial t} \right)^2 + \rho A_{w_y} \left( \frac{\partial w}{\partial t} \right)^2 \right\}_{\xi=\xi_r} d\eta \right] \quad (13)$$

where  $n_x$  and  $n_y$  represent the number of stiffeners in the  $x$  and  $y$  direction, respectively.  $K$  is the shear coefficient, and  $A$  and  $I_R$  are the area and the rotary moment of inertia of the stiffener cross-section, respectively. Further,  $GJ$  is torsional stiffness while  $EI$  is the bending stiffness of the stiffener, considering the plate flange contribution of effective width  $s$  as shown in Fig. 2.

If a plate with partial stiffeners (carlings) is considered, Fig. 3, the potential and kinetic energy yield

$$T_s = \frac{a}{2} \sum_{r=1}^{n_x} \left[ \int_0^1 \left\{ \rho I_{R_{x_r}} \left( \frac{\partial \psi_\xi}{\partial t} \right)^2 + \rho A_{w_{x_r}} \left( \frac{\partial w}{\partial t} \right)^2 \right\}_{\eta=\eta_r} d\xi \right] + \frac{b}{2} \sum_{r=1}^{n_y} \left[ \int_0^1 \left\{ \rho I_{R_{y_r}} \left( \frac{\partial \psi_\eta}{\partial t} \right)^2 + \rho A_{w_{y_r}} \left( \frac{\partial w}{\partial t} \right)^2 \right\}_{\xi=\xi_r} d\eta \right] \quad (14)$$

$$T_s(t) = \frac{a}{2} \sum_{r=1}^{n_x} \left[ \int_{a\xi}^{b\xi} \left\{ \rho I_{R_{x_r}} \left( \frac{\partial \psi_\xi}{\partial t} \right)^2 + \rho A_{w_{x_r}} \left( \frac{\partial w}{\partial t} \right)^2 \right\}_{\xi=\xi_r} d\xi \right] + \frac{b}{2} \sum_{r=1}^{n_y} \left[ \int_{a\eta}^{b\eta} \left\{ \rho I_{R_{y_r}} \left( \frac{\partial \psi_\eta}{\partial t} \right)^2 + \rho A_{w_{y_r}} \left( \frac{\partial w}{\partial t} \right)^2 \right\}_{\eta=\eta_r} d\eta \right] \quad (15)$$

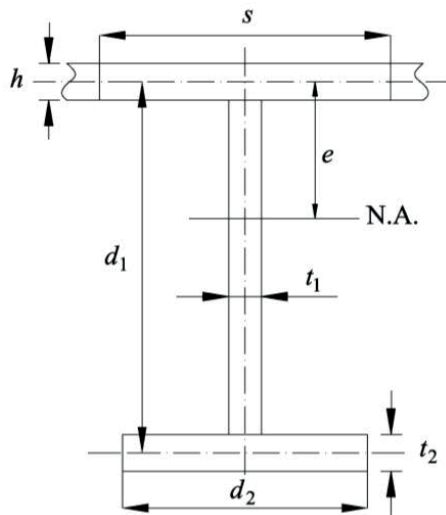


Fig. 2. Cross-section of a stiffener [21]

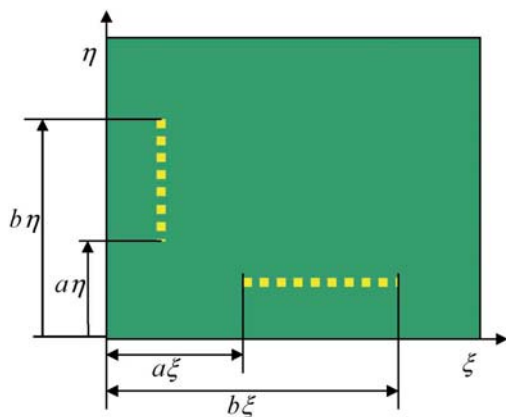


Figure 3 Plate with partial stiffeners

## Outline of the assumed mode method

In the assumed mode method, lateral displacement and rotational angles are expressed by superposing the products of the orthogonal polynomials:

$$w(\xi, \eta, t) = \sum_{m=1}^M \sum_{n=1}^N a_{mn}(t) X_m(\xi) Y_n(\eta),$$

$$\psi_\xi(\xi, \eta, t) = \sum_{m=1}^M \sum_{n=1}^N b_{mn}(t) \Theta_m(\xi) Y_n(\eta), \quad (16)$$

$$\psi_\eta(\xi, \eta, t) = \sum_{m=1}^M \sum_{n=1}^N c_{mn}(t) X_m(\xi) \Phi_n(\eta)$$

where  $X_m(\xi)$ ,  $Y_n(\eta)$ ,  $\Theta_m(\xi)$  and  $\Phi_n(\eta)$  are the orthogonal polynomials satisfying the specified elastic edge constraints with respect to  $\xi$  and  $\eta$  [8], [16], [21]. Furthermore,  $a_{mn}(t)$ ,  $b_{mn}(t)$  and  $c_{mn}(t)$  are the influence coefficients of orthogonal polynomials. Also,  $M$  and  $N$  are the number of orthogonal polynomials used for an approximate solution in the  $\xi$  and  $\eta$  directions, respectively. Equations (16) can be alternatively written in matrix form:

$$\{z(\xi, \eta, t)\} = [H(\xi, \eta)] \{q(t)\} \quad (17)$$

where:

$$\{z(\xi, \eta, t)\} = \{w(\xi, \eta, t), \psi_\xi(\xi, \eta, t), \psi_\eta(\xi, \eta, t)\}^T \quad (18)$$

$$[H(\xi, \eta)] = \begin{bmatrix} X_1 Y_1 \dots X_M Y_N & 0 \dots 0 & 0 \dots 0 \\ 0 \dots 0 & \Theta_1 Y_1 \dots \Theta_M Y_N & 0 \dots 0 \\ 0 \dots 0 & 0 \dots 0 & X_1 \Phi_1 \dots X_M \Phi_N \end{bmatrix} \quad (19)$$

$$\{q(t)\} = \{a_{11} \dots a_{MN} \ b_{11} \dots b_{MN} \ c_{11} \dots c_{MN}\}^T \quad (20)$$

By substituting equations (1) to (4), depending on the system topology, into Lagrange's equation of motion

$$\frac{d}{dt} \left( \frac{\partial T}{\partial \dot{q}_i} \right) - \frac{\partial T}{\partial q_i} + \frac{\partial V}{\partial q_i} = 0 \quad (21)$$

the discrete matrix equation with  $3 \times M \times N$  degrees of freedom is obtained as the following equation:

$$[M] \left\{ \frac{\partial^2 q(t)}{\partial t^2} \right\} + [K] \{q(t)\} = 0 \quad (22)$$

where  $[M]$  and  $[K]$  are the mass matrix and the stiffness matrix, respectively [8], [16], [21]. Their constitution using characteristic orthogonal polynomials is described in detail in [8]. The procedure for the constitution of the stiffness and mass matrices of the attached stiffeners using the same polynomials can also be found in [21].

If we assume harmonic vibrations i.e.

$$\{q(t)\} = \{Q\} e^{i\omega t},$$

$$w(\xi, \eta, t) = W(\xi, \eta) e^{i\omega t},$$

$$\psi_\xi(\xi, \eta, t) = \Psi_\xi(\xi, \eta) e^{i\omega t},$$

$$\psi_\eta(\xi, \eta, t) = \Psi_\eta(\xi, \eta) e^{i\omega t} \quad (23)$$

equation (22) leads to an eigenvalue problem which gives the natural frequencies and eigenvectors of the system, where  $j$  is the imaginary unit and  $\omega$  represents the angular frequency. The mode shape corresponding to each natural frequency is obtained from the following equation:

$$\{W(\xi, \eta), \Psi_\xi(\xi, \eta), \Psi_\eta(\xi, \eta)\}_l^T = [H(\xi, \eta)]\{Q\}_l \quad (24)$$

where  $l$  represents the order of the mode. It should be noted here that when using the assumed mode method, the orthogonal polynomials corresponding to the property of the target model should be applied to achieve accurate analysis. For this purpose, the characteristic orthogonal polynomials having the property of Timoshenko beam functions which satisfies the specified edge constraints are used. Their complete derivation is presented in [8], [21].

### VAPS software

Based on the above described procedure VAPS software for the vibration analysis of plate systems has been developed. Its current version is applicable for the free vibration analysis of thin and thick rectangular plates and stiffened panels with and without openings and with all possible combinations of boundary conditions. VAPS is executed using Windows OS and has graphical user interface which enables almost instantaneous model preparation, Fig. 4. Also, postprocessing of the results and report preparation are very simple and fast. The software was initially developed for the naval architecture purposes and therefore the software automatically checks the compliance of the dynamic response with the rule-based values prescribed by the relevant classification societies, Fig. 5.

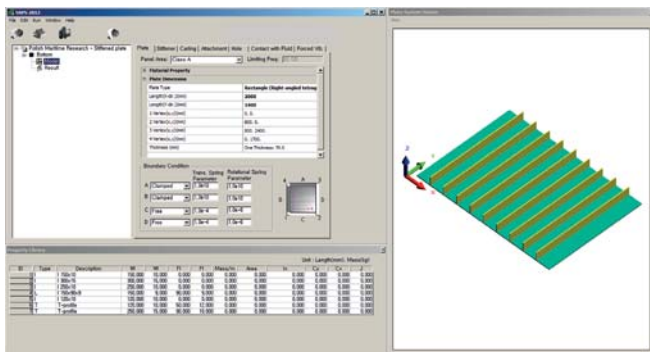


Fig. 4 Model preparation in the graphical user interface of the VAPS software

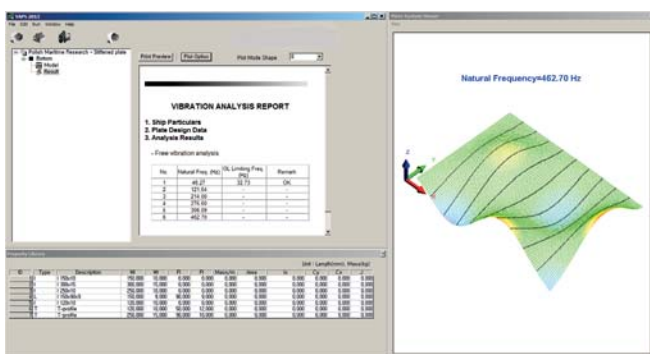


Fig. 5 Postprocessing of the results in the VAPS software

## ILLUSTRATIVE NUMERICAL EXAMPLES

The developed procedure is verified with several numerical examples, where different framing (transverse, longitudinal, mixed), plate thicknesses, and holes of different shapes and sizes are included. In the numerical examples, various boundary conditions are also applied. In all calculations, the values of Young's modulus, material density and Poisson's ratio are set to  $2.1 \times 10^{11}$  N/m<sup>2</sup>, 7850 kg/m<sup>3</sup> and 0.3, respectively. Furthermore, the value of the shear factor  $k$  is adjusted to  $5/6$  and the number of polynomials is set to 13, for both  $\xi$  and  $\eta$  directions, respectively. In the proposed procedure, the beam theory is applied in order to take into account the effect of stiffeners. Therefore, in all calculations the stiffeners are modelled as beam elements in the FE analysis, since a comparison of the results in that case is the most realistic. The results obtained by the VAPS software are denoted with PS (Present Solution) in all numerical examples. Also the designated boundary conditions of clamped, simple and free are denoted by C, S and F, respectively.

### Thick rectangular plate

The vibration analysis of thick square and rectangular plates using the assumed mode method was already performed by Kim et al. [8], using the in-house MATLAB code. In [8] SSSS, SCSC, CCCC and SSFS boundary conditions were taken into account and very good agreement with FEM results was obtained. Here, the VAPS software is applied to a plate with length equal to 2.0 m and width equal to 1.6 m, and FFSS edge constraints. The obtained results together with FEM solutions obtained with NASTRAN [26] are presented in Table 1, and the mode shapes are shown in Fig. 6.

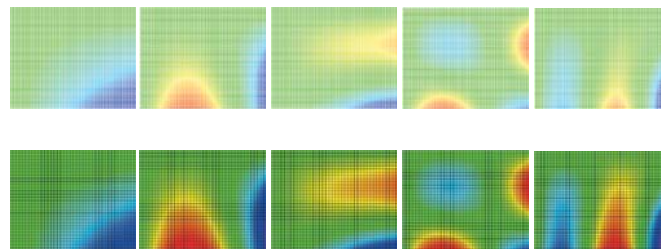


Fig. 6. Mode shapes of a rectangular plate,  $h/a = 0.1$ , FFSS

Tab. 1. Natural frequency  $f$  (Hz) of rectangular plate, FFSS

Mode no.	$h/a$	PS	FEM	Diff., %
1	0.01	5.23	5.21	0.38
	0.1	50.88	50.72	1.76
2	0.01	24.44	24.37	0.29
	0.1	232.79	230.68	0.91
3	0.01	33.78	33.70	0.24
	0.1	319.87	322.00	-0.66
4	0.01	60.15	59.83	0.53
	0.1	544.94	540.67	0.79
5	0.01	66.94	66.79	0.22
	0.1	609.64	620.15	-1.69

### Plate with holes

A plate with length and width equal to 6.0 m and 4.0 m, respectively, and six rectangular holes with dimensions 0.2 x 0.1 m is considered. Results of the free vibration analysis for FCSC boundary conditions and different relative plate thickness  $h/b$  are given in Table 2, where very good agreement of the results is obvious. In the case of the first mode which appears as the most relevant for structural design, discrepancies between VAPS and NASTRAN are within 0.5%. Bird's eye views on the first three natural modes of plate flexural vibrations are presented in Fig. 7 and, as expected, very good agreement in this case also is obvious.

Tab. 2. Natural frequency  $f$  (Hz) of rectangular plate with six rectangular holes, FCSC

Mode no.	$h/b$	PS	FEM	Diff., %
1	0.01	6.87	6.85	0.29
	0.1	65.99	65.68	0.47
2	0.01	14.81	14.57	1.65
	0.1	139.04	136.76	1.67
3	0.01	18.58	17.83	4.21
	0.1	166.62	166.40	0.13

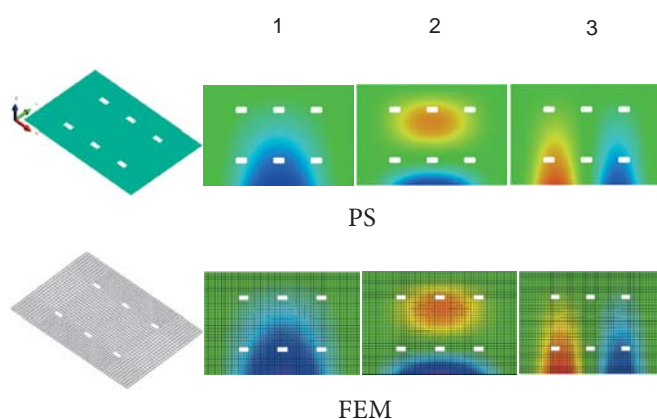


Fig. 7. Models and mode shapes of a rectangular plate with six rectangular holes,  $h/b = 0.01$ , FCSC

### Stiffened panel

The free vibration analysis of the stiffened panel with mixed framing (cross-stiffened panel) and FFCC boundary conditions was conducted, where the effective widths of stiffeners to evaluate the moment of inertia of the beam cross-section were set to the frame intervals. The panel length and width is 5.0 m and 2.5 m, respectively, while the plate thickness is equal to 0.025 m. The same panel, but with different boundary conditions is analysed in [21]. The stiffeners in longitudinal direction are I profiles with height of 120 mm and width of 10 mm, and their spacing equal to 0.5 m. For the transverse direction, 4 equidistant stiffeners with I profile 150 x 12 mm are applied. The corresponding FE model is comprised of 320 finite elements (200 plates and 120 beams). The mode shapes are in good agreement with FEM results, same as the natural frequencies, Fig. 8.

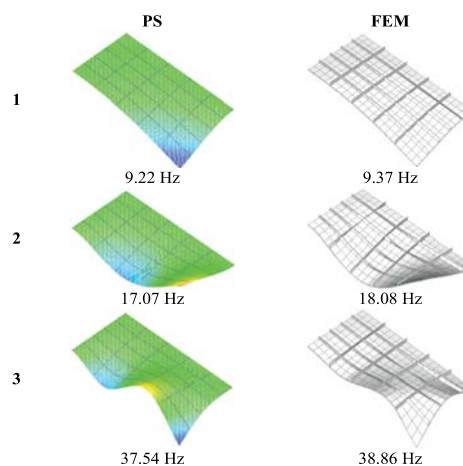


Fig. 8. Mode shapes of a stiffened panel with mixed framing, FFCC

### Stiffened panel with holes

The free vibration analysis of a stiffened panel with oval holes and transverse stiffeners is performed using both VAPS and NASTRAN software. The panel length and width are 4.0 m and 3.2 m, respectively, and the dimensions of the holes are 800 x 600 mm. Three equidistant stiffeners are I profiles with height of 250 mm and width of 10 mm, while the thickness of the panel plate is 15 mm. In this case the corresponding FE model consists of 1150 elements (1072 plates and 78 beams). The natural frequencies and mode shapes for the FCSC boundary conditions are shown in Fig. 9, where very good agreement is also achieved.

In the next numerical example, a stiffened panel with length of 14.0 m and width of 10.0 m. The longitudinal framing (1300 x 15) and six circular holes are considered. The thickness of the plate is 50 mm and the hole diameter is equal to 1000 mm. The FE model of the longitudinally stiffened panel consists of 4100 plate and 280 beam finite elements. The CFCC boundary condition is considered. The natural frequencies of the stiffened panel with circular holes and longitudinal stiffeners are presented in Fig. 10 and the agreement of the results is also good, as was the case in the previous numerical examples.

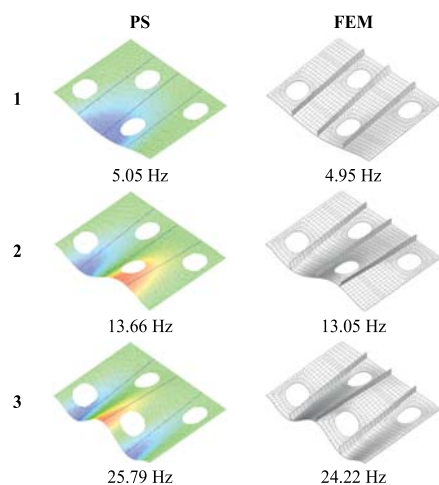


Fig. 9. Mode shapes of a stiffened panel with oval holes and transverse framing, FCSC

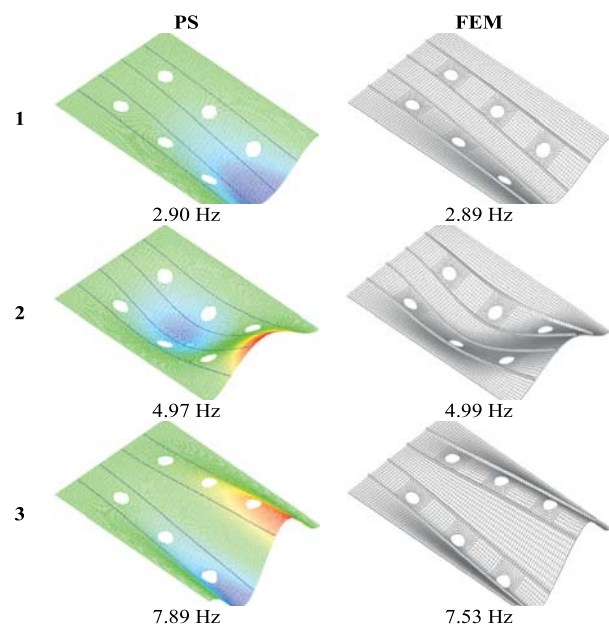


Fig. 10. Mode shapes of a stiffened panel with circular holes and longitudinal framing, CFCC

## CONCLUSION

Application of the assumed mode method to free vibration analysis of different plate systems is reviewed. The developed simplified procedure, based on the energy approach, can be applied to thin and thick plates and stiffened panels with and without holes, respectively. Total potential and kinetic energy should be expressed in a convenient manner depending on the system topology. Based on the Lagrange's equation the governing system of matrix equations is derived. Comparisons with FEM results show that the method is very accurate from an engineering point of view. It should be noted that the method can consider all types of boundary conditions and different relative thicknesses of plates, as well as various framings and hole shapes. Short description of the in-house VAPS software is also provided in the paper. The VAPS software is very user-friendly and can be used for fast model preparation, solving of the eigenvalue problem, and postprocessing of the results.

Future investigations should be oriented to the extension of the developed software package VAPS to the vibration analysis of orthotropic plates assuming different materials, and to more complex structural parts of ships and offshore structures, such as, for instance, stiffened panels with additional attachments (lumped inertia and stiffness elements), thick plates and stiffened panels immersed in the water, etc. Also forced response will be considered.

## ACKNOWLEDGEMENTS

This work was supported by a National Research Foundation of Korea (NRF) grant funded by the Korean Government (MSIP) through GCRC-SOP (Grant No. 2011-0030013).

## BIBLIOGRAPHY

- [1]Reissner E.: The effect of transverse shear deformation on the bending of elastic plate. Transactions of ASME Journal of Applied Mechanics, 12, (1945), pp. 69-77
- Mindlin R. D.: Influence of rotary inertia and shear on flexural motions of isotropic elastic plates. Journal of Applied Mechanics, 18, 1(1951), pp. 31-38
- Liew K. M., Xiang Y., Kitipornchai S.: Research on thick plate vibration: a literature survey. Journal of Sound and Vibration, 180, (1995), pp. 163-176
- Senjanović I., Vladimir N., Tomić M.: An advanced theory of moderately thick plate vibrations. Journal of Sound and Vibration, 332, (2013), pp. 1868-1880
- Senjanović I., Tomić M., Vladimir N.: Cho D. S.: Analytical solution for free vibrations of a moderately thick rectangular plate. Mathematical Problems in Engineering, 2013, (2013), Article ID 207460
- Liew K. M., Xiang Y., Kitipornchai S.: Transverse vibration of thick plates – I. Comprehensive sets of boundary conditions. Computers and Structures, 49, (1993), pp. 1-29
- Dawe D. J., Roufaeil O. L.: Rayleigh-Ritz vibration analysis of Mindlin plates. Journal of Sound and Vibration, 69, 3(1980), pp. 345-359
- Kim K.H., Kim B.H., Choi T.M., Cho D.S.: Free vibration analysis of rectangular plate with arbitrary edge constraints using characteristic orthogonal polynomials in assumed mode method. International Journal of Naval Architecture and Ocean Engineering, 4, (2012), pp. 267-280
- Chung J.H., Chung T.Y., Kim K.C.: Vibration analysis of orthotropic Mindlin plates with edges elastically restrained against rotation. Journal of Sound and Vibration, 163, (1993), pp. 151-163
- Auricchio F, Taylor R.L.: A triangular thick plate finite element with an exact thin limit. Finite Elements in Analysis and Design, 19, (1995), pp. 57-68
- Lovadina C.: Analysis of a mixed finite element method for the Reissner-Mindlin plate problems. Computer Methods in Applied Mechanics and Engineering, 163, (1998), pp. 71-85
- Hughes T.J.R., Tezduyar T.: Finite elements based upon Mindlin plate theory with particular reference to the four-node isoparametric element. Journal of Applied Mechanics, 48, (1981), pp. 587-596

13. Bletzinger K., Bischoff M., Ramm E.: A unified approach for shear-locking free triangular and rectangular shell finite elements. *Computers and Structures*, 75, (2000), pp. 321-334
14. Nguyen-Xuan H., Liu G. R., Thai-Hong C.: Nguyen-Thoi T. An edge-based smoothed finite element method (ES-FEM) with stabilized discrete shear gap technique for analysis of Reissner-Mindlin plates. *Computer Methods in Applied Mechanics and Engineering*, 199, (2010), pp. 471-489
15. Senjanović I., Vladimir N., Hadžić N. Modified Mindlin plate theory and shear locking-free finite element formulation. *Mechanics Research Communications*, 55, (2014), pp. 95-104
16. Cho D.S., Vladimir N., Choi T.M.: Approximate natural vibration analysis of rectangular plates with openings using assumed mode method. *International Journal of Naval Architecture and Ocean Engineering*, 5, 3(2013), pp. 478-491
17. Paramasivam P.: Free vibration of square plates with openings. *Journal of Sound of Vibration*, 30, (1973), pp. 173-178
18. Kwak M.K., Han S.: Free vibration analysis of rectangular plate with a hole by means of independent coordinate coupling method. *Journal of Sound of Vibration*, 306, (2007), pp. 12-30
19. Grossi R.O., del V. Arenas B., Laura P.A.A.: Free vibration of rectangular plates with circular openings. *Ocean Engineering*, 24, 1(1997), pp. 19-24
20. Monahan L.J., Nemergut P.J., Maddux G.E.: Natural frequencies and mode shapes of plates with interior cut-outs. *The Shock and Vibration Bulletin*, 41, (1970), pp. 37-49
21. Cho D.S., Vladimir N., Choi T.M.: Natural vibration analysis of stiffened panels with arbitrary edge constraints using the assumed mode method. *Proceedings of the IMechE, Part M: Journal of Engineering for the Maritime Environment*, (2014), DOI: 10.1177/1475090214521179, published online
22. Samanta A., Mukhopadhyay M.: Free vibration analysis of stiffened shells by the finite element technique. *European Journal of Mechanics, A Solids*, 23, (2004), pp. 159-179
23. Sivasubramonian B., Kulkarni A. M., Rao G.V.; Krishnan A.: Free vibration of curved panels with cutouts. *Journal of Sound and Vibration*, 200, (1997), pp. 227-234
24. Sivasubramonian B., Rao G.V., Krishnan A.: Free vibration of longitudinally stiffened curved panels with cutout. *Journal of Sound and Vibration*, 226, 1(1999), pp. 41-55
25. Srivastava A.K.L.: Vibration of stiffened plates with cutout subjected to partial edge loading. *Journal of the Institution of Engineers (India) Series A*, 93, 2(2012), pp. 129-135
26. MSC. MD Nastran 2010 Dynamic analysis user's guide. MSC Software, 2010

## **CONTACT WITH AUTHOR**

### **Dae Seung Cho**

Pusan National University  
63 beon-gil, Busandaehak-ro  
Geumjeong-gu, Busan, 609-735  
Korea

daecho@pusan.ac.kr

### **Nikola Vladimir**

University of Zagreb  
Faculty of Mechanical Engineering and Naval Architecture  
Ivana Lucica 5, 10000 Zagreb,  
Croatia

nikola.vladimir@fsb.hr

### **Tae Muk Choi**

Createch Co. Ltd.  
Rm. 206, 11 Engineering Bldg.  
San 30, Jangjeon 2-dong, Gumjeong-gu,  
Busan, 609-735  
Korea

taemuk@createch.co.kr

## PROBLEMS OF DETERMINATION OF WELDING ANGULAR DISTORTIONS OF T - FILLET JOINTS IN SHIP HULL STRUCTURES

Janusz Kozak, Prof.

Jakub Kowalski, M.Sc.

Gdańsk University of Technology, Poland

### ABSTRACT

*Ship hull structure elements are usually joined by welding. Welding distortions may cause many problems during manufacturing process. In the literature a wide spectrum of suggestions has been proposed for correct estimation of welding deformation, particularly angular ones, in the fillet welded T-joints. In this work a verification of certain methods selected from the literature is presented basing upon the results of the laboratory measurements. To this end, values determined on the basis of engineering hypotheses have been compared with those obtained from the laboratory tests.*

**Keywords:** welding deformations, ship structure welding, angular distortions in welded T-joints

### INTRODUCTION

During building processes of ship's metal hull joints of structural elements are generally made by means of welding techniques. As a result of using the welding processes, in the area of welded joints and neighbouring structures, arise stresses which – depending on stiffness of the object in question – manifest themselves in the form of deformations of various kinds. They often occur in an uncontrollable way causing many troubles during production, hence they significantly influence manufacturing accuracy of products.

Deformations which exceed allowable values, may cause troubles in assembling hull's sections or make the operation completely unfeasible (Fig. 1), unfavourably influence further manufacturing processes and final quality of a product, lower its usage and aesthetic features.

Welding deformations are strictly associated with welding process hence they influence dimensional deviations of structure after welding. Excessive deformations which exceed permissible limits, require to be removed by straightening or in extremely unfavourable cases a new structure is to be produced, which extends time of manufacturing and rises its cost.



Fig. 1. Welding deformations of a plate section

It should be stressed that already quality of structural design may to a large extent decide on susceptibility of the structure to deforming during production processes. Therefore already in the structural design stage, should be undertaken appropriate measures in order to minimize expected consequences in the area of welding deformations. In the stage of preparation of production process the principle of applying every possible preventing measures against deformations should be used

instead of assuming their removing in general after production of structure. As proved in practice, sum of effects resulting from application of many, rather tiny, preventing measures makes it possible to manufacture whole structure at maintaining the principle of minimizing production troubles and reducing the straightening operation to a “cosmetic” treatment only. Therefore capability of the predicting, estimating and preventing of welding distortions is an important tool in production of a thin – walled metal structure such as a floating object’s hull.

There are engineering ways to minimize quantity of deformations and to remove them. Among them the following may be for instance numbered: correct sequence of assembling and welding operations, application of initial deformations, rigid clamping the elements during welding, loading the elements by external forces to introduce a deflection opposite to that expected. In any case the prediction and compensation of deformations aiming at application of initial deformations require knowledge and skill in determining their form and quantity.

### ANGULAR DEFORMATIONS IN WELDED T- JOINT

Present state of the theory in the field of calculation of welding deformations makes it possible to precisely analyse the issue in order to preliminarily determine deformations and select production methods and means for conducting manufacturing process. During preparation of constructional and technological assumptions appropriate calculation methods should be used, including computer programs. The only problem consists in complexity of computational process. In spite of the fact that the physical background of welding processes has been already formulated and the formulas – mainly empirical - for estimating the deformations, have been elaborated, impact of many structural and technological factors results in that to keep full control over deformations is very difficult.

The formulas met in the literature often give, especially in case of thin-walled structures such as contemporary ship’s hull, results which significantly differ from actual ones. Therefore to verify such data is necessary.

The issue of excessive welding deformations arises especially in manufacturing ship hull structures with thin plates less than 10 mm in thickness. The index should be taken only as approximate one because assessment criteria may depend on requirements put for ready-welded structure, as for instance to get relatively small welding distortions is required to ensure appropriate conditions for assembling and welding propulsion machinery foundations /welded of thick plates/, and - in contrary - large deformations of certain partition walls in superstructure may be tolerated if only they are boarded on both sides and do not participate in carrying local loads.

Since over two decades the Finite Element Analysis (FEA) and Finite Element Method (FEM) have been applied to determination of stress distribution field during welding process. Achieving correct results is complicated by such problems as:

material properties varying during welding process, high temperature gradients, stress and strain development both in the time and space coordinates domain, large deformations of thin-walled structures and phase and structural transitions in material. Majority of presently proposed simulation methods for welding processes is based on the assumption of a small deformation and is limited only to simple structures and shapes (e.g. butt welds) or is focused only on heat affected zone not taking into account surrounding structure. Analysis of small deformations assumes infinitesimal displacements and loads applied to a structure of non-deformed geometry. Examples of such simulations are given in [6] and [9] where impact of a few parameters on welding process model, is presented.

In the amount of welded joints in ship hull structure, fillet welds take a large part. In this case numerical calculations are complicated by the fact that the joints are made in the form of two welds laid often non-simultaneously [3].



Fig. 2. View of a ship performing transport task in stormy weather [33]

In the works [10][7][8] N. O. Okerblom has given the theoretical background for determining welding stresses and strains. In analysis process changes in plastic deformations are considered in every phase of heat cycle to which a given area of cross-section of an element under welding is subjected, as well as the deformations are simulated during whole heat cycle. However to apply the so proposed approach to calculation of angular distortions in T-joint is difficult.

### EXPERIMENTAL DETERMINATION OF WELDING ANGULAR DEFORMATIONS OF FILLET JOINT IN SHIP HULL STRUCTURE [1]

For determination of a typical angular deformation in welded T-joint it was arranged to produce a series of such joints with simultaneous recording process parameters and occurring deformations. It was assumed that the designed joint has been a modification of a typical ship structure joint having weld dimensions in accordance with PRS rules, Part II – Hull [13]. The dimension was 3,5 [mm]. The experiment consisted in determination of angular deformation in the joint both during and after welding a bulb profile stiffener to a plate. The specimens were made of ship structural steel of A grade. The tests were carried out with 5 specimens.

Fig. 3 highlights the concept of test stand , testing and measurement method as well as tested model dimensions.

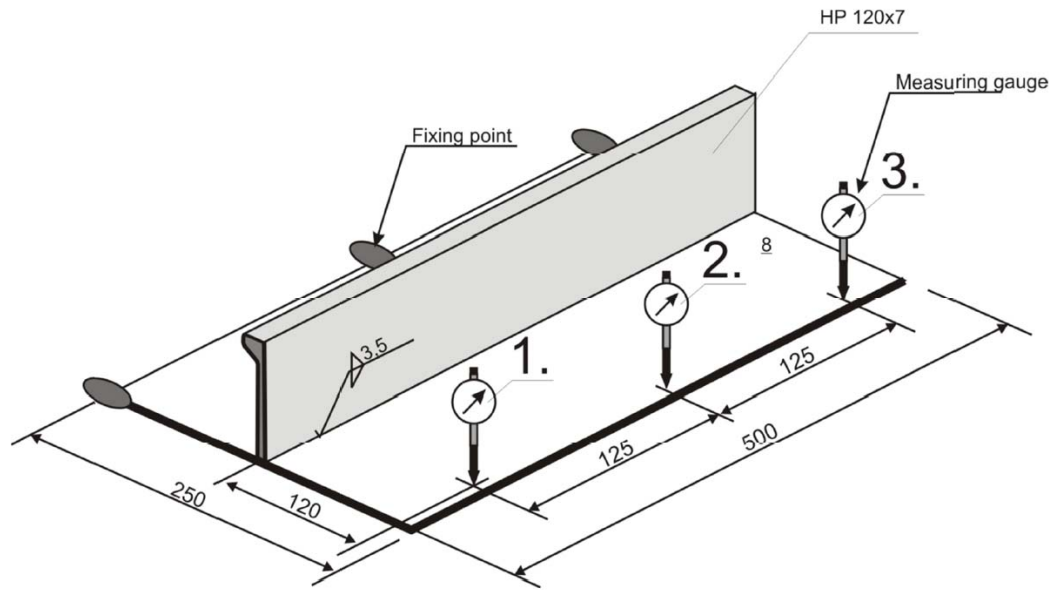


Fig.3. Schematic diagram of tested model and test stand

To eliminate bending deflection during welding positional welds were applied between the plate and stiffener and the specimen was fastened to the welding bench (Fig.4). The welding process was carried out according to the welding procedure (WPS) for the welding method 136 – FCAW (Flux-Cored Arc Welding), approved by PRS.

Procedure of joint preparation, geometry of welds, sequence of runs and welding process parameters are presented in Tab. 1.

Tab. 1 Welding Procedure Specification (WPS)

Welding Procedure Specification for test joint									
Method of preparation		Oxy cutting & grinding		Material thickness		t=7[mm]			
Joint preparation				Welding sequence					
Process	Ru	Size of electrode [mm]	Current [A]	Voltage [V]	Current Polarity	Wire feed speed [m/min]	Weld speed [cm/min]	Heat input [kJ/cm]	
PA,PB	1+	F1,2	190-240	23-27	DC(+)	6,5-10,0	16-23	9,1-19,5	
Shielding gas			EN ISO 14175:M21		Gas flow rate		18-22 [l/min]		
Filler material			T464ZPMIH5		Preheating temperature		Min. 10°C		

During welding all the process parameters were recorded: arc voltage, welding current intensity and weld laying speed. During laboratory tests the T464ZPMIH5 welding wire of the characteristics: 460 MPa minimum yield strength and 20% minimum elongation, was used.

Angular deformation was measured by using M2 TOP dial gauges (Fig. 3 and 4).

After manufacturing the welds their size were measured and for further analysis were taken only the specimens whose welds showed dimensions complying with the assumed value of 3,5[mm]. Results of the performed tests are given in Tab. 2.

Tab. 2. Results of the performed tests [1]

Specimen	No. of run	Voltage U [V]	Current intensity I [A]	Welding time[sec]	Displacements		
					Gauge 1 [mm]	Gauge 2 [mm]	Gauge 3 [mm]
1	1	27,5	184	33,2	1,76	1,73	1,21
	2	27,7	175	20,1	4,85	5,71	4,99
2	1	26,7	172	34,9	1,76	1,60	1,99
	2	26,5	173	38,5	4,87	4,90	5,57
3	1	26,5	185	43,7	1,41	1,97	1,98
	2	26,8	174	39,8	4,11	4,98	4,20
4	1	26,7	182	46,2	1,65	1,71	2,04
	2	27,2	170	34,3	4,31	4,41	4,82
5	1	26,9	185	37,4	1,56	1,79	1,89
	2	27,2	170	45,6	4,45	5,01	4,95

The determined mean total angular deformation resulting from the double fillet weld, recorded in the mid-length point of the specimen (Gauge 2), amounted to 2,39°.



Fig.4. Measurement of angular deformation

## ANALYSIS OF ANGULAR DISTORTION BY USING SELECTED ENGINEERING FORMULAS

### Method 1 [12]:

In this approach it is assumed that angular distortion results from non-uniform distribution of transverse shrinkage of weld itself and its surrounding zone. The distortion is meant to be the deflection angle  $\beta$  of the plates (Fig. 5) in relation to their initial position prior to welding and depends on the weld dimension  $a$ .

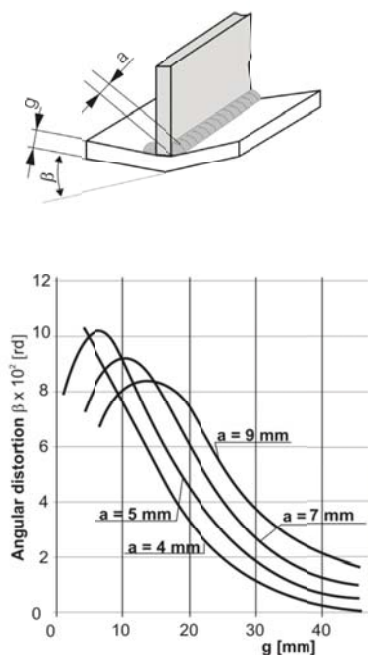


Fig. 5. Nomogram for determining the angular distortion  $\beta$  [4]

For the data of the tested specimens the deflection angle determined by using this method, amounts to  $\beta = 3,30^\circ$

### Method 2 [11]:

In this method it is assumed that quantity of angular distortions depends first of all on the ratio of the fillet weld thickness  $a$  and the flange plate thickness  $g$  (Fig. 6). As results from the analysis of the presented indices, in the case of flange plate of a small thickness, e.g.  $g = 6$  mm, the angular distortions are low as temperature gradients across plate thickness are low. The largest angular distortions occur for the flange plate of 8÷12 mm in thickness. Moreover, it can be observed that for the flange plate of a greater thickness the angular distortions decrease.

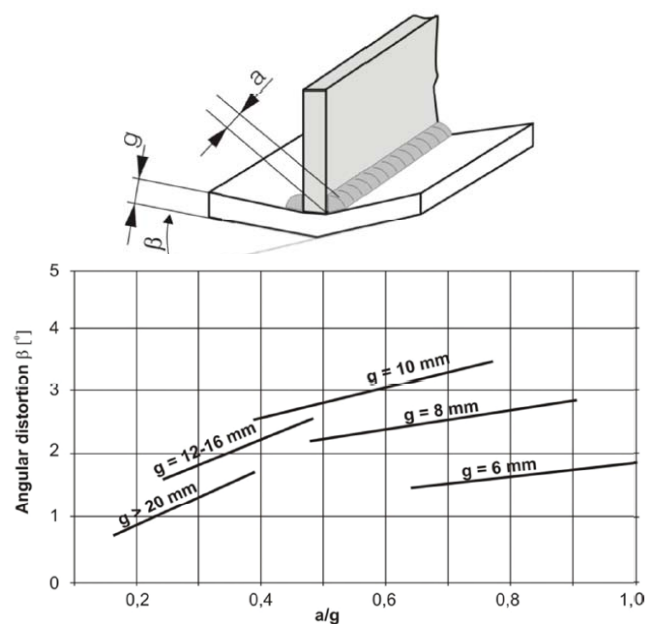


Fig. 6. Data for the plate angular distortion  $\beta$  resulting from fillet welds [3]

For the data of the tested specimens the deflection angle determined by using this method, amounts to  $\beta = 2,20^\circ$

**Method 3 [4]:**

In this method it is assumed that the angular distortion resulting from a single fillet weld may be determined by using the following formula:

$$\beta_0 = 0,005 \left( 14 \frac{a}{g} - 1 \right) [rad]$$

and, for a double fillet weld it may be assumed that the total deflection angle is two times greater:

$$\beta_{1+2} \cong 2\beta_0$$

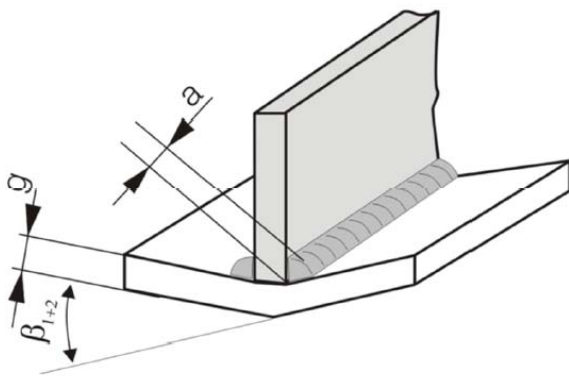
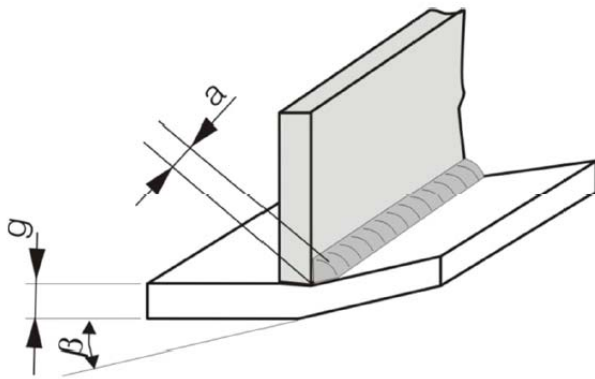


Fig. 7. Definition of the angular distortion according to Method 3 [4]

In case of long welds the angular distortion grows and its extreme value may amount to  $\beta_{1+2} = 3\beta_0$ .

For the data of the tested specimens the deflection angle estimated by using this method, amounts to  $\beta_{1+2} = 2,94^\circ$ .

**Method 4 [2]:**

In this approach it is assumed that the angular distortion results from weld transverse shrinkage (Fig. 8), as well as from surrounding material shrinkage greater than the first one. Occurrence of angular distortion is conditioned by a non-identical plastic deformation of welded material and weld, observed across thickness.

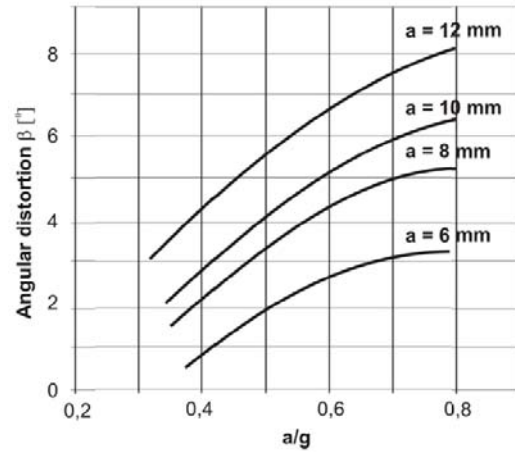


Fig. 8. Indices for estimating the angular distortion resulting from fillet welds [2]

Analytical determination of angular distortion values is not widely used in engineering practice. It results from that it is not possible to take into account, with a sufficient accuracy, many technological factors such as: welding energy, welding method, shape and size of plastic deformation zone, number of runs, plate thickness, weld length, stiffness of welded joint. The formulas met in the literature often provide results which differ from actual ones rather considerably.

The angular distortion value determined for the tested specimen by means of the indices given in Fig. 8, amounts to  $\beta = 2,75^\circ$ .

**Method 5 [5]:**

During T-joint welding the angular distortions are caused by plate's bending due to non-uniform transverse shrinkage across plate thickness as well as by plate's bending resulting from shrinkage of slightly melted metal of weld itself. Fig. 9 presents the mechanism of angular distortion in T-joints.

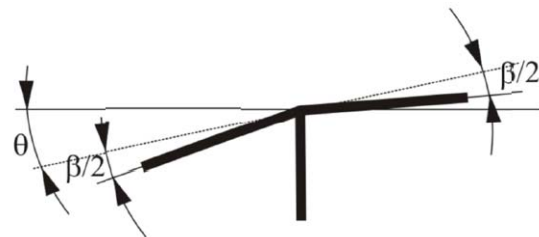


Fig.9. Mechanism of angular distortion in T-joints, assumed in the method in question [5]

During laying the first weld the flange plate will rotate by the angle  $\Theta$  in relation to its initial position as a result of weld metal shrinkage. Moreover, as a result of non-uniform transverse shrinkage across flange thickness its bending will occur by the angle  $\beta_1$  against its initial plane. The angle  $\Theta$  only slightly depends on welding parameters and its value may be assumed equal to  $0,02 \div 0,024$  rad ( $1,2 \div 1,5^\circ$ ). The angle  $\beta_1$ , if the flange is free to deform, can be determined on the basis of the diagram (nomogram) shown in Fig. 10, where the computational thickness  $g_0$  is taken equal to the flange

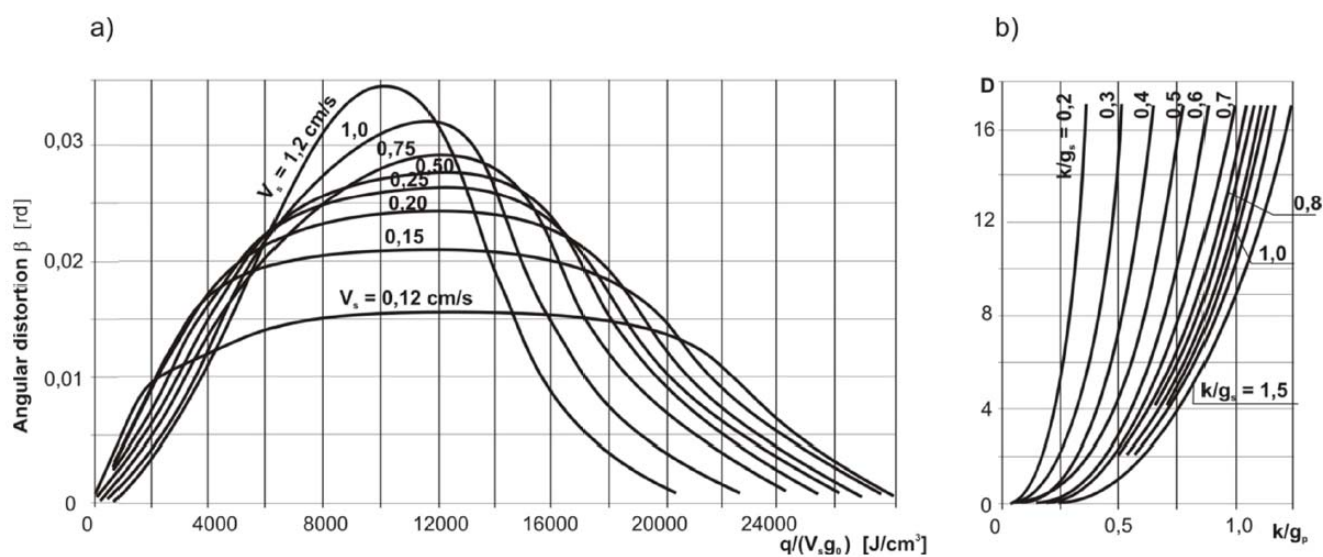


Fig.10. Nomograms: a) for determining the angular distortions  $\beta$  during welding butt welds and T-joints in function of the welding conditions  $q$ ,  $v_s$ , and the computational shell plate thickness  $g_0$ , b) for determining the coefficient  $D$  [5]

thickness  $g_p$ , and the computational value of linear energy is calculated by means of the following formula:

$$q_{l_0} = q_l \frac{2g_p}{2g_p + g_s}$$

where:  $g_p$ - flange plate thickness [cm],  $g_s$  - stiffener thickness [cm].

In the case of double welding in T-joint, the plate deflection angle  $\beta$  is calculated as follows:

$$\beta = \beta_1 + \beta_2 + \beta_k$$

where:  $\beta_1$  and  $\beta_2$ , [rad] - plate deflection angles resulting from non-uniform transverse shrinkage in the first and the second weld, respectively;  $\beta_k$  [rad]- plate deflection angle due to the double welding of the stiffener, resulting from shrinkage of slightly melted metal during second run.

The angle  $\beta_1$  and  $\beta_2$  is determined separately for the weld 1 and 2 by using the nomogram of Fig. 10a in function of welding parameters, thickness of plates and welding speed. The angle  $\beta_k$  is calculated as follows:

$$\beta_k \approx \varepsilon_e D$$

where:  $D$  - a coefficient dependent on the weld leg  $k$ , flange plate thickness  $g_p$  and stiffener thickness  $g_s$ ; its value can be determined from the nomogram of Fig. 10b; and  $\varepsilon_e$  - relative deformation (strain) corresponding to yield strength of weld metal.

For the parameters of the conducted experiment the final angular distortion calculated in compliance with Method 5 is equal to  $\beta = 2,98^\circ$ .

## COMPARISON OF THE OBTAINED RESULTS

Analysis of the results of determination of the angular distortion resulting from double fillet weld in T - joint shows that, except of the approach 2, the remaining methods provide over-estimated results. Values of the distortions calculated by using the selected algorithms are given in Tab. 3 together with results obtained from the conducted experiment.

Tab. 3 Comparison of the obtained results

Method	Obtained angular distortion [°]	Deviation from the mean value from the experiment [%]
No.1 [12]	3,30	+38
No. 2 [11]	2,20	-8
No. 3 [4]	2,94	+23
No. 4 [2]	2,75	+15
No. 5 [5]	2,98	+25
Experiment ( mean value of 5 tests)	2,39	

As can be observed, all the results are comprised within the interval of 2,20÷3,30, hence it may be concluded that on the engineering accuracy level a simplicity and possibility of fast and easy use of a method decide on its practical usefulness.

The result obtained from the approach 2, despite its underestimated value, has appeared to be the closest to the mean value achieved from the performed experiment (see Tab. 3).

## SUMMARY

Value of angular distortions in a welded T-joint depends on many parameters, including: weld geometrical dimensions, weld penetration profile, mechanical and physical-chemical properties of material, electric current source. In some cases calculated values of angular distortions greatly differ from those obtained from the experiment. It results from difficulty and - in many cases - just from inability of determining the impact of all the factors on value of the distortion. Usually, welding deformations lead to a more complex effect than an angular distortion itself, therefore the values obtained by applying theoretical methods should be considered approximate (rough) ones only.

The most effective method in mitigating welding deformations, apart from straightening, is an appropriate preparation of production process.

## BIBLIOGRAPHY

1. Brzozowska A.: Review and verification of formulas for estimating angular distortions in T-joints (in Polish). Diploma thesis, Faculty of Offshore Engineering and Shipbuilding, Gdańsk University of Technology, 2014
2. Ferenc K., Ferenc J.: Welded structures, Joints (in Polish). Wydawnictwa Naukowo-Techniczne (Publishers), Warszawa, 2000
3. Gourd L.M.: Principles of Welding Technology. The Welding Institute, London, 1995
4. Jakubiec M., Lesiński K. J., Czajkowski H.: Welding of steel structures (in Polish). Wydawnictwo Politechniki Gdańskiej (Publishers), Gdańsk, 1987
5. Jakubiec M., Lesiński K., Czajkowski H.: Technology of welded structures (in Polish). Wydawnictwa Naukowo-Techniczne (Publishers), Warszawa 1987
6. Michaleris P., Debiccari A.: Prediction of Welding Distortion, a two-step numerical analysis technique developed to predict welding induced distortion and the structural integrity of large and complex structures. Paper presented at the AWS Annual Convention, April 1996, Chicago, ILL. Welding Research Supplement, April 1997
7. Myśliwiec M.: Thermal – mechanical background of welding technology (in Polish). Wydawnictwa Naukowo-Techniczne (Publishers), Warszawa 1972
8. Myśliwiec M.: Welding technology in shipbuilding (in Polish), Wydawnictwo Morskie (Publishers), Gdańsk, 1971
9. O'Brien, Roger William Predicting weld distortion in the design of automotive components. Durham theses, Durham University, 2007, Available at Durham E-Theses Online: <http://etheses.dur.ac.uk/2462/>
10. Okerblom N. O., Demjancevic V. P., Bajkova I. P.: Proektirovanie technologii izgotovlenija svarnych konstrukcij : rascetnye metody (in Russian).
11. Engineer's handbook : Welding technology, Vol. I (in Polish). Wydawnictwa Naukowo-Techniczne (Publishers), Warszawa, 2003
12. Piwowar S.: Welding technology: Manufacturing techniques (in Polish). Państwowe Wydawnictwo Naukowe (Publishers), Warszawa, 1978
13. Polish Register of Shipping : Rules for the classification and construction of sea-going ships, Part II – Hull (in Polish), Polski Rejestr Statków (Publishers), Gdańsk, 2015
14. Sędek P.: Problems of welding stresses and deformations (in Polish). Wydawnictwo i dystrybucja: Biuro Gamma (Publishing and disposal), Warszawa, 2000

## CONTACT WITH THE AUTHOR

Janusz Kozak,  
Jakub Kowalski

Gdańsk University of Technology  
11/12 Narutowicza St.  
80 - 233 Gdańsk  
**POLAND**

# SELECTED ASPECTS OF BUILDING , OPERATION AND ENVIRONMENTAL IMPACT OF OFFSHORE WIND POWER ELECTRIC PLANTS

Adam Mroziński, Ph. D.  
Izabela Piasecka, Ph. D.  
University of Technology  
and Life Sciences in Bydgoszcz, Poland

## ABSTRACT

*This paper describes essence of work of offshore wind power electric plants and crucial aspects of their building and operating. Prospects for development of global, European and domestic markets of offshore wind power industry have been delineated. A comparative analysis of environmental impact of an offshore and land-based 2MW wind power electric plant has been performed by using LCA method and Ecoindex – 99 ( Ekowskażnik 99 ) modelling.*

**Keywords:** wind energy, offshore wind power electric plants, LCA method , Ekowskażnik 99 (Ecoindex - 99)

## Introduction

Offshore wind power industry plays greater and greater role in the process of providing safety of power supply for Europe. As results from the document of European Commission titled: Offshore wind energy: Activity necessary for reaching aims of energy policy in the perspective up to the year 2020 and further, 40 % of energy production potential connected to network comes from wind power industry. For possible development of offshore wind power industry in Poland it is crucial to have possibility of adjoining new installations to Domestic Electric Power System, to organize own port and shipyard back-up facilities and a stable, effective system for supporting renewable energy sources [7, 16].

Economic conditions and administrative and legal difficulties have been so far substantial obstacles in developing offshore wind power industry. In Poland first steps towards creating favourable legal conditions for offshore sector have been done just in the last years. Owing to changes introduced into the Act on Polish sea territories and maritime administration, in 2011 new conditions for the siting of offshore wind power installations on Polish sea territories came into effect. Area of Polish sea territories amounts to about 33 thousand km<sup>2</sup>, however the total area of sea waters determined by the ministry responsible for maritime economy as potentially accessible for offshore wind power industry, amounts to over 2.000 km<sup>2</sup>. The first offshore wind farm planned to be built in Poland, will have its rated power of about 100 MW [7, 8, 16].

## Major aspects of building the offshore wind power electric plants

Offshore wind farms are consisted of groups of windmills of different number of units. A single offshore wind power electric plant contains a foundation, tower , nacelle and rotor. There are several different design solutions of building the windmill foundations. Their applications depend on water depth and sea bed geological structure in site . Most often applied kinds of foundations are : monopile (74%), (16%), jacket (5%) and tripods (2%) (Fig. 1 and 2) [3, 5, 9].

The monopile is the most often chosen kind of foundation because of its low cost, simplicity and possible implementation in shallow waters (less than 20 m deep). Installation of a monopile does not require any preparation of sea bed - the pile is drilled or driven in it. Monopiles cannot be used in case of sandy bottom or in places where boulders occur. GBS (gravity foundation) has been applied in the beginning of development of wind farms in shallow waters (about 15 m deep), in present they are being adjusted to greater and greater water depths (up to about 30 m). The technology is based on a large surface and mass of foundation that secures the windmill against wave and wind forces. They are almost entirely manufactured on shore with the use of concrete and steel. The tripod is a structure which makes use of the same solution as that applied to monopiles. Its base is supported on three columns - this way it can be used in deeper waters. Three ends of the base are seated on or driven into sea bed to support central part of the facility connected with turbine.

The jacket, in contrast to tripods, is consisted of a more spread structure of steel bars symmetrically arranged beyond the main axis of the entire structure. It leads to a significantly lower consumption of materials [3, 5, 16, 17].

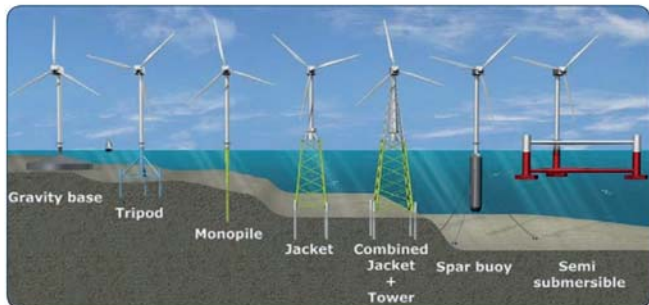


Fig. 1. Various solutions of anchoring the offshore wind power electric plants, depending on water depth [3]

Offshore wind power industry is now in the phase of permanent technological development. Owing to investments into new technologies its continuous evolution can be observed in this sector. Floating foundations which are now under tests, may exemplify this trend. It is expected that, due to development of the solution, the limitations associated with water depth and sea bed structure will be overcome [16, 22].

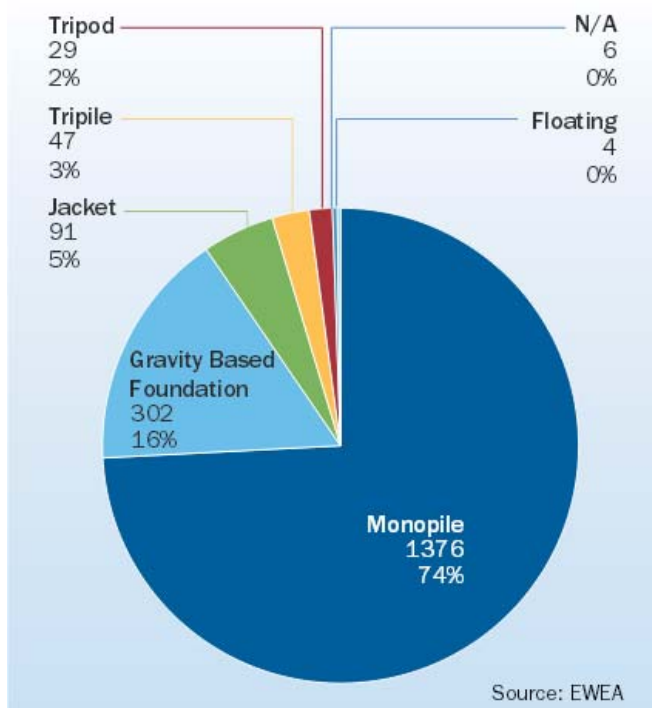


Fig. 2. Relative amount of power installed in 2012, depending on an applied manner of the anchoring of foundation of offshore wind power electric plant [9]

## Selected aspects of operation of offshore wind power electric plants

Regardless of many obstacles indispensably connected with using the offshore windmills, they are expected to form the future of all wind power industry. Main differences between offshore and land-based wind turbines result from two factors: marine environment and high cost of installation. Each of them influences characteristic features of wind farm. Presently investment cost of offshore installation is by 30 ÷ 50 % greater than that of analogous one but based on land. Marine environment requires a special approach to turbine design, which takes into account higher corrosion resistance, design of supporting structure, higher power output, maintenance issues and resistance to heavy weather. Against salt mist corrosion effects, protection means are undertaken in the form of corrosion resisting devices and materials (also application of parts made of stainless steel and glass reinforced plastics- GRP), specialty coating systems for marine applications and accommodations with filtered and conditioned air. Tower anchoring manner and construction for windmills must take into account such factors as: sea tides and currents, height and impacts of waves, possible collisions with ships and icebergs, increased turbulence and wind force during storms. Construction of marine structures is based on principles determined by oil mining industry, adjusted to specificity of offshore wind power electric plants. During erection of an offshore wind farm also ecological aspects are extremely important, especially non-disturbance of ecosystem in waters where a wind farm has to be placed. Wind farms cannot be located along bird flying routes and also more strict preventive means are applied against oil leakage from mechanical devices to sea water (possible in case of an uncontrolled failure) [2, 6, 11, 13, 24, 25].

Among their main drawbacks the following may be distinguished: a more difficult access to objects in comparison to those based on land, a much higher cost of foundation building and wiring to an electric power network, much more expensive maintenance and servicing, necessity of limitation maintenance operations to a minimum (high cost), application of turbines of a much expensive, higher quality in order to limit servicing and replacement of parts, as well as the use of corrosion and erosion preventing means potentially hazardous to the environment, but necessary for construction and foundations. The servicing and maintenance of offshore wind farms is more challenging and costly than in case of land based installations. Duration of maintenance operations reaches 40 ÷ 50 h. Major repair is conducted every fifth year on average, and its expected duration takes about 100 h. Turbines are from time to time not accessible because of strong winds or a low visibility. Experience with offshore wind farms has shown that weather problems make it impossible to perform about 15 % scheduled O&M visits (Operations & Maintenance) [4, 14, 15].

The most important principle of technological development of wind farms is safety of their building. Design features considered in this aspect contain: a permanent integrated platform above splashing zone, fenders absorbing energy of

bumping, elastic gangway ladders for traffic between a ship and turbine, cranes to pull ships closer in case of occurrence of high waves, as well as hoisting and transporting means for carrying personnel and equipment. Certain producers introduce into market a kind of windmills which allow to limit conservation requirements at a simultaneous rise in their reliability and effectiveness, however at the expense of increased cost of the turbine. The features cover also application of direct - drive electric generators (which eliminate transmission gear, i.e. the component most liable to mechanical failures), generators with permanent magnets, which generate a higher voltage and eliminate necessity to install transformers (reducing this way energy losses), entirely covered generators secured this way against effects of marine salty environment, as well as electric control over reduction of deviations, setting the angle of attack of rotor blades, and braking systems in order to eliminate problems occurring in hydraulic systems [1, 10, 14, 15].

The following advantages of offshore wind installations may be considered most important: a more stable action of sea wind, which allows to make use of turbines more effective, a greater wind force at a lower height over sea, which allows to apply towers of a lower height, rise of wind force along with growing distance off the coast, more siting areas, reduction of landscape devastation to a minimum, as well as a limitation of excessive noise close to living buildings, an increase in number of workplaces in comparison with land investments as well as a positive impact on quality of the environment owing to avoidance of contamination emission and the use of a renewable energy source [1, 5, 15].

Main parameters of wind, which influence windmill capacity of generating electric power are: its average and maximum speed, turbulence and drop-offs. Average and maximum wind speeds are greater over sea than land (Fig. 3). Vertical drop-off of wind represents difference in wind speed in relation to difference in level. The wind drop-off is affected by friction of air flow on surface of ground, buildings and other objects which reduce its velocity. In case of offshore wind power electric plants number of potential friction sources is much lower. Similar environmental turbulences due to unevenness of ground surface do not occur at sea [1, 5, 20].

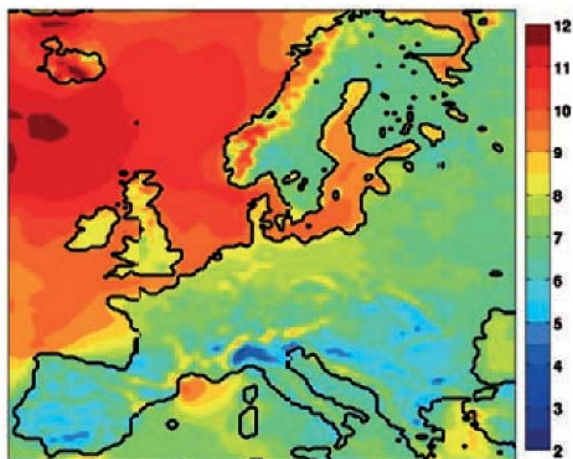


Fig. 3. Yearly average speed of wind ( m/s) at 90 m elevation [9]

Offshore windmills may be also especially favourable for certain aqueous organisms. Fishes may find shelter there since in the wind farm areas the fishing net trawling which can devastate sea bed and endanger organisms living there, is prohibited. The windmills may also be a friendly environment for edible mussels and many kinds of crabs. It is indisputable and beneficial that electric power plants of this kind make acidification of oceans lower by contributing in abatement of CO<sub>2</sub> emission to the atmosphere. However further cooperation of developers, ecologists and scientists dealing with seas and oceans, in the area of research on the impact of windmills onto sea life, is necessary [3, 8].

### Development of offshore wind power industry

Offshore wind power industry is one of the fast developing energy markets in the world. It has been more than 20 years ago when the first in the world wind farm of 5 MW output has been built in Vindeby, Denmark. In Europe over 5 GW electric power generated by offshore wind farms was till now installed, including the amount of over 90 % coming from the North, Baltic and Irish Sea and the English Channel [9, 13]. Among the remaining locations the investment projects sited close to the east coast of China, may be distinguished. Such investment projects become more and more popular in Japan, USA, Canada, Taiwan and India. According to the expectations, up to 2020 even 80 GW new power sources are possible to be installed worldwide. In 2012 the market grown by 1.296 MW, i.e. by 33 % in relation to its level in 2011. Most of the growth (90 %) come from installations in Europe, mainly in Great Britain, Denmark, Belgium, Germany, the Netherlands and Sweden (Tab. 1) [3, 9].

Till 2010, development of offshore wind farm projects has been concentrated on relatively low water depths (up to 10 m) and close-to-shore areas (up to 20 km). Permanent development of technology and growing experience of firms investing into wind power sector have caused that offshore installations are presently sited in areas more and more distant off shore and deeper and deeper waters. For the projects of wind farms executed in 2010 the average water depth amounted to 20 m, and the distance to shore – 30 km. It is expected that till 2030 wind farms would be sited in water areas 60 m deep and 60 km distant off shore. There are also prospects of making use of even more distant water areas (over 60 km), which may be exemplified by German and British projects (Round 3) (Fig. 4) [9]. According to forecasts of European Wind Energy Association the future of the sector of renewable energy sources belongs to offshore facilities. Prior to 2030 power output received either from offshore or land - based windmills may be comparable to each other [9].

### Development prospects for Polish offshore power industry

In Poland, according to the amended act on Polish sea territories, offshore wind farms are allowed to be sited only in the area of exclusive economic zone, i.e. in the distance of 22 km off shore. Polish exclusive economic zone covers the area

Tab. 1. Power output of installations in European offshore and land-based wind power industry in 2012

Country	Land Installations	Offshore Installations	Total
Austria	1.387	0	1.378
Belgium	996	380	1.375
Bulgaria	684	0	684
Cyprus	147	0	147
Denmark	3.241	921	4.162
Estonia	269	0	269
Finland	262	26	288
France	7.564	0	7.564
Greece	1.749	0	1.749
Spain	22.796	0	22.796
Holland	2.144	247	2.391
Ireland	1.713	25	1.738
Lithuania	225	0	225
Luxemburg	45	0	45
Latvia	68	0	68
Malta	0	0	0
Germany	31.027	280	31.307
<b>Poland</b>	<b>2.497</b>	<b>0</b>	<b>2.497</b>
Portugal	4.523	2	4.525
Czech Rep.	260	0	260
Romania	1.905	0	1.905
Slovakia	3	0	3
Slovenia	0	0	0
Sweden	3.582	164	3.745
Hungary	329	0	329
G.B.	5.497	2.948	8.445
Italy	8.144	0	8.144
<b>All together</b>	<b>101.048</b>	<b>4.993</b>	<b>106.041</b>

Source: acc. the authors' own work based on [9]

of about 22,5 thousand km<sup>2</sup>. Theoretical potential of Polish wind power resources amounts to about 130 GW, however it is not practically possible to make use of the whole potential as its estimation has been based on the total area of internal waters and territorial sea. Its technical potential is limited to about 7,5 GW as present limitations for the siting of wind power electric plants in sea areas are much stringer than for land areas. In view of technical possibilities of building wind power electric plants (i.e. sea water depth) and possible conflicts in using the sea space, only a small part of the area (up to 5 %) is deemed to be available for building offshore wind power electric plants up to 2020. Environmental limitations associated with inclusion of large fragments of Polish sea waters into NATURA 2000 network deal consequently also with the sea waters in question, nevertheless the entire area is characteristic of favourable wind conditions. As assumed for offshore wind power electric plants, their whole technical potential may be utilized with a satisfactory economic effect (Tab. 2) [16, 20].

Tab. 2. Predicted potentials of Polish offshore wind power industry

Potential	Power [GW]	Energy [TWh]
Theoretical potential	130	380
Technical potential	130	380
Technical potential under limitations	20	60
Economic potential	7,5	22,5
Market potential in 2020	1,5	4,5

Source: acc. the authors' own work based on [16]

Poland has one of the biggest market potentials of wind farms on the Baltic Sea. As the calculations performed a.o. by the University in Oldenburg, show, the area of Polish exclusive economic zone is one of the territories of the best wind conditions on the Baltic Sea. European Wind Energy Association has estimated that Sweden and Poland, out of all European countries, may install the greatest wind power by 2030, (Fig. 5) [9, 20].

In present, a consortium of private firms has formulated the first development foresight of offshore electric network connecting future wind farms. After preliminary deliberations with authorities responsible for environment protection and land - space economy, have been identified three possible spots where marine electric power cables could be laid onto land; they are located close to Lubiatowo (Choczewo commune, Wejherowo administrative unit, Pomeranian province), Ustka (Ustka commune, Słupsk administrative unit, Pomeranian province) as well as Grzybowo (Kołobrzeg commune, Kołobrzeg administrative unit, West Pomeranian province). For siting offshore windmills altogether 109 places of a total surface area equal to 2503,45 km<sup>2</sup> have been selected, namely in the neighbourhood of Odra Bank (25 places, 637,98 km<sup>2</sup>), Southern Middle Bank (22 places, 501,61 km<sup>2</sup>), Żarnowiec (12 places, 284,22 km<sup>2</sup>) as well as Słupsk Bank (50 places, 1079,64 km<sup>2</sup>) [8, 16, 18].

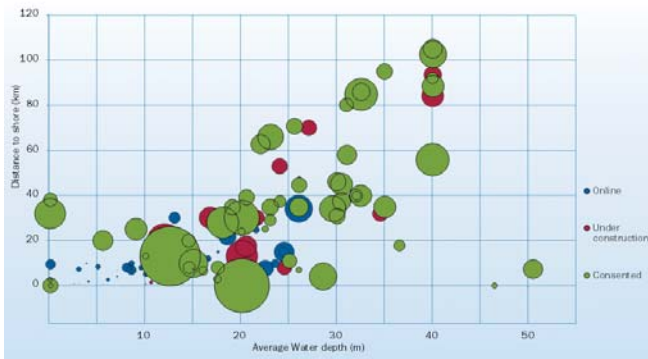


Fig. 4. Development trends in offshore wind power industry in function of distance to shore and water depth in site of new installations [9]

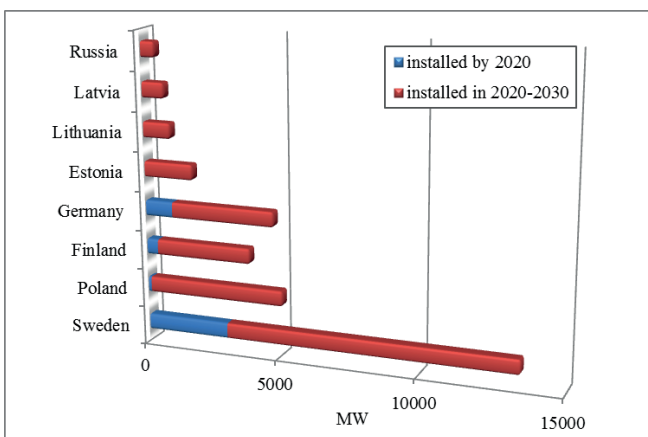


Fig. 5. Scenario of location of wind farm installations on the Baltic Sea up to 2030 Source : acc. the authors' own work based on [9]

## Research methods

The method of environmental assessment of life cycle of products (LCA) serves as a tool for quantitative determination of environmental impact. It is based on collecting environmental factors dealing with a given object. They may also relate to a definite process or other activity conducted within the life cycle beginning from winding up to final recycling. The LCA method makes it possible to identify and assess emission of noxious substances, consumption of materials and energy during all life phases of a given technical object [12, 21].

An Ecoindex - 99 (Ekowskażnik 99) method has been applied to characterize environmental impacts of wind power electric plants. It was developed by an international team of experts representing different European countries (in 1999). It has found application to calculation of maximum detrimental effects onto the environment which may occur on European territory. Some of the processes taking place there have an influence also on global situation. For this reason they are taken into account in calculating the effects in question. Among them the following are counted a.o.: a damage resulting from ozone layer depletion and greenhouse

effect, emission of carcinogenic substances as well as changes occurring in natural resources worldwide. An important factor which influences shape of Ecoindex 99 results is the system of three spheres affecting life cycle: ecosphere, technosphere and evaluation sphere. In the Ecoindex 99 method all the three are taken into consideration to the same extent. Life-cycle model is formulated in technosphere and its results are presented in an inventory table. It is associated with three damage categories modeled in ecosphere. The evaluation sphere is used for assigning appropriate weights in order to obtain a reliable index. When using the Ecoindex 99 method, the following damage categories in which environmental impacts obtained during analysis phase undergo assessment, have been selected on the basis of definition of the environment: ecosystem quality, human health and natural resources [12, 19].

In the considered investigations a 7.1 SimaPro software prepared by PrèConsultants firm, was used. It makes it possible to assess an impact of a given technical object onto the environment during one cycle of its life or solely during its production or operation. It is also possible to conduct comparisons between many objects. Life cycle of an object under consideration is divided into three phases: its production, operation and post-use waste disposal. In each of the phases an amount and kind of used materials, energy and applied technological processes should be defined in compliance with the model. On the basis of the so formed life-cycle model, the software, by making use of the attached data bases, calculates a quantitative impact onto the environment from the side of particular chemical compounds. The impact is manifested in the form of emission of the substances or their absorption from the environment. The emissions and absorptions are grouped into four fields under impact. The emission fields are: air, water and ground, and the absorption field covers raw materials [12].

Two 2MW windmills, one land-based and the other offshore - sited (of monopile type) were subjected to the investigations. In the case of the land windmill its tower was built of steel plates and concrete. Its rotor consisted of three blades, boss and cap. The blades were made of a glass-reinforced epoxy resin (GRP). The entire structure was upgraded by using carbon fibres. The boss was of spherical form and made of spheroidal cast iron. It was assembled directly onto main shaft and had a hole for internal inspection and maintaining hydraulic system in motion. The boss and blade bearings were entirely covered and secured against exposure to external environmental effects by means of a boss cap made of GRP. The nacelle consisted of a cover and load-carrying frame, electric generator, transmission gear, transformer, inclination system and electronic system for control and steering. It was made mainly of copper and steel. Its cover, made of GRP, was intended for the protecting of mechanical elements against external environment impact. The remaining equipment of the nacelle was first of all made of steel and, to a smaller extent, of aluminium, copper, GRP and epoxy resins. Foundations of the typical size 15 x 15 x 2 m, were built of concrete and steel. Construction of the offshore windmill was analogous with the exception that a steel

monopile was used instead of the concrete foundations. Its life cycle was assumed to reach 25 years and location was limited to the European territory.

## Results and their analysis

The analysis of harmful impact levels of the offshore wind power electric plant on the environment, has demonstrated, in comparison with the land - based windmill, its higher negative effects in the category of carcinogenic compounds (0,284 DALY), organic compounds impairing respiratory system (0,002 DALY), substances causing climatic changes (0,379 DALY), radioactive elements (0,0172 DALY) as well as ecotoxic substances (1.320.083,6 PAF\*m2yr). In the six remaining impact categories the land – based wind power turbines showed a higher level of harmful impact (Tab. 3).

In the Ecoindex 99 method, results of the grouping and weighing are presented in the unit of environmental points (1 Pt). One thousand of environmental points represents the environmental impact exerted by an average European per one year [12].

Tab. 3. Results of the assessment of environmental impact characteristics of 2MW wind power electric plant, either land - based or offshore one, by using Ecoindex-99 method [acc. the authors' own work]

Impact category	Land based wind power plant	Offshore wind power plant	Unit
Carcinogens	0,21495017	0,28414975	DALY
Resp. organics	0,001658914	0,001733158	DALY
Resp. inorganics	1,210748	0,95415158	DALY
Climate change	0,35093005	0,37922162	DALY
Radiation	0,010232855	0,010761077	DALY
Ozone layer	0,000673284	0,000583665	DALY
Ecotoxicity	879423,9	1320083,6	PAF*m2yr
Acidification/Eutrophication	29954,917	25882,851	PDF*m2yr
Land use	10910,827	7562,7153	PDF*m2yr
Minerals	512922,39	504011,09	MJ surplus
Fossil fuels	2437145,9	1752643,1	MJ surplus

Fig. 6 shows results of grouping and weighing for 2MW wind power electric plants, both that based on land and offshore. A high level of harmful effects can be observed for life cycle of both the types of wind power plants in the category of fossil fuels ( for land-based one: 58.004 Pt; for offshore one : 41.712 Pt) as well as that of inorganic compounds impairing respiratory system (31.527 Pt and 24.846 Pt, respectively).

Fig. 7 illustrates results of grouping and weighing with taking into consideration the main damage categories , for land-based and offshore wind power electric plants. For life cycle of land-based wind power electric plant a higher level of harmful impact was obtained in the categories of human health (46.590 Pt) and raw materials (70.211 Pt), and, for offshore one - in the category of ecosystem quality (12.905 Pt). A little higher total level of harmful effects onto the environment in all the damage categories is attributed to the land-based wind power electric plant (125.147 Pt), in comparison to that sited offshore (109.074 Pt).

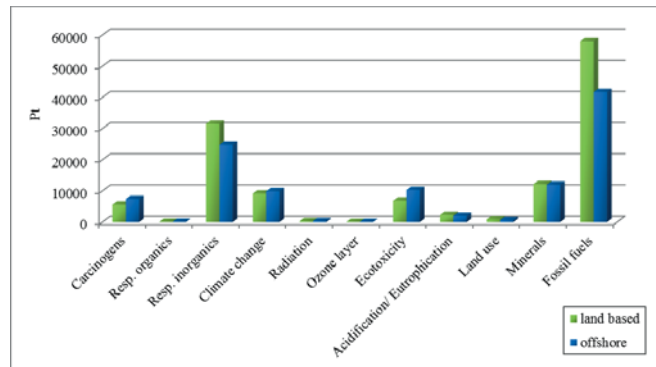


Fig. 6. Results of grouping and weighing for 2MW wind power electric plants, both that based on land and offshore, by using Ecoindex-99 method and taking into account impact categories [acc.the authors' own work]

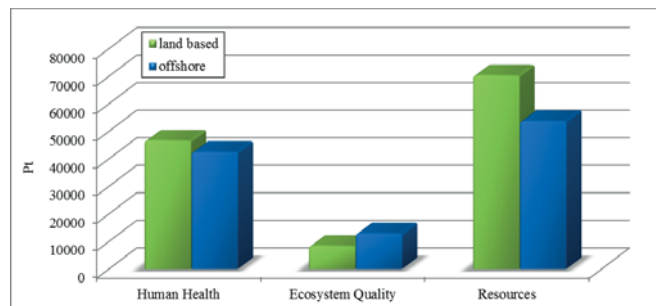


Fig. 7. Results of grouping and weighing for 2MW wind power electric plants, both that based on land and offshore, by using Ecoindex-99 method and taking into account the main damage categories [acc. the authors' own work]

## Summary and conclusions

Due to a relatively simple principle of functioning and application of novel technologies the wind power industry has become one of the most important branches of renewable energy sector. As compared with the land wind power industry, the offshore wind power industry is distinguished by a higher operational effectiveness of turbines, resulting from a greater stability and force of wind blowing over sea regions, as well as a lack of any significant technological limitations as offshore – sited turbines can be much greater in size and more effective [5, 16].

During analysis of environmental impact of life cycle of 2MW wind power electric plant, both that based on land and offshore (with monopile tower) it has been demonstrated that a higher negative impact level is attributed to land-based one in six, out of eleven, impact categories. For both the types of wind power electric plants especially high negative impact levels have been found in the categories of fossil fuels and inorganic compounds impairing respiratory system. Negative impact level in the category of human health and raw materials resources was higher in case of the land-based wind power electric plant, whereas in the category of ecosystem quality – for offshore one. The total negative impact level during one life cycle (25 years) was only a little higher (about 16.000 Pt) in case of the land-based wind power electric plant, compared to offshore one. However it should be remembered that the results may differ depending on an applied kind of the anchoring of offshore wind power electric plant.

## Bibliography

1. ACKERMANN, T.: Transmission systems for offshore wind farms . Wind power in power systems, Stockholm: Royal Institute of Technology Stockholm, 2005.
2. BARLOW, J.: Innovation and learning in complex offshore construction projects, *Research Policy*, 7-8/2000, pp.973-989.
3. carbontrust.com (access on: 2014-08-02)
4. CARMEL, E., AGARWAL, R.: The maturation of offshore sourcing of information technology work. *Information Systems Outsourcing*, 7/2006.
5. CHAKRABARTI, S.: Handbook of offshore engineering. Amsterdam: Elsevier, 2005.
6. COX, S.J., CHEYNE, A.J.T.: Assessing safety culture in offshore environments. *Safety Science*, 1-3/2000, pp. 111-129.
7. ec.europa.eu (access on: 2014-08-02)
8. energetycznie.com.pl (access on: 2014-08-02)
9. ewea.org (access on: 2014-08-02)
10. FLIZIKOWSKI J., BIELIŃSKI K.: Design of environmental energy processors ( in Polish), Wydawnictwa Uczelniane ATR ( Publisher ), Bydgoszcz, 2000.
11. GILL, A.B.: Offshore renewable energy: ecological implications of generating electricity in the coastal zone. *Journal of Applied Ecology*, 4/2005, pp.605-615.
12. GUINEE J.B., GORRREE M.: Handbook on Life Cycle Assessment – Operational Guide to the ISO Standards. Kluwer Academic Publishers, 2002.
13. KORONOWICZ T., SZANTYR J.A.: Comparative analysis of the theoretical models of ideal propulsor, ideal fluid brake, ideal screw propeller and ideal axial wind turbine. *Polish Maritime Research*, No. 2(78), vol. 20 , 2013
14. LEWANDOWSKI, W.M., Proecological renewable energy sources ( in Polish ). Wydawnictwo Naukowo-Techniczne ( Publisher ), Warsaw , 2010.
15. MEARNS, K., WHITAKER, S.M., FLIN, R.: Safety climate, safety management practice and safety performance in offshore environments. *Safety Science*, 8/2003, pp. 641-680.
16. morskiefarmywiatrowe.pl
17. MUSIAL, W., BUTTERFIELD, S., RAM, B.: Energy from offshore wind. Texas: NREL, 2006.
18. OTREMBA Z., ANDRULEWICZ E.: Physical fields during construction and operation of wind farms by example of Polish maritime areas. *Polish Maritime Research*, No 4(84) 2014, vol 21.
19. PIASECKA I., TOMPOROWSKI A.: Impact of a wind power plants life cycle on the state of the atmosphere. *Ekologia i Technika*, No. 5/2013.
20. PIASECKA I.: Development prospects for offshore wind farms ( in Polish). A chapter in the monograph : 7th „Eko-Euro-Energia” [conference] on Engineering of Renewable Energy Sources , A. Mroziński Ed., Wydawnictwo Fundacji Rozwoju Mechatroniki ( Publisher ), ISBN 978-83-938655-1-2, Bydgoszcz 2014, pp. 81-95
21. STRYJECKI, M., MIELNICZUK, K., BIEGAJ, J.: A guide over siting and environmental procedures for wind farms in Polish sea territories ( in Polish). Wyd. Fundacji na rzecz Energetyki Zrównoważonej ( Publisher ) Warsaw 2011
22. ULGIATI S., RAUGEI M., BARGIGLI S.: Overcoming the inadequacy of single-criterion approaches to Life Cycle Assessment. *Ecological Modelling*, vol. 190, 2/2006.
23. WIŚNIEWSKI, G., MICHAŁOWSKA-KNAP, K., DZIAMSKI, P., ONISZK-POPLAWSKA, A., REGULSKI, P.: A vision of development of wind power industry in Poland up to 2020 ( in Polish). Wydawnictwo Polskiego Stowarzyszenia Energetyki Wiatrowej ( Publisher ), Warsaw 2009.
24. ŻÓŁTOWSKI M.: Assessment State of Masonry Components Degradation. *Applied Mechanics and Materials* Vol. 617(2014), Trans Tech Publications, Switzerland 2014, ISSN 1662-7482. pp. 142-147.
25. ŻÓŁTOWSKI M.: Investigations of harbour brick structures by using operational modal analysis. *Polish Maritime Research*, No. 1/ (81), vol.21, ISSN 1233-2585, 2014, pp. 42-54.

## CONTACT WIHT AUTHOR

Adam Mroziński  
Izabela Piasecka

University of Technology  
and Life Sciences in Bydgoszcz  
7 Prof. Kaliskiego Al.  
85-796 Bydgoszcz  
POLAND

# MATHEMATICAL MODELLING OF ELASTIC DEFLECTION OF A TUBULAR CROSS-SECTION

Marcin ZASTEMPOWSKI, Ph.D.

Andrzej BOCHAT, Prof.

UTP University of Science and Technology, Poland

## ABSTRACT

*Cutting a tubular element into thin rings is an operation often used in engineering processes. Total work of the cutting consists of that necessary for initial deflection of cut material and the cutting work itself. This paper presents mathematical models which describe deflection of cross-section of a single tubular element as well as a single layer of tubes under action of external forces (acting and reacting ones). The deflection concerns end part of tube hence the cutting object model has been reduced to a thin ring. Results of calculation by using the developed models are presented for selected materials of tubular elements, which are commonly used for structures of the kind; moreover, they are prepared in a form of dimensionless diagrams, that makes it possible to use them for an arbitrary material.*

**Keywords:** mathematical modelling of elastic deflection, tubular elements, deflection of a ring under action of external forces

## INTRODUCTION

Issues of elastic deflection of tubular cross-sections appear first of all in:

- load carrying structures of machines and devices, including ocean engineering objects,
- steel building structures,
- pipe-line installations, e.g. water supplying, heating and transporting ones,
- technological processes connected with breaking up tubular cross-sections by cutting, used e.g. in machine industry, plastic compound processing, agriculture – cutting plant materials and their breaking up [1, 3, 8].

In machinery construction area, are mainly considered issues dealing with design principles and strength analysis of steel structures [6], principles of FEM application and numerical analysis [2, 5, 6], however detail issues concerning elastic deformations of structural elements are lacking in them.

One of the conditions for fast designing tubular structures or installations of the kind is the having at one's disposal adequate mathematical models describing process of their elastic deformation. In the subject-matter literature models which exactly describe process of elastic deformations of tubular elements under external load, especially in case where they mutually interact, are still lacking.

This work is hence aimed at the developing of mathematical models which describe deflection of a single tubular element

– a ring as well as a layer of rings under action of external forces.

## MATHEMATICAL MODEL OF ELASTIC DEFORMATIONS OF A SINGLE TUBULAR ELEMENT

To the mathematical modelling of tubular element elastic deformations the calculation principle of curved bars, based on Castigliano's theorem, was applied and the following assumptions were made [4, 7]:

1. The tubular element is under action of the force  $P$  and reaction  $R$ ;
2. A single tubular element is taken as a ring of the Young modulus  $E$  and inertia moment  $J$ ;
3. Radius of neutral layer curvature is equal to the mean radius  $r$  of the ring, calculated as follows:

$$r = \frac{d_w + d_z}{2}, \quad (1)$$

where:

$d_w$  – internal diameter of ring,  
 $d_z$  – external diameter of ring.

Energy methods based on Castigliano's and Menabrea's theorems were applied to calculation of deformations [4, 7].

Let's consider the case in which a single tubular element is placed on stiff surface and loaded by the force  $P$  (Fig.1).

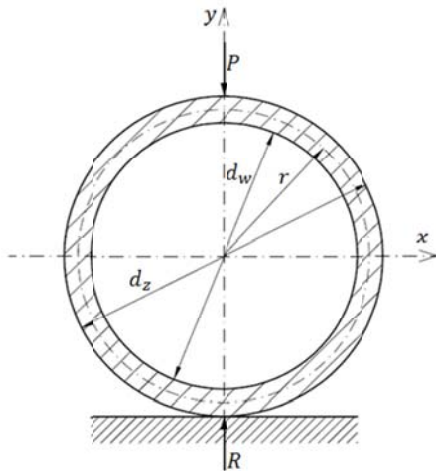


Fig.1. Cross-section of a thin ring under action of the force  $P$

The ring loaded by the force  $P$  and the support reaction  $R$  is in state of equilibrium. To determine internal forces in the ring it is cut along horizontal axis  $x$  into two symmetrical parts. The lower part of it is omitted and in places of cuts the reactions in the form of the force  $\frac{P}{2}$  and bending moment  $M_0$  are applied. The thus obtained system of forces acting on the upper part of the ring is shown in Fig. 2.

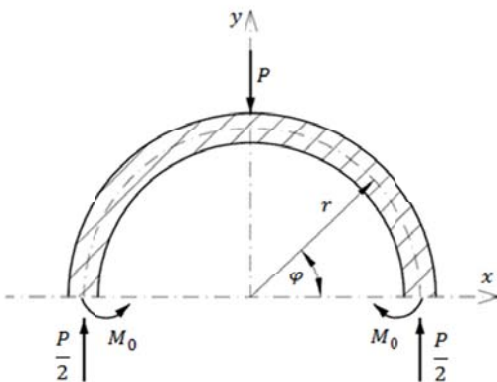


Fig. 2. The system of forces acting on the upper part of the ring

In the cross-section determined by the angle  $\varphi$  in relation to the axis  $x$  the following internal forces are acting (Fig.3):

- the force  $N$  normal to the cross-section,
- the bending moment  $M$ .

In Fig.3 the shear force  $T = \frac{P}{2} \sin \varphi$  is not indicated as it does not appear in the relation (6) which describes the elastic strain energy  $L$ .

In order to determine internal forces a pair of  $P/2$  equilibrating forces is introduced into the middle of the cross-section.

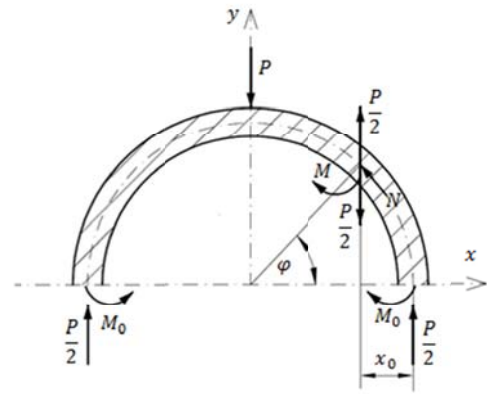


Fig. 3. The system of internal forces within the ring

The force  $N$  can be then presented as follows :

$$N = \frac{P}{2} \cos \varphi, \quad (2)$$

and the internal moment  $M$  - by using the relation :

$$M = M_0 - \frac{P}{2} x_0. \quad (3)$$

Because:

$$x_0 = r (1 - \cos \varphi), \quad (4)$$

the relation (3) takes the form:

$$M = M_0 - \frac{P}{2} r (1 - \cos \varphi). \quad (5)$$

As the moment  $M$  is hyper-static it will be determined by applying the Menabrea's theorem. The elastic strain energy  $L$  accumulated in the ring is a sum of amounts of energy due to the bending moment  $M$  and the compressive force  $N$  [4, 7]:

$$L = \frac{1}{2} \int_0^s \frac{M^2}{EJ} ds + \frac{1}{2} \int_0^s \frac{N^2}{EF} ds, \quad (6)$$

where:

$N$  - compressive force,

$M$  - bending moment,

$E$  - Young modulus,

$J$  - inertia moment,

$F$  - ring cross-section area,

$s$  - arc length of deformed ring,

$ds$  - elementary length of ring arc :  $ds = r d\varphi$ ,

$\varphi$  - cross-section location angle,

$d\varphi$  - elementary angle of  $\varphi$ .

By introducing a polar coordinate system, i.e.  $ds = r d\varphi$  the energy contained in a quarter of ring takes the form:

$$L_1 = \frac{1}{2} \int_0^{\frac{\pi}{2}} \frac{M^2}{EJ} r d\varphi + \frac{1}{2} \int_0^{\frac{\pi}{2}} \frac{N^2}{EF} r d\varphi. \quad (7)$$

Energy for the whole ring, due to its symmetry, amounts to:

$$L = 4 L_1 = \frac{2r}{EJ} \int_0^{\frac{\pi}{2}} M^2 d\varphi + \frac{2r}{EF} \int_0^{\frac{\pi}{2}} N^2 d\varphi. \quad (8)$$

In compliance with Menabrea's theorem the partial derivative of elastic strain energy of a system in relation to statically indeterminate reaction is equal to zero [4, 7]:

$$\frac{\partial L}{\partial M_0} = 0. \quad (9)$$

The relation (9) which makes it possible to determine the moment  $M_0$ , takes, after transformation, the following form:

$$\frac{\partial L}{\partial M_0} = \frac{4r}{EJ} \int_0^{\frac{\pi}{2}} M \frac{\partial M}{\partial M_0} d\varphi + \frac{4r}{EF} \int_0^{\frac{\pi}{2}} N \frac{\partial N}{\partial M_0} d\varphi = 0. \quad (10)$$

Taking into account (2) and (3) one obtains:

$$\frac{\partial M}{\partial M_0} = 1 \quad \text{and} \quad \frac{\partial N}{\partial M_0} = 0$$

The equation (10) may be then presented as follows:

$$\frac{\partial L}{\partial M_0} = \frac{4r}{EJ} \int_0^{\frac{\pi}{2}} M d\varphi = 0. \quad (11)$$

On substitution of the relation (5) into the equation (11) and simplification the following is obtained:

$$\int_0^{\frac{\pi}{2}} \left[ M_0 - \frac{P}{2} r (1 - \cos\varphi) \right] d\varphi = 0, \quad (12)$$

which after integration gives:

$$\left[ M_0 \varphi - \frac{P}{2} r \varphi + \frac{P}{2} r \sin\varphi \right]_0^{\frac{\pi}{2}} = 0 \quad (13)$$

When integration limits are taken into account and reduction is made the following is reached:

$$M_0 = \left( \frac{1}{2} - \frac{1}{\pi} \right) P r. \quad (14)$$

As the expression for the moment  $M_0$  is known, the equation for the bending moment  $M$  in the ring, resulting from the substitution of the expression (14) into the relation (5), takes the form:

$$M = \left( \frac{\cos\varphi}{2} - \frac{1}{\pi} \right) P r. \quad (15)$$

As the expression which describes bending moment is known, deflection of the ring under action of the force  $P$  can be obtained by making use of the Castigliano's theorem. To this end, partial derivative of the elastic strain energy  $L$  in relation to the force  $P$  is calculated.

$$f = \frac{\partial L}{\partial P} = \frac{4r}{EJ} \int_0^{\frac{\pi}{2}} M \frac{\partial M}{\partial P} d\varphi + \frac{4r}{EF} \int_0^{\frac{\pi}{2}} N \frac{\partial N}{\partial P} d\varphi. \quad (16)$$

By taking into account:

$$\frac{\partial M}{\partial P} = \left( \frac{\cos\varphi}{2} - \frac{1}{\pi} \right) r$$

and:

$$\frac{\partial N}{\partial P} = \frac{1}{2} \cos\varphi,$$

the following is obtained:

$$f = -\frac{4r}{EJ} \int_0^{\frac{\pi}{2}} P r^2 \left( \frac{\cos\varphi}{2} - \frac{1}{\pi} \right)^2 d\varphi + \frac{4r}{EF} \int_0^{\frac{\pi}{2}} \frac{P}{2} \cos\varphi \frac{1}{2} \cos\varphi d\varphi. \quad (17)$$

On its integration, the elastic deflection of a ring-form tubular element under action of the force  $P$ , is equal to:

$$f = \left( \frac{\pi}{4} - \frac{2}{\pi} \right) \frac{P r^3}{EJ} + \frac{\pi}{4} \frac{P r}{EF}. \quad (18)$$

The total deflection  $f$  is connected with direct action of the force  $N$  and the bending moment  $M$ . Therefore the total deflection of tubular element cross-section can be described as follows:

$$f = f_1 + f_2, \quad (19)$$

where:

$f_1$  - deflection due to action of the bending moment  $M$ ,

$f_2$  - deflection due to action of the compressive force  $N$ .

By taking into account the equations (18) and (19) the expressions for the deflections  $f_1$  and  $f_2$  take the following forms, respectively:

$$f_1 = \left( \frac{\pi}{4} - \frac{2}{\pi} \right) \frac{P r^3}{EJ} \quad (20)$$

and

$$f_2 = \frac{\pi}{4} \frac{P r}{EF}. \quad (21)$$

As the mean radius of the ring,  $r$ , ring cross-section inertia modulus  $J$  and cross-section area  $F$  are functions of the ratio of ring diameters,  $\frac{d_w}{d_z}$ , results of ring deformation

calculations will be presented in the dimensionless form  $\bar{f}$ . Actual deflection of a ring depends also on its thickness  $b$  and amounts to:

$$f = \bar{f} \frac{P}{E b}, \quad (22)$$

where:

$$\bar{f} = \bar{f}_1 + \bar{f}_2. \quad (23)$$

Fig. 4 presents a diagram of dimensionless deflection of a single ring element in function of the ratio of tubular cross-section diameters.

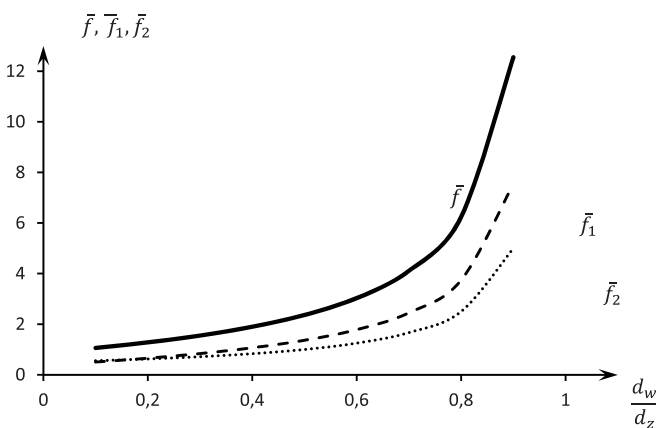


Fig. 4. Dimensionless deflection of a single ring element under action of the force  $P$ :  $\bar{f}$  - relative total deflection,  $\bar{f}_1$  - relative deflection resulting from the bending moment  $M$ ,  $\bar{f}_2$  - relative deflection resulting from the compressive force  $N$ ,  $d_w$  - ring element internal diameter,  $d_z$  - ring element external diameter

From the above presented diagram it results that for the values of the diameters ratio of a single tubular element, contained in the range of  $0,1 \div 0,9$  the relative deformation of its cross-section varies approximately linearly, and for the diameters ratio above  $0,8$  the change departs from linearity and grows fast (approximately exponentially). Run of particular curves is similar while the deflection resulting from action of the bending moment  $M$  takes greater values than that due to action of the compressive force  $N$  at given ratios of tubular element diameters Actual deflection of analysed element depends on the force  $P$ , Young modulus  $E$  and ring thickness  $b$ , that is expressed by the relation (22).

### MATHEMATICAL MODEL OF ELASTIC DEFLECTION OF A LAYER OF TUBULAR ELEMENTS

For the layer of tubular elements it is assumed that they mutually interact and their transverse deflection equals zero (Fig.5). The elements are placed in a stiff casing, free of compression and gaps between them.

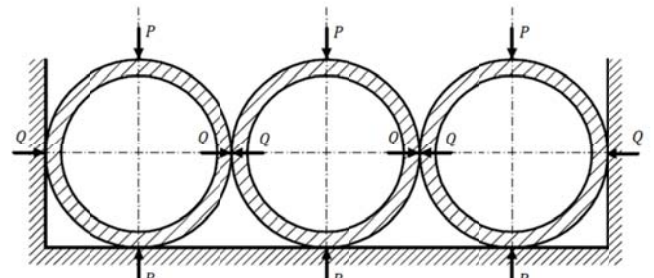


Fig. 5. Layer of ring tubular elements loaded by vertical forces  $P$

In order to solve such a system the model presented in Fig. 6 was assumed, in which the additional force  $Q$  resulting from interaction of neighbouring elements was taken into account.

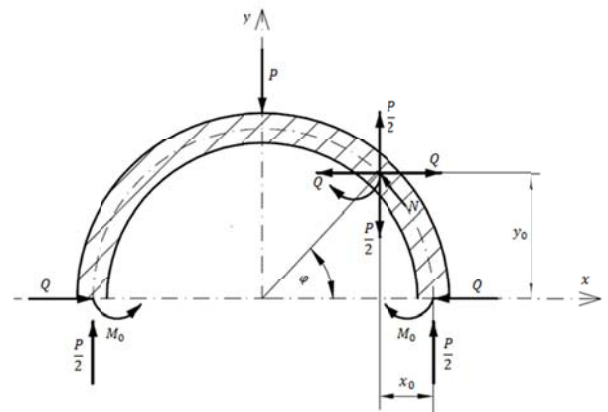


Fig. 6. The system of forces acting onto the upper part of the ring

In the cross-section determined by the angle  $\varphi$  in relation to  $x$  - axis the following internal loads are acting (Fig. 6):

- the compressive force  $N$ ,
- the bending moment  $M$ .

In order to determine the internal loads two pairs of equilibrating forces,  $\frac{P}{2}$  and  $Q$ , are introduced into the middle of the cross-section.

The force  $N$  in an arbitrary cross-section may be then described as follows:

$$N = \frac{P}{2} \cos \varphi + Q \sin \varphi, \quad (24)$$

and

the bending moment  $M$  - by the relation:

$$M = M_0 - \frac{P}{2} x_0 + Q y_0. \quad (25)$$

As:

$$x_0 = (1 - \cos \varphi) r \quad \text{and} \quad y_0 = r \sin \varphi,$$

hence, finally, the moment  $M$  is described by the relation:

$$M = M_0 - \frac{P}{2} r (1 - \cos \varphi) + Q r \sin \varphi. \quad (26)$$

Because the moment  $M_0$  and the force  $Q$  are hyper-static they were determined by using the Menabrea's theorem [4, 7]:

$$\frac{\partial L}{\partial M_0} = 0 \quad \text{oraz} \quad \frac{\partial L}{\partial Q} = 0$$

As a result, the following was obtained:

$$\frac{\partial L}{\partial M_0} = \frac{4r}{EJ} \int_0^{\frac{\pi}{2}} M \frac{\partial M}{\partial M_0} d\varphi + \frac{4r}{EF} \int_0^{\frac{\pi}{2}} N \frac{\partial N}{\partial M_0} d\varphi = 0 \quad (27)$$

and:

$$\frac{\partial L}{\partial Q} = \frac{4r}{EJ} \int_0^{\frac{\pi}{2}} M \frac{\partial M}{\partial Q} d\varphi + \frac{4r}{EF} \int_0^{\frac{\pi}{2}} N \frac{\partial N}{\partial Q} d\varphi = 0. \quad (28)$$

The partial derivatives appearing in the equations (27) and (28) obtain the following values:

$$\frac{\partial M}{\partial M_0} = 1, \quad \frac{\partial M}{\partial Q} = r \sin \varphi, \quad \frac{\partial N}{\partial M_0} = 0, \quad \frac{\partial N}{\partial Q} = \sin \varphi.$$

On their respective introduction to the equations (27) and (28) the following was reached:

$$\frac{\partial L}{\partial M_0} = \frac{4r}{EJ} \int_0^{\frac{\pi}{2}} M d\varphi = 0, \quad (29)$$

and

$$\frac{\partial L}{\partial Q} = \frac{4r}{EJ} \int_0^{\frac{\pi}{2}} M r \sin \varphi d\varphi + \frac{4r}{EF} \int_0^{\frac{\pi}{2}} N \sin \varphi d\varphi = 0. \quad (30)$$

By respective introducing the equations (24) and (26) into the equations (22) i (23) and then integrating and reducing them, the following system of equations was achieved:

$$\begin{cases} \frac{M_0}{r} + \frac{\pi}{4} Q(1 + \delta) + \frac{P}{4}(\delta - 1) = 0, & (31) \end{cases}$$

$$\begin{cases} \frac{\pi}{2} \frac{M_0}{r} + Q - \frac{P}{2} \left( \frac{\pi}{2} \right) - 1 = 0, & (32) \end{cases}$$

where the factor  $\delta$  is equal to:

$$\delta = \frac{J}{Fr^2}. \quad (33)$$

As a result of solving the above presented system of equations the following was obtained:

$$M_0 = \frac{\left( \frac{\pi^2}{2} - \pi \right) (1 + \delta) + 2(\delta - 1)}{\pi^2(1 + \delta) - 8} P r. \quad (34)$$

By assuming that:

$$\gamma = \frac{\left( \frac{\pi^2}{2} - \pi \right) (1 + \delta) + 2(\delta - 1)}{\pi^2(1 + \delta) - 8}. \quad (35)$$

the equation (34) takes the form:

$$M_0 = \gamma P r. \quad (36)$$

As a result of solving the system of the equations (31) and (32) the relation for  $Q$  was obtained:

$$Q = \frac{\pi(1 - \delta) + 4 - 2\pi}{\pi^2(1 + \delta) - 8} P \quad (37)$$

By assuming that:

$$\alpha = \frac{\pi(1 - \delta) + 4 - 2\pi}{\pi^2(1 + \delta) - 8},$$

the relation (37) takes the form:

$$Q = \alpha P \quad (38)$$

As the expressions describing the bending moment  $M_0$  and the force  $Q$  are already known, it is possible to determine the relation for the bending moment  $M$  by introducing the relations (36) and (37) into the expression (26):

$$M = P r \left( \gamma - \frac{1}{2} + \frac{1}{2} \cos \varphi + \alpha \sin \varphi \right). \quad (39)$$

In order to determine deflection of the ring under action of the force  $P$  the Castigliano's theorem should be used by calculating the partial derivative of the elastic strain energy  $L$  against the force  $P$ . Hence:

$$f = \frac{\partial L}{\partial P} = \frac{4r}{EJ} \int_0^{\frac{\pi}{2}} M \frac{\partial M}{\partial P} d\varphi + \frac{4r}{EF} \int_0^{\frac{\pi}{2}} N \frac{\partial N}{\partial P} d\varphi. \quad (40)$$

The total deflection  $f$  is associated with common action the compressive force  $N$  and the bending moment  $M$ . Hence:

$$f = f_1 + f_2, \quad (41)$$

where:

$f_1$ - deflection resulting from the bending moment  $M$ ,  
 $f_2$ - deflection resulting from the compressive force  $N$ .

Therefore :

$$f_1 = \frac{4r}{EJ} \int_0^{\frac{\pi}{2}} M \frac{\partial M}{\partial P} d\varphi. \quad (42)$$

and:

$$f_2 = \frac{4r}{EF} \int_0^{\frac{\pi}{2}} N \frac{\partial N}{\partial P} d\varphi. \quad (43)$$

By taking into account the relation:

$$\frac{\partial M}{\partial P} = r \left( \gamma - \frac{1}{2} + \frac{1}{2} \cos \varphi + \alpha \sin \varphi \right)$$

and :

$$\frac{\partial N}{\partial P} = \frac{1}{2} \cos \varphi + \alpha \sin \varphi,$$

the following is obtained:

$$f_1 = \frac{4Pr^3}{EJ} \int_0^{\frac{\pi}{2}} \left( \gamma - \frac{1}{2} + \frac{1}{2} \cos \varphi + \alpha \sin \varphi \right)^2 d\varphi. \quad (44)$$

And,  $f_2$  is described by the relation :

$$f_2 = \frac{4Pr}{EF} \int_0^{\frac{\pi}{2}} \left( \frac{1}{2} \cos \varphi + \alpha \sin \varphi \right)^2 d\varphi. \quad (45)$$

The equations (44) and (45) may be presented in the form :

$$f_1 = \frac{4Pr^3}{EJ} g_1, \quad (46)$$

$$f_2 = \frac{4Pr}{EF} g_2, \quad (47)$$

by assuming that:

$$g_1 = \int_0^{\frac{\pi}{2}} \left( \gamma - \frac{1}{2} + \frac{1}{2} \cos \varphi + \alpha \sin \varphi \right)^2 d\varphi, \quad (48)$$

$$g_2 = \int_0^{\frac{\pi}{2}} \left( \frac{1}{2} \cos \varphi + \alpha \sin \varphi \right)^2 d\varphi. \quad (49)$$

In view of the complex form of the equations (48) and (49) the factors  $g_1$  and  $g_2$  were determined by numerical calculations whose results are presented in Tab. 1.

Tab. 1. Results of calculation of the factors  $g_1$  and  $g_2$

$\frac{d_w}{d_z}$	0,1	0,2	0,3	0,4
$g_1$	0,0305	0,0273	0,0248	0,0231
$g_2$	0,2243	0,2412	0,2553	0,2664

$\frac{d_w}{d_z}$	0,5	0,6	0,7	0,8	0,9
$g_1$	0,0219	0,0211	0,0206	0,0203	0,0200
$g_2$	0,2748	0,2808	0,2849	0,2874	0,2887

In Fig. 7 is presented a diagram of dimensionless deflection of a ring tubular element layer in function of the ratio of tubular element diameters.

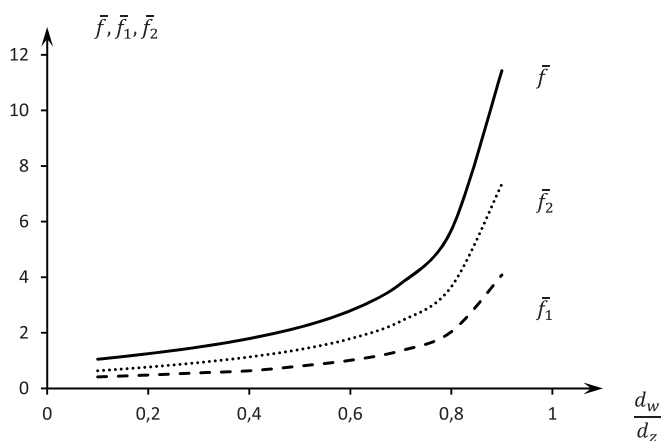


Fig. 7. Dimensionless deflection of ring tubular elements placed in a layer under action of the force  $P$ :  $\bar{f}$  - relative total deflection,  $\bar{f}_1$  - relative deflection resulting from the bending moment  $M$ ,  $\bar{f}_2$  - relative deflection resulting from the compressive force  $N$ ,  $d_w$  - tubular element internal diameter,  $d_z$  - tubular element external diameter

From the above presented diagram it results that for the values of the ratio of diameters of tubular elements placed in a layer, contained in the range of 0,1÷0,9 the relative deformation of their cross-sections varies approximately linearly, and for the diameters ratio above 0,8 the change departs from linearity and grows fast (approximately exponentially). Run of particular curves is similar and - in contrast to a single element - the deflection of tubular element layer due to action of the compressive force  $N$  takes greater values than that resulting from action of the bending moment  $M$  at given ratios of tubular element diameters. Actual deflection of the analysed tubular element system depends on the force  $P$ , Young modulus  $E$  and diameter  $d_z$ .

Exemplary calculations of deformations of tubular element cross-sections were additionally performed for selected

materials. In the calculations the tubular elements of commercial dimensions characteristic for a given material were considered.

Tab. 2 presents calculation results of deflection of a single tubular element and a layer of tubular elements under action of external forces, made of steel of the Young modulus  $E = 210$  GPa, under action of the force  $P = 100$  N. The calculations were performed for the element thickness  $b = 10$  mm.

Tab. 2. Values of deflection of tubular elements made of steel

No.	Element dimensions	Deflection $f$ [ $\mu\text{m}$ ]	
		Single element	Tubular elements layer
1	¼" (13,5x2,35)	1,22	0,43
2	½" (21,3x2,65)	3,84	0,97
3	¾" (26,9x2,65)	8,32	1,78
4	1" (33,7x3,25)	8,92	1,89
5	1½" (48,3x3,25)	28,56	5,21

Tab. 3 presents calculation results of deflection of a single tubular element and a layer of tubular elements under action of external forces, made of copper of the Young modulus  $E = 110$  GPa, under action of the force  $P = 100$  N. The calculations were performed for the element thickness  $b = 10$  mm.

Tab. 3. Values of deflection of tubular elements made of copper

No.	Element dimensions	Deflection $f$ [ $\mu\text{m}$ ]	
		Single element	Tubular elements layer
1	10x1	15,11	3,27
2	12x1	27,40	5,40
3	15x1	56,17	10,22
4	18x1	100,3	17,45
5	22x1	188,6	31,71

Tab. 4 presents calculation results of deflection of a single tubular element and a layer of tubular elements under action of external forces, made of aluminium of the Young modulus  $E = 70$  GPa, under action of the force  $P = 100$  N. The calculations were performed for the element thickness  $b = 10$  mm.

Tab. 4. Values of deflection of tubular elements made of aluminium

No.	Element dimensions	Deflection $f$ [ $\mu\text{m}$ ]	
		Single element	Tubular elements layer
1	6x1	4,27	1,43
2	8x1	11,33	2,86
3	10x1	23,75	5,14
4	12x1	43,05	8,49
5	15x1	88,27	16,06

## SUMMARY

The mathematical models presented in this work make it possible to carry out simulation of the process of elastic deflection of tubular elements in the form of rings. It has been proved that, according to the developed model, mutual interaction of elements (rings) placed in a layer significantly influences values of obtained deflections. It can be read from the results of simulation calculations presented in this work. The results are given in a form of dimensionless diagrams as well as in the tables containing values of deflections of tubular element (ring) cross-sections, calculated for selected commercial dimensions and materials.

After positive experimental verification, the developed models would be ready for application in design stage of selected structures.

## BIBLIOGRAPHY

1. Bochat A., Grzonkowski R., Zastempowski M.: Analysis of plant stalk cutting and a novel cutting drum unit (in Polish). *Inżynieria i Aparatura Chemiczna*, No.1-2/2005.
2. Bohdal I., Kukielka L.: Application of variational and FEM methods to the modelling and numerical analysis of guillotine process for geometrical and physical nonlinearity. *Mechanika* vol. 20, No. 2, 2014. pp. 197-204.
3. Chattopahyay P.S., Pandey K.P.: Mechanical properties of sorghum in relation to quasi-static deformation. *Journal of Agricultural Engineering Research*. Vol.73, 1999.
4. Jakubowicz A, Orłoś Z.: *Strength of materials* (in Polish). WNT Publishers, Warsaw, 1999.
5. Malag L, Kukielka L.: The sensitivity analysis of influence of chosen material parameters on the properties of surface layer product after burnishing. *Steel Research International*. Volume SPL. ISSUE, 2012, pp. 1335-1338.
6. Malag L., Kukielka L., Kukielka K., Kulakowska A., Bohdal L., Patyk R.: Problems determining of the mechanical properties of metallic materials from the tensile test in the aspect of numerical calculations of the technological

processes. Applied Mechanics and Materials. Vol. 474, 2014, pp. 454-459

7. Niezgodziński M.E., Niezgodziński T.: Strength of materials ( in Polish ). PWN Publishers, Warsaw, 1984.
8. O'Doherty M.J., Huber J.A., Dyson J., Marshall C.J.: A study of the physical and mechanical properties of wheat straw. Journal of Agricultural Engineering Research, Vol.62, 1995.
9. Szala G. Comments on linear summation hypothesis of fatigue failures. Polish Maritime Research. Nr 3 (83) Vol.21, 2014. pp. 77-85.

#### **CONTACT WITH THE AUTHOR**

Marcin ZASTEMPOWSKI,  
Andrzej BOCHAT

UTP University of Science and Technology  
20 Ks. Kordeckiego St.  
85-225 Bydgoszcz  
**POLAND**

# LOW TEMPERATURE PROPERTIES OF FUEL MIXTURES OF KEROSENE AND FAME TYPE USED TO SUPPLY TURBINE ENGINES IN MARINE AND OTHER NON-AERONAUTICAL APPLICATIONS

Wojciech Dzięgielewski, Ph. D  
Bartosz Gawron, Ph. D  
Andrzej Kulczycki, Assoc. Prof.  
Air Force Institute of Technology

## ABSTRACT

*A worldwide trend to popularise gradually increasing use of biofuels in various applications was a motivation for gaining interest in FAME as a commonly available biocomponent to fuels combusted in turbine engines. These engines are mainly used in aeronautics, but many of them are also used in other, non-aeronautical areas, including marine navigation. Specific conditions in which fuels are combusted in turbine engines used in these applications are the reason why fuel mixtures of kerosene and FAME type should reveal relevant low temperature characteristics. The article presents results of tests of low temperature properties of mixtures of the jet fuel Jet A-1 and methyl esters of higher fatty acids (FAME). The prepared mixtures contained different contents of FAME. The obtained results present changes of: viscosity, cloud point, pour point, crystallising point, and cold filter plugging point, depending on the percentage by volume of FAME. They also prove that the course of changes of low temperature properties of these mixtures is affected by chemical structure of the biocomponent.*

**Keywords:** jet fuel, biocomponents, marine turbine engine, low temperature properties

## Introduction

The idea of introducing biocomponents to liquid fuels combusted in engines in all transport sectors has been popularised since the turn of the twenty-first century. Possible applications of biofuels in land and sea transport, and in aviation were indicated. The idea of using biocomponents in fuels also expanded to the area of fuel supply for various types of engines, including combustion engines of both piston and turbine type [1 – 4].

In years 2007-2009, a research programme was conducted in the Air Force Institute of Technology which was oriented on examining the applicability of the biocomponent of FAME type – methyl esters of higher fatty acids, in aircraft turbine engines. The performed tests [5] have revealed limited applicability of the 1<sup>st</sup> generation biocomponent – FAME as the component of fuels used in aircraft applications. It turned out that the most severe limitation is imposed by the effect of esters on fuel properties associated with water separation, which in case of aeronautical applications can constitute a threat to the safety of operation. Even small additive of FAME leads to remarkable changes in the fuel surface tension, thus disturbing the mechanism of water separation from fuel

in coalescer filters. As a result, the water cannot be removed and the risk of trouble in low temperature operation increases. However, the above problem does not disqualify the FAME type biocomponent as the component of fuels used to supply turbine engines in other transport sectors. [6,7].

Due to their numerous structural and operating advantages, turbine engines are being more and more commonly used in other areas of engineering than aviation. In particular, they find wide application as watercraft propulsion units. High costs of new engine designs are a reason why marine turbine engines are frequently derived from tried and tested aircraft structures of propeller and helicopter types. As far as the supply system is concerned, their modernisation consists in adapting these engines to combust diesel fuels and work in sea environment [8]. Turbine engines can also be used as propulsion for power generating sets, or stationary peak power plants.

In real operation the dependence of fuel properties on temperature is of high importance. When the temperature decreases, essential rheological properties of the operating liquid change. Loss of fluidity of the fuel can lead to filter plugging or the increase of pumping resistance loss, which can make pumping the fuel from tanks to the engine impossible.

Low temperature properties are extremely important when FAME is added to the fuel, as a main disadvantage of this biocomponent is that it reveals remarkably worse low temperature properties than oil products.

The paper presents results of tests of low temperature properties of mixtures of the jet fuel Jet A-1 with FAME in different proportions. Discussed are changes of essential low temperature parameters of the tested mixtures depending on the percentage by volume of FAME in the fuel, and on differences in chemical structure of the biocomponent itself. The obtained results reveal that low temperature properties of Jet A-1/FAME mixtures are subject to changes depending on concentration of the biocomponent. These changes are not monotonous in nature and strongly depend on the chemical structure of FAME.

## 2. Materials and research methodology

### Fuel mixtures

Samples of Jet A-1 fuel for aircraft turbine engines which were used in the tests came from two different sources. Moreover, the used methyl esters of higher fatty acids also came from different agro refineries. One sample was prepared from a mixture of different esters.

Initially, test were performed for individual basic components, i.e. the jet fuel Jet A-1 and FAME which were then used for preparing the mixtures. All samples met basic standard requirements, but differences between properties of particular FAME samples suggested different chemical composition.

Basic components which were used to prepare mixtures were:

1. JetA-1 (source 1) and FAME (agro refinery) –symbol M1.
2. JetA-1 (source 1) and FAME (mixture) – symbol M2.
3. JetA-1 (source 2) and FAME (agro refinery) – symbol M3.
4. JetA-1 (source 2) and FAME (mixture) – symbol M4.

Each mixture contained different percentages of methyl esters of higher fatty acids – 0,5%, 1%, 2%, 3%, 4%, 5%, 6%, 7%, 8%, 9%, 10%, 11%, 12%, 13%, 14%, 15%, 16%, 17%, 18%, 19% and 20% (V/V).

### Research methodology

Low temperature properties of the mixtures were tested in the Division of Propellants and Greases, Air Force Institute of Technology, based on standardised and accredited test methods.

Basic low temperature properties of fuels include: kinematic viscosity, crystallising point, cloud point – CP, pour point – PP, and cold filter plugging point – CFPP. A detailed description of the procedure used to assess each of these properties is given in the test method (Table 1).

Tab. 1. Test methods used to examine low temperature properties of kerosene fuel

Name of property	Test method
Kinematic viscosity at temperature -20 °C, 0 °C, +20 °C	PN-EN ISO 3104
Crystallising point	ASTM D 2386
Cloud point	ASTM D 2500
Pour point	ASTM D 97
Cold filter plugging point	PN-EN-116

## Results of tests and their discussion

The effect of FAME content on kinematic viscosity of the selected mixtures M2 and M4 at the temperatures of -20 °C, 0 °C, and +20 °C is illustrated in Figs. 1 and 2. For two remaining mixtures the qualitative course of kinematic viscosity changes at the above temperatures was similar.

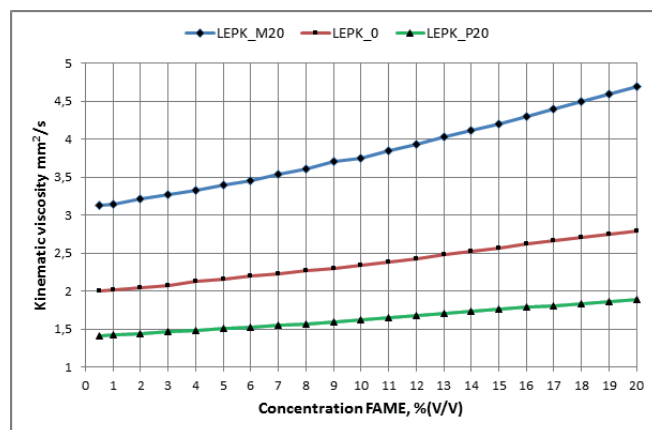


Fig.1. Viscosity changes of mixture M2 depending on FAME concentration and test temperature (LEPK\_M20 – kinematic viscosity at temp. of -20°C, LEPK\_0 – kinematic viscosity at temp. of 0 °C, LEPK\_P20 – kinematic viscosity at temp. of +20 °C)

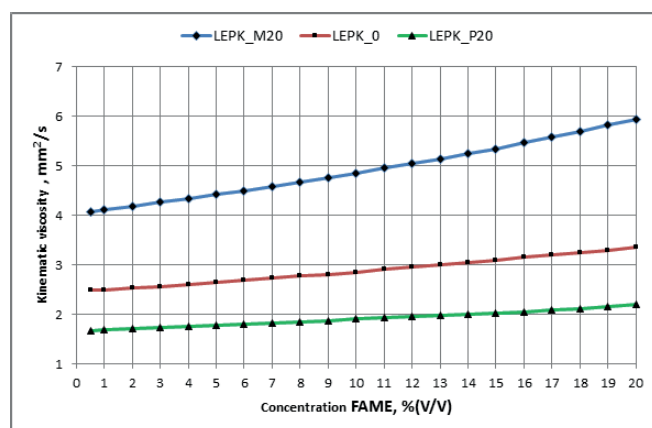


Fig.2. Viscosity changes of mixture M4 depending on FAME concentration and test temperature (LEPK\_M20 – kinematic viscosity at temp. of -20°C, LEPK\_0 – kinematic viscosity at temp. of 0 °C, LEPK\_P20 – kinematic viscosity at temp. of +20 °C)

For all types of mixtures, kinematic viscosity values at temperatures of -20 °C, 0 °C, and +20 °C reveal an increasing trend with the increase of the content of esters. Up to 20%(V/V) of FAME content, the values of this parameter are within the limits of the standards [9,10] for jet fuel (max. 8,0 mm<sup>2</sup>/s at temp. of -20 °C). The highest kinematic viscosity, equal to 5,937 mm<sup>2</sup>/s at temp. of -20 °C, was obtained for mixture M4 and FAME content equal to 20%.

Below given are the results and analysis of the effect of FAME content on typical low temperature properties of fuel mixtures.

Taking into account physical properties of the biocomponent (Table 2) – especially worsening of these properties in low temperatures (methyl esters of fatty acids produced from rapeseed oil – RME (rapeseed methyl ester) – lose fluidity at temperatures below -18 °C, while for esters produced from other vegetable or animal fats this temperature is even higher), an expected result was remarkable worsening of low temperature properties of the prepared mixtures.

Tab.2. Low temperature properties of basic fuels, based on literature data [11] and in-house tests

Parameter	RME		JetA-1	
	Results acc. to [11]	In-house test	Results acc. to [11]	In-house test
Pour point (PP), °C	-12	-	-51	-
Cloud point(CP), °C	-4.1	-	-26.0	-
Crystallising point, °C	-	-	-	-55
Cold filter plugging point(CFPP), °C	-15	-15	-46	-49

Results of pour point (PP) tests for mixtures containing different contents of FAME are shown in Fig. 3.

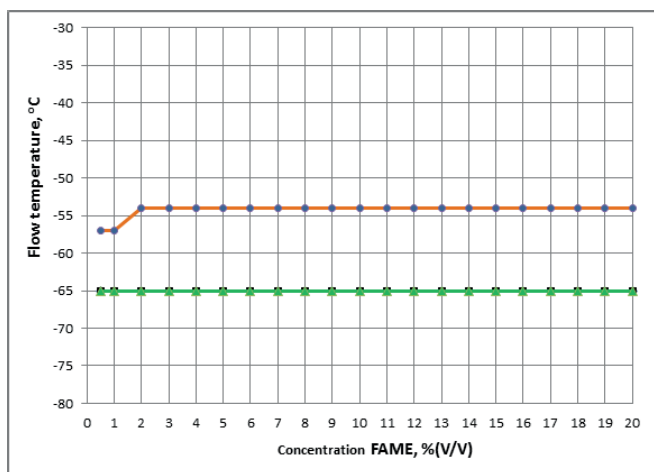


Fig. 3. Pour point changes for mixtures of jet fuel Jet A-1 with different FAME contents

The obtained results differ from those expected, as for all tested samples of mixture the pour point does not change with the increasing FAME content in the jet fuel JetA-1, while the results presented in Ref. [11] suggest that the increasing content of FAME in the mixture should increase the pour

point of this mixture. The pour point for the pure jet fuel is approximately equal to -51 °C, while the results obtained in the tests suggest that the pour points of the prepared mixtures are lower.

The course of changes of the cloud point (Fig. 4) for all mixtures and the FAME content from 0 to 20% (V/V) also differs from that shown in Ref. [11]. Some similarities can only be observed for the FAME content above 10%, when for the increased content of this biocomponent in the tested mixtures a regular cloud point increase is observed. The highest cloud point value, equal to -27 °C, occurs for all tested mixtures when the FAME content in the fuel is 20% (V/V).

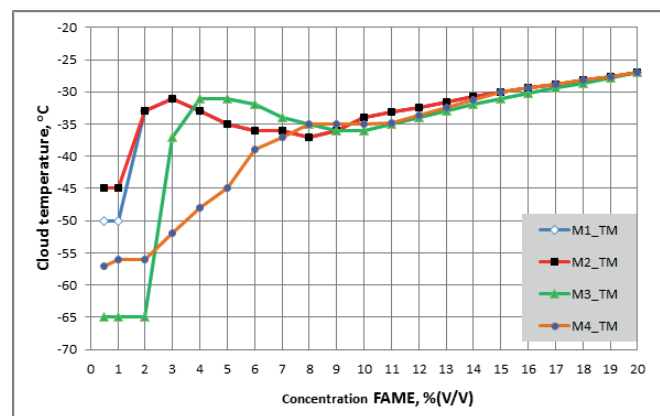


Fig. 4. Cloud point changes for mixtures of jet fuel JetA-1 with different FAME contents.

The highest irregularities are observed within the FAME content range of up to about 10%. Here, a general trend of cloud point changes for all three mixtures is similar, i.e. for low FAME content the cloud point increase rapidly, and then decreases with the increasing FAME content. The obtained results are in opposition to commonly accepted opinions that the FAME content only leads to worsening of low temperature properties of the fuel mixture. The presented tests reveal that a certain FAME content can result in decreasing of the cloud point. This effect can be explained by the existence of different mechanisms of cooperation of fuel components at their different concentrations in the mixture. Only for the mixture M4 a continuous increasing trend of this parameter is observed for the increasing FAME content. Different patterns of particular curves clearly indicate the effect of differences in the chemical composition of FAME (esters in particular mixtures came from different deliverers) on the cloud point of the examined mixtures.

The course of changes of the crystallising point in relation to FAME content is very irregular for the examined mixtures (Fig. 5), with no clear trend observed for this parameter.

Up to about 10% (V/V) of FAME content, the crystallising point for all mixtures changes intensively and irregularly (its values increase and decrease), while above 10%(V/V) of FAME content in the fuel, curve patterns become more regular. In cases of mixtures M1 and M2 the crystallising point values decrease with the increasing FAME content. For mixture M4 its values initially increase and then decrease,

and for mixture M3 the crystallising point values slightly increase. All this means that also for the crystallising point, certain FAME content in the fuel can decrease its value i.e. improve low temperature properties of the mixture. Like for previous parameters, this conclusion is also in some opposition to common opinions. It is noteworthy that the tests brought numerous crystallising point values for Jet A-1/FAME mixtures which were lower than  $-55^{\circ}\text{C}$ , which is the crystallising point for pure jet fuel (Table 2).

Other data than that published in the literature [11] was also obtained in cold filter plugging point (CFPP) tests. These results are shown in Fig. 6.

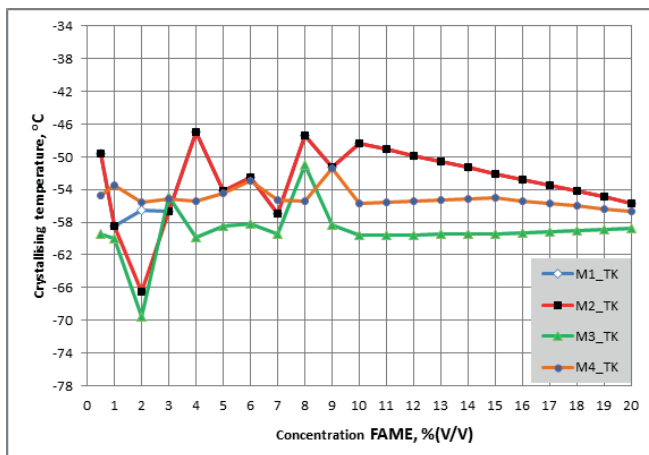


Fig. 5. Crystallising point changes for mixtures of jet fuel JetA-1 with different FAME contents.

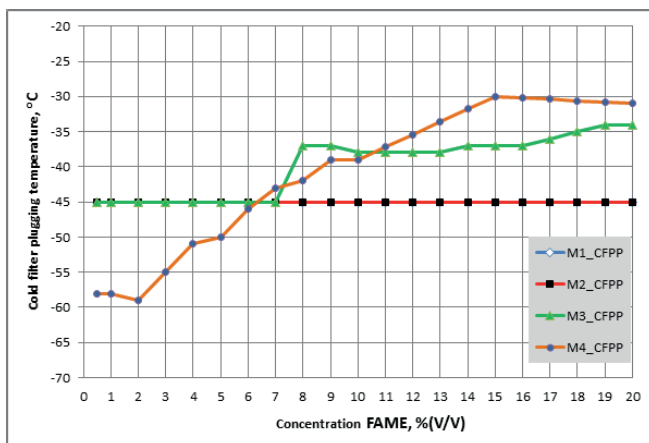


Fig. 6. Cold filter plugging point changes for mixtures of jet fuel JetA-1 with different FAME contents.

The increasing FAME content in the fuel does not affect this parameter in case of mixtures M1 and M2, as well as for mixture M3 with FAME content of up to 7% (V/V). For the latter mixture, within the FAME content above 7% (V/V) the values of this parameter increase with the increasing FAME content. Only in case of mixture M4 almost regular relation between CFPP and FAME content was observed:

the increasing FAME content in the mixture led to the increase of CFPP. The above results illustrate high importance of chemical composition of the prepared mixtures, which decides about the existence of certain mechanisms of cooperation between particular components and thus affects the cold filter plugging point value. Also in this case, a statement that the presence of FAME definitely worsens low temperature properties concerning CFPP is not true.

## Summary and concluding remarks

1. The performed tests of low temperature properties of Jet A-1/FAME mixtures have indicated some potential for the use of this biocomponent to supply turbine engines in marine and other non-aeronautical applications. Pure FAME reveals poor low temperature properties, which limits its applicability. However, low temperature properties of oil fuel mixtures with this biocomponent allow them to be used within temperatures down to about  $-25^{\circ}\text{C}$ , as the highest value of the cold filter plugging point recorded during the tests was approximately equal to  $-30^{\circ}\text{C}$ , and the highest cloud point value was  $-27^{\circ}\text{C}$ .
2. In case of turbine engines used in marine engineering, there is no threat for the fuel to be exposed to such low values. Consequently, introducing FAME to the fuel will not endanger engine operation in this area.
3. Low temperature properties of mixtures of the jet fuel Jet A-1 and FAME depend on FAME content by volume in the fuel and its chemical composition. Differences in chemical composition of FAME which are significant to low temperature properties result from the quality and type of raw materials used by different producers and the applied transesterification technology.
4. Low temperature parameters of Jet A-1/FAME fuels do not change in proportion to the content of this biocomponent in the fuel. Within some ranges the increased FAME content in the fuel worsens its low temperature properties, although some improvement is also observed for low FAME contents.
5. The above conclusions clearly indicate the existence of some cooperation between FAME components and those of the mineral fuel Jet A-1. The mechanism of this cooperation is strongly affected by chemical composition of FAME. An attempt to recognise the course and reasons of this mechanism will be the subject of further research.

## References

1. Dziągiewski W., Karp G., Factors and Threats Regarding Sustainability criteria Meeting In Chain of Fuels' Biocomponents Production in Poland; Polish Journal of Environmental Studies, vol. 22, No. 6A (2013), ss. 7 – 11.
2. Kaźmierczak U., Kulczycki A., The Possibilities of

Biocomponents to Meet the Sustainability Criteria Turing years 2017 and 2018 in the Extend of GHG Emission by Modification of their Production Technology and using RES in Energy Infrastructure, Polish Journal of Environmental Studies, vol. 22, No. 6A (2013), ss. 18 – 21.

3. Dziągiewski W., Gawron B., Kaźmierczak U., Kulczycki A., Butanol / biobutanol as a Component of an Aviation and Diesel Fuels; Journal of Kones Powertrain and Transport, vol. 21, No. 2 2014, ss. 69 – 76
4. Wright M., Biomass to Alcohol to Jet/Diesel; Research Department Chemistry Division Naval Air Warfare Center Weapons Division, China Lake, CA 93555
5. Dziągiewski W., Biofuel for aircraft turbine engines (in Polish), Final report from the research and development project “Biofuel for aircraft turbine engines”, ITWL 2010.
6. Dziągiewski W., Gawron B., Testing applicability of 1st generation biocomponents for fuels used in aircraft turbine engines (in Polish), Prace Naukowe Instytutu Technicznego Wojsk Lotniczych, nr 30 2012.
7. Dziągiewski W., Kulczycki A., Aircraft biofuels based on biohydrocarbons and other biocomponents (in Polish), Journal of KONBIN, nr 1(17) 2011.
8. Niedziałek B., Balicki W., Gryglewski W., The applicability of GTD-350 engine for non-aeronautical purposes (in Polish), Conference „Silwoj”, Jurata 2003.
9. Defence Standard NO-91-A258-4 „Propellants and greases. Fuel for aircraft turbine engines (in Polish) . Paliwokod NATO F-35”.
10. Aviation Fuel Quality Requirements For Jointly Operated Systems (AFQRJOS) Issue 26 – May 2012.
11. Baczewski K., Szczawiński S., Investigation properties of rapeseed oil methyl esters/aviation turbine fuel Jet A-1 blends, Journal of KONES Powertrain and Transport, Vol. 18, No. 1 2011.

## CONTACT WITH AUTHOR

Wojciech Dziągiewski  
Bartosz Gawron  
Andrzej Kulczycki

Air Force Institute of Technology  
6 Księcia Bolesława St.  
01-494 Warszawa  
**POLAND**